

Pavan Kumar · Haroon Sajjad  
Bhagwan Singh Chaudhary  
J. S. Rawat · Meenu Rani *Editors*

# Remote Sensing and GIScience

Challenges and Future Directions

 Springer

# Remote Sensing and GIScience


Pavan Kumar • Haroon Sajjad  
Bhagwan Singh Chaudhary • J. S. Rawat  
Meenu Rani  
Editors

# Remote Sensing and GIScience

Challenges and Future Directions

 Springer

*Editors*

Pavan Kumar   
College of Horticulture and Forestry  
Rani Lakshmi Bai Central Agricultural  
University  
Jhansi, Uttar Pradesh, India

Haroon Sajjad  
Department of Geography, Faculty of  
Natural Sciences  
Jamia Millia Islamia  
New Delhi, Delhi, India

Bhagwan Singh Chaudhary  
Department of Geophysics  
Kurukshetra University  
Kurukshetra, Haryana, India

J. S. Rawat  
Remote Sensing and GIS  
Kumaun University  
Almora, Uttarakhand, India

Meenu Rani  
Department of Geography  
Kumaun University  
Nainital, Uttarakhand, India

ISBN 978-3-030-55091-2      ISBN 978-3-030-55092-9 (eBook)  
<https://doi.org/10.1007/978-3-030-55092-9>

© The Editor(s) (if applicable) and The Author(s), under exclusive license to Springer Nature Switzerland AG 2021

This work is subject to copyright. All rights are solely and exclusively licensed by the Publisher, whether the whole or part of the material is concerned, specifically the rights of translation, reprinting, reuse of illustrations, recitation, broadcasting, reproduction on microfilms or in any other physical way, and transmission or information storage and retrieval, electronic adaptation, computer software, or by similar or dissimilar methodology now known or hereafter developed.

The use of general descriptive names, registered names, trademarks, service marks, etc. in this publication does not imply, even in the absence of a specific statement, that such names are exempt from the relevant protective laws and regulations and therefore free for general use.

The publisher, the authors, and the editors are safe to assume that the advice and information in this book are believed to be true and accurate at the date of publication. Neither the publisher nor the authors or the editors give a warranty, expressed or implied, with respect to the material contained herein or for any errors or omissions that may have been made. The publisher remains neutral with regard to jurisdictional claims in published maps and institutional affiliations.

This Springer imprint is published by the registered company Springer Nature Switzerland AG  
The registered company address is: Gewerbestrasse 11, 6330 Cham, Switzerland

# Foreword

Remote sensing (RS) has emerged as an important technique and tool that blends developments in computer science and Geographical Information System (GIS) for analyzing the various dimensions of the environment and adheres to its applications in almost every field. Remote sensing being cost and time effective is helpful in analyzing the temporal and spatial pattern of natural resources and distribution of population. The multispectral remote sensing datasets have provided effective assessment of natural resources and their management. These datasets are also promising in determining the population pattern, urban sprawl, and changes in land use/land cover. RS and GIScience have been proved effective tools for the scientific community to analyze spatial phenomena on Earth and consequently for policy formulation globally. However, certain challenges in handling large datasets and complex data formats still remain.

This book provides a comprehensive compilation of the use of remote sensing and GIS for different applications. Agriculture productivity, air pollution, habitat suitability mapping, assessment of vegetation vigor, as well as various data sets and their applications in assessment of natural resources, mapping the population pattern, and land use/land cover will help the readers to obtain insightful information about the complexity and challenges in their assessment. This book provides imperative assessment based on remote sensing technique for measuring the spatio-temporal variability of population, dynamics of land use, natural resources, and their sustainable management. I believe this work will help different stakeholders to understand different aspects of remote sensing along with the application of GIScience for various applications.

I congratulate the editors, the contributors' from different parts of the country, and the publisher for bringing out a timely publication depicting challenges and future directions in remote sensing and GIScience and hope that this important book shall serve as a reference for different institutions working in this area.

Vice-Chancellor, Rani Lakshmi Bai  
Central Agricultural University, Jhansi,  
Uttar Pradesh, India

Prof. Arvind Kumar

# Contents

## Part I General

|   |          |
|---|----------|
| <b>Introduction to Challenges and Future Directions in Remote Sensing and GIScience . . . . .</b> | <b>3</b> |
| Raihan Ahmed, Pavan Kumar, and Meenu Rani   |          |

## Part II Challenges in Sustainable Natural Resources Management

|  |           |
|--|-----------|
| <b>Environmental and Livelihood Impact Assessment of 2013 Flash Flood in Alakananda and Mandakini River Valley, Uttarakhand (India), Using Environmental Evaluation System and Geospatial Techniques . . . . .</b> | <b>11</b> |
| Shruti Tripathi, G. Areendran, N. C. Gupta, Krishna Raj, and Mehebab Sahana  |           |
| <b>Assessment of Vegetation Vigor Using Integrated Synthetic Aperture Radars . . . . .</b>   | <b>35</b> |
| Suman Sinha  |           |
| <b>Landslide Susceptibility Mapping Using Bivariate Frequency Ratio Model and Geospatial Techniques: A Case from Karbi Anglong West District in Assam, India . . . . .</b>   | <b>59</b> |
| Raihan Ahmed, Ravinder Singh, and Haroon Sajjad  |           |
| <b>Retreating Glacier Dynamics Over the Last Quarter of a Century in Uttarakhand Region Using Optical Sensor Time Series Data . . . . .</b>  | <b>75</b> |
| Himanshu Kalita, Tapan Ghosh, Meenu Rani, J. S. Rawat, Ram Kumar Singh, Susheel Kumar Singh, and Pavan Kumar   |           |

### **Part III Remote Sensing and GIScience in Urban Growth Management**

|  |     |
|--|-----|
| <b>Studying the Impact of Urbanization on HYV Rice Fields at a Local Level Using Fine Resolution Temporal RISAT-1 Datasets</b> . . . . .                                       | 97  |
| Koel Roychowdhury  |     |
| <b>Identification of Impervious Built-Up Surface Features Using ResourceSat-2 LISS-III-Based Novel Optical Built-Up Index</b> . . . . .  | 113 |
| Abhisek Santra, Shreyashi Santra Mitra, Suman Sinha, Shidharth Routh, and Akhilesh Kumar   |     |
| <b>Subsidence Assessment of Building Blocks in Hanoi Urban Area from 2011 to 2014 Using TerraSAR-X and COSMO-SkyMed Images and PSInSAR</b> . . . . .                           | 127 |
| Van Anh Tran, Quoc Cuong Tran, Duc Anh Nguyen, Tong Minh Dinh Ho, Anh The Hoang, Trung Khien Ha, and Dieu Tien Bui   |     |
| <b>Analysis of Land Use/Land Cover Mapping for Sustainable Land Resources Development of Hisar District, Haryana, India</b> . . . . .  | 151 |
| B. S. Chaudhary, Reeta Rani, Sanjeev Kumar, Y. P. Sundriyal, and Pavan Kumar   |     |
| <b>Part IV Challenges and Future Directions in GIScience</b>   |     |
| <b>A Spatial Investigation of the Feasibility of Solar Resource Energy Potential in Planning the Solar Cities of India</b> . . . . .   | 169 |
| Koel Roychowdhury and Radhika Bhanja   |     |
| <b>Mapping Rice Growth Stages Employing MODIS NDVI and ALOS AVNIR-2</b> . . . . .  | 185 |
| Dyah R. Panuju, David J. Paull, Amy L. Griffin, and Bambang H. Trisasongko   |     |
| <b>Habitat Suitability Mapping of Sloth Bear (<i>Melursus ursinus</i>) in the Sariska Tiger Reserve (India) Using a GIS-Based Fuzzy Analytical Hierarchy Process</b> . . . . . | 205 |
| Purva Jain, Raihan Ahmed, Haroon Sajjad, Meheeb Sahana, Abolfazl Jaafari, Jie Dou, and Haoyuan Hong  |     |
| <b>Estimation of Air Pollution Using Regression Modelling Approach for Mumbai Region, Maharashtra, India</b> . . . . .   | 229 |
| Maya Kumari, Shivangi S. Somvanshi, and Syed Zubair  |     |
| <b>Mapping of Agriculture Productivity Variability for the SAARC Nations in Response to Climate Change Scenario for the Year 2050</b> . . . . .                                | 249 |
| Ram Kumar Singh, Vinay Shankar Prasad Sinha, Pawan Kumar Joshi, and Manoj Kumar  |     |

**Part V GIScience for Revolution in Science and Society**

**Future Direction of GIScience for Revolution in Science and Society Over the Past 20 Years . . . . . 265**

Bharat Lal, Susheel Kumar Singh, Meenu Rani, Abhishek Kumar Shukla, and Pavan Kumar



## About the Editors

**Pavan Kumar** is a Faculty Member at the College of Horticulture and Forestry, Rani Lakshmi Bai Central Agricultural University, Jhansi, U.P., India. He obtained his Ph.D. degree from the Faculty of Natural Sciences, Jamia Millia Islamia, New Delhi. Dr. Kumar completed his B.Sc. (Botany) and M.Sc. (Environmental Science) at Banaras Hindu University, Varanasi, India, and subsequently obtained Master's degree in Remote Sensing (M.Tech.) from Birla Institute of Technology, Mesra Ranchi, India. His current research interests include climate change and coastal studies. He is recipient of Innovation China National Academy Award for Remote Sensing. Dr. Kumar has published 50 research papers in national journals and authored a number of books. He has visited countries like the USA, France, the Netherlands, Italy, China, Indonesia, Brazil, and Malaysia for various academic/scientific assignments, workshops, and conferences. Dr. Kumar is member of the International Association for Vegetation Science, USA and Institution of Geospatial and Remote Sensing, Malaysia.

**Haroon Sajjad** is Professor in the Department of Geography, Faculty of Natural Sciences, Jamia Millia Islamia, New Delhi, India. His present research interests include environmental management, sustainable development, watershed management, and applications of remote sensing and GIS. He authored four books and has published more than hundred research papers in journals of international repute. Prof. Sajjad has presented 50 research papers at national and international conferences. Ten scholars have been awarded doctoral degrees under his supervision. He is reviewer of many scientific research journals and member of various scientific bodies.

**Bhagwan Singh Chaudhary** is currently working as Professor and Chairman in the Department of Geophysics at Kurukshetra University, India, since December 2017. He is also Registrar (offg.) of Kurukshetra University since June 5, 2020. Prof. Chaudhary has also worked as Founder Registrar at Chaudhary Bansi Lal University,

Bhiwani, from Aug. 2014 to Dec. 2017. He started his career as Scientist at Haryana Space Application Centre, Hisar, in 1990 and worked there till 2004. Prof. Chaudhary was awarded DAAD Fellowship at the University of Freiburg, Germany, from 1997 to 1999. He has been working in the domain of geospatial technology for natural resources for about 30 years and has published more than 70 research papers in various national and international journals/conferences. Prof. Chaudhary has visited many countries like the USA, the UK, Austria, Germany, France, the Netherlands, Switzerland, Poland, China, South Africa, Indonesia, Bangladesh, Sri Lanka, Nepal, and Thailand for various academic/scientific assignments and conferences.

**J. S. Rawat** is presently Director of the Centre of Excellence for Natural Resources Data Management System in Uttarakhand (COE NRDMS), Coordinator of M.Sc. Remote Sensing and GIS Course at Kumaun University, and Director of Uttarakhand Centre on Climate Change. He is a Gold Medalist of Kumaun University and was awarded Senior Fulbright Fellowship by the Council for International Exchange of Scholars, Washington, D. C., USA, in 1988. Prof. Rawat has published about 122 research papers in international/national journals/books; written 3 books; participated in 15 international conferences including in Canada, Germany, and China; and participated in 89 conferences/expert committee meetings in India.

**Meenu Rani** received her M. Tech. degree in Remote Sensing from Birla Institute of Technology, Ranchi, India. She is currently affiliated to the Department of Geography, Kumaun University, Nainital, Uttarakhand, India. Dr. Rani has worked on remote sensing applications as a Junior Research Fellow at HARSAC and as Research Associate at the Indian Council of Agricultural Research and GB Pant National Institute of Himalayan Environment and Sustainable Development. Dr. Rani has authored and co-authored several peer-reviewed scientific research papers and presented works at many national and international conferences including the USA, Italy, and China. She has been awarded with various fellowships from the International Association for Ecology, Future Earth Coast, and SCAR Scientific Research Programme. Dr. Rani received early career scientists achievement award in 2017 at Columbia University, New York, USA.

# **Part I**

## **General**

# Introduction to Challenges and Future Directions in Remote Sensing and GIScience



Raihan Ahmed, Pavan Kumar , and Meenu Rani

**Abstract** This book provides an overview of remote sensing and GIScience (GIS) and their challenges and future directions. Modern technology like remote sensing and GIS with timely and accurate information helps to monitor and analyze a wide range of phenomena like water, vegetation, land, and human activities. Interdisciplinary studies are also noticed in human–environment interaction between stakeholders and decision makers for real world applications. Remote sensing data products and their limitations are also discussed in the book. To overcome this situation, artificial intelligence (AI), along with cloud computing and big data analytics, is the need of the hour. Decision support system based on the AI in remote sensing and GIS is key to the implementation of decision-making and planning in a sustainable manner. The book is segregated into 5 parts spreading over 15 chapters. Part I discusses the challenges and future direction of remote sensing and GIS in various fields. Chapters 2–5 in the second part are devoted to challenges in sustainable natural resources management. Various applications of remote sensing and GIS in urban growth management are presented in Chapters 6–9 of Part III. In Part IV, challenges and future directions in GIS have been discuss in Chapters 10–14 through GIS modeling. Part V devoted to one chapter deals with the GIS revolution in science and society.

**Keywords** Remote sensing · GIScience · Challenges and Future direction

---

R. Ahmed  
Department of Geography, Faculty of Natural Science, Jamia Millia Islamia, New Delhi,  
Delhi, India

P. Kumar (✉)  
College of Horticulture and Forestry, Rani Lakshmi Bai Central Agricultural University, Jhansi,  
Uttar Pradesh, India

M. Rani  
Department of Geography, Kumaun University, Nainital, Uttarakhand, India

Development of remote sensing and GIScience (GIS) is crucial for scientific exploration of the earth's system, such as hydrosphere, lithosphere and biosphere. The phenomenon of the earth's system such as natural and human-induced has much significance in today's world. Remote sensing and GIS are modern technologies with timely and accurate information. Information access through these technologies helps to monitor and analyze a wide range of phenomena like water, vegetation, land, and human activities. It also helps to explore the potential natural resources for human use. Therefore, it is being used widely in various disciplines and multi-disciplinary subject areas for decision-making and problem-solving processes.

The human–environment interaction (HEI) plays a key role in the dynamics of global environmental system. HEI analysis uses disparate datasets for every particular study. However, there are some similarities between methods and techniques in remote sensing and GIS practitioners. It creates an inter-disciplinary study in HEI and collaboration between authors of various disciplines. Increased collaboration beyond academics is also seen nowadays by stakeholders and decision makers for real world applications. Remote sensing and GIS provide information through data mining and processing. Therefore, ground reference data inclusion in remote sensing and GIS are crucial for the relevance of every study.

In the era of industrialization and climate change, HEI deteriorates the earth's biosphere and its carbon and hydrological cycles. To overcome this problem, a large amount of data and processing power is required along with the decision-making system. This is the main challenge for remote sensing and GIS, which have large spectrum of data with various limitations. Remote sensing data products are available with various spatial, spectral, and temporal resolutions. Therefore, studies use site-specific data products to fulfill the need of the specific study. For example, temporal changes in urban land use need high spatial, which requires large storage of data with specific time interval. Therefore, storage as well as processing need time for this kind of research. Some studies need spectral resolution for identifying the objects. Hyperspectral remote sensing data products with high spectral resolution have provided satisfactory results for this kind of research.

Promising solutions for these challenges can be obtained with the help of cloud computing and big data analytics. It is obvious that artificial intelligence (AI), along with cloud computing and big data analytics, is the future of remote sensing and GIS. Decision support system based on AI in remote sensing and GIS is the key to the implementation of decision-making and planning in a sustainable manner. Visualization of spatial data in GIS is a way forward to achieve planning and decision-making for stakeholders. It helps decision makers to take action based on the data visualization through GIS, e.g., natural hazards, urban planning, environmental management, and crime. Prediction and modeling of natural hazards are extremely difficult in the real world due to its complex nature. Till date, there is no such method to predict the results with zero uncertainty. AI has achieved the deal with precision modeling for complex problems of the earth's system. It can analyze the different aspects with sufficient detail and iteration for a complex problem.

Google Earth Engine is a platform based on cloud computing to analyze the geospatial data. It has massive computational capabilities to analyze a large amount

of spatial data in a short time period. The advantage of this platform is to analyze spatial data without storing them in personal computers. Therefore, it helps to process large scale studies such as those at regional and country levels with efficient results. An attempt has been made in this book by the contributors to evaluate the efficiency of remote sensing and GIS techniques through various studies. Chapters in this volume have been grouped into five parts: General, Challenges in Sustainable Natural Resources Management, Remote Sensing and GIScience in Urban Growth Management, Challenges and Future Directions in GIScience, and GIScience for Revolution in Science and Society. Part I deals with the usefulness of remote sensing and GIS in various field of study. It covers the applicability of remote sensing and GIS in HEI, natural hazards, and environmental management. The future of remote sensing and GIS in the light of AI, cloud computing, and big data analytics is also focused on in this part.

Part II deals with the Challenges in Sustainable Natural Resources Management. It comprises four chapters concentrating on flood, vegetation, landslide, and glacier retreat and their direct and indirect impact on natural resources. In chapter “[Environmental and Livelihood Impact Assessment of 2013 Flash Flood in Alakananda and Mandakini River Valley, Uttarakhand \(India\) Using Environmental Evaluation System and Geospatial Techniques,](#)” Tripathi et al. made an attempt for environmental and livelihood impact assessment of 2013 disastrous flood in Mandakini valley. They used Landsat data product for preparing land use land cover (LULC) maps and the statistical changes were estimated in the respective LULC classes. The results showed significant changes in terms of LULC dynamics in the whole region. In chapter “[Assessment of Vegetation Vigor Using Integrated Synthetic Aperture Radars,](#)” Sinha assessed the vegetation using Integrated Synthetic Aperture Radars (SAR). In the study, the author uses SAR data to estimate forest biomass. Study shows a suitable approach in assessing vegetation vigor from above ground biomass through SAR. In the chapter “[Landslide Susceptibility Mapping using Bivariate Frequency Ratio Model and Geospatial Techniques: A Case from Karbi Anglong West District in ASSAM, India,](#)” Ahmed et al. made an attempt to prepare an inventory map of landslide susceptibility using geospatial technology and bivariate frequency ratio model for Karbi Anglong West district. The study revealed that frequency ratio model along with geospatial technique helped not only in identifying landslide prone areas but also proved to be instrumental in examining level of susceptibility. In the chapter “[Retreating Glacier Dynamics Over the Last Quarter of a Century at Uttarakhand Region Using optical Sensors Time Series Data,](#)” Kalita et al. examined the retreating glacier dynamics over the last quarter of a century in Uttarakhand. In their study, they used optical remote sensing data products for examining the changes from 1994 to 2015 and changes detected for snow and vegetation were 1377 km<sup>2</sup> and 896 km<sup>2</sup>, respectively. The study results showed the actual determination of glacier dynamics and its kinetic of change rate and how climate is impacting over snow and ice resources.

Part III deals with the Remote Sensing and GIScience in Urban Growth Management. It contains four chapters focusing on the impact of urbanization on agriculture, impervious built-up, building subsidence, and LULC for land resource development.

In the chapter “[Studying the Impact of Urbanization on HYV Rice Fields at a Local Level Using Fine Resolution Temporal RISAT-1 Datasets](#),” Roychowdhury and Bhanja assessed the Impact of urbanization on High Yielding Variety (HYV) rice fields at a local level. Their study estimates the HYV rice fields vulnerable to conversion due to non-farm uses around sprawling urban settlements. In the chapter “[Identification of Impervious Built-Up Surface Features Using Resources at 2 LISS-III Based Novel Optical Built-Up Index](#),” Santra et al. tried to identify the impervious built-up surface through built-up index. In their study, they used several built-up indices for comparison. Their newly developed Impervious Built-up Index shows the maximum accuracy, i.e., 92.33%. In the chapter “[Subsidence Assessment of Building Blocks in Hanoi Urban Area from 2011 to 2014 Using TerraSAR-X and COSMO-SkyMed Images and PSInSAR](#),” Anh et al. assessed building subsidence in Hanoi urban area from 2011 to 2014 by high resolution radar satellite images. Their results revealed that high precision leveling is the key to assess the accuracy of subsidence determination of buildings. In the chapter “[Analysis of Land Use/Land Cover Mapping for Sustainable Land Resources Development of Hisar District, Haryana, India](#),” Rani et al. mapped the LULC for sustainable land resource development in Hisar district. They used IRS/LANDSAT data products to analyze various land resource constraints by taking collateral information on soil types, groundwater quality, and depth along with geomorphological constraints.

Part IV deals with the challenges and future directions in GIScience. The part consists of five chapters concentrating on solar energy potential, rice growth stage mapping, habitat suitability mapping, air pollution modeling, and agricultural productivity mapping. In the chapter “[A Spatial Investigation of the Feasibility of Solar Resource Energy Potential in Planning the Solar Cities of INDIA](#),” Roychowdhury and Bhanja investigated the feasibility of solar resource energy potential in planning the solar cities of India. Their study focused on identifying solar hotspots of India and how the spatial distribution of solar energy resources accentuate or hinder the performance of the solar cities. The study also conducted a techno-economic feasibility using solar resource datasets derived from high resolution satellites. In the chapter “[Mapping Rice Growth Stages Employing MODIS NDVI and ALOS AVNIR-2](#),” Panuju et al. mapped rice growth stages using MODIS NDVI and ALOS AVNIR-2. They used time-series NDVI for growth-stage indication and five classifiers for mapping the growth stages. The study revealed the efficiency of neural network and support vector machine in mapping growth stages. In the chapter “[Habitat Suitability Mapping of Sloth Bear \(\*Melursus ursinus\*\) in the Sariska Tiger Reserve \(India\) Using a GIS-Based Fuzzy Analytical Hierarchy Process](#),” Jain et al. mapped the habitat suitability of the sloth bear (*Melursus ursinus*) in the Sariska Tiger Reserve (India) using a GIS-based fuzzy analytical hierarchy process. Nine parameters have been used for assessing sloth bear habitat suitability in the study. Their suitability classes were validated through zonal statistics of beat wise habitat intensity data of sloth bear in the Reserve. In the chapter “[Estimation of Air Pollution Using Regression Modelling Approach for Mumbai Region Maharashtra, India](#),” Kumari et al. estimated air pollution using regression model for Mumbai. The study was an integrated approach to attain the spatio-temporal attributes of air pollution

index of particulate matter (PM<sub>10</sub> and PM<sub>2.5</sub>) and trace gas (O<sub>3</sub>, NO<sub>2</sub>, and CO) pollutants in Mumbai. They used spatial variation of API for different air pollutants to simulate the Inverse Distance Weighted method of interpolation. In the chapter “[Mapping of Agriculture Productivity Variability for the SAARC Nations in Response to Climate Change Scenario for the Year 2050](#),” Singh et al. mapped the agriculture productivity variability for the SAARC nations in response to climate change scenario for the year 2050. They assessed the impacts of climate change on agriculture productivity net primary productivity using Joint UK Land Environment Simulator. Results of the study revealed a slight decrease in productivity with spatial variability across the SAARC nations.

Part V deals with the GIScience for Revolution in Science and Society. It comprises one chapter focused on the revolution of GIS in science and society for solving the future challenges in spatial information. In the chapter “[Future Direction of GIScience for Revolution in Science and Society Over the Past Twenty Years](#),” Lal et al. emphasized the need of GIS in society for problem-solving with the help of spatial data and modeling as GIS plays a vital role in monitoring the physical characteristics of the earth’s surface over decades. The advancement of GIS technologies, specifically in GIS geomorphologic mapping, has provided us with core data of landform development, including those due to geophysical or climatic events such as earthquake, volcanic eruption, landslides, and cyclone.



**Part II**  
**Challenges in Sustainable Natural**  
**Resources Management**

# Environmental and Livelihood Impact Assessment of 2013 Flash Flood in Alakananda and Mandakini River Valley, Uttarakhand (India), Using Environmental Evaluation System and Geospatial Techniques



Shruti Tripathi, G. Areendran, N. C. Gupta, Krishna Raj, and Meheeb Sahana

**Abstract** India has been historically susceptible to natural disasters due to its unique geo-climatic conditions in which the Himalayan ecosystem is very fragile and a little disturbance can cause harmful effects. The present work is an attempt to assess the environmental and livelihood impact of the 2013 flood in Mandakini valley, Uttarakhand (India), using geospatial techniques and an environmental evaluation system. The land use land cover (LULC) maps for the years 2011, 2014, and 2017 (Alaknanda basin) and 1997, 2011, and 2017 (Mandakini basin) were prepared using Landsat satellite imageries, and the statistical changes were estimated in the respective LULC classes derived. The results showed significant changes in terms of LULC dynamics in the whole region. Further, to analyze changes in vegetation cover in the region, Normalized Difference Vegetation Index was calculated, depicting the overall decrease in vegetation cover. By using Battelle Columbus method of environmental evaluation system, the impact of the flood on ecological and cultural aesthetics and human interests, with and without the disaster is also derived. A questionnaire-based survey was conducted in Gaurikund and Kedarnath to assess the repercussions of the flood on the livelihoods of inhabitants. It showed that the stoppage of tourism-based livelihood activities, which were critical to the local people, deems it necessary to map the footprint of the flood on livelihood generation activities. The overall result of this study is that there are significant impacts of flood on both the environment and people residing in the region, and anthropogenic activities were major contributors to the catastrophe. The major outcomes of this analysis will help in creating the baseline data for major

---

S. Tripathi · N. C. Gupta  
Guru Gobind Singh Indraprastha University, New Delhi, India

G. Areendran · K. Raj · M. Sahana (✉)  
IGCMC, WWF–India, New Delhi, India  
e-mail: [gareendran@wwfindia.net](mailto:gareendran@wwfindia.net); [kraj@wwfindia.net](mailto:kraj@wwfindia.net); [msahana@wwfindia.net](mailto:msahana@wwfindia.net)

disastrous studies in India and also support sustainable management strategies in response to these extreme events.

**Keywords** Mandakini valley · Geospatial techniques · LULC · Livelihood framework · NDVI · Battelle Columbus method

## 1 Introduction

India is highly prone to floods, droughts, cyclones, and earthquakes. The frequency of avalanches, forest fire, and landslides is high in the Himalayan region of northern India (Sahana and Sajjad 2017; Sahana et al. 2018; Khatun et al. 2018; Areendran et al. 2020). In India, 25 out of 36 states/union territories are more vulnerable to natural calamities. Around 50 million people in the country are affected by one or the other disaster every year on an average, besides the loss of property worth several million (Sharma 2005). The Himalayan region is seismically and tectonically active, geologically unstable, remotely located and ecologically most fragile (Sati 2008). In successive years, the same area encounters one or more disasters. Many people live in these disaster-prone areas and generate a livelihood from available natural resources (Sahana and Sajjad 2019). The World Bank has stated that a large number of people who come under the extremely poor section live on “insubstantial” lands, including forest ecosystems, slopes, and poor soils (World Bank 2003, p. xvi). Around 240 million people live in forested areas, constituting 18.5% of the 1.3 billion people living in environmentally fragile lands (World Bank 2003, p. 60). If all these natural disasters could be predicted and prevented with a state of preparedness and ability to respond quickly to the calamity, it can considerably cut or mitigate the loss of life and property.

In June 2013, heavy rainfall triggered flash flooding and landslides throughout the Indian Himalayan state of Uttarakhand, which killed more than 6000 people. The destruction and fatalities resulted directly from a lake outburst and debris flow originating from above the village of Kedarnath (Allen et al. 2016). The heavy downpour (>400 mm) created a huge flash flood causing damage to agricultural fields, settlements, and infrastructure and loss of human and animal lives, and widespread devastation of natural resources in different parts of the state (Uttarakhand). Around 100,000 pilgrims and tourists were stuck because of the destruction of trekking routes and roads until civic and military authorities arrived and evacuated them (Martha et al. 2015; Sharma and Tyagi 2013). There were two landslides that occurred in Kedarnath on the 16th of (month?), one in the North East and the other in the North West, both originating around the glacier. Debris flow was initiated by the landslide in the North East that ran down en-route. In the North West, conditions are very different. Landslides and moraines left by retreating glaciers blocked drainage and allowed the formation of a pool that overtopped the moraine barrier and led to a catastrophic breach (Sahana and Sajjad 2017). This released high volumes of water downstream in the low-lying area, causing a flash flood (Patley

2013). The reason for maximum devastation in Kedarnath valley was the breach of the moraine-dammed Chorabari Lake that was situated 1.5 km above Kedarnath town from where the unconsolidated moraine debris was deposited and breached down to the town. Landslides due to floods damaged several houses and killed many people who were trapped in these structures. Entire villages and settlements such as Gaurikund and the market town of Rambada got damaged, while the market town of Sonprayag suffered heavy damage and loss of lives (Indian Disaster Report 2013). The total roof area in Kedarnath before the disaster was 37,299 m<sup>2</sup> (259 structures), 44.2% of which were completely destroyed and 26.7% were partly damaged, representing 138 and 56 structures, respectively. Around 26.9% of the roof area of partly destroyed structures was gone. Only the Kedarnath temple emerged as an unharmed structure in this disaster (Das et al. 2015).

The study of the socio-economic impact of the disaster consists of both qualitative and quantitative approaches. Quantitative household questionnaires and qualitative key informant's interviews were used to collect data. Among all-natural disasters, floods are the most frequent and 33 million people were affected by floods from 1953 to 2000 (Syed et al. 2013; Mohapatra and Singh 2003). A study was conducted by Belaid (2003) to show urban-rural land use change using remote sensing and GIS and concluded that these technologies together with secondary data can be used to assist decision-makers to prepare future plans in order to find out the appropriate solution to urbanization (Syed et al. 2013). Four hundred and eighty people inhabit Kedarnath during the summer months and also from neighboring towns. People come every year in search of livelihood and leave during the winters like the rest of the residents. Roughly, around 5000 people arrive and leave daily during pilgrimage time. People who live in the town earn through tourist-related activities during yatra time. This is also because of the harsh winter season (<https://www.yatra.com/india-tourism/Kedarnath/people>). In 2012, the number of pilgrims reached a high of 259,900 (by a tour of India) and they provide a variety of income-generating sources. People have been engaged in tourism-based activities for generations. So, this flood had snatched their main income-generating source for almost 2–3 years. Many researchers tried to map the impact of the flood on livelihood in other disasters like Pakistan which faced a tragic flood in 2010 that affected more than 20.1 million people in the whole country (Ashraf et al. 2013). Ashraf et al. in 2013 conducted a study in southern Punjab to explore the effect of floods on food security and the livelihood of rural communities. Results revealed that flood affected the natural capitals (land, irrigation, orchards, and livestock) pushing the income-generating sources into darkness. Flood becomes a hazard only where human encroachment occurs in flood-prone areas (Smith and Ward 1998; Sahana et al. 2015; Sahana and Patel 2019). A study that was undertaken in Scotland suggests that social impacts are linked to the level of wellbeing of individuals, communities, and societies. It also includes aspects that are related to education and literacy, the existence of security and peace, basic human rights, good governance, positive traditional value, social equity, custom and ideological belief, knowledge structure, and overall organization systems. Some groups are more vulnerable to floods than others like the poor and under-privileged (Nott 2006). Poor people are more

vulnerable to disasters because they lack physical, social, and knowledge-based resources to respond to and prepare for threats. Because they are poor, they are more vulnerable, and hence are at greater risk in the face of hazard, leading to disasters (Das et al. 2005; Rehman et al. 2019; Bjarstig and Stens 2018). The loss in case of flooding has many dimensions; in addition to economic loss and loss of life or injury, there may be irreversible loss of land and of history of cultural ecological valuables (Muis et al. 2015). Among natural hazards, flooding claimed more lives than any other single hazard from 1986 to 1995. Flooding accounted for 31% of global economic losses from natural catastrophes and 55% casualties (De Bruin et al. 2014).

These conditions lead to food insecurities and food deficits as people use contaminated commodities, especially water (Sahana et al. 2020). So, taking all this into consideration, this paper's major focus is on the impact of the flood on the environment and livelihood of the people involved in Kedarnath yatra every year. Other papers tried to discover the reason for the floods and damage caused. It is very important to map the footprint of the flood on livelihoods. It will help policymakers and institutions help these vulnerable people and make their livelihood sustainable.

## 2 Study Area

Uttarakhand is predominantly a hill state, having international boundaries with China in the north and Nepal in the east. The Himalayan region in Uttarakhand (~53,483 km<sup>2</sup>) lies between Kali Ganga (bordering with Nepal) and Tons-Yamuna (bordering with Himachal Pradesh). Around 10% of the total area of Uttarakhand is covered by snow, ice, and glaciers. These are the perennial source of water for four major river systems, viz. Yamuna, Bhagirathi, Alaknanda, and Kali (Singh and Rawat 2011; Dobhal et al. 2013). In Uttarakhand, 4 districts were majorly affected by the flood in which Rudraprayag district saw greater loss in terms of lives and property (NIDM Report 2013). Many lost their family members, houses, jobs, shelter, and so on. In this study, Mandakini valley was selected to understand the effects of the disaster. Figure 1 shows the study site.

Alaknanda basin is located at 30.1333° latitude and 78.6029° longitude. Its main tributaries are Mandakini, Nandakini, and Pinder and considered to rise at the foot of the Satopath glacier in Uttarakhand (Sati 2009). The Alaknanda river basin is sandwiched between the crystalline of lesser and higher Himalayas. It is characterized by high-grade metamorphic rocks of higher Himalayan crystalline in the north and lesser Himalayan sequence in the south (Metcalf 1993; Valdiya et al. 2000; Valdiya 1995). High mountainous ranges in the northern part, particularly in the north eastern and north western part of the watersheds, are covered with snow-fields or glaciers. The rivers of Alaknanda basin are perennial, since runoff in these rivers is controlled by both precipitation and glacial melt (Sati 2009).

River Mandakini, the main river of the Alaknanda basin and valley, is a major tributary of River Alaknanda and originates from the Chorabari Glacier, situated just

### Location of the study area in Uttarakhand Himalaya

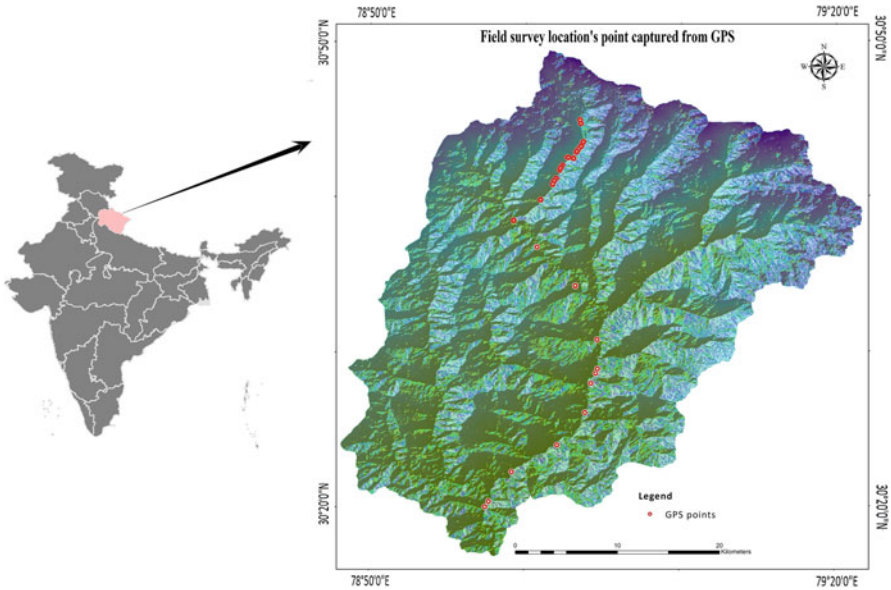


**Fig. 1** Location map of Alaknanda and Mandakini basin and the GPS points collected during the field survey

2 km above Shri Kedarnath shrine. The Shri Kedarnath town is situated in the Central Himalayas (30° 44' 6.7" N; 79° 04' 1"E) in the Mandakini River valley. The catchment area is situated in the glacier-modified U-shaped valley; the altitude ranges from 1700 m asl to 6578 m asl. Such a variation in the altitude provides various landscapes. BhartKhunta (6578 m), Kedarnath (6940 m), Mahalaya peak (5970 m), and Hanuman top (5320 m) are major peaks in the area. The climate of the region largely depends on altitude as elevation ranges between 1600 m and 6500 m asl. Winter is from mid-October to April. The slope of the study area lies between 30 and 60° and toward the South East aspect. The alpine habitat usually starts at timberline and is characterized by the complete absence of trees. The soil in Kedarnath valley is dark brown on the surface and yellowish-brown below (Singh et al. 1986). Floristic composition shows mixed forests of rhododendron, *Quercusleuco trichophora* (Banj), *Quercus floribunda* (Moru), and *Quercusseme carpifolia* (Kharsu), *Buxus wallichiana* (papri), *Acer* spp. (Kaijal), *Betula alnoides* (Katbhuj), and *Alnus nepalensis* (Utis) up to an elevation and the rest are alpine pastures. This area has traditionally occupied an important position in the socio-cultural, spiritual, and medicinal arena of rural and tribal lives of Uttarakhand (Rawat 2016). According to the report of Climate Himalaya on plausible reasons for this flood, the root of the disaster is in the Chorabari Glacier located in Mandakini valley. This is why Mandakini valley was chosen as the study area to access environmental damage and its impact on the livelihoods of inhabitants.

### 3 Material and Methodology

#### 3.1 Data Collection

Materials that were used during the study are various websites from the internet like Earth Explorer, Bhuvan, and Diva GIS; GIS software like ERDAS Imagine and Arcmap10; national and international journals, a questionnaire for the assessment of damage and pre-disaster livelihood options. Satellite images used in this study are mentioned in Table 1.

#### 3.2 Data Collection for the Survey

Field survey was conducted to assess the impact of the flood on socio-economic parameters of the valley's residents. For that purpose, livelihood's 5 capitals were studied, i.e., physical, natural, financial, health, and social capitals. Sample data were collected through the questionnaire-based survey in Gaurikund village, en-route to Kedarnath temple and in Kedarnathghati. Figure 1 shows the GPS points that were selected by random selection method to select the interviewees. It was learned that, in Mandakini valley, en-route Kedarnath temple, many people earn their livelihood from various food stalls or carrying people to the temple using horses and on their back. Figure 2 shows various types of livelihoods in which inhabitants are engaged in.

**Table. 1** Satellite images used in this study

| S. no.                     | Name of satellite | Year             | Resolution |
|----------------------------|-------------------|------------------|------------|
| <b>For Alaknanda basin</b> |                   |                  |            |
| 1.                         | Landsat 5         | January 2011     | 30 m       |
| 2.                         | Landsat 8         | January 2014     | 30 m       |
| 3.                         | Landsat 8         | January 2017     | 30 m       |
| <b>For Mandakini basin</b> |                   |                  |            |
| 1.                         | Landsat 5         | January, 1997    | 30 m       |
| 2.                         | Landsat 5         | January 2011     | 30 m       |
| 3.                         | Landsat 8         | June 2013        | 30 m       |
| 4.                         | Landsat 8         | January 2014     | 30 m       |
| 5.                         | Landsat 8         | January 2017     | 30 m       |
| <b>For rainfall</b>        |                   |                  |            |
| 1.                         | TRMM (Netcdf)     | 2001–2016 (June) | 0.25°      |



Fig. 2 Field photographs of livelihood types in the Kedarnath and Gaurikund regions

### 3.3 Analysis of the Satellite Images for Impacts of Flood

#### 3.3.1 Image Acquisition

Satellite images that were used in this study are mentioned in Table 1. These images were downloaded from USGS Earth Explorer official site and Bhuvan. These imageries are freely available on the mentioned portals.

#### 3.3.2 Georectification

The topographical maps were georectified by selecting ground control points throughout the area projected in the projection system geographic (Lat/long) with spheroid and datum being WGS 84. From georeferenced imageries, the study area was obtained through a subset using the AOI boundary vector file (Hughes et al. 2006).

#### 3.3.3 Image Extraction (Subset/Mosaicking)

Satellite images that were downloaded from the Earth Explorer website were opened in ARC GIS, and the area of interest was extracted from that image to use for further study. However, in our case, our area of interest was spread across two satellite



images. So, we used the Mosaic tool in ERDAS Imagine to mosaic the images and then extracted our study of area from it.

### **3.3.4 Image Classification**

The purpose of image classification was to categorize all pixels in an image into different land cover classes. Digital image classification uses the spectral information represented by the digital numbers in one or more spectral bands to classify each pixel. This process assigns each pixel in an image to a particular class or theme based on the statistical characteristics of the pixel brightness values (Guo and Zhang 2009).

### **3.3.5 Unsupervised Classification**

In unsupervised classification, outcomes are based on the software analysis of an image without the user providing sample classes (Source [Extension.org](http://Extension.org)). In this type of classification, spectral classes were grouped first into 85 classes, based solely on the numerical information in the data. The classes that result from unsupervised classification are spectral classes distinguishing urban from the open area, agriculture from forest class, etc., and is often difficult because of similar reflectance patterns. Therefore, for more accurate classification, the number of classes classified initially was more. References like Google Earth maps prepared by other sources were used to recode and clean the initially classified image. AOI tools like polygon/polyline were used for cleaning.

### **3.3.6 Digitization (for Vector Layer)**

Different features like roads, rivers, towns, and soil types were extracted from scanned and georeferenced images using ArcGIS 10 digitization tools. Features like water bodies and settlements were extracted using Google Earth. The files obtained were in .kmz format, which were converted to shapefile using ArcGIS 10 conversion tools. Digitization was carried out manually. All the features were digitized as point, line, or polygon. Figure 3 shows the methodological framework used in this study.

## ***3.4 Environmental Impact Assessment of Flood***

Many research papers used Land Use Land Cover (LULC) analysis to assess the impact of flood on environmental settings and on human settlements (Sinha 1998; Ferrari et al. 2009). The method described in Fig. 4 was used to generate the LULC. We first downloaded the satellite images that are mentioned in Table 1 study area and then digitized and classified the post-flood-affected area in Uttarakhand. After

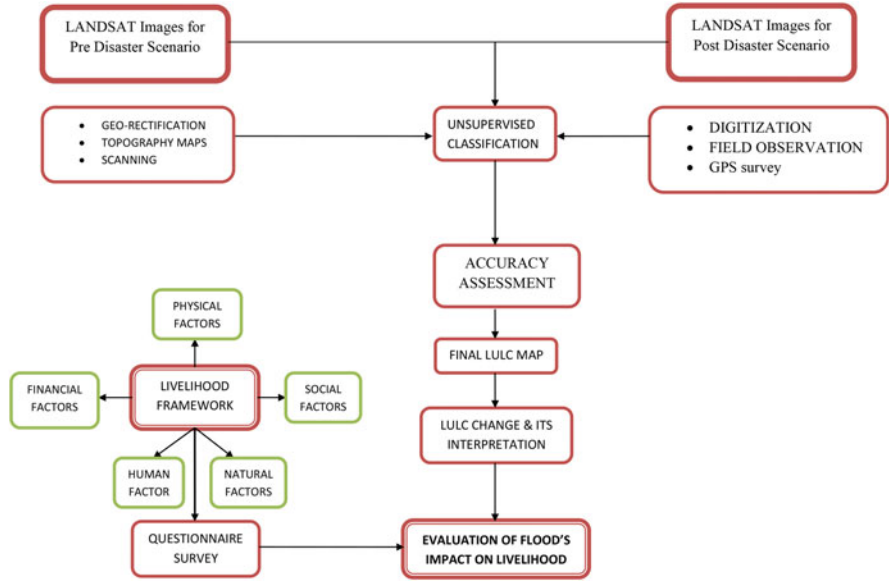


Fig. 3 Methodological framework used in this study

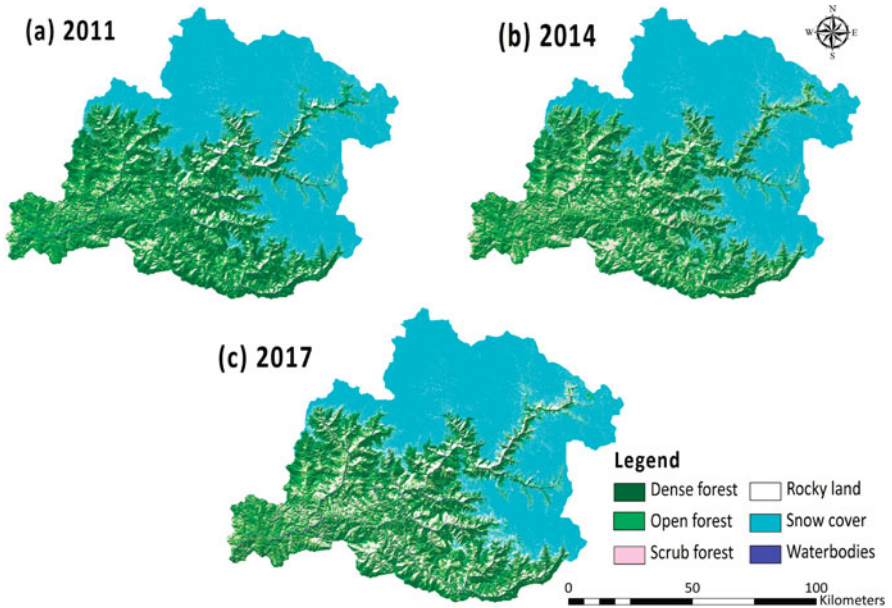


Fig. 4 Land use land cover pattern of Alaknanda basin (a) 2011, (b) 2014, and (c) 2017

that, we compared it with pre-disaster images to analyze the most to least affected areas. Landsat 8 images were used to digitize the flood-affected area with the help of data that was taken from the Bhuvan portal. Using Google Earth, roads, agricultural land, and settlements were digitized and then compared with flood-affected areas to analyze the damage caused by this flood in Mandakini valley.

We used the **Battelle Columbus** method for environmental impact assessment to evaluate environmental settings before and after the disaster. Battelle method is a quantitative method where 78 measurable environmental parameters are divided into 4 categories: environmental contamination, ecology, aesthetics, and human interest. In this method, 2 steps are involved; first is to convert parametric estimates into an environmental quality (EQ) scale that ranges between 0 and 1, where 0 denotes very bad quality and 1 denotes good quality. The second step is the multiplication of EQ values with the respective parameter importance unit values to obtain environmental impact units (EIU) for each parameter. Composite score is obtained by the addition of all EIU values. The total environmental impact is calculated by evaluating the expected future condition of the EQ with and without the project (Syed et al. 2013).

$$EI = \sum_{i=1}^m (V_i)1Wi - \sum_{i=1}^m (V_i)2Wi \quad (1)$$

Where

$E_1$  = Environmental impact

$(V_i)_1$  = Value in the EQ of parameter i with a project.

$(V_i)_2$  = Value in EQ of parameter i without a project.

$W_i$  = Relative weight (importance) of parameter i

$m$  = Total number of parameters

To do this, a checklist with all environmental parameters was made and assessed during the field visit and compared by weightage underlined in the Battelle method.

### 3.5 Normalized Difference Vegetation Index (NDVI)

This is a numerical indicator that uses the red and near-infrared spectral bands. NDVI is highly associated with **vegetation content**. High NDVI values correspond to areas that reflect more in the near-infrared spectrum. Higher reflectance in the near-infrared correspond to **dense and healthy vegetation**.

$$NDVI = \frac{\text{Band5} - \text{Band 4}}{\text{Band 5} + \text{Band4}} \quad (\text{using Landsat 8 data}) \quad (2)$$

### 3.6 *Livelihood Impact Assessment*

To fulfill the second major objective of this study to link the impact of the flood on the livelihood of inhabitants, we did a questionnaire survey during Kedarnath yatra in June 2017. The random selection method was applied to select the interviewee. The questionnaire was based on five pillars of sustainable livelihood framework (DFID 2009). In Kedarnath yatra, we can find different types of livelihood options, i.e., food stalls, hotels, horse sawari, pitthusawari, and so on. In this survey, we tried to incorporate all kinds of livelihood options. Here we questioned the interviewees who are currently engaged in some kind of work to generate income from yatra. The questions were framed according to the five livelihood capitals (Scoones 1998). Answer options were in the form of 1 (low intensity), 2 (medium intensity), and 3 (High intensity). Here intensity means the effect of the flood on a particular parameter.

## 4 Result/Discussions

### 4.1 *Land Use Changes in Alaknanda and Mandakini Basin*

Land cover maps from Landsat images from 2011–2017 (Alaknanda basin) have shown considerable changes in the study area (Fig. 4). The study area was divided into 7 different classes. LULC maps were prepared for 3 time periods, i.e., January 2011, January 2014, and January 2017 and changes in these LULC classes were analyzed in the present study. Classified images of the study area of 2011, 2014, and 2017 as well as changes in the abovementioned classes are demonstrated percentage wise to have a clear view on this, as mentioned in Table 2.

The study area was divided into 7 different classes. LULC map was prepared for 3 time periods: January 1997, January 2011, and January 2017; changes in these LULC classes were analyzed in the present study (Fig. 5). Classified images of the study area of 1997, 2011, and 2017 are shown. The LULC classification is summarized for the years 1997, 2011, and 2017 in Table 3. From 1997 to 2017, dense forest, scrub forest, water bodies, and snow cover decreased. On the other hand, open forest,

**Table 2** Statistical representation of area under different classes in Alaknanda basin

| Classes      | 2011 area |         | 2014 area |         | 2017 area |         |
|--------------|-----------|---------|-----------|---------|-----------|---------|
|              | (hectare) | (%)     | (hectare) | (%)     | (hectare) | (%)     |
| Dense forest | 290,761   | 26.3097 | 265,584   | 24.079  | 256,577   | 23.2604 |
| Open forest  | 178,675   | 16.1675 | 158,991   | 14.4148 | 143,966   | 13.0515 |
| Scrub forest | 67032.8   | 06.0655 | 92448.9   | 08.3818 | 89329.9   | 08.0983 |
| Water bodies | 7661.06   | 0.6932  | 7593.01   | 00.6884 | 7522.78   | 0.682   |
| Snow cover   | 489,680   | 44.309  | 489,672   | 44.3958 | 478,228   | 43.3546 |
| Rocky land   | 71337.8   | 06.455  | 88679.2   | 08.0401 | 127,439   | 11.5532 |

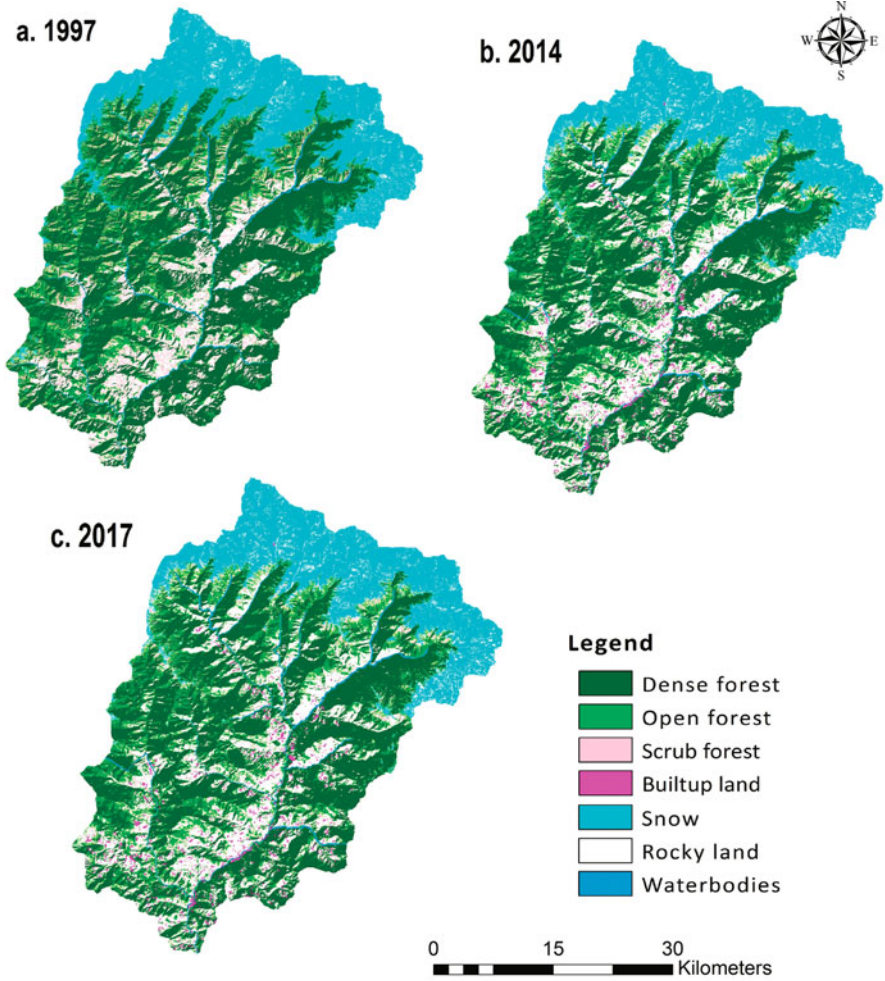


**Fig. 5** Land use land cover pattern of Mandakini basin, (a) 2011, (b) 2014, and (c) 2017

built-up land, and rocky land cover increased. We can have a clear view of this in Table 3. Therefore, the changes in dense forests are due to the climate change effect over the years and some parts changed into open forest. Over 20 years' time, there was an increase in built-up land and agricultural land that shows high anthropogenic activities in this fragile ecosystem.

**Table 3** Statistical representation of area under different classes in Alaknanda basin

| Classes       | 1997 area      |       | 2011 area       |       | 2017 area       |       |
|---------------|----------------|-------|-----------------|-------|-----------------|-------|
|               | (hectare)      | (%)   | (hectare)       | (%)   | (hectare)       | (%)   |
| Dense forest  | 740447.7       | 45.44 | 67272.4         | 41.27 | 56464.5         | 34.68 |
| Open forest   | 16774.6        | 10.29 | 20330.3         | 12.45 | 22285.2         | 13.68 |
| Scrub forest  | 15625.6        | 9.5   | 10690.5         | 6.55  | 13730.5         | 8.43  |
| Built-up land | 574.016        | 0.3   | 2298.47         | 1.41  | 2296.13         | 1.43  |
| Snow cover    | 35493.5        | 21.7  | 29395.6         | 18.03 | 28996.4         | 17.9  |
| Rocky land    | 17735.4        | 10.8  | 31503.7         | 19.32 | 32284.5         | 19.83 |
| Water bodies  | 740447.7       | 1.6   | 1497.63         | 0.91  | 1926.69         | 1.1   |
| <b>Total</b>  | <b>162,926</b> |       | <b>162988.6</b> |       | <b>162787.9</b> |       |

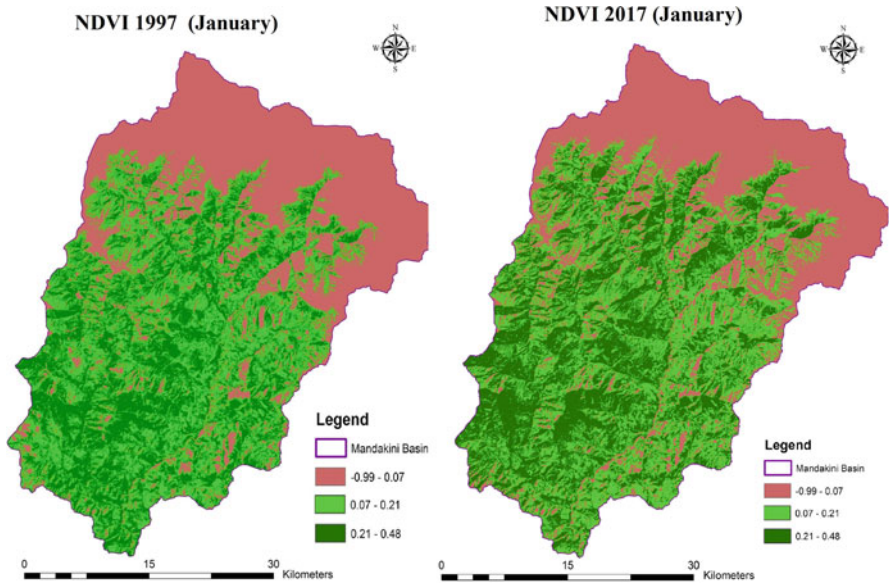


**Fig. 6** Comparative NDVI of Mandakini Basin between 1997 and 2017

### 4.2 Changes in Forest Cover

The pixel value of the NDVI data layer ranges from  $-1$  to  $+1$  and is scaled from 0 to 255. NDVI was used to depict healthy vegetation in the Mandakini basin. Low value depicts no vegetation or very little, and higher value indicates a densely forested area. By observing the entire image, we can infer that vegetation has drastically decreased from 1997 to 2017 (Fig. 6) in the Mandakini basin.

### 4.3 Damage Caused by the Flood

Due to cloudbursts, landslide occurred at various places in the Alaknanda basin. In Fig. 7, we have shown the landslide areas in Mandakini basin (Source; Bhuvan). Due to flooding and landslide, houses, roads, and agricultural land were severely affected. The extent of the flood-affected area is shown in Fig. 8 (damage on agriculture land), Fig. 9 (damage on villages), and Fig. 10 (roads that were affected by flood and landslide). Affected roads, bridges, agricultural land, and village data are shown in Tables 4 and 5 (Source: Rapid Damage Assessment for the Mandakini Valley by Bisht).

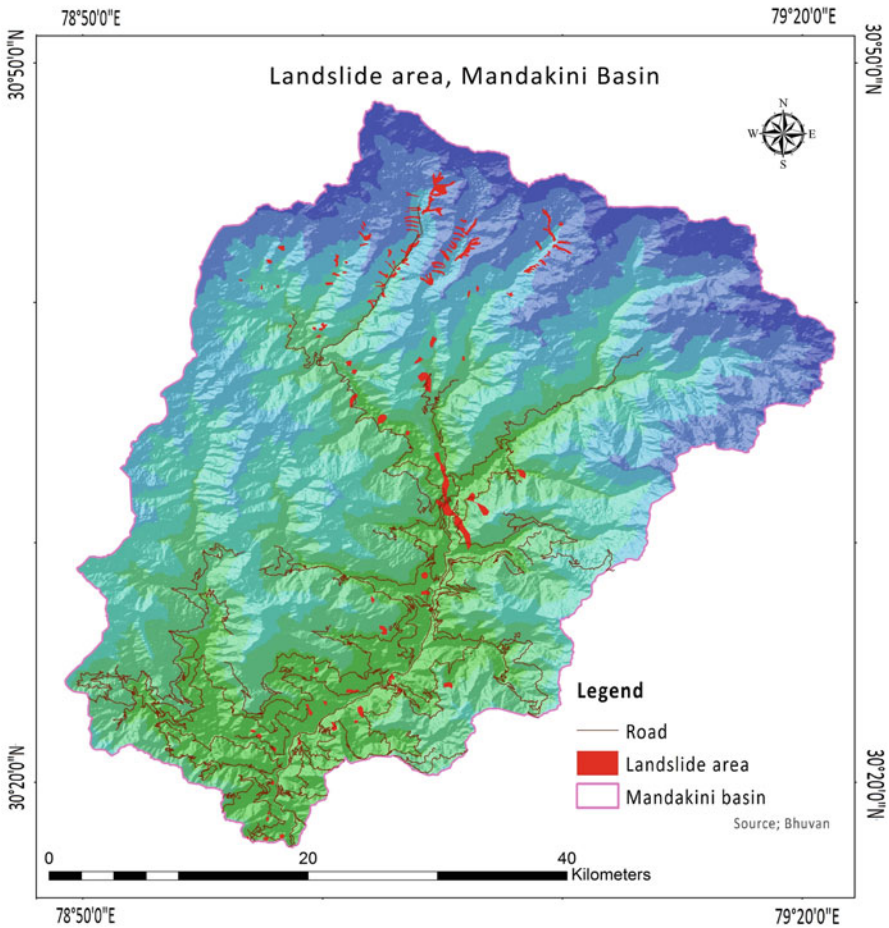


Fig. 7 Landslide area in the month of June 2013

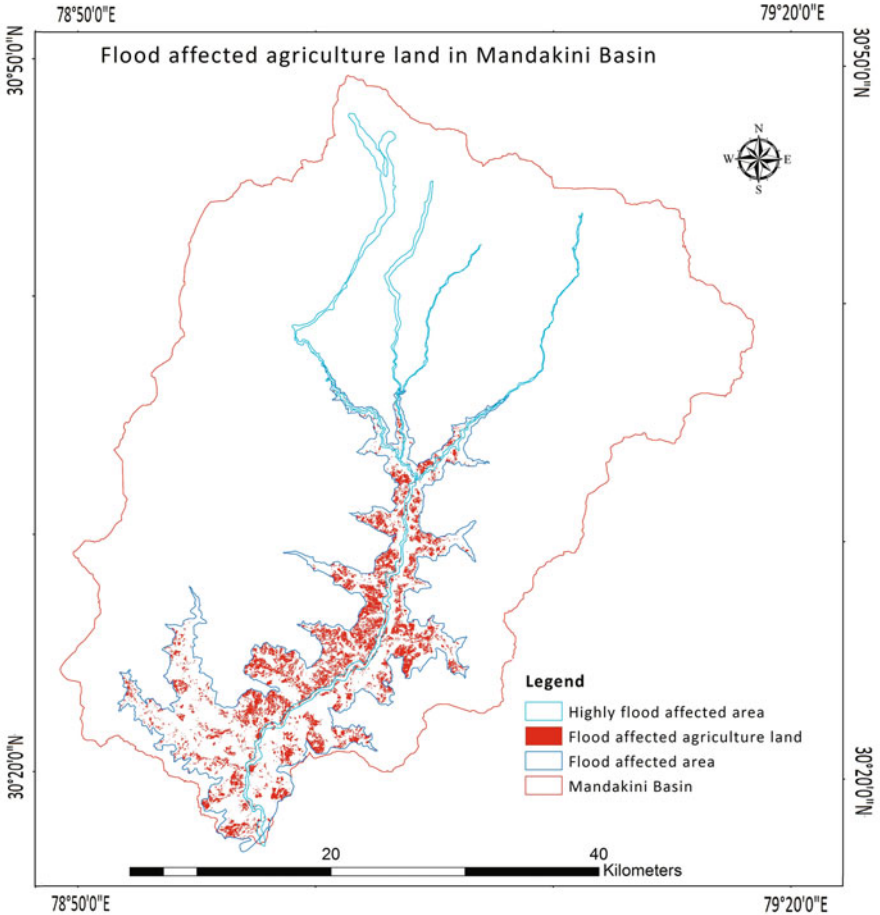
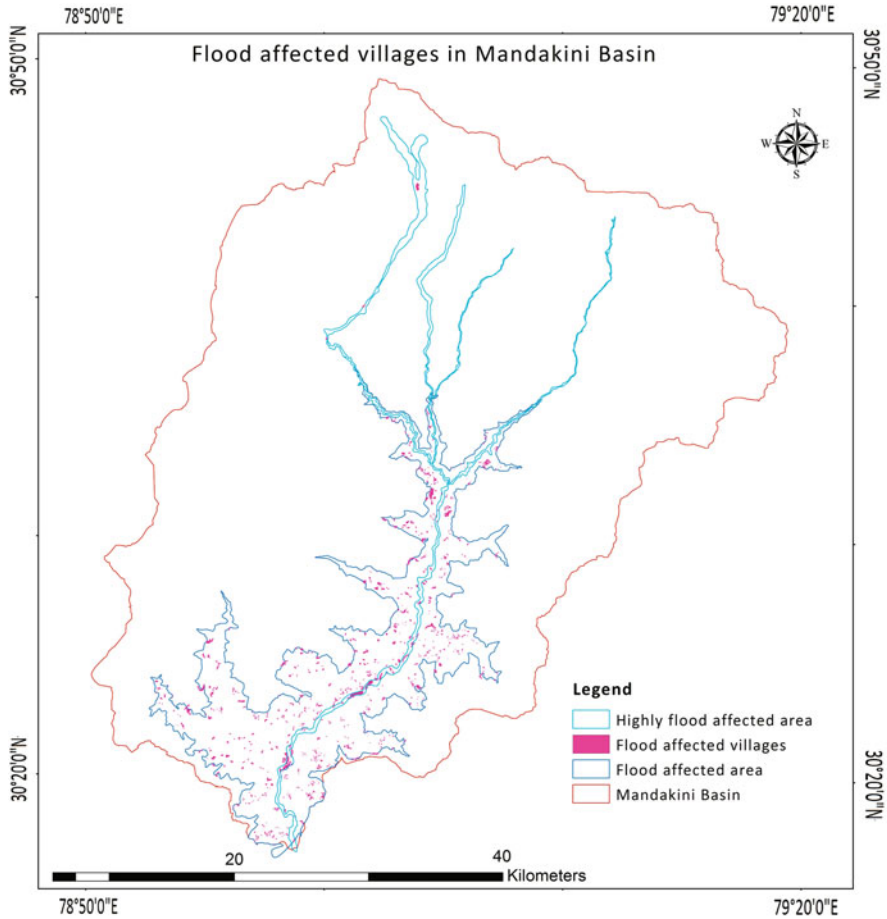


Fig. 8 Affected agriculture map in the month of June 2013

#### 4.4 Assessment of the Impact of the Flood on the Livelihood of Inhabitants

A survey was conducted to assess the impact of the disaster on the livelihood of people in Mandakini basin. This questionnaire-based assessment is divided among people of three age groups who were working in Gaurikund, Kedarnath, and in the route between Gaurikund and Kedarnath temple. Fig. 11a-e demonstrates various capitals of livelihood framework that were damaged or impacted by the flood, and Fig. 12 shows the final impact on the capitals, which we can construe from the analysis that there is a deviation in the result that is derivative of flood causatum.





**Fig. 9** Affected village map in the month of June 2011

#### ***4.5 Environmental Evaluation System Using the Battelle Method***

In this study, flood disaster is denoted as a project. The environmental parameter is organized into three main categories (Dee et al. 1973).

1. Ecological
2. Physio-chemical
3. Human interest

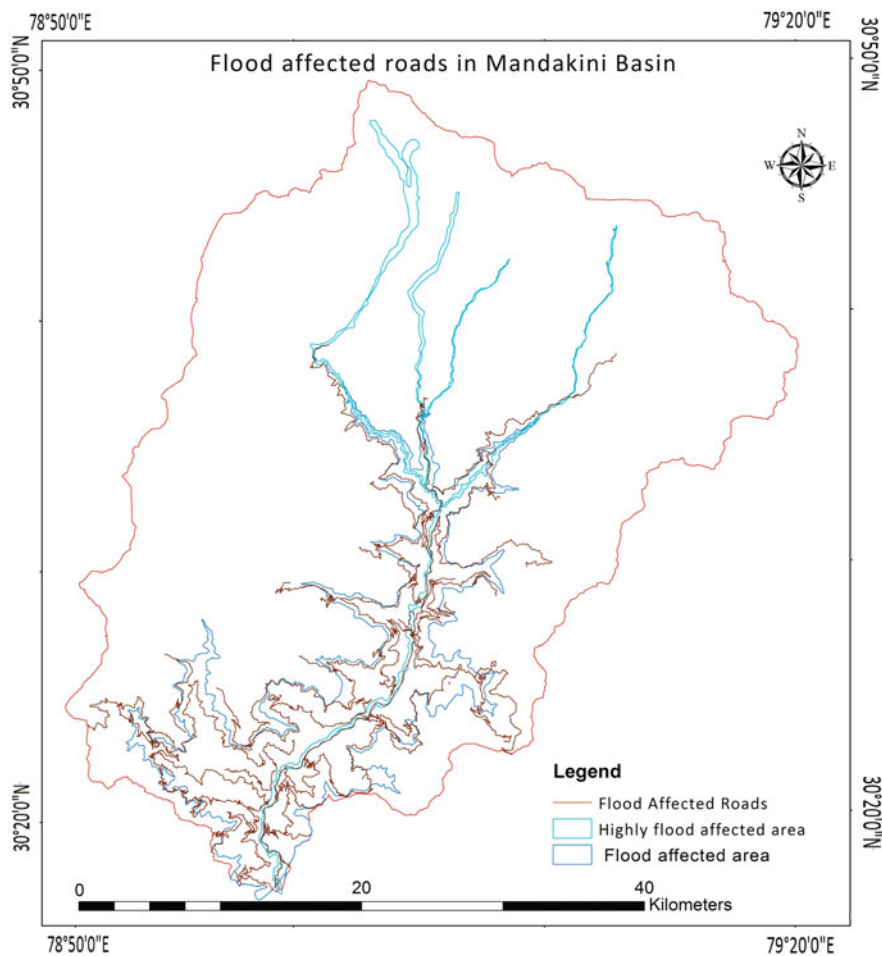


**Fig. 10** Affected road map in the month of June 2013

**Table 4** Distribution of affected roads and agriculture land

| Sl. no. | Road type        | Affected area (km <sup>2</sup> ) |        | Crop type   | Affected area (ha) |         |
|---------|------------------|----------------------------------|--------|-------------|--------------------|---------|
|         |                  | Min.                             | Max.   |             | Min.               | Max.    |
| 1.      | National Highway | 56.42                            | 87.41  | Kharif crop | 2267.25            | 4346.14 |
| 2.      | District road    | 37.44                            | 46.72  | Rabi crop   | 356.15             | 527.44  |
| 3.      | Village road     | 134.58                           | 269.92 | Zaid crop   | 26.41              | 35.36   |

These parameters that are mentioned in Table 6 are subdivided according to the environmental settings of the area. Each sub parameter has its own weightage.

So, all the parameters that get damaged in flood can be evaluated using the following formula:

**Table 5** Distribution of bridges/cross drainage structures and affected bridges

| S. no. | Block name | Affected bridges/cross drainage structures |      | Affected villages |      |
|--------|------------|--|------|-------------------|------|
|        |            | Min.                                       | Min. | Max.              | Max. |
| 1.     | Agastmuni  | 174  | 100  | 144               | 347  |
| 2.     | Jakholi    | 65   | 34   | 44                | 100  |
| 3.     | Ukhimath   | 72   | 69   | 71                | 96   |
| 4.     | Total      | 311  | 203  | 259               | 543  |

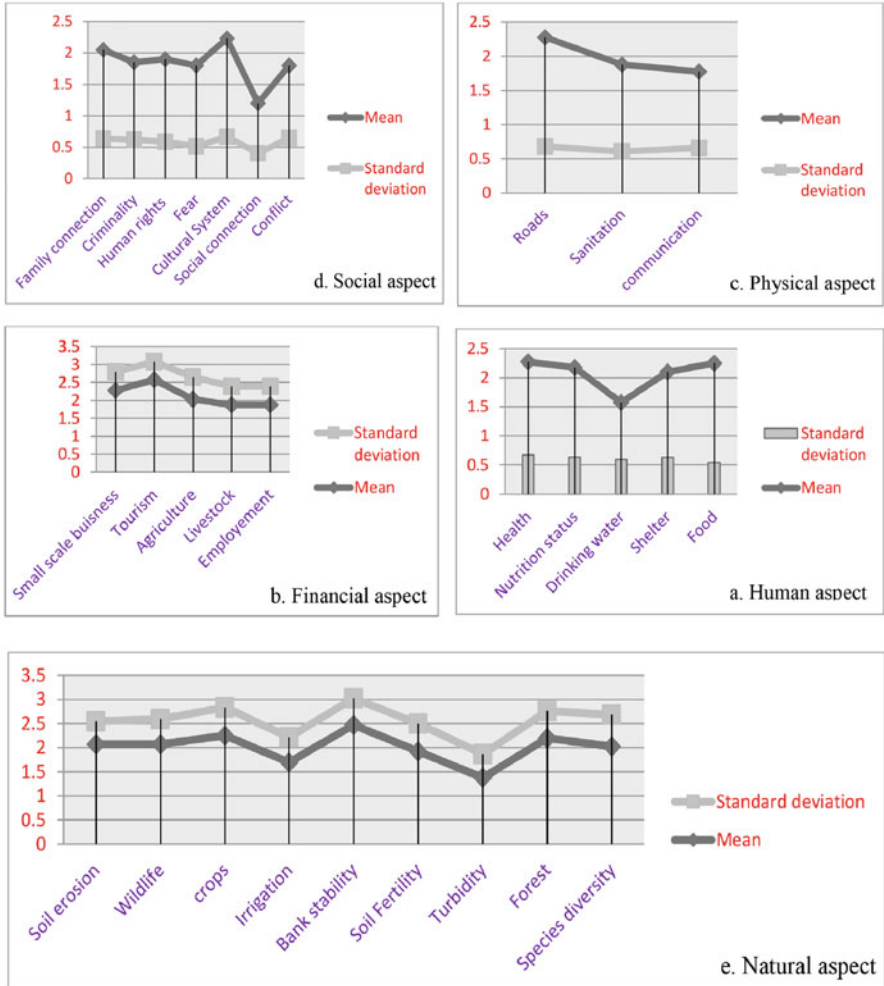


**Fig. 11** (a). Affected Human capitals; (b). Affected financial capitals; (c). Affected Physical capitals; (d). Affected Social capitals; (e). Affected Natural capitals

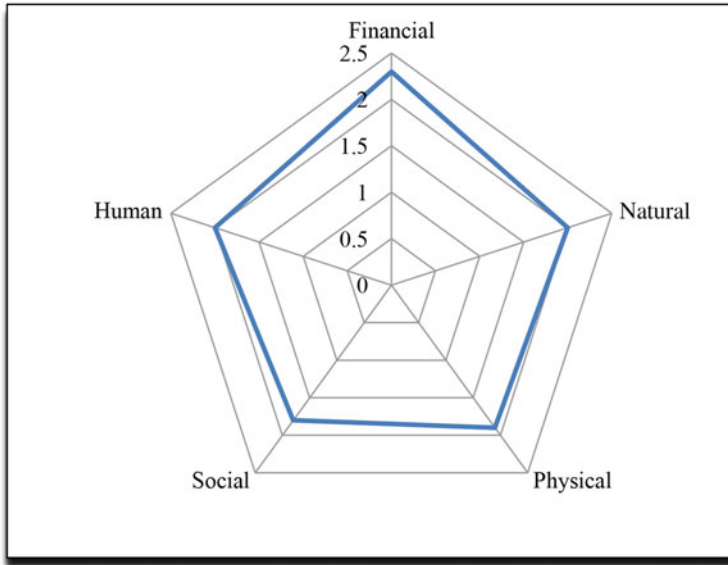


Fig. 12 Spider gram of all five capitals of sustainable livelihood framework

$$NET = \text{Weightage} \times \text{withflood} - \text{weightage} \times \text{withoutflood} - 46.1 \quad (3)$$

Where

NET = Net Environmental impact

This negative sign means that the health of the environment and other physical assets were drastically affected. This deteriorated the living condition of the region and also forced the people to leave their homes and migrate to safer place and start their life from scratch.

## 5 Discussion and Conclusion

Over the years, development in the Himalayan region has caused many changes that have had a deleterious effect on the environment and inhabitants in many ways. They may be summarized as:

### Ecological

Loss of approximately 10% of dense forest in the Mandakini valley causes disturbance in ecological cycling (Aerts and Honnay 2011) and forest plays an important role in the social, cultural, economic, and industrial development of any country (Björstig et al. 2018). Besides this, forests also maintain the moisture content in the soil, increase soil fertility and act as a habitat for many wild species. Due to

**Table 6** Environmental parameters with weightage with or without project

| Environmental categories    | PIU | (EQi) <sub>1</sub> | (EQi) <sub>2</sub> | EIU   |
|-----------------------------|-----|--------------------|--------------------|-------|
| Forest                      | 9   | 0.7                | 0.9                | -1.8  |
| Wildlife                    | 9   | 0.7                | 0.8                | -0.9  |
| Species diversity           | 9   | 0.7                | 0.9                | -1.8  |
| Species diversity Aq.       | 9   | 0.5                | 0.9                | -3.6  |
| Rare and endangered Sp. Aq. | 9   | 0.6                | 0.8                | -1.8  |
| Soil erosion                | 8   | 0.5                | 0.8                | -2.4  |
| Soil fertility              | 9   | 0.6                | 0.8                | -1.8  |
| Bank stability              | 9   | 0.6                | 0.9                | -2.7  |
| Sedimentation               | 9   | 0.7                | 0.9                | -1.8  |
| Seismicity                  | 7   | 9                  | 9                  | 0     |
| Flow variation              | 9   | 0.7                | 0.8                | -0.9  |
| Evaporation                 | 9   | 0.7                | 0.8                | -0.9  |
| Temperature stratification  | 9   | 0.8                | 0.9                | -0.9  |
| Turbidity                   | 9   | 0.6                | 0.8                | -1.8  |
| Parasitic disease           | 7   | 0.5                | 0.7                | -1.4  |
| Public sanitation           | 8   | 0.8                | 0.9                | -0.6  |
| Nutrition                   | 7   | 0.8                | 0.9                | -0.7  |
| Crop production             | 8   | 0.5                | 0.8                | -2.4  |
| Water supply                | 8   | 0.5                | 0.8                | -2.4  |
| Power supply                | 8   | 0.7                | 0.8                | -0.8  |
| Navigation                  | 7   | 0.6                | 0.9                | -2.1  |
| Irrigation                  | 8   | 0.5                | 0.9                | -3.2  |
| Flood control               | 8   | 0.7                | 0.8                | -0.8  |
| Highway relocation          | 10  | 0.8                | 0.9                | -1    |
| Reservoir leakage           | 9   | 0.7                | 0.8                | -0.9  |
| Climatic changes            | 9   | 0.8                | 0.8                | 0     |
| Archaeology treasure        | 9   | 0.6                | 0.9                | -2.7  |
| Water quality               | 8   | 0.7                | 0.8                | -1    |
| Transmission lines          | 10  | 0.7                | 0.8                | -1    |
| Recreation                  | 10  | 0.8                | 0.9                | -1    |
| Landscape                   | 10  | 0.8                | 0.9                | -1    |
| Total                       |     |                    |                    | -46.1 |

PIU parameter importance unit

fragmentation of forests by this flash flood, the threat of local extinction of many wild species of plant and animal has increased. Native flora and fauna are key to the structure and function of an ecosystem and any kind of alteration in this disturbs the basic ecological balance. By ground-truthing, we observed that dense forest pixels have been converted into open forest pixels and open to scrub forest pixels. It is showing how the health of the ecosystem is gradually decreasing over the decades in this valley. Also, during field observations, we found that water resources and springs on which native inhabitants are completely dependent, are dying, and/or

degrading. In our study, we have also found that water resources are depleting gradually over the decades and that springs and streams are dying. That will lead to more soil erosion and cause a negative impact on the ecological health of the valley area. Soil erosion has reduced the fertility of agricultural lands which forces people either to encroach upon common lands or to migrate.

### **Socio-ethno Damage and Insecurity to Livelihood**

This place is socio-ethnologically very rich, due to which, it is highly vulnerable to climate change. People in this region are mainly dependent on natural resource-based livelihood options (agriculture, fishery, tourism, livestock, etc.). So, damage to the ecosystem causes a very severe impact on the inhabitant's financial condition. To estimate the causes of flash flood, LULC map of both Alaknanda and Mandakini basin that demonstrates various changes in this fragile ecosystem was prepared. In the Alaknanda basin, there is a diminution in dense forest, open forest, and snow cover by 3.04%, 3.11%, and 0.9%, respectively, and expansion in built-up land. The same scenario shows up in the land cover map of Mandakini basin, where dense forest, scrub forest, and snow cover have decreased by 10.76%, 1.07%, and 3.85, respectively, in the last 20 years along with inflation in built-up land. Anthropogenic activities include urban sprawl of overall 1.43% of the total geographical area in the Mandakini basin. But major expansion occurred around the river bed or highly vulnerable places. Rambara is totally submerged in water and all the infrastructure has vanished from that area. During the field survey, one person said that once he had a big hotel in Rambara region and that after the disaster, he was left with no choice except taking pilgrims to the Kedarnath temple with the help of horses. So, he is a classic example of livelihoods damaged by the disaster. Dams and hotel construction around the river bed and other developmental activities have a negative impact that has emerged as a devastating flash flood on June 16, 2013. This natural disaster caused havoc due to over population in the town. June is a peak month in terms of visitors and the whole state of Uttarakhand is crowded with people. The abnormal timing of heavy rainfall and its emanation does not allow them even to find ways to travel. If the same mishap had happened in the winters, the loss of property and casualties would have been less because during the summer the population is very high in the study area.

By analyzing the impact on the livelihood of inhabitants by questionnaire-based survey method, it was found that all the five capitals were heavily affected as mainly they are dependent on tourism-based activities. So, these livelihood activities are not sustainable. People were jobless for 2–3 years. Most people depend on natural resources. So, these kinds of disasters are a nightmare to the native people. Policymakers and government bodies should make them aware of other livelihood generation options and train them in that particular field. By analyzing ecological settings and other available literature, we have tried to suggest some supplementary livelihood options for the Mandakini valley inhabitants in this paper.

Also, this study will help researchers as a baseline study for upcoming research. Data can be used for future flood mapping and livelihood assessment studies. Updated data on disaster and effect on natural and physical assets are essential for

planning and prevention from these disasters. This data will also help to lower the effect of disasters on humans and the natural environment. The baseline study is very important for future work to compare the present scenario or to drive conclusions on how much change has already occurred and what would be the consequences of these changes in the natural and physical environment.

## References

- Aerts, R., & Honnay, O. (2011). Forest restoration biodiversity and ecosystem function. *BMC Ecology*, *11*, 29.
- Allen, S., Rastner, P., Arora, M., Huggel, C., & Stoffel, M. (2016). Lake outburst and debris flow disaster at Kedarnath, June 2013: Hydro-meteorological triggering and topographic predisposition. *Landslides*, *13*(6), 1479–1491.
- Areendran, G., Sahana, M., Raj, K., Kumar, R., Sivadas, A., Kumar, A., et al. (2020). A systematic review on high conservation value assessment (HCVs): Challenges and framework for future research on conservation strategy. *Science of the Total Environment*, *709*, 135425.
- Ashraf, S., Iftikhar, M., Shahbaz, B., Khan, G. A., & Luqman, M. (2013). Impacts of flood on livelihoods and food security of rural communities: a case study of southern Punjab, Pakistan. *Pakistan Journal of Agricultural Sciences*, *50*(4) 751–758.
- Bjarstig, T., & Stens, A. (2018). Social value of forests and production of new goods and services: The views of Swedish family forest owners. *Small-Scale Forestry*, *17*(1), 125–146.
- Das, R., Borbora, T. K., Sarma, M. K., & Sarma, N. K. (2005). Genotypic variability for grain yield and flood tolerance in semi deep-water rice (*Oryza sativa* L.) of Assam. *Oryza*, *42*(4), 313.
- Das, S., Kar, N. S., & Bandyopadhaya, S. (2015). Glacial lake outburst flood Kedarnath, Indian Himalaya a study using digital elevation model and satellite images. *Natural Hazard*, *77*(2), 769–786.
- De Bruin, W. B., Wong-Parodi, G., & Morgan, M. G. (2014). Public perceptions of local flood risk and the role of climate change. *Environment Systems and Decisions*, *34*(4), 591–599.
- Dee, N., Baker, J., Drobny, N., Duke, K., Whitman, I., & Fahrings, D. (1973). An environmental system for water resource planning. *Water Resource Research*, *9*(3), 523–535.
- Dobhal, D. P., Mehta, M., & Srivastava, D. (2013). Influence of debris cover on terminus retreat and mass changes of Chorabari glacier, Garhwal region, central Himalaya, India. *Journal of Glaciology*, *59*(217), 961–971.
- Ferrari, J. R., Lokkingbill, T. R., McCormick, B., Toumund, P. A., & Eshleman, K. N. (2009). Surfacing and reclamation effects on flood response of watersheds in the central Appalachean plateau region. *Water Resource Research*, *45*(4).
- Guo, B., & Zhang, G. (2009). Land-use change in farming pastoral region of inner magnolia based on GIS and Markov model. *Transaction of Chinese Society of Agriculture Engineering*, *25*/121, 291–298.
- Hughes, M. L., McDowell, P. F., & Marcus, W. A. (2006). Accuracy assessment of georectified aerial photographs: Implications for measuring lateral channel movement in a GIS. *Geomorphology*, *74*(1–4), 1–16.
- Khatun, S., Sahana, M., Jain, S. K., & Jain, N. (2018). Simulation of surface runoff using semi distributed hydrological model for a part of Satluj Basin: Parameterization and global sensitivity analysis using SWAT CUP. *Modeling Earth Systems and Environment*, *4*(3), 1111–1124.
- Martha, T. R., Roy, P., Govindharaj, K. B., Kumar, K. V., Diwakar, P. G., & Dadhwal, V. K. (2015). Landslides triggered by the June 2013 extreme rainfall event in parts of Uttarakhand state, India. *Landslides*, *12*(1), 135–146.

- Metcalfe, R. P. (1993). Pressure, Temperature and time constraints and metamorphism across the main central thrust zone and high Himalayan slab in Garhwal Himalaya. *Geological Society*, 74 (1), 485–509.
- Mohapatra, P. K., & Singh, R. D. (2003). *Flood management in India, flood problem and management in South Asia* (pp. 131–143). Cham: Springer.
- Muis, S., Güneralp, B., Jongman, B., Aerts, J. C., & Ward, P. J. (2015). Flood risk and adaptation strategies under climate change and urban expansion: A probabilistic analysis using global data. *Science of the Total Environment*, 538, 445–457.
- Nott, J. (2006). *Extreme events: A physical reconstruction and risk assessment* (NIDM Report 2013) (Vol. 51). New York: Cambridge University Press. <https://nidm.gov.in/PDF/pubs/India%20Disaster%20Report%202013.pdf>.
- Rawat, R. K. (2016). Dalit and tribal identity in journalism and media (a study on Dalit and tribal news published in various newspapers and web portals). *International Journal on Transformations of Media, Journalism & Mass Communication*. (Online ISSN: 2581-3439), 1, 2.
- Rehman, S., Sahana, M., Hong, H., Ahmad, B. B., & Sajjad, H. (2019). A systematic review on approaches and methods used for flood vulnerability assessment: Framework for future research. *Natural Hazards, Springer*, 1–24. ISSN: 0921-030X (Print) 1573-0840 (Online).
- Sahana, M., & Patel, P. P. (2019). A comparison of frequency ratio and fuzzy logic models for flood susceptibility assessment of the lower Kosi River basin in India. *Environmental Earth Sciences*, 78(10), 289.
- Sahana, M., & Sajjad, H. (2017). Evaluating effectiveness of frequency ratio, fuzzy logic and logistic regression models in assessing landslide susceptibility: A case from Rudraprayag district, India. *Journal of Mountain Science*, 14(11), 2150–2167. Springer ISSN: 1672-6316 (print) 1993-0321 (online).
- Sahana, M., & Sajjad, H. (2019). Vulnerability to storm surge flood using remote sensing and GIS techniques: A study on Sundarban biosphere reserve, India. *Remote Sensing Applications: Society and Environment*, 13, 106–120.
- Sahana, M., Sajjad, H., & Ahmed, R. (2015). Assessing spatio-temporal health of forest cover using forest canopy density model and forest fragmentation approach in Sundarban reserve forest, India. *Modeling Earth Systems and Environment*, 1(4), 49.
- Sahana, M., Hong, H., & Sajjad, H. (2018). Analyzing urban spatial patterns and trend of urban growth using urban sprawl matrix: A study on Kolkata urban agglomeration, India. *Science of the Total Environment*, 628, 1557–1566.
- Sahana, M., Hong, H., Sajjad, H., Liu, J., & Zhu, A. X. (2018). Assessing deforestation susceptibility to forest ecosystem in Rudraprayag district, India using fragmentation approach and frequency ratio model. *Science of the Total Environment*, 627, 1264–1275.
- Sahana, M., Rehman, S., Sajjad, H., & Hong, H. (2020). Exploring effectiveness of frequency ratio and support vector machine models in storm surge flood susceptibility assessment: A study of Sundarban biosphere reserve, India. *Catena*, 189, 104450.
- Sati, V. P. (2008). Natural resource management and food security in the Alaknanda Basin of Garhwal Himalaya. *ENVIS Bulletin: Himalayan Ecology*, 16(2), 1–11.
- Sati, V. P. (2009). Traditional farming systems and sustainability issues: A case for the Garhwal Himalaya, India. In *Peer reviewed proceedings of the fourth international scientific conference 'rural development* (pp. 399–407).
- Sati, V. P. (2013). Extreme weather related disasters: A case study of two flashfloods hit areas of Badrinath and Kedarnath valleys, Uttarakhand Himalaya, India. *Journal of Earth Science and Engineering*, 3(8), 562.
- Scoones, I. (1998). Sustainable rural livelihoods: a framework for analysis.
- Sharma, V. K. (2005). *Natural disaster management in India environment and development viewpoint*. TERI University.
- Sharma, M., & Tyagi, S. (2013). The impact of torrential Rainfall in Kedarnath, Uttarakhand, India during June. *International Research Journal of Environment Science*, 2(9), 34–37.
- Singh, G., & Rawat, G. S. (2011). Ethnomedical survey of Kedarnath wildlife sanctuary in Western Himalaya, India. *Indian Journal of Fundamental and Applied Life Sciences*, 1(1), 35–46.



- Singh, A. K., Parsad, A., & Singh, B. (1986). Availability of phosphorus and potassium and its relationship with physico-chemical properties of some forest soils of Pali-range (Shahdol, M. P.). *Indian For*, 112(12), 1094–1104.
- Sinha, S. (1998). Environmental impact assessment: An effective management tool. *TERI Information monitor on Environmental Science*, 3(1), 1–7.
- Smith, K., & Ward, R. (1998). *Floods: Physical processes and human impacts*. John Wiley and Sons Ltd.
- Syed, M., Wagh, G., & Supekar, A. (2013). Assessment of impact on the groundwater quality due to urbanization by hydrogeochemical facies analysis in SE part of Pune city, India. *Proceedings of the International Academy of Ecology and Environmental Sciences*, 3(2), 148.
- Valdiya, K. S. (1995). Proterozoic sedimentation and Pan-African geodynamic development in the Himalaya. *Precambrian Research*, 74(1–2), 35–55.
- Valdiya, K. S., Chandra, S. K., Bhakuni, T., & Upadhyaya, R. C. (2000). Tectonic and lithological characterization of Himadri (Great Himalaya) between Kali and Yamuna rivers, central Himalaya. *Himalayan Geology*, 20(10), 1–11.
- World Bank (IBRD). (2003). *Lifelong learning in the global knowledge economy: Challenges for developing countries: A World Bank report*. Washington, District of Columbia: World Bank.

# Assessment of Vegetation Vigor Using Integrated Synthetic Aperture Radars



Suman Sinha

**Abstract** Vegetation health is dependent on various biophysical, geographical, and meteorological factors. The floral biomass can be used as the proxy for vegetation vigor. Accurate and precise assessment of biomass is henceforth important for specifying the health of vegetation that is indicative of a collection of several environmental factors. Remote sensing has currently emerged to be the most important and widely utilized tool for biomass assessment. Synthetic Aperture Radars (SARs) offer more accurate forest biomass estimates than optical multispectral remote sensing due to the absence of distinctive intrinsic characteristics of radars. The capability of multi-polarized COSMO-SkyMed (X-band), Radarsat-2 (C-band), and ALOS PALSAR (L-band) was investigated for biomass retrieval in a moist tropical virgin forest landscape of India. Backscatter values generated from the raw SAR images were correlated with field above-ground biomass (AGB) values and were modeled using Multiple Linear Regression analysis to generate best-fit models for AGB estimates with single and combined frequencies of X-, C-, and L-bands. The integrated model for AGB estimation involving X-, C-, and L-bands achieved an accuracy of 75.3% with  $r^2 = 0.90$  and RMSE = 15.29 t/ha. On validating the above-said models, the integrated model involving X-, C-, and L-bands showed the best results among all other models with  $r^2 = 0.95$ , RMSE = 14.81 t/ha, and data agreement of 0.95. Most of the biomass ranged within 125 Mg/ha in the study site. Hence, the study presents a suitable approach in assessing vegetation vigor from AGB from SAR, thus contributing to the ecological and forestry realms.

**Keywords** Synthetic aperture radar · Multi-frequency · Polarization · Backscatter · Deciduous forest · Biomass

---

S. Sinha (✉)

Department of Geography, Amity Institute of Social Sciences, Amity University Kolkata, Kolkata, West Bengal, India

e-mail: [ssinha1@kol.amity.edu](mailto:ssinha1@kol.amity.edu)

© The Editor(s) (if applicable) and The Author(s), under exclusive license to Springer Nature Switzerland AG 2021

P. Kumar et al. (eds.), *Remote Sensing and GIScience*,

[https://doi.org/10.1007/978-3-030-55092-9\\_3](https://doi.org/10.1007/978-3-030-55092-9_3)

## 1 Introduction

The health of forest is reflected by its biomass. The biomass is the most vital ingredient in understanding the carbon cycle and conveys information related to climate change and forest health or vigor (Sinha et al. 2018a). Vegetation with higher biomass content is generally considered to have greater vigor than that having lower biomass level. Biomass also serves as an indicator of carbon concentration that is stored in floral species and released into atmosphere during forest fires (Sharma et al. 2012). The concentration of atmospheric carbon is ever-increasing and the global carbon dioxide (CO<sub>2</sub>) level crossed the critical mark of 400 ppm during 2016, an irreversible phenomenon called “400 ppm World” (Sinha and Santra 2019). The Earth’s atmospheric CO<sub>2</sub> concentration has surpassed 415 ppm ever since humans came into existence in millions of years during the first half of May 2019 (Sinha et al. 2020). So, there exists a relationship between the carbon released, carbon/biomass sequestered by plants, and the vigor of the forest. Forests serve a dual function in both acting as carbon sink and source. Forests, among entire terrestrial ecosystems, are the utmost repository of carbon under natural circumstances; however, under stressed situations, they emit huge carbon in the atmosphere, thus regulating the land-atmosphere CO<sub>2</sub> exchange (Sinha et al. 2019a). Sources of atmospheric CO<sub>2</sub> can either be natural or anthropogenic; the anthropogenic activities being more detrimental. Reducing emissions from deforestation and forest degradation (REDD) accounts for the enumeration of this carbon balance in the environment that helps to maintain and monitor this atmospheric carbon balance (Sharma et al. 2013). More than one-third of the terrestrial carbon storage is concentrated in the tropical forests that further harbor a fifth of total anthropogenic CO<sub>2</sub> emissions to the atmosphere on deforestation (Sinha et al. 2019b). Carbon stored in the forests can be assessed in terms of above-ground bole biomass stored in the plants that can ultimately result in the calculation of carbon dioxide released in atmosphere due to forest loss (Sharma et al. 2013; Sinha et al. 2017; Waikhom et al. 2017).

Integrated geospatial techniques that incorporate remote sensing, geographic information system (GIS), and Global Positioning System technologies provide the best probable approach quantifying the forest AGB for precise continual monitoring over large areas with varying scales (Sinha et al. 2015a), in context to REDD (De Sy et al. 2012). AGB estimation is done with inputs from tree allometry, combined with integrated geospatial techniques that contribute to the multi-scale AGB estimations (Sinha et al. 2015a). Often using multispectral optical remote sensing sensors for AGB estimation (Lu 2006; De Sy et al. 2012; Sharma et al. 2013; Kumar et al. 2013; Dube et al. 2016; Sinha 2018), however, they suffer from less sensitivity to forest parameters and saturate early, unlike Synthetic Aperture Radar (SAR) sensors that are currently more frequently used owing to the distinct intrinsic characteristics of SAR that overcomes the constraints of optical remote sensing sensors (De Sy et al. 2012; Sinha et al. 2015a; Villard et al. 2016; Sinha et al. 2016; Kumar and Mutanga 2017; Santoro and Cartus 2018).

Frequent cloudy sky mostly in tropical regions often restrains the collection of good quality of remote sensing data by optical sensors. In this condition, microwaves can provide feasible option in remote acquisition of earth's surface data. This unique feature of microwave remote sensing widens its use in different fields of research including flood studies, forest mapping, and biomass estimation (Lu 2006). SAR is applied widely in assessing forest biomass because of its capability of penetrating through forest canopies. This enables the volumetric estimation of forest. The estimation is sensitive to microwave frequency as well as polarization. Higher wavelengths can penetrate the canopy more. Similarly, cross-polarized waves are more sensitive to biomass. Furthermore, microwaves are sensitive to plant moisture content as well (Sinha et al. 2015a). These clear-cut advantages over the optical sensors made better estimation of forest AGB by SAR with less uncertainty in comparison with its optical sensing competitors.

SAR data is captured in K-, X-, C-, L-, and P-bands under varied polarization, range, and azimuth resolution. Microwave sensors transmit polarized wave. Horizontally polarized (H) and vertically polarized (V) wave generates when the electrical field of the electromagnetic wave oscillates horizontally and vertically, respectively. Dual-polarized sensors can transmit and receive both the polarizations. However, fully polarimetric quad-polarized sensors can transmit and receive the complete polarization vector of the backscatter signal. Vegetated areas produce higher backscattered signal intensity in comparison with bare ground and calm water due to multiple scattering of vegetation (Balzter 2001).

Variations in microwave data produce different significant forest stand characteristics (Leckie 1998). X-band relates to canopy surface information as it specifically interacts with the top of the canopy cover (including leaves, small branches, etc.) without much penetration; C-band having greater penetration interacts with the small branches and underlying objects within the canopy; L- and P-bands infiltrate the surface canopy layers and have high interaction with major forest parameters including the main branches and the trunk of the trees that contributes primarily to the biophysical parameters like AGB, DBH, stand height, and basal area (Sinha et al. 2020). Hence, for biomass studies, L-band SAR is more suitable and fitting than the rest of the spaceborne SAR bands (Lu 2006; Le Toan et al. 1992). Longer wavelength and lesser frequency SAR data from L- and P-bands with maximum penetration capabilities are scattered and attenuated by the main woody portions of trunk and main branches that relates maximum to the forest biophysical parameters (Sinha et al. 2015a). Like-polarized HH and VV and shorter wavelengths or higher frequency with less penetration are generally less sensitive to biomass than the cross-polarized HV or VH and higher wavelength or low frequency with greater penetration (Pandey et al. 2010; Wollersheim et al. 2011; Sinha et al. 2015a). Yet instances are observed when like-polarized data show greater sensitivity to AGB (Sharma et al. 2014; Sinha et al. 2016, 2017). Ratio of polarized data can be investigated for the same as this too has great prospects (Sinha et al. 2018b). SAR interferometry and polarimetry also have potentialities in AGB assessment (Kumar 2009; Sinha et al. 2015b; Sinha 2016; Kumar et al. 2017).

Among the spaceborne radars till date, L-band is the most suitable for measuring biomass, even for the complex tropical forest ecosystems (Hamdan et al. 2011). Beaudoin et al. (1994) showed that high frequency SAR bands with VV and HV polarization were solely linked to crown biomass, while HH data at lower frequencies (P- and L-bands) were related to trunk along with crown biomass. Harrell et al. (1997) compared several AGB estimation techniques using Shuttle Imaging Radar (SIR) C- and L-band multi-polarized radar data for pine species and commented that the HH polarized L-band data were the decisive components in AGB estimates.

The performance of estimation improved when HH or HV polarized C-band data was added in the regression equations. Kuplich et al. (2000) found that the Japan Earth Resource Satellite (JERS)-1/SAR data has the potential to estimate biomass for young, regenerating forests. The double bouncing scattering and forest structural-physiognomic characteristics of JERS-1/SAR data are found to be important for AGB estimation of forest and savanna (Santos et al. 2002). In case of biomass estimation of forest stands in mountainous regions, the multi-polarized L-band SAR data are found to be very useful (Sun et al. 2002). Castel et al. (2002) established a significant relationship between the backscatter coefficient of JERS-1/SAR data and pine plantation biomass. Most of these studies applied the single polarized and low resolution JERS-1, European Remote Sensing satellites ERS-1/2 SAR data with mono incident angle. However, introduction of the ALOS Phased Array type L-band Synthetic Aperture Radar (PALSAR) and C-band RADARSAT-2 data created more opportunity to the scientific community to re-evaluate the potential of SAR data in forest biomass estimation (Kumar et al. 2015). Le Toan et al. (2011) applied PAL SAR data to map Amazonian and Siberian forests. However, the results exclude most of the tropical and temperate forests. Use of texture analysis in biomass assessment is an important aspect that needs focus. Sarker (2010) has used texture measures for biomass estimation using optical and SAR data. Sarker et al. (2013) inquired the utility of the C-band RADARSAT-2 fine beam dual-polarized (HH and HV) data for AGB estimation in complex subtropical forest and found interesting results. Despite good results from the backscatter data, there exists a saturation problem specifically in handling complex forest stand structure. Lu (2006) enlisted the factors that include SAR frequency, wavelengths and polarizations, and vegetation structure and ground characteristics, on which the saturation levels depend on. However, the combined use of C- and L-bands can reduce the problem (Hoekman and Quinones 1997). Synergistic use of multi-frequency SAR data has enhanced potentialities in the estimates (Sinha et al. 2017). It is observed that the ratio between SAR bands provides valuable solution to the saturation problem (Santos et al. 2002). Spectral information from optical data, along with the multi-frequency X-, C-, and L-SAR data integrated together can be the best solution for biomass estimation that reduces the uncertainty and saturation problems (Sinha et al. 2020). At AGB less than 150 t/ha, models integrating forest succession and radar information produced precise results (Ranson et al. 1997). Feasible solution can be obtained on considering the landscape characteristics (Austin et al. 2003).

SAR interferometry (InSAR) offers valuable results in reducing the saturation problem (Ghasemi et al. 2011). This also helps in nullifying the terrain effects

without any extra data resulting in backscatter variations due to alterations in the target characteristics (Balzter 2001). De Zan et al. (2013) and Treuhaft et al. (2015) applied TanDEM-X interferometry to assess biomass of tropical forests. Semi-empirical models like Water Cloud Model (WCM) and Interferometric WCM (IWCM) are important in tree volume estimation for biomass (Kumar 2009; Lucas et al. 2006).

The biomass-backscatter coefficient curve demarcates the saturation mark as the slope tends to zero (Sinha et al. 2019a). Uncertainties arise as the saturation values depend on the SAR and reference data (Englhart et al. 2011), along with the forest parameters. Saturation levels of C-, L-, and P-bands were determined by Nizalapur et al. (2010) in the tropical forests of India. Moreover, the saturation values are also established in several other studies (Lucas et al. 2006; Nizalapur et al. 2010; Pandey et al. 2010; Englhart et al. 2011; Ghasemi et al. 2011; Sinha et al. 2015a; Sinha et al. 2017). It is already mentioned earlier that the saturation problem creates havoc in AGB estimation. However, InSAR can cope with this saturation problem as the technology can enhance this limit (Fransson et al. 2001), although the accuracy relies on certain factors that inherit dynamic vegetation including the study area's natural conditions. Multi-temporal SAR images under favorable conditions may enhance the accuracy. This approach produced acceptable results in boreal forests (Fransson et al. 2001; Pulliainen et al. 2003; Sinha et al. 2015a).

A detailed review of SAR techniques for biomass estimation is mentioned in Sinha et al. (2015a). The combined application of optical and SAR offers better results for biomass estimates over the single use of any sensor (Sinha et al. 2016) and even enhance the saturation level (Sinha et al. 2019a). Sarker (2010) used multi-sensor approach including SPOT-5, AVNIR-2, PALSAR, and Radarsat-2 for biomass estimation. Sinha et al. (2016) showed an improvement in the analysis of biomass on integrating models with Landsat TM and ALOS PALSAR data. Forest biomass and structural parameters were analyzed by Hyde et al. (2006) using multi-sensor synergy approach incorporating optical, SAR, interferometry, and LiDAR technologies. SAR has an obvious upper-hand than other sensors for biomass assessment due to their distinctive characteristics that make them superior over others (Sinha et al. 2015a). Alappat et al. (2011), Englhart et al. (2011), and Sinha et al. (2019b) have used integrated multi-frequency SAR for retrieval of biomass. This approach can even improve the estimation by enhancing the saturation point (Sinha et al. 2020). As the optical has low saturation levels, integrating multi-frequency SAR data instead of optical and SAR can probably produce higher saturation levels. Hence, the current study utilizes multi-frequency L-, C-, and X-bands from band ALOS PALSAR (HH/HV dual-polarized), Radarsat-2 (HH/VV/HV full polarized), and COSMO-SkyMed (HH/VV dual-polarized) data for AGB assessment of Bhimbandh Wildlife Sanctuary in Munger (Bihar, India), which is a tropical mixed deciduous forests.

## 2 Study Area and Datasets

### 2.1 Study Area

Bhimbandh Wildlife Sanctuary in Munger, Bihar (India), is the selected study site, which is a tropical deciduous mixed forest having geo-locations of 25°19'30"N-24°56'50"N latitude and 86°33'33"E-86°11'51"E longitude, covering an area of approximately 672.5 km<sup>2</sup> (Fig. 1). Sinha et al. (2013) illustrated the land-use/land-cover features of the area. The area includes reserved forests (approx. 257.50 km<sup>2</sup>) and protected forests (approx. 424.40 km<sup>2</sup>) (Sinha and Sharma 2013). It is a virgin patch with limited anthropogenic hindrances that make this site ideal for experimentation (Sinha et al. 2016). Total area (89%) is under forest cover with open to moderately dense forests (Sinha et al. 2013). The dominant floral species are *Shorea robusta*, *Acacia catechu*, *Madhuca longifolia*, *Dendrocalamus strictus*, *Diospyros melanoxylon*, and *Terminalia tomentosa*. The principal floral species found in the area is *Shorea robusta* or the sal and then *Acacia catechu* or the khair. As per 2012 statistics, sal-mixed and khair-mixed vegetation covers 49.68% and 20.66% of the total study area, respectively, thereby totaling to more than 70% of the area (Sinha et al. 2013). Soil texture is medium to heavy with clay, somewhat alkaline. Soil color is gray to dark gray. The mean annual rainfall is 1078.7 mm, the maximum temperature is about 45 °C during summers, while minimum temperature ranges between 3.5 °C and 9 °C during winters. Topography of the area is marked with several peaks with heights up to approximately 450 m. It is a forested table top hill with deep lateritic layer. The forest patch is matured with limited biomass change and anthropogenic interventions. The forest is undisturbed patch ideal as an experimental site.

### 2.2 Datasets

False Color Composite of the ALOS PALSAR dual-polarized (HH/HV) data of 2007, 2009, and 2010; C-band RADARSAT-2 full polarized (HH/VV/HV) data of 2011 and X-band COSMO-Skymed dual-polarized (HH/VV) data of 2011 are used (Fig. 1). Table 1 enlists the satellite data specifications.

## 3 Method

The methodology (Fig. 2) comprises the following sections: (a) above-ground biomass (AGB) assessment from in-situ field measurements, (b) SAR data processing, (c) AGB assessment from SAR backscatter measurements, and (d) regression analysis.

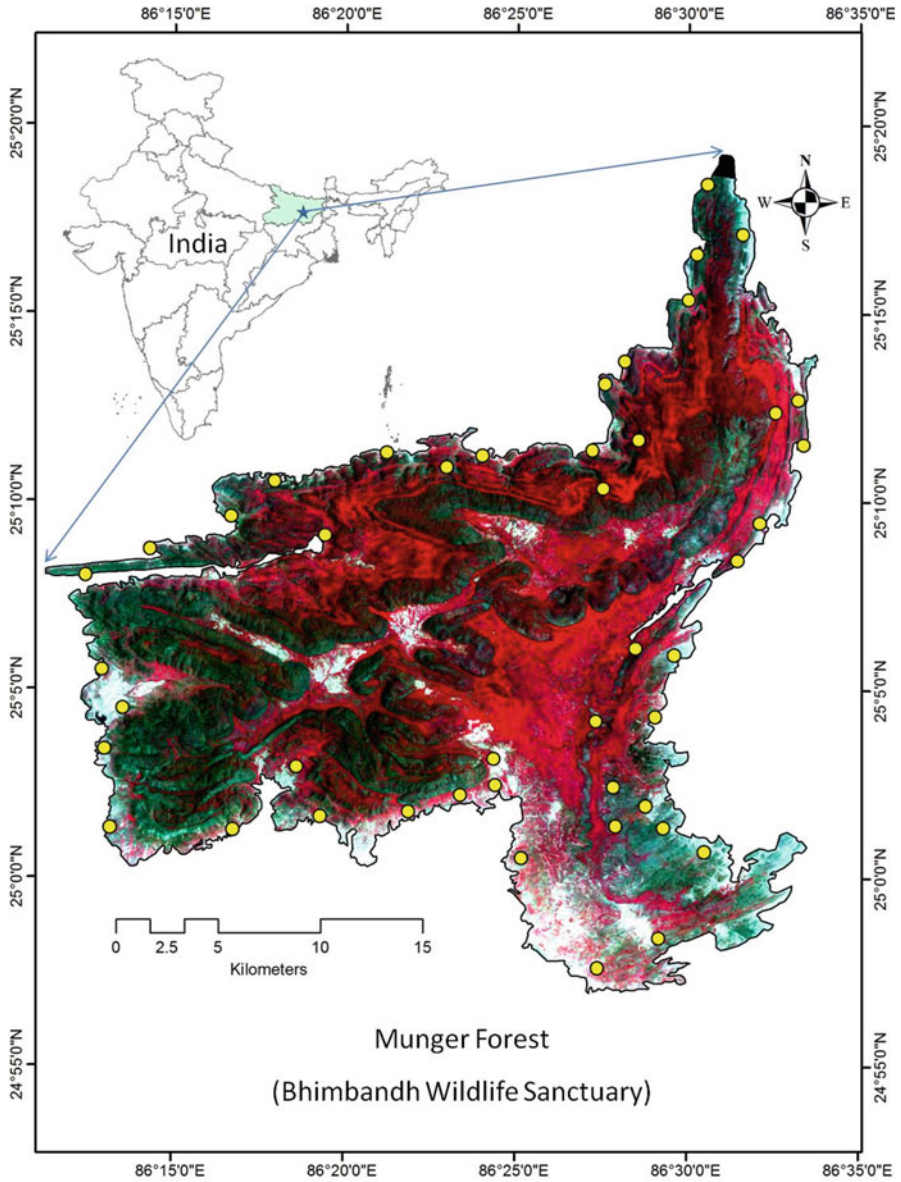


Fig. 1 Location of the study area

### 3.1 In-Situ Measurements

Field data was collected from 45 randomly selected square sample plots with area of 0.1 hectare each during 2010–2011 via random sampling method. The dimensions of



**Table 1** Satellite data specifications

| Parameters                              | SAR Remote Sensing data  |   |  |
|---|--|---|--|
| Satellite                               | COSMO-Skymed   | Radarsat-2                                | ALOS   |
| Sensor/<br>payload                      | SAR  | SAR                                       | PALSAR   |
| Launching<br>country<br>(Organization)  | Italy (ASI)  | Canada<br>(CSA)                           | Japan (JAXA)   |
| Date of launch                          | June 8, 2007, December<br>9, 2007, October 25, 2008,<br>November 5, 2010 | December<br>14, 2007                      | January 24, 2006   |
| Spatial<br>resolution                   | 15 m   | 25 m                                      | 25 m   |
| Swath width                             | 30 km  | 25 km                                     | 70 km (34.3° incident angle),<br>30 km (21.5° incident angle)                        |
| Wavelengths/<br>bands                   | X-band   | C-band                                    | L-band   |
| Mode and<br>Polarization                | PINGPONG; dual<br>(HH/VV)  | Standard<br>quad-pol<br>(HH/HV/VH/<br>VV) | Fine beam single (HH), fine<br>beam dual (HH/HV), quad<br>Polarimetric (HH/HV/VH/VV) |
| Number of<br>looks (azi-<br>muth:Range) | 3:1  | 3:1                                       | 3:1 (FBS), 4:1 (FBD), 7:1 (PLR)  |
| Year of data<br>acquisition             | 2011   | 2011                                      | 2007, 2009, 2010   |
| Data acquiring<br>source                | ASI (Italy)  | CSA<br>(Canada)                           | JAXA (Japan)   |

the plots being 31.6 m × 31.6 m matches approximately the pixel dimensions (30 m × 30 m) of the resampled satellite data used. The sample plots were concentrated mostly near the periphery due to inaccessibility of the interior portions. However, it was noted that representative samples were selected from every forest stratum, thus addressing the variability in the area. Information regarding forest types, species composition, stand height, and girth at breast height is collected from each such plot. The plots were randomly segregated into 80:20 ratio (Sinha et al. 2020), wherein 80% of the total sample plots, i.e., 36, were randomly selected to be used for establishing a relation between field AGB and SAR backscatter; while the remaining 20%, i.e., 9, for the model validation. Volumetric equations (FSI 1996) and specific gravity (FRI 1996) of the floral species were used to calculate the plot biomass.

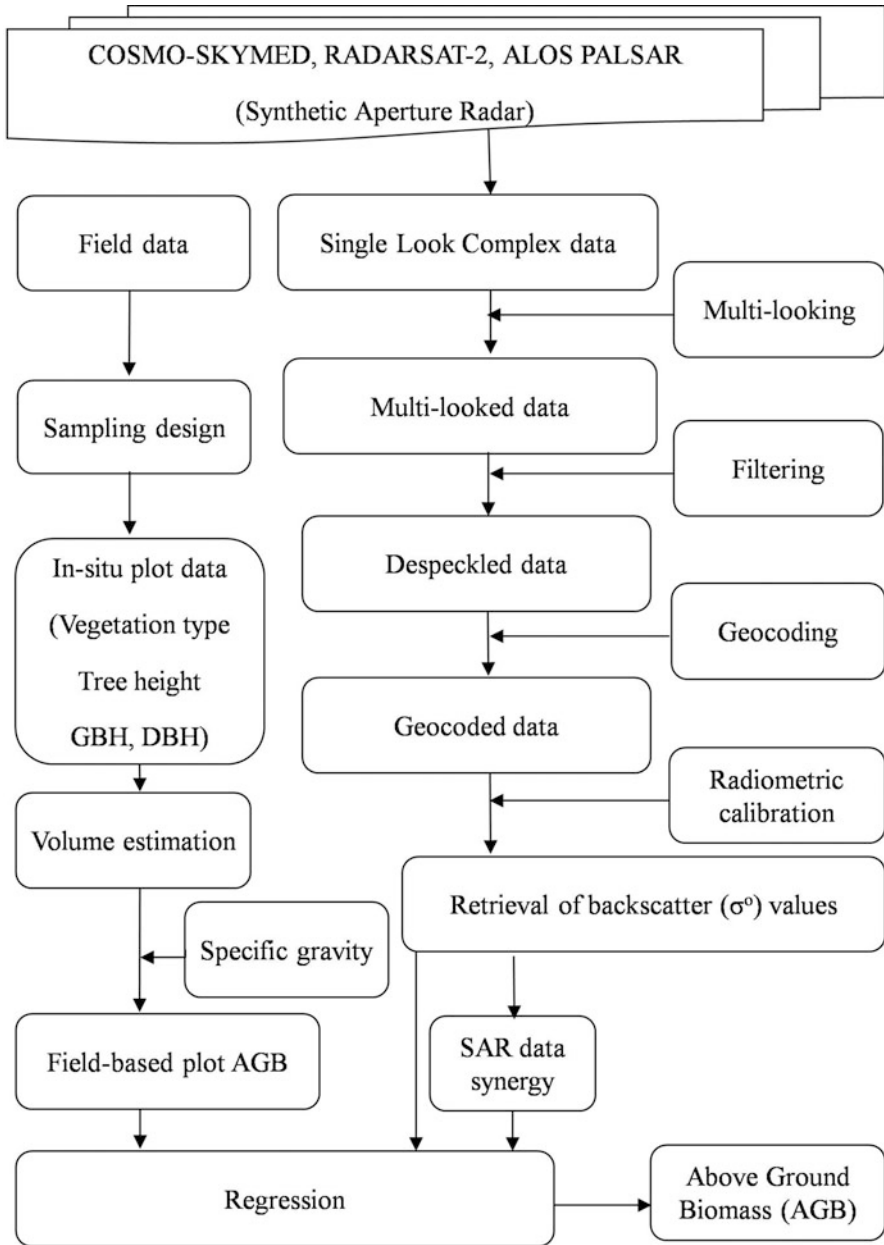


Fig. 2 Approach of the study

## 3.2 SAR Data Processing

Raw Single Look Complex (SLC) ALOS PALSAR and COSMO-SkyMed data were preprocessed in SARscape software, and Radarsat-2 SLC data was preprocessed in Geomatica software to create the backscatter or sigma naught ( $\sigma^0$ ) image (Fig. 2).

### 3.2.1 Conversion from Slant to Ground Range

This step is performed to remove the impact of the slant range distortions, thus resulting in equally spaced pixels of SLC in the range direction. If  $\theta_d$  is the depression angle, with pulse duration ( $t$ ) and velocity of light ( $c$ ), the ground range resolution ( $R_r$ ) is given by

$$R_r = ct \div 2 \cos \theta_d \quad (1)$$

As the radar beam is bifurcated into numerous small sub-beams with independent look and speckles, the speckles are minimized via multi-looking, thus generating an undistorted image with almost square pixels, but at the cost of its spatial resolution.

### 3.2.2 Generation of Amplitude and Power Images

SLC occurs as complex numbers, with real ( $x$ ) and imaginary ( $y$ ) elements that refer to the SAR signals with magnitude and phase information. Amplitude (AMP) image from complex SLC is converted to power image that are now floating real values.

$$AMP = \sqrt{x^2 + y^2} \quad (2)$$

$$Power = (AMP)^2 \quad (3)$$

### 3.2.3 Geocoding

The satellite data need to be georectified before further processing. The process was done considering the satellite orbital parameters using SRTM DEM as reference with terrain correction from Range-Doppler mechanism, thereafter resampling the data to 25 m pixel size following the nearest neighborhood algorithm re-projected to the UTM-WGS84 coordinate system.

### 3.2.4 Radiometric Calibration

The radar equation is used for radiometric calibration. Backscatter coefficient or sigma naught ( $\sigma^0$ ) values are generated with units in decibels (dB). The values depend on the sensor characteristics (signal wavelength or frequency, polarization, incidence angle) and the target properties (dielectricity, roughness, moisture content of the scatterers). The calibration is done via the equation (Shimada et al. 2009):

$$\sigma^0 = 10 * a \log_{10}(DN) + A_0 \quad (4)$$

where DN is the Digital Number of the power (or intensity) image,  $A_0$  is the sensor specific calibration factor.  $A_0 = -115$  dB for ALOS PALSAR 1.1 product dataset,  $A_0 = -59.62$  dB and  $-58.88$  dB for HH and VV polarized COSMO-SkyMed respectively. The value of  $A_0$  varies for every line in Radarsat-2 that is processed in Geomatica (Sinha et al. 2018a).

### 3.2.5 Speckle Filtering

Multi-looking reduces speckles; however, simultaneous use of speckle filtering can be beneficial but at an expense of modification in the original backscatter values. Mean filters of  $3 \times 3$  window size was used to suppress the speckles avoiding much alteration in the backscatter values.

## 3.3 Integrated Regression Model

Relationship between the  $\sigma^0$  from Eq. 4 and plot AGB is used to develop the best-fit AGB predicting model. The  $\sigma^0$  values are statistically integrated in various combinations to generate models that are again tested with the reference plot AGB to select the most accurate and best-fit AGB predicting model.

## 3.4 Statistical Metrics

All the models developed are statistically evaluated and results statistically validated with various statistical measures as mentioned and described in Sinha et al. (2016) at 95% confidence interval. The models are validated with an additional 9 random plots that comprised 20% of the total sample plots, and finally the best-fit is adopted.

## 4 Results

### 4.1 Model Structure

Relationship between the field generated AGB and the corresponding backscattering coefficients was examined for each of the SAR X-, C-, and L-bands individually. After carefully inspecting and understanding all the corresponding curve progression for the correlation between AGB and SAR signals, the optimal log transformed least squares linear regression equation was designed as:

$$y = a * \exp(b * \sigma^o) \quad (5)$$

where  $y = \text{AGB}$ ,  $\sigma^o = \text{backscatter coefficient}$ , and  $a$  and  $b = \text{sensor coefficients}$ . Similar Log models have been adopted by most of the investigators for relationship between biomass and SAR-derived information. The total 45 sample plots comprise 36 randomly selected plots (80%) for model development and the remaining 9 (20%) for subsequent independent validation.

### 4.2 AGB-SAR Relationship

Datasets from multi-frequency SAR sensors, namely COSMO-SkyMed (X-band, HH/VV dual-polarized), Radarsat-2 (C-band, HH/HV/VV quad-polarized) and ALOS PALSAR (L-band, HH/HV dual-polarized) are used in the study. Table 1 documents the data specifications. The coefficient of determination between the backscatter and AGB values was determined and documented in Table 2. The randomly selected plots showed 11.35 Mg/ha, 172.07 Mg/ha and 73.31 Mg/ha as the minimum, maximum and the mean plot AGB values, respectively. The standard deviation was 40.62 Mg/ha that signifies the wide spread of the sample data having huge variation.

Relation between the AGB and backscatter values shows a logarithmic relation that gets saturated at a certain point (Fig. 3a) that is radar wavelength-dependent, since on increase of wavelength, saturation also increases. It is evident from Fig. 3 that L-band has higher saturation level than C-band, which has greater saturation than X-band. So, lesser frequency (or greater wavelength, like L- and P-bands) signals can be used for the detection of higher biomass levels. Table 2 and Fig. 3b show that VV polarization interacts with the biomass more than HH polarization. Therefore, it can be inferred that X-band retrieves information of the top canopy biomass and generally not for the bole biomass. On the other hand, Table 2 suggests improved correlation of biomass with the C-band, specifically with the HH polarization, as it has greater penetrability than X-band, thus providing information of the canopy biomass. The L-band shows the best relationship with the highest penetration capability among the three bands under investigation, thus revealing the bole

**Table 2** Correlation between SAR backscatter and plot AGB

| SAR datasets      | Polarization | Date       | Correlation ( $r^2$ ) |
|-------------------|--------------|------------|-----------------------|
| COSMO-SkyMed      | HH           | 2011       | 0.0123                |
| COSMO-SkyMed      | VV           | 2011       | 0.0201                |
| Radarsat-2        | HH           | 2011       | 0.4606                |
| Radarsat-2        | HV           | 2011       | 0.3446                |
| Radarsat-2        | VV           | 2011       | 0.4300                |
| ALOS PALSAR (FBS) | HH           | 2009       | 0.5134                |
| ALOS PALSAR (FBD) | HH           | 2007       | 0.5919                |
| ALOS PALSAR (FBD) | HV           | 2007       | 0.5369                |
| ALOS PALSAR (FBS) | HH           | Jan 2010   | 0.4796                |
| ALOS PALSAR (FBS) | HH           | March 2010 | 0.5261                |
| ALOS PALSAR (FBD) | HH           | July 2010  | 0.8490                |
| ALOS PALSAR (FBD) | HV           | July 2010  | 0.5645                |
| ALOS PALSAR (PLR) | HH           | 2010       | 0.3431                |
| ALOS PALSAR (PLR) | HV           | 2010       | 0.4442                |
| ALOS PALSAR (PLR) | VH           | 2010       | 0.4421                |
| ALOS PALSAR (PLR) | VV           | 2010       | 0.2170                |

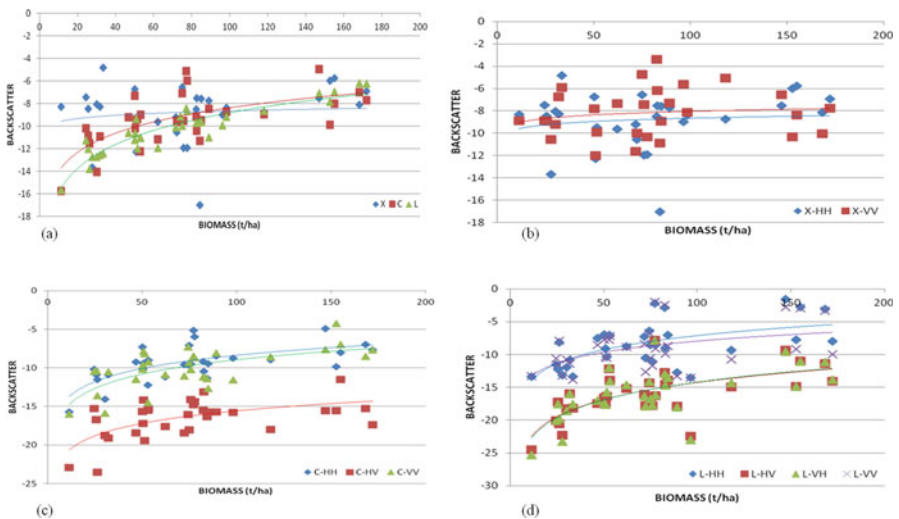


**Fig. 3** Variation of backscatter (in dB units) with plot AGB in (a) different wavelength SAR bands, (b) different polarizations of X-band, (c) different polarizations of C-band and (d) different polarizations of L-band

biomass of any tree. Both HH and HV polarizations show highly positive relationship with the bole biomass; however, HH revealed better results in our study (Table 2), while several other studies suggest cross-polarized data, like HV, to give better correlation than co-polarized data for retrieving biomass (Sinha et al.

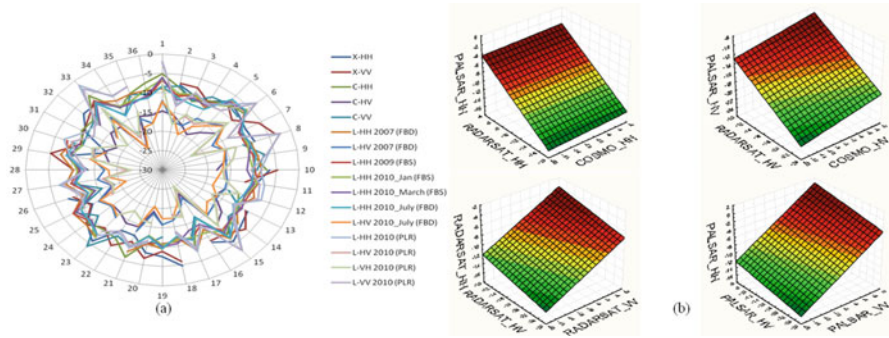


**Fig. 4** (a) Behavior of multi-frequency multi-polarized SAR signals in the forest study site. (b) Correlations between multi-frequency multi-polarized SAR signals in the forest study site

2015a). Table 2 also confirms that in our study, HH is superior to HV for Fine Beam Single (FBS) and Fine Beam Dual (FBD) products, but the reverse for full polarimetric (PLR) product. C- and L-band HH polarization demonstrated high backscattering values than other polarized data (Fig. 3c, d). However, among all the datasets, L-band FBD HH polarized data gave the highest correlation of 0.849 with the bole AGB. Theoretically, it is obvious for L-band HH polarized data to show the greatest interaction with the trunk that contributes primarily for the bole biomass due to the vertical structure of the trunk, i.e., volume scattering. X- and L-band backscatter had the highest and least values, respectively, due to greater canopy scattering for X-band and attenuation of the L-band signals due to canopy penetration interacting with the trunk. Also, the backscatter is dielectricity-dependent and varies with the moisture content of the various tree compartments. The backscatter also depends on the target scatterers on ground, like the size, number, structure, and orientation of the scatterers. Observations reveal that cross-polarizations, like HV/VH, have less values of backscatter than co-polarizations, like HH/VV, and the penetration capability enhances on decreasing radar signal frequencies. Thus, L-band HH polarization gave accurate estimates of AGB.

Co-polarizations have high backscattering coefficient values ( $\sigma^0$ ) than cross-polarizations, and increase in the wavelength leads to increase in the penetration capability of the radar signals, thus providing more accurate information related to the bole biomass (Sinha 2017). The performance of the SAR signals in forests is depicted in Fig. 4a that differentiates the low and high values of the respective cross and co-polarizations conspicuously. The interrelationships between the variably polarized multi-frequency radar signals are depicted in Fig. 4b. Equations 6, 7, and 8 are finally designed using information from X-, C-, and L-band SAR data, respectively, that had the best correlation with the field AGB data for developing the best-fit AGB prediction synergic model.

$$AGB = 94.984 * e^{(0.044 * \sigma_{X-VV}^2)} \quad (6)$$

$$AGB = 380.58 * e^{(0.187 * \sigma_C^2)} \quad (7)$$

$$AGB = 1067.3 * e^{(0.276 * \sigma_L^2)} \quad (8)$$

### 4.3 Synergy Model

L-band backscatter is more responsive to AGB than both X- and C-bands owing to greater backscatter range; however, due to higher variance, the accuracy in small biomass range is low. Figure 3 depicts the relationships between AGB and radar signals of COSMO-SkyMed (X-band), Radarsat-2 (C-band), and ALOS PALSAR (L-band) in scatterplots. With an increase in the field inventoried AGB, there is simultaneous increase in the backscattering coefficient, which gradually attains saturation at a certain level (Fig. 3).

Figure 3 also shows that the backscatter coefficient of L-band is lesser than the C-band, the backscatter coefficient of which is even lesser than the X-band. This phenomenon is attributed to the fact that X-band interacts primarily with the canopy top structures, and hence, the scattering is highest. The C-band shows more canopy scattering as it mainly interacts within the canopy. L-band penetrates deep, bypassing the canopy layer causing attenuation of the backscattered waves primarily interacting with the woody portions of the trees. In this study, X-band saturates earlier at about 40–50 t/ha, while C-band saturates next nearly at 100 t/ha. The saturation is highest for L-band among the three, at about 160–180 t/ha (Fig. 3). The saturation level depends on the radar frequency, polarization, and vegetation types. Only those sample plots common in all the datasets out of the total 36 plots were considered for developing the synergic model. Models were developed using Multiple Linear Regression of Eqs. 6, 7, and 8 where the data were used singly as well as in different combinations to show the accuracy in the prediction of AGB for generating final synergic modeling for AGB assessment. The following models developed using SAR are enlisted in Table 3.  $r^2$  values for each of the models designed between the AGB and SAR backscatter coefficient were calculated and summarized in Table 4 that also contains values calculated for other statistical metrics for evaluation of the models developed, as mentioned above.

According to Table 4, models 3, 5, 6 and 7 are found to give significant  $r^2$  relationship between the predicted and estimated values that lie within the range of 0.87–0.90; model accuracy is more than 75% and show better results. Slope values greater than 0.9 with low RMSE are observed for models 3 and 7. Models 3, 5, 6 and 7 are observed to perform well and statistically significant, considering all the statistical metrics adopted in the study. Hence, it is evident that model 3 comprising



**Table 3** Models for predicting AGB

| Model | Model   | Input SAR information        |
|-------|---|------------------------------|
| 1     | $94.984 * e^{(0.0442 * \sigma_{X\_VV}^o)}$  | X (VV)                       |
| 2     | $380.58 * e^{(0.1874 * \sigma_{C\_HH}^o)}$  | C (HH)                       |
| 3     | $1067.3 * e^{(0.2765 * \sigma_{L\_HH}^o)}$  | L (HH)                       |
| 4     | $355.2714 * e^{(0.1874 * \sigma_{C\_HH}^o)} - 7.5322 * e^{(0.0442 * \sigma_{X\_VV}^o)} + 22.0898$   | C (HH),<br>X (VV)            |
| 5     | $88.5536 * e^{(0.0442 * \sigma_{X\_VV}^o)} + 988.3198 * e^{(0.2765 * \sigma_{L\_HH}^o)} - 53.1242$  | L (HH),<br>X (VV)            |
| 6     | $1029.0906 * e^{(0.2765 * \sigma_{L\_HH}^o)} - 46.9255 * e^{(0.1874 * \sigma_{C\_HH}^o)} + 11.7315$   | C (HH),<br>L (HH)            |
| 7     | $103.504 * e^{(0.0442 * \sigma_{X\_VV}^o)} - 44.3375 * e^{(0.1874 * \sigma_{C\_HH}^o)} +$<br>$1028.984 * e^{(0.2765 * \sigma_{L\_HH}^o)} - 58.8778$ | L (HH),<br>C (HH),<br>X (VV) |

**Table 4** Statistical metrics for model evaluation (rounded to two decimal places)

| Model | r <sup>2</sup> | RMSE (t/ha) | ND RMSE | MAD   | ND MAD | MBE    | ND MBE | Slope | ϕ     |
|-------|----------------|-------------|---------|-------|--------|--------|--------|-------|-------|
| 1     | 0.01           | 46.18       | 1.19    | 34.80 | 0.64   | -13.13 | 0.26   | 0.01  | 35.84 |
| 2     | 0.28           | 37.24       | 0.26    | 28.88 | 0.42   | -6.27  | 0.11   | 0.36  | 58.09 |
| 3     | 0.87           | 16.06       | 0.07    | 12.45 | 0.19   | -1.11  | 0.03   | 0.94  | 80.60 |
| 4     | 0.33           | 37.21       | 0.59    | 29.35 | 0.52   | 0.00   | 0.30   | 0.33  | 47.78 |
| 5     | 0.89           | 15.12       | 0.11    | 12.64 | 0.24   | 0.00   | 0.10   | 0.89  | 76.12 |
| 6     | 0.88           | 15.49       | 0.12    | 12.83 | 0.24   | 0.00   | 0.10   | 0.88  | 75.97 |
| 7     | 0.90           | 15.29       | 0.14    | 12.34 | 0.25   | 0.00   | 0.11   | 0.90  | 75.29 |

L-band information is the best model among the single sensor models for biomass estimation. However, integrating information from multiple SAR bands as in models 5, 6 and 7, the correlation between the predicted and estimated values have considerably improved. Out of these synergic models, model 7, integrating all the multi-frequency SAR data of X-, C- and L-bands, emerge as the best-fit for AGB estimation.

#### 4.4 Model Statistics

Twenty percent of the randomly selected sample data are used for statistical validation all the models generated in terms of the statistical measures as mentioned in Sinha et al. (2016, 2020), and the results are documented in Table 5. The table shows

**Table 5** Statistical measures for AGB model validation

| Model | $r^2$ | RMSE (t/ha) | NDRMSE | MAD    | NDMAD | MBE     | NDMBE  | Slope  | Av. Abs. Accuracy | Willmott's Index ( $d$ ) |
|-------|-------|-------------|--------|--------|-------|---------|--------|--------|-------------------|--------------------------|
| 1     | 0.094 | 32.151      | 0.779  | 26.986 | 0.605 | -7.422  | 0.265  | 0.105  | 39.478            | 0.306                    |
| 2     | 0.002 | 50.083      | 3.047  | 43.106 | 1.080 | -11.296 | 0.438  | -0.050 | 7.961             | -0.095                   |
| 3     | 0.713 | 22.340      | 0.216  | 19.669 | 0.382 | -12.281 | -0.085 | 0.871  | 61.768            | 0.883                    |
| 4     | 0.006 | 48.479      | 4.371  | 41.685 | 1.188 | 0.325   | 0.723  | -0.079 | 18.833            | -0.170                   |
| 5     | 0.891 | 16.640      | 0.063  | 14.277 | 0.220 | -12.613 | -0.189 | 0.905  | 78.031            | 0.934                    |
| 6     | 0.665 | 22.617      | 0.214  | 19.923 | 0.384 | -12.015 | -0.046 | 0.720  | 61.625            | 0.859                    |
| 7     | 0.954 | 14.813      | 0.105  | 13.032 | 0.251 | -13.032 | -0.251 | 0.964  | 78.894            | 0.950                    |

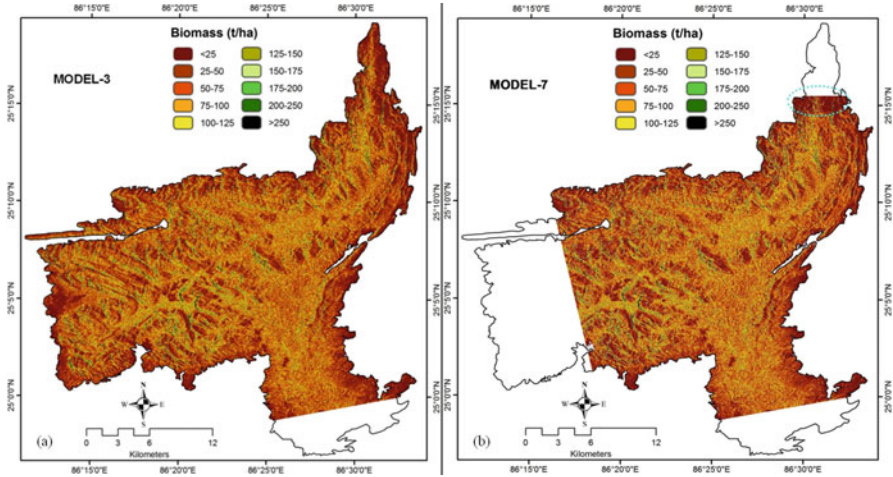


**Fig. 5** Biomass maps from (a) Model 3 (L-band data) and (b) Model 7 (X-, C- and L-band data synergy)

that model 7 outperforms all other models (1 to 6), having the highest correlation between the field and the modeled values, least RMSE, high accuracy of prediction, least over- or under-estimates, and the best data agreement, which reveal its acceptability over other models in the study area. Among the models involving single sensors, model 3 showed the best results (Table 5).

AGB maps (Fig. 5a, b) are prepared from the best-fit models (Models 3 and 7 respectively) and are reclassified based on biomass concentration from very low (<25 t/ha and 25–50 t/ha), low (50–75 t/ha and 75–100 t/ha), moderate (100–125 t/ha and 125–150 t/ha), high (150–175 t/ha and 175–200 t/ha) to very high (>250 t/ha). Both the figures have regions, marked white within the study area boundary that suffers from absence of SAR data. North portion of the of study site in Fig. 5b shows erroneous results due to non-overlapping data.

Model evaluation results (Table 5) depict that L-band data (Model 3) provides the best prediction for AGB among the models developed from single SAR sensors (X, C, and L), based on which the AGB map is generated as shown in Fig. 5a. Simultaneously, Table 5 reveals Model 7 to be the most accurate among all the single SAR sensor and combined models adopted in the study.

Fig. 5b portrays the AGB map derived from ‘Model 7’, which clearly demonstrates that the less vegetative parts with low biomass levels of <50 t/ha surrounding the study area periphery, water bodies, and the built-up regions. The biomass range for the maximum extent of the forested region is observed to lie within 25–100 t/ha. High-density vegetation is observed to have 75–125 t/ha of biomass, generally in the interior parts; however, with some scattered areas with even higher biomass values, that too are generally restricted to the interior regions. Relative early biomass saturation for single SAR frequency data can be neutralized with the integrated use of multi-frequency SAR data due to the better relationship of AGB (crown,

branch and stem) to each of the SAR frequency bands (Fig. 3; Tables 4 and 5). Hence, the synergic model presented the best results for biomass assessment.

## 5 Discussion

Climate abnormality and related issues are the greatest nuisance that the world has to tolerate that needs focal attention. Precise monitoring of the quality and quantity of the world's forest is prerequisite for accounting this change to a great extent. Biomass or carbon accumulated in the vegetation is indicative of its health and vigor that ultimately recount to the climate patterns.

The study undertaken aims in using multi-frequency SAR data to calculate the biomass that has the potential to give better results in comparison to any optical data as well as any single frequency spaceborne SAR data till date. Due to its intrinsic capabilities, L-band gives the best results for biomass estimation among the spaceborne SAR sensors with X-, C-, and L-bands. However, the accuracy and precision of estimation enhances on integrating all the three SAR data. Exponential model offered the best-fit model for estimating biomass among the regression models tested. Most of the forested area is observed to have biomass within 25–100 t/ha, wherein high-density vegetation is mostly observed to have 75–125 t/ha of biomass. It can be also noticed that the relatively early saturation for single SAR frequency data can be reduced by integrating multi-frequency SAR data because of the wholesome interaction with all the vegetation compartments. Hence, the integrated multi-frequency SAR model produced the best results in predicting AGB.

The synergic use of SAR X-, C- and L-bands has made this study unique by itself, since all previous studies have either used single or double frequency SAR data for biomass assessment. For instance, combination of X- and L-bands was used by Englhart et al. (2011, 2012) for AGB measurements with  $r^2 = 0.53$  and RMSE of 79 t/ha over tropical forests. Under Indian conditions, Alappat et al. (2011) achieved the best correlation of  $r^2 = 0.75$  for forest stand variables with SAR C- and L-bands. The current study achieved the best  $r^2$  value of 0.90 and RMSE of 15.29 t/ha with synergic use of spaceborne SAR X-, C- and L-bands. These results are comparable when SAR L-band was used in synergy with optical Landsat TM data-derived metrics that involved several indices, image transformations, and texture measures, and hence cumbersome as compared to the current study. Likewise, a comparable yet complex study was carried out by Sarker (2010) that integrated texture measures from C-band RADARSAT-2, L-band PALSAR, SPOT-5 and AVNIR-2 to achieve comparable results over subtropical forests. Thermal properties of vegetation can also be used for retrieving biomass information as it shows unique profiling separating different land cover features (Sinha et al. 2015c) and even observed to show relationship with biomass (Sinha and Sharma 2013).

Saturation levels can be improved with the simultaneous use of multi-frequency SAR (Sinha et al. 2015a, 2020). Furthermore, the use of SAR interferometry, SAR

polarimetry, data fusion, ratioing of polarized data, texture analysis, etc. in biomass prediction is a matter of extensive research and beyond the scope of the current study. Wise selection of the representative plots with non-erroneous field measurements is important for accurate estimates of biomass with limited field data. This technique of combined use of multi-source data suggests a simple yet effectual approach to augment the accurateness of AGB estimates over tropical deciduous mixed forests that is excessively intricate otherwise. The tropical forests are important components of REDD, carbon cycles and climate change studies.

There are numerous parameters that affect the SAR-based backscatter analysis that need to be addressed, for instance edaphic parameters, moisture content, dielectricity, surface roughness, etc. In spite of all these complexities in the analysis, SAR offers immense potential for enumerating biomass with enhanced accuracies even with limited field data. The approach can be well executed to measure and monitor biomass and carbon stock dynamics, which act as vital components of REDD and forest health-related issues.

## 6 Conclusions

In this '400 ppm World', global climate change is the most alarming situation that this world is experiencing. In this context, REDD and associated concepts are gaining attention; henceforth, biomass/carbon assessment is becoming crucial to address this issue. The current study assesses above-ground bole biomass and in turn the forest carbon stock over a tropical deciduous heterogeneous virgin forest patch of Munger in India. Synergic use of multi-frequency SAR has the potential to augment AGB estimations in comparison to any optical data as well as any single frequency spaceborne SAR data till date. Out of the X-, C- and L-bands, the best model predicting AGB comprises L-band information. Subsequently, the estimation improves on integrating all the three SAR wavelength bands. The exponential model was observed as the best-fit model for estimating biomass on regressing SAR backscatter values to plot estimated AGB. The validated integrated model showed high correlation (0.95) and accuracy (79%), low RMSE (14.81 t/ha), and Willmott's index of data agreement of 0.95 without much over or under-estimation as denoted by the slope value of 0.9. The consequence of the approach in resolving the relative early saturation of biomass with optical remote sensing data or single SAR frequency data alone is evident; thus, it can be counteracted with the integrated use of multi-frequency SAR data due to the better relationship of AGB compartments. Hence, in this study, a synergy regression model for predicting AGB was developed with synergic use of SAR multi-frequency X-, C- and L-band information.

Biomass has the characteristics of extensive discrete distribution with significant relationship with multifaceted environmental and geographical factors. GIScience, integrated with satellite information, can capture, represent, process and analyse the geographic information to develop models that can be represented spatially as maps.

Hence, the integrated geospatial techniques help in decision making for forest resource management and its temporal or continuous monitoring, thus making the cumbersome laborious process timely, easy and accurate.

**Acknowledgments** The author sincerely acknowledges Space Application Centre (ISRO, India) for providing technical help and JAXA (Japan), CSA (Canada) and ASI (Italy) for providing SAR data through ALOS-RA Cosmo Skymed A.O. project. The author expresses sincere gratitude to Science and Engineering Research Board (SERB), Department of Science and Technology (DST), Government of India for providing funds under SERB National Post-Doctoral fellowship (SERB NPDF) scheme (File Number: PDF/2015/000043/EAS) during 2016–2018 when a significant portion of the research was carried out. Also, thanks to Amity University, Kolkata, for providing infrastructure where the remaining portion of the work was done.

## References

- Alappat, V. O., Joshi, A. K., & Krishnamurthy, Y. V. N. (2011). Tropical dry deciduous forest stand variable estimation using SAR data. *Journal of the Indian Society of Remote Sensing*, 39, 583–589.
- Austin, J. M., Mackey, B. G., & Van Niel, K. P. (2003). Estimating forest biomass using satellite radar: An exploratory study in a temperate Australian Eucalyptus forest. *Forest Ecology and Management*, 176(1), 575–583. [https://doi.org/10.1016/S0378-1127\(02\)00314-6](https://doi.org/10.1016/S0378-1127(02)00314-6).
- Balster, H. (2001). Forest mapping and monitoring with interferometric synthetic aperture radar (InSAR). *Progress in Physical Geography*, 25(2), 159–177.
- Beaudoin, A., Le Toan, T., Goze, S., Nezry, E., Lopes, A., Mougin, E., Hsu, C. C., Han, H. C., Kong, J. A., & Shin, R. T. (1994). Retrieval of forest biomass from SAR data. *International Journal of Remote Sensing*, 15(14), 2777–2796. <https://doi.org/10.1080/01431169408954284>.
- Castel, T., Guerra, F., Caraglio, Y., & Houllier, F. (2002). Retrieval biomass of a large Venezuelan pine plantation using JERS-1 SAR data. Analysis of forest structure impact on radar signature. *Remote Sensing of Environment*, 79(1), 30–41. [https://doi.org/10.1016/S0034-4257\(01\)00236-X](https://doi.org/10.1016/S0034-4257(01)00236-X).
- De Sy, V., Herold, M., Archard, F., Asner, G. P., Held, A., Kellndorfer, J., & Verbesselt, J. (2012). Synergies of multiple remote sensing data sources for REDD+ monitoring. *Current Opinion in Environment Sustainability*, 4(6), 696–706.
- De Zan, F., Krieger, G., & López-Dekker, P. (2013). On some spectral properties of TanDEM-X interferograms over forested areas. *IEEE Geoscience and Remote Sensing Letters*, 10(1), 71–75.
- Dube, T., Gara, T. W., Mutanga, O., Sibanda, M., Shoko, C., Murvira, A., Masocha, M., Ndaimani, H., & Hatendi, C. M. (2016). Estimating forest standing biomass in savanna woodlands as an indicator of forest productivity using the new generation WorldView-2 sensor. *Geocarto International*. <https://doi.org/10.1080/10106049.2016.1240717>.
- Englhart, S., Keuck, V., & Siegert, F. (2011). Aboveground biomass retrieval in tropical forests — The potential of combined X- and L-band SAR data use. *Remote Sensing of Environment*, 115, 1260–1271.
- Englhart, S., Keuck, V., & Siegert, F. (2012). Modelling aboveground biomass in tropical forests using multi-frequency SAR data – A comparison of methods. *The IEEE Journal of Selected Topics in Applied Earth Observations*, 5(1), 298–306.
- Fransson, J. E. S., Smith, G., Askne, J., & Olsson, H. (2001). Stem volume estimation in boreal forests using ERS-1/2 coherence and SPOT XS optical data. *International Journal of Remote Sensing*, 22(14), 2777–2791. <https://doi.org/10.1080/01431160010006872>.
- FRI. (1996). *Indian woods*. Dehradun: Forest Research Institute.
- FSI. (1996). *Volume equations for forests of India, Nepal and Bhutan; Forest survey of India, Ministry of Environment and Forests*. Dehradun: Government of India.

- Ghasemi, N., Sahebi, M. R., & Mohammadzadeh, A. (2011). A review on biomass estimation methods using synthetic aperture radar data. *International Journal of Geomatics and Geosciences*, 1(4), 776–788.
- Hamdan, O., Aziz, H. K., & Rahman, K. A. (2011). Remotely sensed L-band SAR data for tropical forest biomass estimation. *Journal of Tropical Forest Science*, 23, 318–327.
- Harrell, P. A., Kasischke, E. S., Bourgeau-Chavez, L. L., Haney, E. M., & Christensen, N. L. (1997). Evaluation of approaches to estimating aboveground biomass in Southern pine forests using SIR-C data. *Remote Sensing of Environment*, 59(2), 223–233. [https://doi.org/10.1016/S0034-4257\(96\)00155-1](https://doi.org/10.1016/S0034-4257(96)00155-1).
- Hoekman, D. H., & Quinones, M. J. (1997, August 3–8). Land cover type and forest biomass assessment in the Colombian Amazon. In: *Geoscience and remote sensing, 1997. IGARSS'97. Remote sensing – A scientific vision for sustainable development, 1997 IEEE International*, Vol. 1724, pp 1728–1730. <https://doi.org/10.1109/igarss.1997.609045>
- Hyde, P., Dubayah, R., Walker, W., Blair, J. B., Hofton, M., & Hunsaker, C. (2006). Mapping forest structure for wildlife habitat analysis using multi-sensor (LiDAR, SAR/InSAR, ETM+, Quickbird) synergy. *Remote Sensing of Environment*, 102, 63–73.
- Kumar S. (2009). *Retrieval of forest parameters from Envisat ASAR data for biomass inventory in Dudhwa National Park, UP, India* [dissertation]. Dehradun: Indian Institute of Remote Sensing (IIRS) and Enschede: University of Twente (ITC).
- Kumar, L., & Mutanga, O. (2017). Remote sensing of above-ground biomass. *Remote Sensing*, 9, 935. <https://doi.org/10.3390/rs9090935>.
- Kumar, P., Sharma, L. K., Pandey, P. C., Sinha, S., & Nathawat, M. S. (2013). Geospatial strategy for tropical forest-wildlife reserve biomass estimation. *The IEEE Journal of Selected Topics in Applied Earth Observations*, 6, 917–923.
- Kumar, L., Sinha, P., Taylor, S., & Alqurashi, A. F. (2015). Review of the use of remote sensing for biomass estimation to support renewable energy generation. *Journal of Applied Remote Sensing*, 9, 0976961–0976928. <https://doi.org/10.1117/1.JRS.9.097696>.
- Kumar, S., Khati, U. G., Chandola, S., Agrawal, S., & Kushwaha, S. P. S. (2017). Polarimetric SAR interferometry based modeling for tree height and aboveground biomass retrieval in a tropical deciduous forest. *Advances in Space Research*, 60, 571–586.
- Kuplich, T. M., Salvatori, V., & Curran, P. J. (2000). JERS-1/SAR backscatter and its relationship with biomass of regenerating forests. *International Journal of Remote Sensing*, 21(12), 2513–2518. <https://doi.org/10.1080/01431160050030600>.
- Le Toan, T., Beaudoin, A., Riom, J., & Guyon, D. (1992). Relating forest biomass to SAR data. *IEEE Transactions on Geoscience and Remote Sensing*, 30(2), 403–411. <https://doi.org/10.1109/36.134089>.
- Le Toan, T., Quegan, S., Davidson, M. W. J., Balzter, H., Paillou, P., Papathanassiou, K., Plummer, S., Rocca, F., Saatchi, S., Shugart, H., & Ulander, L. (2011). The BIOMASS mission: Mapping global forest biomass to better understand the terrestrial carbon cycle. *Remote Sensing of Environment*, 115(11), 2850–2860. <https://doi.org/10.1016/j.rse.2011.03.020>.
- Leckie, D. G. (1998). Forestry applications using imaging radar. In F. M. Henderson & A. J. Lewis (Eds.), *Principles and applications of imaging radar. Manual of remote sensing* (Vol. vol 2, 3rd ed., pp. 437–509). Chichester: Wiley.
- Lu, D. (2006). The potential and challenge of remote sensing based biomass estimation. *International Journal of Remote Sensing*, 27, 1297–1328.
- Lucas, R. M., Cronin, N., Lee, A., Moghaddam, M., Witte, C., & Tickle, P. (2006). Empirical relationships between AIRSAR backscatter and LiDAR-derived forest biomass, Queensland, Australia. *Remote Sensing of Environment*, 100(3), 407–425.
- Nizalapur, V., Jha, C. S., & Madugundu, R. (2010). Estimation of above ground biomass in Indian tropical forested area using multi-frequency DLR-ESAR data. *International Journal of Geomatics and Geosciences*, 1(2), 167–178.
- Pandey, U., Kushwaha, S. P. S., Kachhwaha, T. S., Kunwar, P., & Dadhwal, V. K. (2010). Potential of envisat ASAR data for woody biomass assessment. *Tropical Ecology*, 51(1), 117–124.

- Pulliaainen, J., Engdahl, M., & Hallikainen, M. (2003). Feasibility of multi-temporal interferometric SAR data for stand-level estimation of boreal forest stem volume. *Remote Sensing of Environment*, 85(4), 397–409. [https://doi.org/10.1016/S0034-4257\(03\)00016-6](https://doi.org/10.1016/S0034-4257(03)00016-6).
- Ranson, K. J., Sun, G., Weishampel, J. F., & Knox, R. G. (1997). Forest biomass from combined ecosystem and radar backscatter modeling. *Remote Sensing of Environment*, 59(1), 118–133. [https://doi.org/10.1016/S0034-4257\(96\)00114-9](https://doi.org/10.1016/S0034-4257(96)00114-9).
- Santoro, M., & Cartus, O. (2018). Research pathways of forest above-ground biomass estimation based on SAR backscatter and interferometric SAR observations. *Remote Sensing*, 10, 608. <https://doi.org/10.3390/rs10040608>.
- Santos, J. R., Lacruz, M. S. P., Araujo, L. S., & Keil, M. (2002). Savanna and tropical rainforest biomass estimation and spatialization using JERS-1 data. *International Journal of Remote Sensing*, 23(7), 1217–1229. <https://doi.org/10.1080/01431160110092867>.
- Sarker, M. L. R. (2010). *Estimation of forest biomass using remote sensing [dissertation]*. Hong Kong: The Hong Kong Polytechnic University.
- Sarker, M. L. R., Nichol, J., Iz, H. B., Ahmad, B. B., & Rahman, A. A. (2013). Forest biomass estimation using texture measurements of high-resolution dual-polarization C-band SAR data. *IEEE Transactions on Geoscience and Remote Sensing*, 51(6), 3371–3384. <https://doi.org/10.1109/tgrs.2012.2219872>.
- Sharma, L. K., Kanga, S., Nathawat, M. S., Sinha, S., & Pandey, P. C. (2012). Fuzzy AHP for forest fire risk modeling. *Disaster Prevention and Management*, 21(2), 160–171.
- Sharma, L. K., Nathawat, M. S., & Sinha, S. (2013). Top-down and bottom-up inventory approach for above ground forest biomass and carbon monitoring in REDD framework using multi-resolution satellite data. *Environmental Monitoring and Assessment*, 185, 8621–8637.
- Sharma, L. K., Sinha, S., Nathawat, M. S., & Jeganathan, C. (2014). Uses of multi-polarized ALOS PALSAR data for biomass assessment of tropical forests: A step towards REDD. In S. Naithani & C. Jeganathan (Eds.), *Remote sensing and GIS in environmental resource management* (pp. 183–192). New Delhi: Gaura Books India Pvt Ltd..
- Shimada, M., Isoguchi, O., Tadono, T., & Isono, K. (2009). PALSAR radiometric and geometric calibration. *IEEE Transactions on Geoscience and Remote Sensing*, 47(12), 3915–3932.
- Sinha, S. (2016). Polarimetric scattering parameter products of ALOS PALSAR for forest biomass assessment. *Research & Reviews: Journal of Space Science & Technology*, 5(1), 1–9.
- Sinha, S. (2017). *Multi-sensor SAR-optical synergic modeling in retrieving forest parameters over deciduous landscape [dissertation]*. India: Birla Institute of Technology, Mesra.
- Sinha, S. (2018). Accounting forest carbon sequestration using integrated geospatial techniques. *Environment & We: An international Journal of Science*, 13, 1–8.
- Sinha, S., & Santra, A. (2019). Estimation of change in forest aboveground carbon in Bhimbandh Wildlife Sanctuary, Bihar, India between 2007 and 2016. *Current Science*, 117(6): 1090–1094. <https://doi.org/10.18520/cs/v117/i6/1090-1094>.
- Sinha, S., & Sharma, L. K. (2013). Investigations on potential relationship between biomass and surface temperature using thermal remote sensing over tropical deciduous forests. *Research & Reviews: Journal of Space Science & Technology*, 2(3), 13–18.
- Sinha, S., Sharma, L. K., & Nathawat, M. S. (2013). Integrated geospatial techniques for land-use/land-cover and forest mapping of deciduous Munger forests (India). *Universal Journal of Environmental Research and Technology*, 3(2), 190–198.
- Sinha, S., Jeganathan, C., Sharma, L. K., & Nathawat, M. S. (2015a). A review of radar remote sensing for biomass estimation. *International journal of Environmental Science and Technology*, 12, 1779–1792.
- Sinha, S., Sharma, L. K., Jeganathan, C., Nathawat, M. S., Das, A. K., & Mohan, S. (2015b). Efficacy of InSAR coherence in tropical forest remote sensing in context of REDD. *International Journal of Advanced Remote Sensing and GIS Geography*, 3(1a), 38–46.
- Sinha, S., Sharma, L. K., & Nathawat, M. S. (2015c). Improved land-use/land-cover classification of semi-arid deciduous forest landscape using thermal remote sensing. *Egyptian Journal of Remote Sensing and Space Science*, 18, 217–233.



- Sinha, S., Jeganathan, C., Sharma, L. K., Nathawat, M. S., Das, A. K., & Mohan, S. (2016). Developing synergy regression models with space-borne ALOS PALSAR and Landsat TM sensors for retrieving tropical forest biomass. *Journal of Earth System Science*, *125*, 725–735.
- Sinha, S., Santra, A., Mitra, S. S., Jeganathan, C., Sharma, L. K., Nathawat, M. S., Das, A. K., & Mohan, S. (2017, 23–27 October). Multi-frequency SAR capabilities for forest biomass and carbon inventory for REDD monitoring. In: *The 38th Asian conference on remote sensing-space applications: Touching human lives (ACRS-2017)*. Asian Association on Remote Sensing, Asian Institute of Technology, Thailand. Curran associates, Inc. New York, USA, pp. 2565–2571.
- Sinha, S., Santra, A., Sharma, L. K., Jeganathan, C., Nathawat, M. S., Das, A. K., & Mohan, S. (2018a). Multi-polarized Radarsat-2 satellite sensor in assessing forest vigor from above ground biomass. *Journal of Forest Research*, *29*(4), 1139–1145. <https://doi.org/10.1007/s11676-017-0511-7>.
- Sinha, S., Santra, A., & Mitra, S. S. (2018b). A method for built-up area extraction using dual polarimetric ALOS PALSAR. *ISPRS Annals of the Photogrammetry, Remote Sensing and Spatial Information Sciences*, *IV-5*, 455–458. <https://doi.org/10.5194/isprs-annals-IV-5-455-2018>.
- Sinha, S., Santra, A., Das, A. K., Sharma, L. K., Mohan, S., Nathawat, M. S., Mitra, S. S., & Jeganathan, C. (2019a). Accounting tropical forest carbon stock with synergistic use of space-borne ALOS PALSAR and COSMO-SkyMed SAR sensors. *Tropical Ecology*, *60*, 83–93. <https://doi.org/10.1007/s42965-019-00011-6>.
- Sinha, S., Santra, A., Das, A. K., Sharma, L. K., Mohan, S., Nathawat, M. S., Mitra, S. S., & Jeganathan, C. (2019b). Regression-based integrated bi-sensor SAR data model to estimate forest carbon stock. *Journal of the Indian Society of Remote Sensing*, *47*(9), 1159–1608. <https://doi.org/10.1007/s12524-019-01004-7>.
- Sinha, S., Mohan, S., Das, A. K., Sharma, L. K., Jeganathan, C., Santra, A., Mitra, S. S., & Nathawat, M. S. (2020). Multi-sensor approach integrating optical and multi-frequency SAR for carbon stock estimation over a tropical deciduous forest in India. *Carbon Management*, *11*(1), 39–55. <https://doi.org/10.1080/17583004.2019.1686931>.
- Sun, G., Ranson, K. J., & Kharuk, V. I. (2002). Radiometric slope correction for forest biomass estimation from SAR data in the Western Sayani Mountains, Siberia. *Remote Sensing of Environment*, *79*(2), 279–287. [https://doi.org/10.1016/S0034-4257\(01\)00279-6](https://doi.org/10.1016/S0034-4257(01)00279-6).
- Treuhaft, R., Gonçalves, F., dos Santos, J. R., Keller, M., Palace, M., Madsen, S. N., Sullivan, F., & Graça, P. M. (2015). Tropical-forest biomass estimation at X-band from the spaceborne TanDEM-X interferometer. *IEEE Geoscience and Remote Sensing Letters*, *12*(2), 239–243.
- Villard, L., Le Toan, T., Minh, DHT, Mermoz, S., & Bouvet, A. (2016). Forest biomass from radar remote sensing. In: Baghdadi, N, Zribi, M (Ed.). *Land surface remote sensing in agriculture and forest*. pp. 363–425. <https://doi.org/10.1016/B978-1-78548-103-1.50009-1>.
- Waikhom, A. C., Nath, A. J., & Yadava, P. S. (2017). Aboveground biomass and carbon stock in the largest sacred grove of Manipur, Northeast India. *Journal of Forest Research*, *29*(2), 425–428. <https://doi.org/10.1007/s11676-017-0439-y>.
- Wollersheim, M., Collins, M. J., & Leckie, D. (2011). Estimating boreal forest species type with airborne polarimetric synthetic aperture radar. *International Journal of Remote Sensing*, *32*, 2481–2505.

# Landslide Susceptibility Mapping Using Bivariate Frequency Ratio Model and Geospatial Techniques: A Case from Karbi Anglong West District in Assam, India



Raihan Ahmed, Ravinder Singh, and Haroon Sajjad

**Abstract** The study attempts to prepare an inventory map of landslide susceptibility using geospatial technology and bivariate frequency ratio model for Karbi Anglong West district in Assam, India. Past landslide locations were extracted from the landslide hazard zonation map of Assam for preparing landslide susceptibility. Of the total past landslide locations, 70% locations were utilized for building the model and 30% locations for validating landslide susceptibility map. Geology, lineament, slope, aspect, drainage, land use/land cover, and soil conditioning parameters were integrated through frequency ratio model to prepare the susceptibility map. High and moderate susceptibility areas were found in the south and south-western parts having steep slopes, while low susceptibility areas were distributed sparsely over areas having gentle slope in the district. Validation of landslide susceptibility map revealed its accordance with the past landslide locations. The accuracy of the landslide susceptibility map was assessed through receiver operating characteristics curves. Prediction rate and success rate under curves were found to be 0.884 and 0.854, respectively. The map produced through the integration of landslide causative factors and frequency ratio model helped not only in identifying landslide-prone areas but also proved to be instrumental for analyzing level of susceptibility. Thus, the methodology can be employed for monitoring and assessing landslide susceptibility.

**Keywords** Landslide susceptibility · Landslide-conditioning factors · Frequency Ratio · Geospatial techniques

---

R. Ahmed · R. Singh · H. Sajjad (✉)

Department of Geography, Faculty of Natural Science, Jamia Millia Islamia, New Delhi, Delhi, India

## 1 Introduction

Landslides can occur in many forms including debris flows, rock falls, rockslides, rock avalanches, soil slips, and mud-flows. Such disasters constitute about 9% of the total natural disasters occurring globally but some frequent landslides may cause destruction, devastation, and loss of life and property (Gokceoglu et al. 2005). Landslide is considered as an often occurring natural hazard in the hilly regions of India during monsoon season. These hilly tracts have been categorized into five earthquake zones by the Indian Meteorological Department where the strongest earthquake has also been found. One of the causes of triggering landslides particularly in critically exposed areas is unstable slope. Of the total geographical area of India, 15% of its landmass (0.49 million sq. km) is considered to be landslide-prone (Geological Survey of India 1998). Nearly 20% area in north-eastern India experiences frequent landslides. Hence, identification, monitoring, and assessment of landslide susceptibility is essential for reducing disaster risk in such areas. Some scholars emphasized the significance of the slope instability processes in identifying landslide-prone areas (Dai and Lee 2002; Ercanoglu and Gokceoglu 2002; Akgun et al. 2008). Most of earlier researches on susceptibility of landslide mapping before the advent of geospatial techniques were solely dependent on field survey and visual interpolation methods (Gupta and Joshi 1990; Pachauri and Pant 1992; Montgomery and Dietrich 1994).

The years after 2000 witnessed quantitative and qualitative assessment of landslide susceptibility using remote sensing and geographic information system (GIS) techniques (Ayalew and Yamagishi 2005, Shahabi et al. 2012; Chalkias et al. 2014; Torkashvand et al. 2014; Raghuvanshi et al. 2015). Remote sensing data, GIS, and ground-based information have been proved effective tools in identifying landslide potential areas, susceptibility mapping, and reducing the impact of hazards through efficient management and planning. Later, statistical and mathematical models were also extensively used in geospatial environment for assessing landslide susceptibility (Dhakal et al. 2000, Dai et al. 2001; Lin and Tung 2004; Süzen and Doyuran 2004; Sahana and Sajjad 2017). Saaty (1980) introduced the concept of analytical hierarchy process for decision making and later was used by many scholars for deriving weights for conditioning factors of landslides (Barredo et al. 2000; Yagi 2003; Ayalew and Yamagishi 2005; Pourghasemi et al. 2012). Some scholars also used artificial neural network for assigning weights to influencing factors of landslide (Beguería and Lorente 2007; Lee et al. 2004). Thus, landslide susceptibility map can best be utilized for assessing current and predicting future risks (Neuhäuser and Terhorst 2007). Landslide susceptibility map can help in establishing early warning system. It can also be utilized for constructing varied structures of houses (Hong and Adler 2007). Many scholars used fuzzy logic, support vector machine, evidential belief function, and decision tree model in GIS environment for landslide susceptibility assessment (Ermini et al. 2005; Kanungo et al. 2006; Lee and Pradhan 2006; Tangestani 2009; Wan 2009; Saito et al. 2009; Pradhan and Lee 2010; Pradhan 2011), while many others utilized multi criteria decision analysis for susceptibility

assessment in different landslide-prone areas (Ayalew and Yamagishi 2005; Yalcin 2008; Akgun 2012; Demir et al. 2013).

The present study utilized bivariate frequency ratio model to assess landslide susceptibility using site-specific landslide-conditioning factors. The model makes landslide susceptibility analysis simpler than other models (Lee and Pradhan 2007; Yilmaz 2009). It also helps in establishing relationship between landslide-conditioning factors and landslide occurrence (Akgun et al. 2008). Thus, the model can be effectively utilized for landslide susceptibility analysis in different geographical regions at spatial scales.

## 2 Study Area

Karbi Anglong West district of Assam in north-eastern India extends between  $25^{\circ}33'$  N and  $26^{\circ}35'$  N latitudes and  $92^{\circ}10'$  E and  $93^{\circ}50'$  E longitudes (Fig. 1). The study area enjoys tropical monsoon climate and receives most of its rainfall during summer season. The average annual rainfall of the district is about 2416 mm. The topography of the district is characterized by undulating surface where *Jhum* cultivation (slash and burn agriculture) along the slope of hills is the dominant activity. Schists, Quartz-sericite-schist-conglomerate, undifferentiated fluvial sediments, and porphyritic coarse granite are the major types of lithology in the study area. Schist is the dominant lithology found in the central part of the district. Generally, five types of soil covers are found in the study area viz. typichapludalfs, typicdystrochrepts, aquicudifluvents, typicudipsamments, and mollichapludalf. The typichapludalfs occupies the largest area of the district.

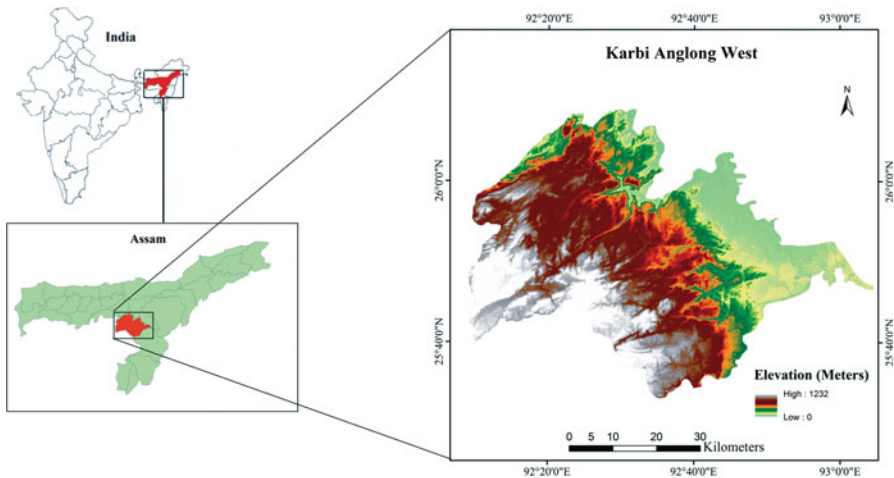


**Fig. 1** Location of Karbi Anglong West District in India

### 3 Database and Methodology

Landsat 8 OLI (02 November 2014), Cartosat 1 DEM (Digital Elevation Model), and geological and soil data were utilized for preparing landslide susceptibility map. We selected landslide-conditioning factors, namely slope, aspect, lineament, drainage, and soil and land use/land cover and created thematic layers in GIS environment. These factors were assigned through the frequency ratio model. Past landslide locations (2011–2015) were extracted from the landslide hazard map of Assam. The pixels of the thematic layers and past landslide locations were integrated and their weights were obtained through frequency ratio model. A detail of the data base used for landslide susceptibility mapping is presented in Table 1.

#### 3.1 *Landslide Inventory Map*

Many scholars prepared landslide inventory maps based on past account of studies, enormous ground truth of geomorphological factors, remote sensing data, and aerial photograph interpretation (Hansen 1984; Galli et al. 2008). For this study, National Institute of Disaster Management Landslide map of Assam was used for extracting past landslide locations of the district (National Institute of Disaster Management 2011). Of the total past landslides locations in the study area (229), 70% locations were used for preparing landslide susceptibility model through frequency ratio and 30% locations for validating the model (Fig. 2).

#### 3.2 *Landslide-Conditioning Parameters*

Thematic layers of slope, aspect, geology, soil type, lineament density, drainage density, and land use/land cover were integrated through frequency ratio model to produce landslide susceptibility map. Slope is a significant factor for determination of landslide. Higher slope angle exerts stress on the soil, leading to increase in intensity of landslide occurrence. The slope map was derived from Cartosat-1 DEM satellite data. Slope classes were categorized as low to high based on the steepness. In order to understand lithology of the study area, a general geological map was prepared with the help of Geological Survey of India (1998) map. Soil map of the region was generated from National Bureau of Soil Survey and Land Use Planning (1999) map for assessing influence of soil composition on landslide occurrence. Automated DEM technique was used to extract surface streams of the study area. Further, direction of surface flow determined through DEM surface was used to obtain the flow accumulation dataset. The drainage of the study area was extracted

**Table 1** Frequency ratio of factors to landslide occurrence

| Data layers         | Classes                                 | Pixels in domain | Pixel (%) <sup>a</sup> | Landslide occurrence points | Landslide occurrence points (%) <sup>b</sup> | Frequency ratio <sup>b/a</sup> |
|---------------------|---|------------------|------------------------|-----------------------------|--|--------------------------------|
| Slope               | 0–15°                                   | 157,325          | 17.7                   | 0                           | 0.0  | 0.00                           |
|                     | 15–30°                                  | 202,487          | 22.8                   | 1                           | 0.6  | 0.03                           |
|                     | 30–45°                                  | 214,351          | 24.2                   | 9                           | 5.6  | 0.23                           |
|                     | 45–60°                                  | 79,648           | 9.0                    | 23                          | 14.4   | 1.60                           |
|                     | 60–75°                                  | 133,654          | 15.1                   | 42                          | 26.3   | 1.74                           |
|                     | Above 75°                               | 99,452           | 11.2                   | 85                          | 53.1   | 4.74                           |
| Drainage density    | High                                    | 172,216          | 19.4                   | 65                          | 40.6   | 2.09                           |
|                     | Moderate                                | 95,161           | 10.7                   | 34                          | 21.3   | 1.98                           |
|                     | Low                                     | 106,994          | 12.1                   | 21                          | 13.1   | 1.09                           |
|                     | Very low                                | 512,546          | 57.8                   | 40                          | 25.0   | 0.43                           |
| Lineament density   | High                                    | 136,913          | 15.4                   | 35                          | 21.9   | 1.42                           |
|                     | Moderate                                | 77,948           | 8.8                    | 25                          | 15.6   | 1.78                           |
|                     | Low                                     | 98,491           | 11.1                   | 53                          | 33.1   | 2.98                           |
|                     | Very low                                | 573,565          | 64.7                   | 47                          | 29.4   | 0.45                           |
| Geology             | Schist's                                | 218,948          | 24.7                   | 65                          | 40.6   | 1.65                           |
|                     | Quartz-sericite schist and conglomerate | 99,491           | 11.2                   | 7                           | 4.4  | 0.39                           |
|                     | Porphyritic coarse granite              | 398,835          | 45.0                   | 86                          | 53.8   | 1.20                           |
|                     | Undifferentiated fluvial sediments      | 169,643          | 19.1                   | 2                           | 1.3  | 0.07                           |
| Soil                | Typic hapludalfs                        | 311,577          | 35.1                   | 83                          | 51.9   | 1.48                           |
|                     | Typic dystochrepts                      | 236,985          | 26.7                   | 70                          | 43.8   | 1.64                           |
|                     | Aquic udifluvents                       | 86,536           | 9.8                    | 0                           | 0.0  | 0.00                           |
|                     | Typic udipsamments                      | 132,781          | 15.0                   | 0                           | 0.0  | 0.00                           |
|                     | Mollic hapludalf                        | 119,038          | 13.4                   | 7                           | 4.4  | 0.33                           |
| Land use/land cover | Built-up                                | 41,932           | 4.7                    | 27                          | 16.9   | 3.57                           |
|                     | Paddy cultivation                       | 135,171          | 15.2                   | 1                           | 0.6  | 0.04                           |
|                     | Jhum cultivation                        | 20,795           | 2.3                    | 16                          | 10.0   | 4.27                           |
|                     | Water body                              | 3947             | 0.4                    | 0                           | 0.0  | 0.00                           |
|                     | Vegetation                              | 655,579          | 73.9                   | 45                          | 28.1   | 0.38                           |
|                     | Barren land                             | 29,493           | 3.3                    | 71                          | 44.4   | 13.34                          |
| Aspect              | North                                   | 104,854          | 11.8                   | 19                          | 11.9   | 1.00                           |
|                     | North east                              | 88,711           | 10.0                   | 27                          | 16.9   | 1.69                           |
|                     | East                                    | 152,897          | 17.2                   | 16                          | 10.0   | 0.58                           |
|                     | South east                              | 68,965           | 7.8                    | 19                          | 11.9   | 1.53                           |
|                     | South                                   | 119,789          | 13.5                   | 20                          | 12.5   | 0.93                           |
|                     | South west                              | 135,978          | 15.3                   | 24                          | 15.0   | 0.98                           |
|                     | West                                    | 125,826          | 14.2                   | 18                          | 11.3   | 0.79                           |
|                     | North west                              | 89,897           | 10.1                   | 17                          | 10.6   | 1.05                           |

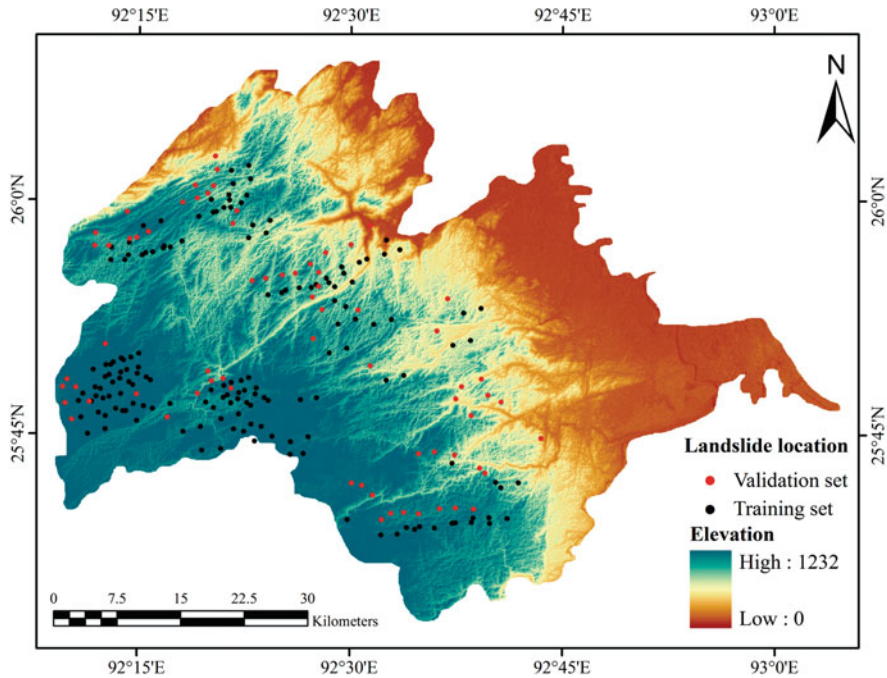


**Fig. 2** Landslide inventory map of the study area

from flow accumulation dataset on 1:2500 scale. The drainage density was calculated to understand the intensity of landslide zones. On screen digitization was carried out to extract lineament from the satellite imagery using fractures and fault lines. The lineament density map was prepared by taking 200-m radius from a lineament. Land use/land cover has profound effects on the occurrence of landslides. Land use/land cover map was prepared using supervised classification.

### ***3.3 Landslide Susceptibility Model (Frequency Ratio)***

Probability of future landslides occurrence is more in those areas with similar conditions of past landslides (Lee and Talib 2005; Huang et al. 2015). Frequency ratio model for landslides can be determined as the ratio of percentage of landslide pixels and domain pixels of each class of causative factors (Lee and Sambath 2006; Pradhan and Youssef 2010; Pourghasemi et al. 2013). The model can also be utilized for establishing the relation of causal factors with the spatial distribution of landslide occurrences and nonoccurrences (Lee and Sambath 2006; Pourghasemi et al. 2013). Frequency ratio and landslide susceptibility index can be expressed as follows:

$$Fr = \frac{\text{landslideoccurrenceratio}}{\text{arearatio}} \quad (1)$$

$$LSI = \sum Fr_a \quad (2)$$

Where  $Fr_a$  is the frequency ratio of each causative factor type or range and landslide susceptibility index (LSI) is the landslide susceptibility index. Frequency ratio for each class of factors is shown in Table 1. If the value of frequency ratio is 1 or more then the area is said to have high frequency of landslide occurrence.

### 3.4 Validation of the Map

The accuracy of the model was determined using receiver operating characteristics (ROC) curves. Training dataset was used for determining success rate, while testing dataset and susceptibility map provided prediction rate. Landslide susceptibility assessment and frequency of future landslide occurrence were analyzed through success rate and prediction rate curves, respectively.

## 4 Results

Higher susceptibility was found on hill slopes having a gradient of  $>60^\circ$ . Steep slope was observed in the south-western part where south facing slope had lesser vegetation density and high rate of erosion in comparison with the north-facing slope (Fig. 3). Past landslide location map also showed similar pattern where south- and east-facing slopes were found to have more susceptibility for landslides. Moderate susceptibility areas were located on the slope with gradient values of  $30^\circ$  to  $60^\circ$ . Low landslide susceptibility was found scattered in the study area due to low slope gradients and surface materials with low tendency to cause landslide. Landslide-free areas were found in the north-eastern part having plain surface morphology.

From the lithological perspective, high landslide susceptibility was found especially in south and south-western parts having schist lithology. Typichapludalf and typicdystrochrept soil types covered large area and were susceptible to landslide hazards due to their grain size. Moderate and high susceptibility areas were identified within the vicinity of these soils (Fig. 4). Undifferentiated fluvial sediments were found in the north, and eastern parts of the district did not experience landslides. Aquicudifluent and typicudipsamment soil types were found in the plain areas of study area where flood occurred every year and thus were free from landslide occurrence.

Distance from drainage and lineament were negatively related with landslide occurrence. Intensity of landslide susceptibility decreased as the distance from the



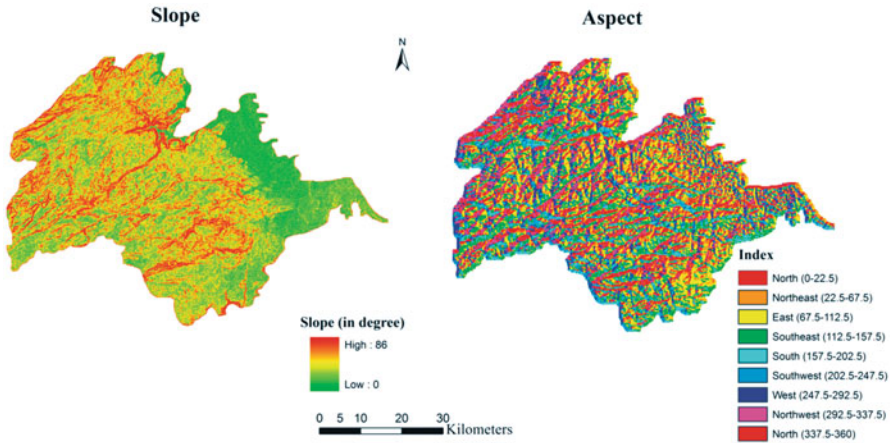


Fig. 3 Layers of slope and aspect

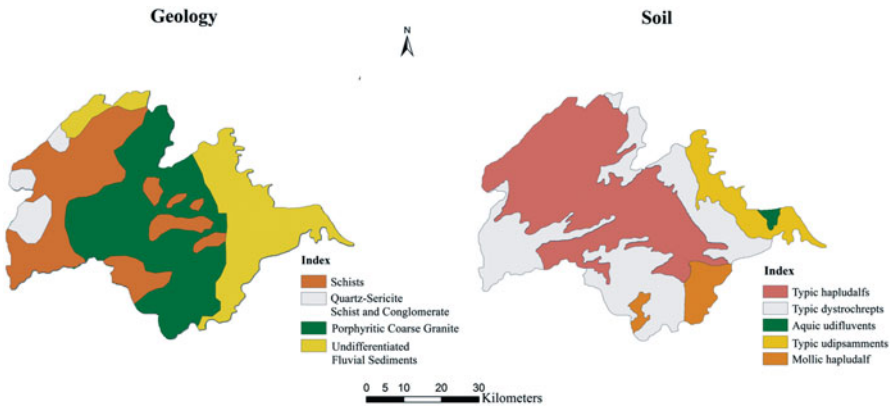
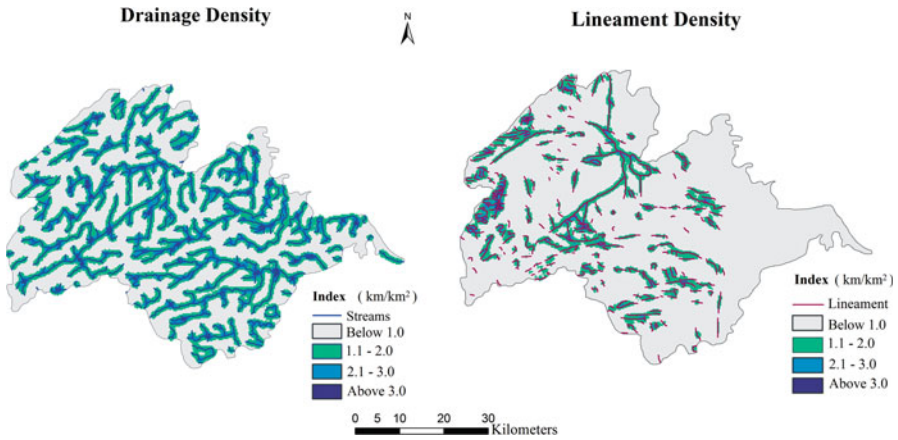


Fig. 4 Layers of geology and soil

drainage and lineament increased. High and moderate susceptibility classes were observed in those areas with high density of drainage and lineament (Fig. 5).

Vegetation cover had a significant resistance on landslide triggered by rainfall in the study area. It covered large area due to irregular terrain and scattered settlement (Table 2). Most of the built-up area and area under paddy cultivation were found in the plain areas. A small proportion of built-up area is found in the hilly terrain and was found susceptible to landslides. Barren land and *Jhum* cultivation along hill slopes provide favorable conditions for landslide through the permeability of water. These two classes of land uses were highly susceptible to landslides (Fig. 6). Marked variations were observed in the spatial distribution of landslide susceptibility in the study area (Fig. 7). Of the total area of the study area (2391 km<sup>2</sup>), about 4% area was vulnerable to landslides. Of the total landslide-vulnerable area, 0.6% was found



**Fig. 5** Layers of drainage density and lineament density

**Table 2** Areas under land use/land cover classes in 2014

| LU/LC Class       | Area (km <sup>2</sup> ) | Area in percentage |
|-------------------|-------------------------|--------------------|
| Built-up area     | 113.10                  | 4.73               |
| Jhum cultivation  | 56.60                   | 2.37               |
| Water body        | 9.68                    | 0.40               |
| Paddy cultivation | 365.68                  | 15.29              |
| Barren land       | 79.36                   | 3.32               |
| Vegetation        | 1766.75                 | 73.89              |
| <b>Total</b>      | <b>2391.17</b>          | <b>100</b>         |

Source: Author’s calculation from Land Use Land Cover Classification

under high susceptibility category, 1.3% under moderate, and 2.2% under low category of landslide susceptibility (Table 3).

### 4.1 Validation

The accuracy of the model was assessed through the area under the ROC curves. LSI values of all pixels were arranged in descending order to obtain the relative rank of each predictor. The pixel values (100 classes) were plotted as cumulative percentage on the y-axis. On the x-axis, LSI and landslide occurrence were plotted with accumulated 1% interval. High susceptibility zones were explained by 50% in success rate and 60% in prediction rate of all the landslides in 90%–100% (10%) cell class. The moderate susceptibility zones were determined by 72% of the landslides in the success rate and 80% in prediction rate in 80%–100% (20%) cell class. Likewise, the class of 60–100% (40%) could explain 92% in success rate and 91% in prediction rate of all landslides classified as low susceptibility zones.

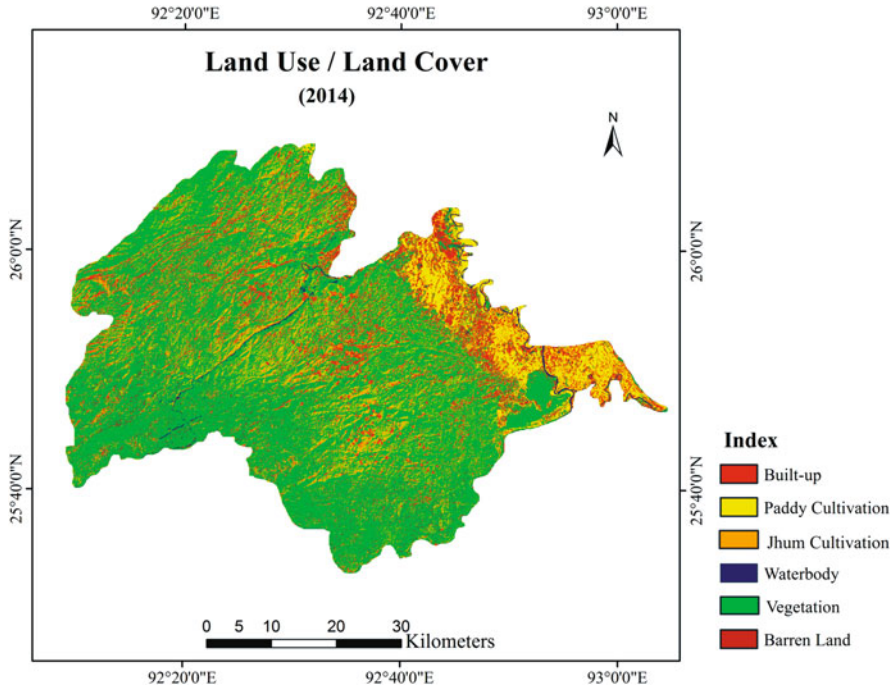


**Fig. 6** Land use/land cover classes of study area in 2014

Nonsusceptibility zones were explained by 100% in success rate with cell class range of 0%–100% (100%). The area under the curve was also assessed to determine the overall efficiency of the model. The curve revealed that the prediction rate (0.884) was found to be higher than the success rate (0.854) in the study area (Fig. 8).

## 5 Conclusion

The paper presented a methodology for preparing landslide susceptibility map. Evidence was given from Karbi Anglong West district in Assam, India. Past landslide locations were used for preparing landslide inventory map. These locations were used for analyzing landslide susceptibility through frequency ratio model and validating the susceptibility map. Slope, lineament, aspect, land use/land cover, geology, soil, and drainage landslide-conditioning factors were selected to analyze landslide susceptibility in the district. The integrated thematic layers of landslide parameters and past landslide pixels were used to prepare landslide susceptibility map through frequency ratio model. The susceptibility map showed high and moderate susceptibility in areas having steep slopes. These slopes had high density of drainage and lineament and were mainly utilized for practicing shifting

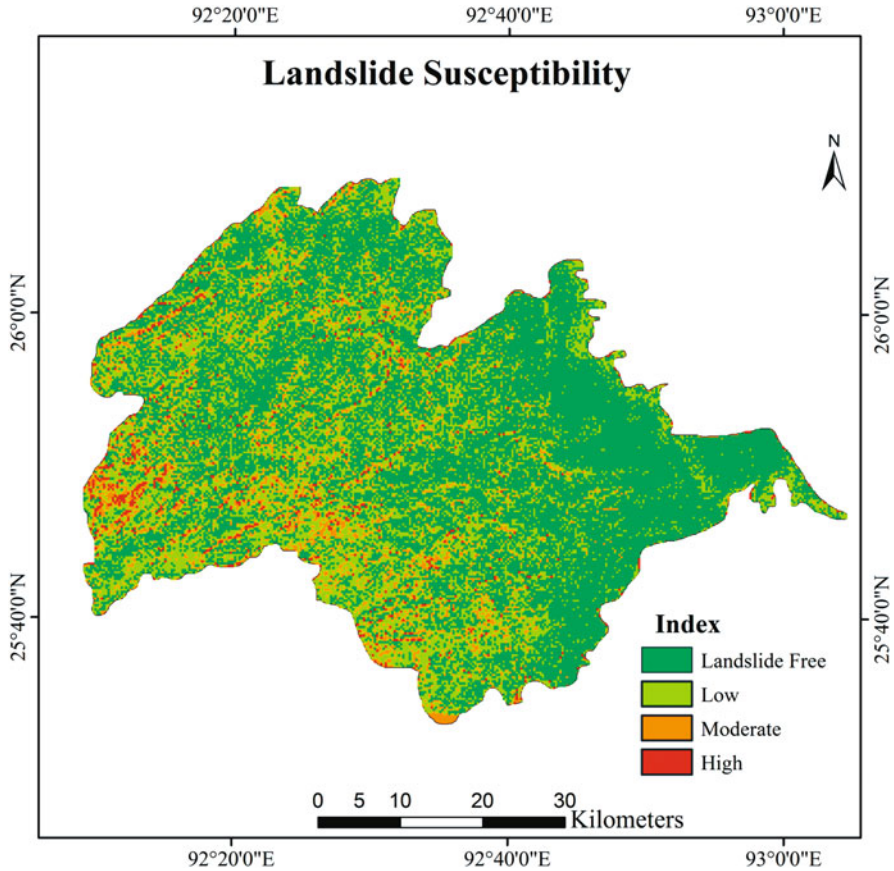


**Fig. 7** Landslide susceptibility classes of study area

**Table 3** Area under landslide susceptibility in 2014

| Susceptibility | Area (km <sup>2</sup> ) | Percentage |
|----------------|-------------------------|------------|
| Landslide-free | 2290                    | 95.79      |
| Low            | 53.31                   | 2.23       |
| Moderate       | 31.89                   | 1.33       |
| High           | 15.29                   | 0.63       |

Source: Authors' calculation from susceptibility map

agriculture. Low susceptibility areas were found scattered throughout the study area. These areas possessed low slope gradient with low intensity of drainage and lineament density. Success and prediction rates under ROC curve were found to be 0.854 and 0.884, respectively. Thus, susceptibility map was found in tune with past landslide events. The susceptibility map identified not only the landslide-prone areas requiring immediate attention but also measured the susceptibility intensity where efforts could be made to safeguard the local community from the hazard.

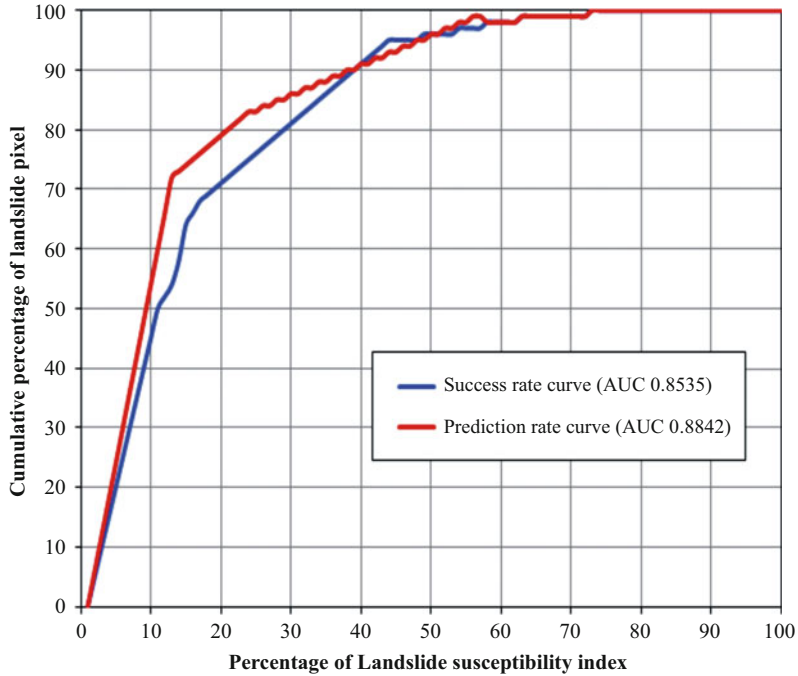


**Fig. 8** ROC curves of prediction rate and success rate

The map may also help planners and decision makers in identifying housing sites and planning of infrastructural development in the study area. Thus, the methodology adopted in this study can help in analyzing landslide susceptibility in different landslide-vulnerable geographical regions at various scales.

## References

- Akgun, A. (2012). A comparison of landslide susceptibility maps produced by logistic regression, multi-criteria decision, and likelihood ratio methods: A case study at İzmir, Turkey. *Landslides*, 9, 93–106. <https://doi.org/10.1007/s10346-011-0283-7>.
- Akgun, A., Dag, S., & Bulut, F. (2008). Landslide susceptibility mapping for a landslide-prone area (Findikli, NE of Turkey) by likelihood-frequency ratio and weighted linear combination models. *Environmental Geology*, 54, 1127–1143. <https://doi.org/10.1007/s00254-007-0882-8>.
- Ayalew, L., & Yamagishi, H. (2005). The application of GIS-based logistic regression for landslide susceptibility mapping in the Kakuda-Yahiko Mountains, Central Japan. *Geomorphology*, 65, 15–31. <https://doi.org/10.1016/j.geomorph.2004.06.010>.
- Barredo, J., Benavides, A., Hervás, J., & van Westen, C. J. (2000). Comparing heuristic landslide hazard assessment techniques using GIS in the Tirajana basin, gran Canaria Island, Spain. *International Journal of Applied Earth Observation and Geoinformation*, 2, 9–23.

- Beguiría, S., & Lorente, A. (2007). *Landslide hazard mapping by multivariate statistics: Comparison of methods and case study in the Spanish Pyrenees* (Technical report). Zaragoza: Instituto Pirenaico de Ecología.
- Chalkias, C., Ferentinou, M., & Polykretis, C. (2014). GIS-based landslide susceptibility mapping on the Peloponnese Peninsula, Greece. *Geosciences*, 4, 176–190. <https://doi.org/10.3390/geosciences4030176>.
- Dai, F. C., & Lee, C. F. (2002). Landslide characteristics and slope instability modeling using GIS, Lantau Island, Hong Kong. *Geomorphology*, 42, 213–228. [https://doi.org/10.1016/S0169-555X\(01\)00087-3](https://doi.org/10.1016/S0169-555X(01)00087-3).
- Dai, F. C., Lee, C. F., Li, J. X. Z. W., & Xu, Z. W. (2001). Assessment of landslide susceptibility on the natural terrain of Lantau Island, Hong Kong. *Environmental Geology*, 40, 381–391.
- Demir, G., Aytekin, M., Akgün, A., İkizler, S. B., & Tatar, O. (2013). A comparison of landslide susceptibility mapping of the eastern part of the North Anatolian Fault Zone (Turkey) by likelihood-frequency ratio and analytic hierarchy process methods. *Natural Hazards*, 65, 1481–1506. <https://doi.org/10.1007/s11069-012-0418-8>.
- Dhakal, A. S., Amada, T., & Aniya, M. (2000). Landslide hazard mapping and its evaluation using GIS: An investigation of sampling schemes for a grid-cell based quantitative method. *PE&RS, Photogrammetric Engineering & Remote Sensing*, 66, 981–989.
- Ercanoglu, M., & Gokceoglu, C. (2002). Assessment of landslide susceptibility for a landslide-prone area (north of Yenice, NW Turkey) by fuzzy approach. *Environmental Geology*, 41, 720–730.
- Ermini, L., Catani, F., & Casagli, N. (2005). Artificial neural networks applied to landslide susceptibility assessment. *Geomorphology*, 66, 327–343. <https://doi.org/10.1016/j.geomorph.2004.09.025>.
- Galli, M., Ardizzone, F., Cardinali, M., Guzzetti, F., & Reichenbach, P. (2008). Comparing landslide inventory maps. *Geomorphology*, 94, 268–289.
- Geological Survey of India. (1998). *Geology and mineral map of north East India*. New Delhi: Ministry of Mines, Government of India.
- Gokceoglu, C., Sonmez, H., Nefeslioglu, H. A., Duman, T. Y., & Can, T. (2005). The 17 March 2005 Kuzulu landslide (Sivas, Turkey) and landslide-susceptibility map of its near vicinity. *Engineering Geology*, 81, 65–83. <https://doi.org/10.1016/j.enggeo.2005.07.011>.
- Gupta, R. P., & Joshi, B. C. (1990). Landslide hazard zoning using the GIS approach—A case study from the Ramganga catchment, Himalayas. *Engineering Geology*, 28, 119–131.
- Hansen, A. (1984). Landslide hazard analysis. In D. Brunsten & E. Prior (Eds.), *Slope instability* (pp. 523–602). New York: Wiley.
- Hong, Y. A. N. G., & Adler, R. F. (2007). Towards an early-warning system for global landslides triggered by rainfall and earthquake. *International Journal of Remote Sensing*, 28, 3713–3719. <https://doi.org/10.1080/01431160701311242>.
- Huang, J., Zhou, Q., & Wang, F. (2015). Mapping the landslide susceptibility in Lantau Island, Hong Kong, by frequency ratio and logistic regression model. *Annals of GIS*, 21, 191–208. <https://doi.org/10.1080/19475683.2014.992373>.
- Kanungo, D. P., Arora, M. K., Sarkar, S., & Gupta, R. P. (2006). A comparative study of conventional, ANN black box, fuzzy and combined neural and fuzzy weighting procedures for landslide susceptibility zonation in Darjeeling Himalayas. *Engineering Geology*, 85, 347–366. <https://doi.org/10.1016/j.enggeo.2006.03.004>.
- Lee, S., & Pradhan, B. (2006). Probabilistic landslide hazards and risk mapping on Penang Island, Malaysia. *Journal of Earth System Science*, 115, 661–672. <https://doi.org/10.1007/s12040-006-0004-0>.
- Lee, S., & Pradhan, B. (2007). Landslide hazard mapping at Selangor, Malaysia using frequency ratio and logistic regression models. *Landslides*, 4, 33–41. <https://doi.org/10.1007/s10346-006-0047y>.

- Lee, S., & Sambath, T. (2006). Landslide susceptibility mapping in the DamreiRomel area, Cambodia using frequency ratio and logistic regression models. *Environmental Geology*, *50*, 847–855.
- Lee, S., & Talib, J. A. (2005). Probabilistic landslide susceptibility and factor effect analysis. *Environmental Geology*, *47*, 982–990.
- Lee, S., Ryu, J. H., Won, J. S., & Park, H. J. (2004). Determination and application of the weights for landslide susceptibility mapping using an artificial neural network. *Engineering Geology*, *71*, 289–302.
- Lin, M. L., & Tung, C. C. (2004). A GIS-based potential analysis of the landslides induced by the Chi-Chi earthquake. *Engineering Geology*, *71*, 63–77.
- Montgomery, D. R., & Dietrich, W. E. (1994). A physically based model for the topographic control on shallow landsliding. *Water Resources Research*, *30*, 1153–1171.
- National Bureau of Soil Survey and Land Use Planning. (1999). *Soils of Assam for optimising land use*. Nagpur: Ministry of Agriculture, Government of India.
- National Institute of Disaster Management. (2011). *Assam: National disaster risk reduction portal*. New Delhi: Ministry of Home Affairs.
- Neuhäuser, B., & Terhorst, B. (2007). Landslide susceptibility assessment using “weights-of-evidence” applied to a study area at the Jurassic escarpment (SW-Germany). *Geomorphology*, *86*, 12–24. <https://doi.org/10.1016/j.geomorph.2006.08.002>.
- Pachauri, A. K., & Pant, M. (1992). Landslide hazard mapping based on geological attributes. *Engineering Geology*, *32*, 81–100.
- Pourghasemi, H. R., Pradhan, B., & Gokceoglu, C. (2012). Application of fuzzy logic and analytical hierarchy process (AHP) to landslide susceptibility mapping at Haraz watershed, Iran. *Natural Hazards*, *63*, 965–996. <https://doi.org/10.1007/s11069-012-0217-2>.
- Pourghasemi, H. R., Jirandeh, A. G., Pradhan, B., Xu, C., & Gokceoglu, C. (2013). Landslide susceptibility mapping using support vector machine and GIS at the Golestan Province, Iran. *Journal of Earth System Science*, *122*, 349–369.
- Pradhan, B. (2011). Use of GIS-based fuzzy logic relations and its cross application to produce landslide susceptibility maps in three test areas in Malaysia. *Environmental Earth Sciences*, *63*, 329–349. <https://doi.org/10.1007/s12665-010-0705-1>.
- Pradhan, B., & Lee, S. (2010). Regional landslide susceptibility analysis using back-propagation neural network model at Cameron Highland, Malaysia. *Landslides*, *7*, 13–30. <https://doi.org/10.1007/s10346-009-0183-2>.
- Pradhan, B., & Youssef, A. M. (2010). Manifestation of remote sensing data and GIS on landslide hazard analysis using spatial-based statistical models. *Arabian Journal of Geosciences*, *3*, 319–326.
- Raghuvanshi, T. K., Negassa, L., & Kala, P. M. (2015). GIS based grid overlay method versus modeling approach – A comparative study for landslide hazard zonation (LHZ) in Meta Robi District of West Showa Zone in Ethiopia. *The Egyptian Journal of Remote Sensing and Space Science*, *18*, 235–250.
- Saaty, T. L. (1980). *The analytical hierarchy process*. New York: McGraw Hill.
- Sahana, M., & Sajjad, H. (2017). Evaluating effectiveness of frequency ratio, fuzzy logic and logistic regression models in assessing landslide susceptibility: A case from Rudraprayag district, India. *Journal of Mountain Science*. <https://doi.org/10.1007/s11629-017-4404-1>.
- Saito, H., Nakayama, D., & Matsuyama, H. (2009). Comparison of landslide susceptibility based on a decision-tree model and actual landslide occurrence: The Akaishi Mountains, Japan. *Geomorphology*, *109*, 108–121. <https://doi.org/10.1016/j.geomorph.2009.02.026>.
- Shahabi, H., Ahmad, B. B., & Khezri, S. (2012). Landslide susceptibility mapping using image satellite and GIS technology. *International Journal of Recent Technology and Engineering*, *1*, 1–5.
- Süzen, M. L., & Doyuran, V. (2004). A comparison of the GIS based landslide susceptibility assessment methods: Multivariate versus bivariate. *Environmental Geology*, *45*, 665–679.

- Tangestani, M. H. (2009). A comparative study of Dempster–Shafer and fuzzy models for landslide susceptibility mapping using a GIS: An experience from Zagros Mountains, SW Iran. *Journal of Asian Earth Sciences*, 35, 66–73. <https://doi.org/10.1016/j.jseaes.2009.01.002>.
- Torkashvand, A. M., Irani, A., & Sorur, J. (2014). The preparation of landslide map by landslide numerical risk factor (LNRF) model and geographic information system (GIS). *The Egyptian Journal of Remote Sensing and Space Science*, 17, 159–170.
- Wan, S. (2009). A spatial decision support system for extracting the core factors and thresholds for landslide susceptibility map. *Engineering Geology*, 108, 237–251. <https://doi.org/10.1016/j.enggeo.2009.06.014>.
- Yagi, H. (2003). Development of assessment method for landslide hazardness by AHP. In *Abstract volume of the 42nd annual meeting of the Japan Landslide Society*, pp. 209–212.
- Yalcin, A. (2008). GIS-based landslide susceptibility mapping using analytical hierarchy process and bivariate statistics in Ardesen (Turkey): Comparisons of results and confirmations. *Catena*, 72, 1–12. <https://doi.org/10.1016/j.catena.2007.01.003>.
- Yilmaz, I. (2009). Landslide susceptibility mapping using frequency ratio, logistic regression, artificial neural networks and their comparison: A case study from Kat landslides (Tokat—Turkey). *Computers & Geosciences*, 35, 1125–1138. <https://doi.org/10.1016/j.cageo.2008.08.007>.



# Retreating Glacier Dynamics Over the Last Quarter of a Century in Uttarakhand Region Using Optical Sensor Time Series Data



Himanshu Kalita, Tapan Ghosh, Meenu Rani, J. S. Rawat,  
Ram Kumar Singh , Susheel Kumar Singh, and Pavan Kumar 

**Abstract** The Uttarakhand glaciers have been melting over the last half of a century. Local climatic variation has influenced the glacier retreat but these phenomena do not appear to affect the glacier health over long period of time. The increased availability of geospatial technology, global coverage and very low financial costs allows for fast, semi-automated, and cost-effective assessment of changes in glacier parameters over large areas. Geospatial technology allow for regular monitoring of the properties of Uttarakhand glaciers such as terminus position and ice extent from which glacier mass balance can be inferred. Geospatial technology is the only technique that can help to determine it using different platform like space-borne and air-borne sensors. The basic semantic characterization of geospatial technology is primarily used for spectral characterization in Uttarakhand glacial and depicting snow and ice top. Semi-automated geospatial technique helps in

---

H. Kalita

Department of Science & Technology, Haryana Space Applications Centre (HARSAC), Hisar, India

T. Ghosh

Punjab Remote Sensing Centre, Ludhiana, India

M. Rani

Department of Geography, Kumaun University, Nainital, Uttarakhand, India

J. S. Rawat

Remote Sensing and GIS, Kumaun University, Almora, Uttarakhand, India

R. K. Singh

Department of Natural Resources, TERI School of Advanced Studies, New Delhi, India

S. K. Singh

Department of Soil Science and Agricultural Chemistry, College of Agriculture, Rani Lakshmi Bai Central Agricultural University, Jhansi, Uttar Pradesh, India

P. Kumar (✉)

College of Horticulture and Forestry, Rani Lakshmi Bai Central Agricultural University, Jhansi, Uttar Pradesh, India

processing all data collected from on-board and off-board systems. This research analyzed the Normalized Difference Snow Index (NDSI) for showing snow cover delineation area and Normalized Difference Vegetation Index (NDVI) for vegetation cover delineation. The study aim to refer the changes from 1994 to 2015 and detected for snow and vegetation changed over quarter of the century. The study will helps to determine glacier dynamics and its kinetic change rate and also useful to global level studies and snow change detection.

**Keywords** Glacier dynamics · Climate change · NDSI · NDVI

## 1 Introduction

One of the largest collections of glaciers of 9600 glaciers cover 33,000 km<sup>2</sup> (Dyurgerov and Meier 1997) in the Indian Himalayas (Raina and Srivastava 2008). The Indian Himalayan mountain has experienced widespread accelerated recession (area and length), detachment, fragmentation, and mass loss with above average warming over the last quarter of century (Shukla and Qadir 2016; Haritashya et al. 2006; Bhutiyani 2016; Kumar et al. 2008; Raina 2004; Ratan Kar et al. 2002; Kulkarni and Karyakarte 2014; Schickhoff et al. 2016; Bolch et al. 2019; Zemp et al. 2009). The rising consumption of global energy due to emission of greenhouse gases mainly caused by anthropogenic activities (Berthier et al. 2010; Bhambri et al. 2012). Several studies conducted in the Indian Himalayan glaciers suggest irregular glacier response patterns and spatial variability across the Uttarakhand Himalayan mountain (Kumar et al. 2009; Azam et al. 2018; Berthier et al. 2007; Kääh et al. 2015). This spatially variable glacier response is associated with the spatial variability of changing climatic circumstances such as precipitation and temperature trends with geomorphic factors. The major spatial variability includes thickness of debris cover, slope of glacier bed, slope aspects, glacial-lake activities and glacier geometry (Singh et al. 2008; Khopkar et al. 2013; Venkatesh et al. 2013; Bhambri and Bolch 2009; Nainwal et al. 2016; Lu et al. 2005; Shukla and Qadir 2016).

Several studies have also demonstrated difficulties in mapping the glacier due to debris-covered portions and in mixed accumulation zones of glaciers. Normalized Difference Snow Index (NDSI) (Sidjak and Wheate 1999; Andreassen et al. 2008; Raina 2010; Hall et al. 2002; Deota et al. 2011; Tong and Velicogna 2010), object-based classification (Gao et al. 2007; Rastner et al. 2013; Csatho et al. 1999; Robson et al. 2015; Rastner et al. 2014), Principal Component Analysis (Dedieu et al. 2013; Sagredo and Lowell 2012; Sidjak and Wheate 1999; Sidjak 1999; Sibandze et al. 2014), and band rationing (Pandey et al. 2011; Karimi et al. 2012a, b; Bajracharya et al. 2014; Atif et al. 2016; Hall et al. 1987; Raj and Babu 2011; Paul and Kääh 2005; Parrot et al. 1993; Haq and Jain 2012) have been used for assessment of Himalayan glaciers. However, procurement of suitable threshold values from several approaches to map glaciers still remains a prominent test. Validation of assessment

of Himalayan glaciers derived through remote sensing data was also attempted with field-based data having utilized several automated and semi-automated method for retrieving glaciers (Zemp et al. 2015; Racoviteanu et al. 2009; Huss et al. 2017; Smith et al. 2015; Paul et al. 2013; Giesen and Oerlemans 2013; Bolch et al. 2007; Marzeion et al. 2017). Many studies have shown effectiveness of vegetation indices in analyzing relationship between vegetation and snow. Snow cover information can be derived from optical remote sensing data. The most accurate and conventional approach is manual delineation (on-screen digitization) based on field measurements for glacier mapping in the deeply debris-covered ablation and various mixed accumulation zones, but such methods are costly, time-consuming, and involve high man power. Geospatial techniques have been extensively used to collective information and to examine snow cover at large scales. Therefore, integrating remote sensing and GIS technique can help in snow cover mapping (Fallourd et al. 2011; Parajka and Blöschl 2008; Huang and Li 2011; Liang et al. 2008; Karimi et al. 2012a, b; Klein and Barnett 2003; Linsbauer et al. 2012; Walker et al. 1993; Paul and Linsbauer 2012; Strozzi et al. 2002).

The emphasis of the present study is on the Uttarakhand glaciers, which has been subjected to satellite data and field investigation-based monitoring for over the last quarter of a century. Studies reveal that NDSI is a useful index for discriminating snow and clouds as clouds show even high reflectance in the SWIR region. We observed that there is a non-existence of comprehensive study, high-resolution recent satellite images to evaluate the recession of the Uttarakhand glaciers. We also analyzed that spectral curve plays significant roles to discriminate among snow, vegetation, barren land, and water bodies using geospatial datasets. Therefore, in the present study, we aimed at retreating glacier dynamics and their assessment using time series satellite data of the Uttarakhand glaciers based on ground survey data historical maps and optical satellite data.

## 2 Material and Methodology

### 2.1 Study Area

Uttarakhand glaciers of the Himalayas are for their beauty. Here we focused on the Uttarakhand glacier region (Fig. 1) extending between  $29^{\circ}27'30''\text{N}$  to  $31^{\circ}29'30''\text{N}$  latitudes and  $77^{\circ}53'40''\text{E}$  to  $81^{\circ}11'55''\text{E}$  longitudes. The total glacier region area of Uttarakhand is  $30,636\text{ km}^2$ . High peaks and glaciers of wide variety cover the most northern part of Uttarakhand. The Himalayan range has a southern slope covering the entire vegetation and very steep elevation; Uttarakhand is situated in the sub-tropical forest zone region. The main hill combination found in Uttarakhand is the Northern Kumaun region and Western Garhwal region. Some of the river basins that originated from Uttarakhand are Ganga (Gangotri) and Yamuna (Yamunotri). The

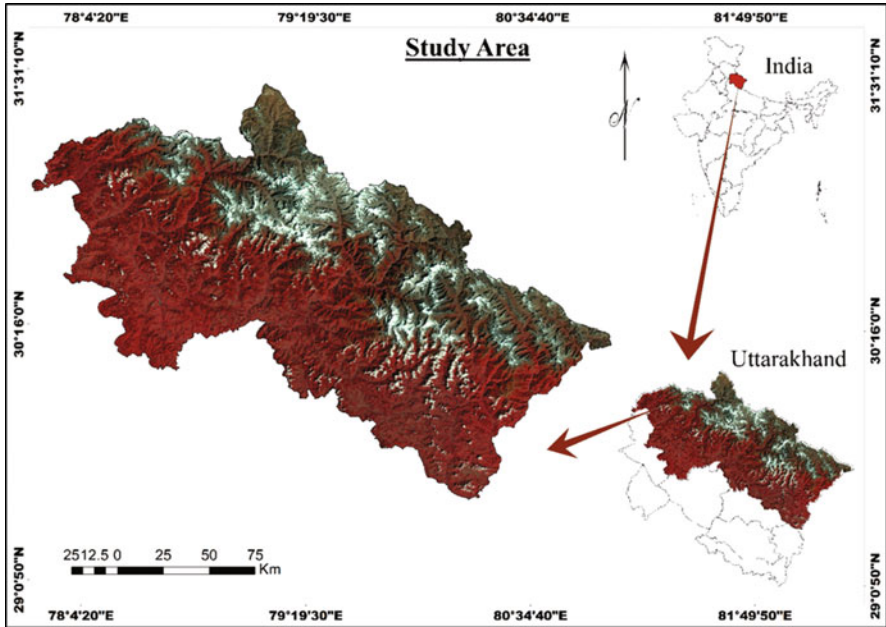


Fig. 1 The location of the study area

two most holy places in Hindu mythology are also to be found in Uttarakhand, i.e., Badrinath and Kedarnath. Glaciers are also to be found here and include Pindari, Gangotri, Milam, and Bunderpuuch. Some other names of popular glaciers found here are Sunderdhunga Ralam, Kaphinni, Dokhriani, Doonagiri, and Khatling.

## 2.2 Data Used

The Landsat satellite program, a space operation jointly done by NASA and USGS, is the longest and most durable global dataset of Earth's pure surface. Mostly, Landsat is widely used to optimize spectral bands with track efficiency for land use monitoring. The ground resolution of Landsat was documented for orthodox use of climate change detection, monitoring wildfire, urbanization planning, drought capture and so many man-based activities, which indicates danger for natural surface. In this study, we used the 1994 as well as 2015 Landsat data for smoother detection with decadal change. Landsat-5 data with Thematic Mapper (TM) sensor is specifically used for the 1994 dataset. The TM imagery mainly consists of seven spectral bands, with a resolution of 30 m for the specific band of bands 1–5 and band seven. Band 6 consists of 120-m resolution resample, with 30-m pixel level data

**Table 1** Specification and acquisition time of data used

| Data        | Spatial resolution            | No. of bands            | Path/Row |    | Date of acquisition |
|-------------|-------------------------------|-------------------------|----------|----|---------------------|
| Landsat TM  | 30 m(MSS),<br>120 m (thermal) | 6 (MSS),<br>1 (thermal) | 144      | 39 | October 2, 1994     |
|             |                               |                         | 145      | 39 | October 9, 1994     |
|             |                               |                         | 146      | 38 | September 30, 1994  |
|             |                               |                         | 146      | 39 | September 30, 1994  |
| Landsat-OLI | 30 m (MSS),<br>30 m (thermal) | 8(MSS)<br>2 (thermal)   | 144      | 39 | October 2, 2015     |
|             |                               |                         | 145      | 39 | October 20, 2015    |
|             |                               |                         | 146      | 38 | October 10, 2015    |
|             |                               |                         | 146      | 39 | October 10, 2015    |

being a thermal infrared band. The main use of TM band in Landsat imagery is to determine ice degradation due to glacier loss for temperature factor or melting. For the 2015 dataset, we used Landsat 8 data, which is suitable for all land imager operation and capable with two thermal infrared sensors. The Operational Land Imager (OLI) and Thermal Infrared Sensor images consist of nine different bands with spectral signature with 30-m resolution for all. Landsat 8 dataset is highly useful for coastal area operation, aerosol detection, and cirrus cloud-based operation (Table 1).

### 2.3 Data Calibration

Radiance, reflectance, and atmospheric conditions affect the digital number (DN) values of Landsat satellite data. Radiometric calibration employs algorithms that improve satellite data. This is done by converting the DN values to spectral radiance, and then to reflectance followed by the removal of atmospheric effects. Dataset validation is approached with this empirical system, and image processed is washed-out to this algorithm. The main aim of this algorithm is to calibrate the obtained product with the bottom of the atmosphere reflectance as well as aerosol and water content in the vapor form. During the ortho-rectification process, the topography is corrected using the empirical system and calibration over the in-orbit phase discrepancy.

Actually, the empirical-based formula for Top of the Atmosphere (TOA), which can be determined by  $\rho$ , is calibrated for the other parameters having spectral band ( $k$ ) and for each and every pixel image form ( $i, j$ ) with the attrite of a digital counter number. This TOA conversion is followed by an empirical formula where the numeric equalized digital count for each pixel value ( $CN_{k,NTDI}$ ) is multiplied with  $vb\pi$ . The values for  $\pi$  is constant as universal constant value and other coefficient term is numerically sustained. This multiplied value is then divided by another empirical term. This empirical term is the multiplication of several constant values

and some vector emption. This multiplication follows  $\theta_s$  (the solar direction by its zenith angle), and its cosine value multiplied by  $E_s$ , i.e., solar terrestrial spectrum and  $A_k$  [absolute calibration of instrument (sensor)]. Again, the entire term is differentiated with respect to the Sun–Earth distance correction variable and  $d(t)$  with respect to the digital pixel count.

The numeric form is captualized in equation number (1) as follows:

$$\rho k(i, j) = \frac{vb\pi * CN_{k,NTDI}(i, j)}{A_{k,NTDI} * E_s * d(t) * \cos(\theta_s(i, j))} \quad (1)$$

Again, the term Sun–Earth distance correction variable, i.e.,  $d(t)$  comes under a differentiation term that undergoes inverse multiplication of the present Julian date for image-taking sensors ( $t$ ) multiplied by two another constant values: the eccentricity of the Earth’s orbit (0.01673) and the angular velocity of the Earth ( $V_e = 0.0172$ ).

$d(t)$  can be presented mathematically and is shown in equation number (2) as follows:

$$d(t) = \frac{1}{1 - 0.01673 * \cos(0.0172 * (t - 2))^2} \quad (2)$$

### 2.3.1 Digital Number to Radiance

The Digital Number (DN) values are converted to radiance values for the four bands in case of Landsat TM imagery, which is used in this research paper for the 1994 dataset. The bands that had undergone DN to reflectance are Blue, Green band, SWIR band, and thermal band of imagery. The Spectral Radiance of the sensor’s aperture is termed as  $L_\lambda$ , and the unit is  $W/(m^2 \cdot sr \cdot \mu m)$ . This  $L_\lambda$  is coined by the addition of two empirical values (Paul and Linsbauer 2012). The first term is sophisticated by the subtraction of Maximum Spectral Radiance ( $L_{max}$ ) from Minimum Spectral Radiance ( $L_{min}$ ), which is then multiplied by quantized calibrated pixel value in DNs ( $Q_{calmin}$  and  $Q_{calmax}$ ). The second term is Spectral Radiance, which is scaled to  $W/(m^2 \cdot sr \cdot \mu m)$ , i.e.,  $L_{MIN}_\lambda$ . Then both these values are added for resultant empirical results.

The empirical formula for the said description of the 1994 dataset to conversion of DN to radiance is shown in Eq. (3) as follows:

$$L_\lambda = \left( \frac{L_{MAX}_\lambda - L_{MIN}_\lambda}{Q_{cal}} \right) Q_{cal} + L_{MIN}_\lambda \quad (3)$$

Again, for the 2015 dataset, we used Landsat-OLI imagery. This dataset value is determined for radiance conversion from DN values using Blue, Green, SWIR, and

thermal bands of master data, i.e., 2015 dataset. The Spectral Radiance  $L_\lambda$  for this data is measured as the addition of two different terms (Dedieu et al. 2013; Nainwal et al. 2016). The first term is the multiplication of Multiplicative Band Index for radiance value and pixel value in DN appraise ( $Q_{cal}$ ). The second term of the addition formula is the Additive Band of Radiance value (AL). The metadata of the master imagery provides all these necessary information to calculate the radiance value.

The abovementioned term is numerically coined for the 2015 dataset and shown in Eq. (4) as follows:

$$L_\lambda = ML * Q_{cal} + AL \quad (4)$$

### 2.3.2 Radiance to Reflectance

The radiance was converted to reflectance with a unitless conversion for planetary reflectance ( $p_\lambda$ ). This  $p_\lambda$  is a numerical formula that is formed by the division of two factors (Hock 2014; Smith et al. 2015; Atif et al. 2016). The numerator is the multiplication product of  $\pi$  with Spectral Radiance of the sensor's aperture ( $L_\lambda$ ) and the Earth–Sun distance ( $d$ ). The denominator is again the multiplication product of the mean value for solar exo-atmospheric aperture ( $E_{SUN}$ ) and the cosine value of the Sun Zenith Angle in degree unit ( $\theta_s$ ).

This can be shown in Eq. (5) as follows:

$$p_\lambda = \pi * L_\lambda * d^2 / ESUN_\lambda * \cos\theta_s \quad (5)$$

On the other hand, for the 2015 dataset Landsat imagery, the OLI-based reflectance is used. Here, reflectance from the radiance value ( $p_\lambda$ ) is an additional term for two different numeric characters (Smith et al. 2015; Atif et al. 2016). The first character is the multiplication product of reflectance multiband ( $Mp$ ) with pixel value for quantized and calibrated standard product of sensors ( $Q_{cal}$ ). The second character is the reflectance additive band for the sensors ( $Ap$ ).

This is mathematically expressed in Eq. (6) as follows:

$$p_\lambda = Mp * Q_{cal} + Ap \quad (6)$$

### 2.3.3 Radiance to Brightness

The radiance value was converted to brightness value. Brightness value ( $\tau$ ) is the sum of two characters, where the first one is a variable and the second is a constant

with a value 1. The denominator is the logarithmic value of  $(\frac{K_1}{T})$  multiplied by Spectral Radiance of satellite sensor's aperture ( $L_\lambda$ ), where  $K_1$  is the calibration constant 1 and  $T$  is the effective temperature of surface reflectance (Robson et al. 2015; Kaser et al. 2006).

The above can be shown in equation (7):

$$\tau = K_2 / \ln(K_1/T)L_\lambda + 1 \quad (7)$$

## 2.4 Indices

Two indicators, namely Normalized Difference Vegetation Index (NDVI) and NDSI, were derived to examine the relationship between biophysical characteristics of snow and vegetation. The technique of rationing bands involves dividing the spectral response value of a pixel in one band with the spectral value of the corresponding pixel in another band.

### 2.4.1 Normalized Difference Vegetation Index

NDVI is a measure of monitoring changes in vegetation. It gives the assessment of the healthy vegetation cover. Chlorophyll is naturally present in trees and it is a natural sign of vegetation. NDVI is primarily analyzed for predicting vegetation cover. The higher values of NDVI confine a larger dissimilarity in Red and NIR band where low NDVI value indicates less chlorophyll content in the vegetation. Water is also very less reflecting to NIR but less absorption to Red band. So NDVI provides details information of vegetation cover and water chlorophyll activity. The earliest reported use of NDVI in the Great Plains was a study by Rouse et al. 1974 (Table 2).

$$(NDVI = (NIR_{\text{reflectance}} - RED_{\text{reflectance}}) / (NIR_{\text{reflectance}} + RED_{\text{reflectance}})) \quad (8)$$

**Table 2** Threshold value for NDVI-based classification

| NDVI-based classification | Value of threshold |
|---------------------------|--------------------|
| Bare area                 | <0.1               |
| Soil                      | 0.1–0.2            |
| Grass and scrubs          | 0.2–0.3            |
| Vegetation                | >0.3               |



**Table 3** Threshold value for NDSI-based classification

| NDSI-based classification | Threshold Value |
|---------------------------|-----------------|
| Water body, barren land   | <0.4            |
| Granular snow             | 0.4–0.5         |
| Moderate snow             | 0.5–0.6         |
| Clean snow                | >0.6            |

### 2.4.2 Normalized Difference Snow Index

NDSI is effective in mapping snow and non-snow cover area using the reflectance values of snow. Normally, snow shows very high reflectance in visible regions and appears white, while in *SWIR* regions, it has very low reflectance and generally appears black. The algorithm (9) uses *SWIR* and Green band for evaluating *NDSI*. Hall et al. (2001) developed *NDSI*.

$$NDSI = (Green_{\text{reflectance}} - SWIR_{\text{reflectance}} / Green_{\text{reflectance}} + SWIR_{\text{reflectance}}) \quad (9)$$

*NDSI* is a useful index for discriminating snow and clouds as clouds show even higher reflectance in the *SWIR* region. *NDSI* values also have been used to identify snow or non-snow pixels under mountain shadow regions to some extent. Threshold values used for classifying snow are listed below (Table 3).

## 3 Results and Discussion

The glacier area of Uttarakhand is rapidly changing due to different atmospheric phenomena. Mountain systems have recently attracted unprecedented global attention because of vulnerabilities highlighted by receding glacier and growing glacial lakes, which are indicators of climate change. Climate change is producing greater temperature changes at higher altitudes, and most glaciers in the Uttarakhand region are shrinking and retreating rapidly.

### 3.1 Spectral Curve

As shown in Fig. 2, the reflectance value of snow under visible band is higher than other wavelengths because visible band reflect more radiation under snow and barren land. Reflectance value of vegetation is high under visible (R) and NIR (0.6–1.5) band because chlorophyll strongly absorbs energy.

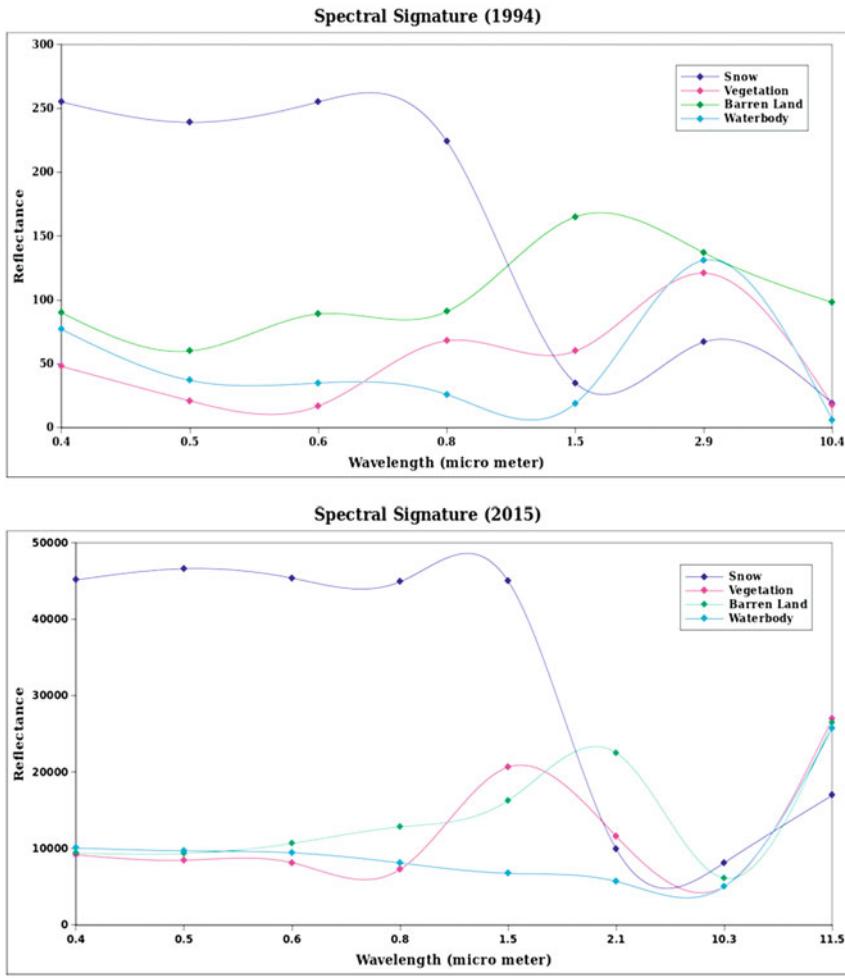


Fig. 2 Spectral curve of snow, vegetation, barren land, and water body

In 2015 image, spectral reflectance of vegetation increases from 0.8 (NIR) due to the forest fire in some of this region, which suppressed the properties of vegetation (such as chlorophyll and water content in leaves).

### 3.2 Histogram

Histogram of Landsat imagery shows the number of pixels at a certain DN value. We obtained four major peaks from the histogram (Fig.3) of two Landsat data (1994 and

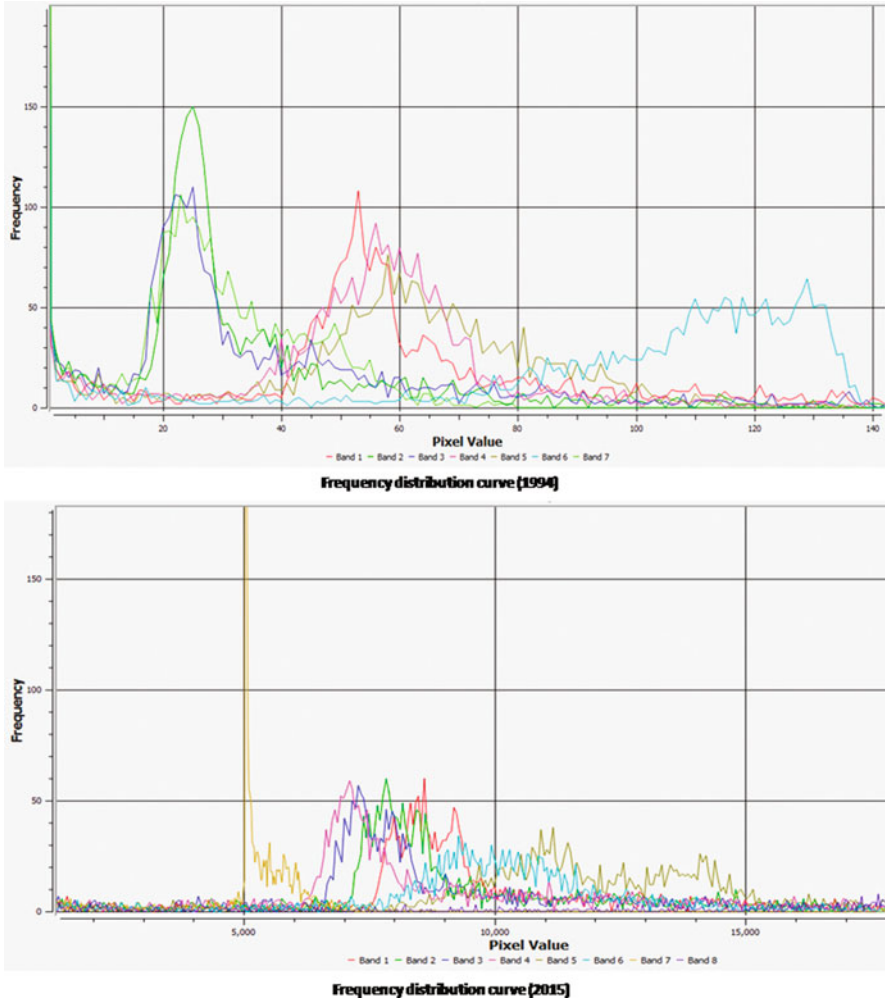


Fig. 3 Frequency Distribution Curve of 1994 and 2015 data

2015). These histograms helped us in image interpretation and image classification for choosing possible classes. After visual interpretation, we identified four major classes: snow, vegetation, barren land, and other land.

### 3.3 Normalized Difference Vegetation Index

NDVI values varied from  $-0.600231$  to  $0.748215$ , with a standard deviation and mean of  $0.17$  and  $0.11$ , respectively (Fig. 4). Almost 97% NDVI values were

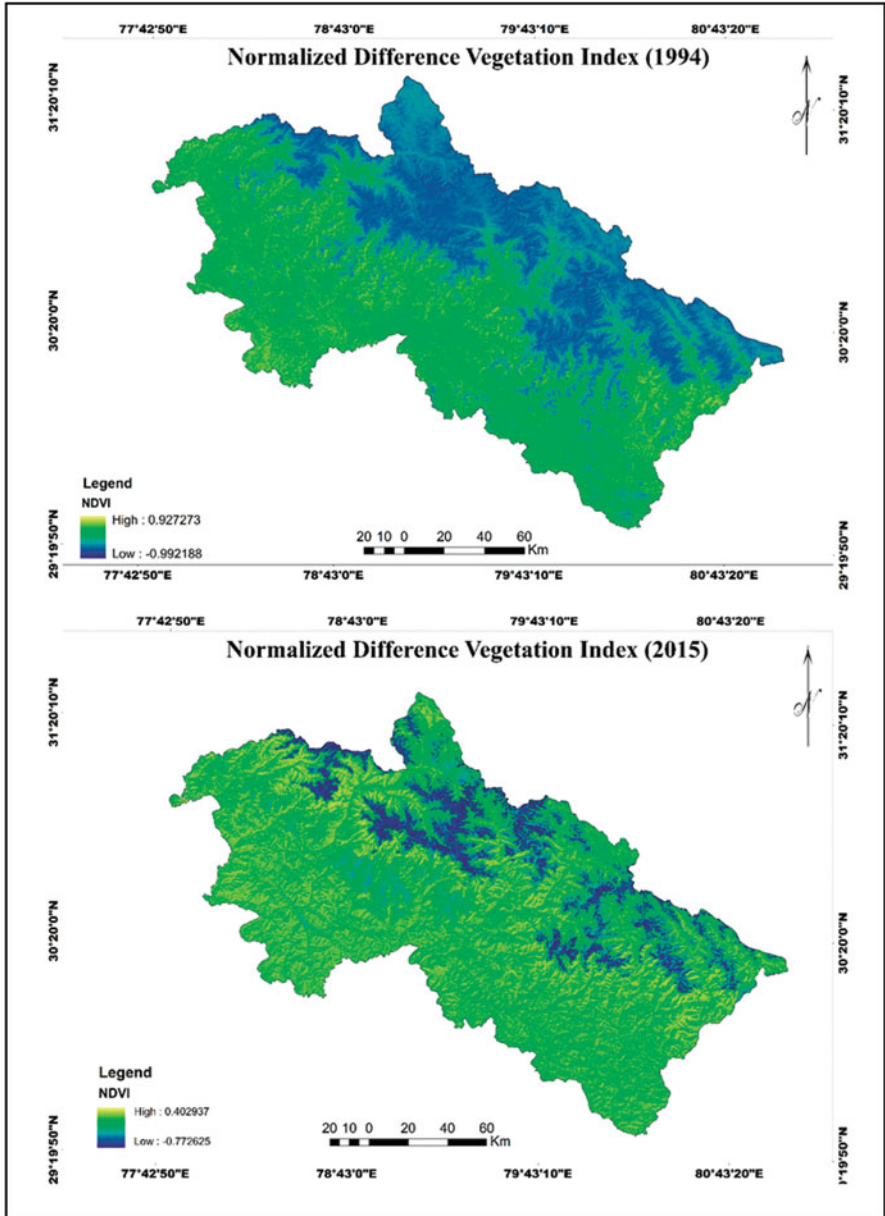


Fig. 4 Color-coded Normalized Difference Vegetation Index

positive (closer to +1), which indicated healthy vegetation in STR. The central part of the study area was dotted with healthy vegetation. To determine the density of greenness on a patch of land, it is important to observe the distinct colors of visible and near-infrared sunlight by plants. If the reflectance of light in near-infrared

**Table 4** Threshold value for timber-covered area

| Year                   | 1994                  | 2015                  |
|------------------------|-----------------------|-----------------------|
| Range (NDVI)           | -0.600231 to 0.748215 | -0.470545 to 0.764391 |
| Threshold value (NDVI) | 0.5155                | 0.62                  |

wavelength is more than that in the visible wavelength, vegetation in that pixel is likely to be dense. Light green areas show dense vegetation and dark blue areas show less/no vegetation (such as barren land, soil, water body, etc.).

We used threshold values to reclassify NDVI image, which is given below (Table 4).

The resulted forest cover for 1994 was 10,558 km<sup>2</sup>. Here, the area is calculated by multiplying the total histogram value under the threshold value. Similarly, the forest cover for 2015 was 11454 km<sup>2</sup> after applying the threshold 0.25.

### 3.4 Normalized Difference Snow Index

We cannot delineate glacier and non-glacier (water body, snow, etc.) areas from the resulted NDSI image. NDSI image (Fig. 5) suggests that this index either overestimates the delineation of snow area or underestimates the zone.

In this case, we have applied the threshold values of snow and non-snow area for mapping the glacier region (Table 5).

The snow cover area for 1994 data was 4717.89 km<sup>2</sup>, and for 2015, the area was calculated to be 3340.62 km<sup>2</sup> (Similar to NDVI).

### 3.5 Zonal Change

Changes to snow and vegetation from 1994 to 2015 were monitored. The changes are highlighted (Fig. 6) and stored according to the amount of change detected, making the result highly efficient. After calculation, we observed change in vegetation area as 896 km<sup>2</sup> and change in snow area as 1377.27 km<sup>2</sup> during 21 years.

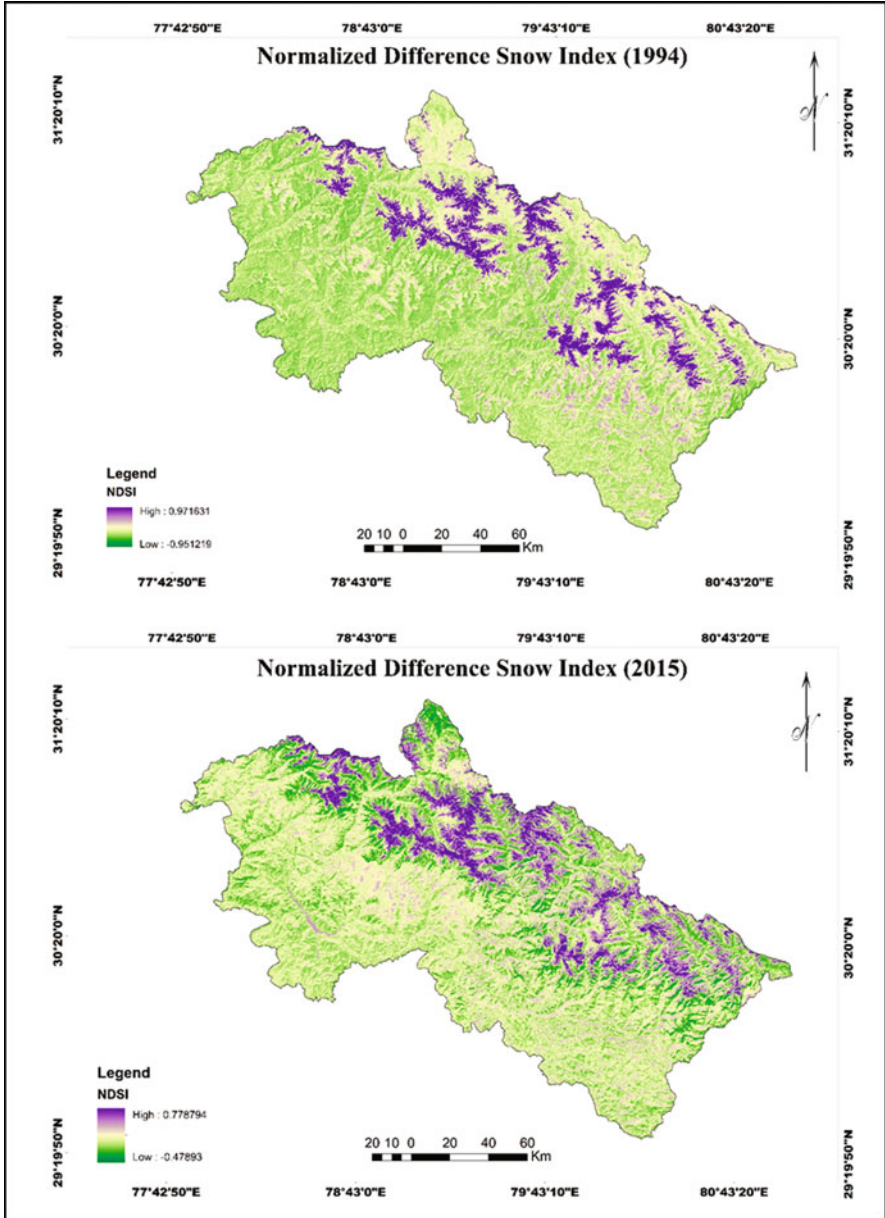
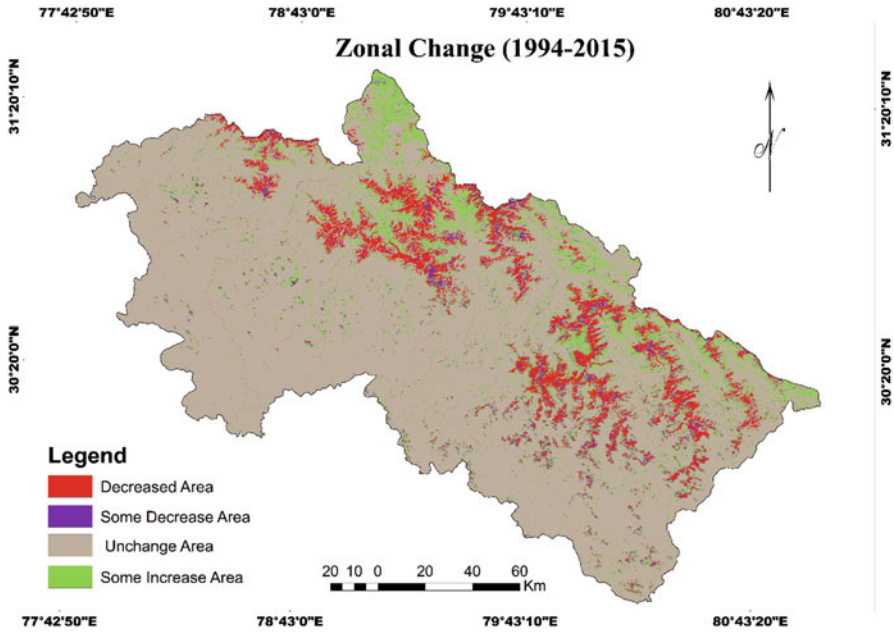


Fig. 5 Color-coded Normalized Difference Snow Index

**Table 5** Threshold value for snow-covered area

| Year                   | 1994                  | 2015                  |
|------------------------|-----------------------|-----------------------|
| Range (NDSI)           | -0.684225 to 0.907898 | -0.470545 to 0.764391 |
| Threshold value (NDSI) | 0.48                  | 0.62                  |



**Fig. 6** Zonal change from 1994 to 2015

### 4 Conclusion

The study was conducted in the Uttarakhand state of Central Himalaya located in the foothill zones of the Kumauni Lesser Himalaya. NDSI and NDVI maps were generated from optical satellite data, which can be used to extract information about snow, vegetation, soil, and other land. NDSI value remains consistent with discrepancies between slope and aspect. We got a drastic change in vegetation area (1994–2015) of 896 km<sup>2</sup> and change in snow area of 1377.27 km<sup>2</sup>. This study indicates that the atmosphere in the Himalayas has undergone significant changes since 1994. Vegetation ingress was noticed in higher altitudes that were previously under snow and ice. The results clearly show that the glacier area in the Uttarakhand region is decreasing at a rapid rate and that individual glaciers are shrinking, retreating, and fragmenting. This paper uses a technique based on NDVI

and NDSI, which help us obtain information about the vegetation in visible and NIR band reflectance and about snow in Green and SWIR band reflectance in the Uttarakhand glacier region, which consists of rugged terrain, contaminated snow and patchy snow, snow under forest, etc. Therefore, the result of this study demonstrated the potential of optical satellite imagery to map the actual area of Uttarakhand glaciers.

## References

- Andreassen, L. M., Paul, F., Kääb, A., & Hausberg, J. E. (2008). Landsat-derived glacier inventory for Jotunheimen, Norway, and deduced glacier changes since the 1930s. *The Cryosphere*, 2, 131–145.
- Andreassen, L., Huss, M., Melvold, K., Elvehøy, H., & Winsvold, S. (2015). Ice thickness measurements and volume estimates for glaciers in Norway. *Journal of Glaciology*, 61, 763–775.
- Atif, I., Iqbal, J., & Mahboob, M. A. (2016). Modelling semi-automated delineation of supra-glacial debris and clean ice glacial changes of Shigar basin. *Geosciences*, 9, 259.
- Azam, M. F., Wagnon, P., Berthier, E., Vincent, C., Fujita, K., & Kargel, J. S. (2018). Review of the status and mass changes of Himalayan-Karakoram glaciers. *Journal of Glaciology*, 64, 61–74.
- Bajracharya, S. R., Maharjan, S. B., & Shrestha, F. (2014). The status and decadal change of glaciers in Bhutan from the 1980s to 2010 based on satellite data. *Annals of Glaciology*, 55, 159–166.
- Berthier, E., Arnaud, Y., Kumar, R., Ahmad, S., Wagnon, P., & Chevallier, P. (2007). Remote sensing estimates of glacier mass balances in the Himachal Pradesh (Western Himalaya, India). *Remote Sensing of Environment*, 108, 327–338.
- Berthier, E., Schiefer, E., Clarke, G. K. C., Menounos, B., & Rémy, F. (2010). Contribution of Alaskan glaciers to sea-level rise derived from satellite imagery. *Nature Geoscience*, 3, 92–95.
- Bhambri, R., & Bolch, T. (2009). Glacier mapping: A review with special reference to the Indian Himalayas. *Progress in Physical Geography*, 33, 672–704.
- Bhambri, R., Bolch, T., & Chaujar, R. K. (2012). Frontal recession of Gangotri Glacier, Garhwal Himalayas, from 1965 to 2006, measured through high resolution remote sensing data. *Current Science*, 00113891, 102.
- Bhutiyan, M. R. (2016). Spatial and temporal variability of climate change in high-altitude regions of NW Himalaya. In R. B. Singh, U. Schickhoff, & S. Mal (Eds.), *Climate change, glacier response, and vegetation dynamics in the Himalaya* (pp. 87–101). Cham: Springer.
- Bolch, T., Buchroithner, M. F., Kunert, A., & Kamp, U. (2007, June). Automated delineation of debris-covered glaciers based on ASTER data. In Geoinformation in Europe. *Proceedings of the 27th EARSeL Symposium*, pp. 4–6.
- Bolch, T., Shea, J. M., Liu, S., Azam, F. M., Gao, Y., Gruber, S., et al. (2019). Status and Change of the Cryosphere in the Extended Hindu Kush Himalaya Region. In P. Wester, A. Mishra, A. Mukherji, & A. B. Shrestha (Eds.), *The Hindu Kush Himalaya Assessment* (pp. 209–255). Cham: Springer.
- Csatho, B., Schenk, T., Lee, D., & Filin, S. (1999). Inclusion of multispectral data into object recognition. *International Archives of Photogrammetry and Remote Sensing*, 32, 53–61.
- Dedieu, J-P., Mathieu, J., Besic, N., Durand, Y., & Gottardi, F. (2013). Dry snow analysis in Alpine regions using RADARSAT-2 full polarimetry data. Comparison with in situ measurements. *International Geoscience and Remote Sensing Symposium (IGARSS)*, 1558.
- Deota, B. S., Trivedi, Y. N., Kulkarni, A. V., Bahuguna, I. M., & Rathore, B. P. (2011). RS and GIS in mapping of geomorphic records and understanding the local controls of glacial retreat from the Baspa Valley, Himachal Pradesh, India. *Current Science*, 100, 1555–1563.



- Dyurgerov, B. M., & Meier, M. F. (1997). Mass balance of mountain and subpolar glaciers: A new global assessment for 1961–1990. *Arctic and Alpine Research*, 29(4), 379–391.
- Fallourd, R., Harant, O., Trouvé, E., Nicolas, J.-M., Gay, M., Walpersdorf, A., Mugnier, J.-L., Serafini, J., Rosu, D., Bombrun, L., et al. (2011). Monitoring temperate glacier movement by multi-temporal TerraSAR-X images and continuous GPS measurements. *IEEE Journal of Selected Topics in Applied Earth Observations and Remote Sensing*, 4, 372–386.
- Gao, Y., Mas, J., Niemeyer, I., Marpu, P., & Palacio, J. (2007). Object-based image analysis for mapping land-cover in a forest area.
- Giesen, R. H., & Oerlemans, J. (2013). Climate-model induced differences in the 21st century global and regional glacier contributions to sea-level rise. *Climate Dynamics*, 7, 3283–3300.
- Hall, D. K., Ormsby, J. P., Bindschadler, R. A., & Siddalingaiah, H. (1987). Characterization of snow and ice reflectance zones on glaciers using Landsat thematic mapper data. *Annals of Glaciology*, 9, 104–108.
- Hall, D. K., Riggs, G. A., Salomonson, V. V., Barton, J. S., Casey, K. L., Chien, N. E., DiGirolamo, A. G., Klein, H., Powell, W., & Tait, A. B. (2001). Algorithm theoretical basis document (ATBD) for the MODIS snow and sea ice-mapping algorithms. *viewed*, (3 October 2013).
- Hall, D. K., Riggs, G. A., Salomonson, V. V., DiGirolanno, N. E., & Bayr, K. J. (2002). MODIS snow-cover products. *Remote Sensing of Environment*, 83, 181–194.
- Haq, M. A., & Jain, K. (2012). Development of New Thermal Ratio Index for Snow/Ice Identification. *International Journal of Soft Computing and Engineering (IJSCE)*, 1, 282.
- Haritashya, U. K., Singh, P., Kumar, N., & Gupta, R. P. (2006). Suspended sediment from Gangotri glacier: Quantification, variability and associations with discharge and air temperature. *Journal of Hydrology*, 321, 116–130.
- Hock, R. (2014). Glaciers and climate change, in global environmental change. *New york, ny, usa: springer*, 205–210.
- Huang, L., & Li, Z. (2011). Comparison of SAR and optical data in deriving glacier velocity with feature tracking. *International Journal of Remote Sensing*, 32, 2681–2698.
- Huss, M., Bookhagen, B., Huggel, C., Jacobsen, D., Bradley, R. S., Clague, J. J., Vuille, M., Buytaert, W., Cayan, D. R., Greenwood, G., et al. (2017). Toward mountains without permanent snow and ice: Mountains without permanent snow and ice. *Earth's Future*, 5, 418–435.
- Kääb, A., Treichler, D., Nuth, C., & Berthier, E. (2015). Brief communication: Contending estimates of 2003–2008 glacier mass balance over the Pamir-Karakoram-Himalaya. *The Cryosphere*, 9, 557–564.
- Karimi, N., Farokhnia, A., Karimi, L., Eftekhari, M., & Ghalkhani, H. (2012a). Combining optical and thermal remote sensing data for mapping debris-covered glaciers (Alamkouh Glaciers, Iran). *Cold Regions Science and Technology*, 71, 73–83.
- Karimi, N., Farokhnia, A., Shishangosht, S., Elmi, M., Eftekhari, M., & Ghalkhani, H. (2012b). Elevation changes of Alamkouh glacier in Iran since 1955, based on remote sensing data. *Int. J. Appl. Earth Obs. Geoinformation*, 19, 45–58.
- Kaser, G., Cogley, G. J., Dyurgerov, B. M., Meier, F., & Ohmura, A. (2006). Mass balance of glaciers and ice caps: Consensus estimates for 1961–2004. *Geophysical Research Letters*, 33(1), 19501.
- Khopkar, P., Jawak, S., Jadhav, S., & Luis, A. (2013). Customization of normalized difference snow index for extraction of snow and/or ice cover from cryospheric surface using worldview-2 data.
- Klein, A. G., & Barnett, A. C. (2003). Validation of daily MODIS snow cover maps of the upper Rio Grande River basin for the 2000–2001 snow year. *Remote Sensing of Environment*, 86(2), 162–176.
- Kulkarni, A. V., & Karyakarte, Y. (2014). Observed changes in Himalayan glaciers. *Current Science*, 106, 237–244.
- Kumar, K., Dumka, R.K., Miral, M.S., Satyal, G.S. and Pant, M. (2008). Estimation of retreat rate of Gangotri glacier using rapid static and kinematic GPS survey *Current Science*, 94, 2.

- Kumar, K., Miral, M. S., Snehjoshi, N. P., & VarunJoshi, L. M. J. (2009). Solute dynamics of meltwater of Gangotri glacier, Garhwal Himalaya, India. *Environmental Geology*, *58*, 1151–1159.
- Liang, T., Zhang, X., Xie, H., Wu, C., Feng, Q., Huang, X., & Chen, Q. (2008). Toward improved daily snow cover mapping with advanced combination of MODIS and AMSR-E measurements. *Remote Sensing of Environment*, *112*(10), 3750–3761.
- Linsbauer, A., Paul, F., & Haeberli, W. (2012). Modeling glacier thickness distribution and bed topography over entire mountain ranges with GlabTop: Application of a fast and robust approach. *Journal of Geophysical Research*, *117*.
- Lu, S., Oki, K., & Omasa, K. (2005). Mapping snow cover using AVHRR/NDVI 10-day composite data. *Journal of Agricultural Meteorology*, *60*(6), 1215–1218.
- Marzeion, B., Champollion, N., Haeberli, W., Langley, K., Leclercq, P., & Paul, F. (2017). Observation-based estimates of global glacier mass change and its contribution to sea-level change. *Surveys in Geophysics*, *38*, 105–130.
- Nainwal, H. C., Banerjee, A., Shankar, R., Semwal, P., & Sharma, T. (2016). Shrinkage of Satopanth and BhagirathKharak glaciers, India, from 1936 to 2013. *Annals of Glaciology*, *57*, 131–139.
- Pandey, A. C., Ghosh, S., & Nathawat, M. S. (2011). Evaluating patterns of temporal glacier changes in Greater Himalayan range, Jammu and Kashmir, India. *Geocarto International*, *26*, 321–338.
- Parajka, J., & Blöschl, G. (2008). Spatio-temporal combination of MODIS images—potential for snow cover mapping. *Water Resources Research*, *44*(3).
- Parrot, J. F., et al. (1993). SPOT multispectral data and digital terrainmodel for the analysis of ice-snow fields on Antarctic glaciers. *International Journal of Remote Sensing*, *14*(3), 425–440.
- Paul, F., & Kääb, A. (2005). Perspectives on the production of a glacier inventory from multispectral satellite data in Arctic Canada: Cumberland Peninsula, Baffin Island. *Annals of Glaciology*, *42*, 59–66.
- Paul, F., & Linsbauer, A. (2012). Modeling of glacier bed topography from glacier outlines, central branch lines, and a DEM. *International Journal of Geographical Information Science*, *26*, 1173–1190.
- Paul, F., Barrand, N. E., Baumann, S., Berthier, E., Bolch, T., Casey, K., et al. (2013). On the accuracy of glacier outlines derived from remote-sensing data. *Annals of Glaciology*, *54*(63), 171–182.
- Racoviteanu, A. E., Paul, F., Raup, B., Khalsa, S. J. S., & Armstrong, R. (2009). Challenges and recommendations in mapping of glacier parameters from space: Results of the 2008 global land ice measurements from space (GLIMS) workshop, Boulder, Colorado, USA. *Annals of Glaciology*, *50*(53), 53–69.
- Raina, V. K. (2004). Is the Gangotri glacier receding at an alarming rate? *Journal of Geological Society of India*, *64*, 819–821.
- Raina, V. K. (2010). *MoEF discussion paper: Himalayan glaciers – A state-of-art review of glacial studies, glacial retreat and climate change*. Almora: Ministry of Environment and Forests and GB Pant Institute of Himalayan Environment and Development.
- Raina, K. V., & Srivastava, D. (2008). *Glacier atlas of India*. Bangalore: Geological Society of India.
- Raj, G., & Babu, K. (2011). Recession and reconstruction of Milam glacier, Kumaon Himalaya, observed with satellite imagery. *Current Science* *100*(9), (00113891).
- Rastner, P., Bolch, T., Notarnicola, C., & Paul, F. (2013). A comparison of pixel- and object-based glacier classification with optical satellite images. *IEEE Journal of Selected Topics in Applied Earth Observations and Remote Sensing*, *7*(3), 853–862.
- Rastner, P., Bolch, T., Totarnicola, C., & Paul, F. (2014). A comparison of pixel- and object-based glacier classification with optical satellite images. *IEEE Journal of Selected Topics in Applied Earth Observations and Remote Sensing*, *7*, 853–862.

- Ratan Kar, P.S. Ranhotra, , Bhattacharyya, A. and Sekar, B. (2002): Vegetation vis-à-vis climate and glacial fluctuation of the Gangotri glacier since 2000 years. *Current Science*, 82, 347–351.
- Robson, B. A., Nuth, C., Dahl, S. O., Hölbling, D., Strozzi, T., & Nielsen, P. R. (2015). Automated classification of debris-covered glaciers combining optical, SAR and topographic data in an object-based environment. *Remote Sensing of Environment*, 170, 372–387.
- Rouse JW, Hass RH, Schell JA, Deering DW (1974) Monitoring vegetation system in the great plains in the ERTS 309-317.
- Sagredo, E. A., & Lowell, T. V. (2012). Climatology of Andean glaciers: A framework to understand glacier response to climate change. *Global and Planetary Change*, 86, 101–109.
- Schickhoff, U., Singh, R. B., & Mal, S. (2016). Climate change and dynamics of glaciers and vegetation in the Himalaya: an overview. In R. B. Singh, U. Schickhoff, & S. Mal (Eds.), *Climate change, glacier response, and vegetation dynamics in the Himalaya* (pp. 1–26). Cham: Springer.
- Shukla, A., & Qadir, J. (2016). Differential response of glaciers with varying debris cover extent: Evidence from changing glacier parameters. *International Journal of Remote Sensing*, 37, 2453–2479.
- Sibandze, P., Mhangara, P., Odindi, J., & Kganyago, M. (2014). A Comparison of Normalised Difference Snow Index (NDSI) and Normalised Difference Principal Component Snow Index ( NDPCSI) techniques in distinguishing snow from related cover types. *South African Journal of Geomatics*, 3, 197–209.
- Sidjak, R. W. (1999). Glacier mapping of the Illecillewaet ice field, British Columbia, Canada, using Landsat TM and digital elevation data. *International Journal of Remote Sensing*, 20(2), 273–284.
- Sidjak, R. W., & Wheate, R. D. (1999). Glacier mapping of the Illecillewaet icefield, British Columbia, using Landsat TM and digital elevation data. *International Journal of Remote Sensing*, 20(2), 273–284.
- Singh, P., Haritashya, U. K., & Kumar, N. (2008). Modelling and estimation of different components of stream flow for Gangotri glacier basin Himalayas. *Hydrological Sciences Journal*, 53, 309–322.
- Smith, T., Bookhagen, B., & Cannon, F. (2015). Improving semi-automated glacier mapping with a multi-method approach: Applications in central Asia. *Cryosphere*, 9(5), 1747–1759.
- Strozzi, T., Luckman, A., Murray, T., Wegmuller, U., & Werner, C. L. (2002). Glacier motion estimation using SAR offset-tracking procedures. *IEEE Transactions on Geoscience and Remote Sensing*, 40, 2384–2391.
- Tong, J., & Velicogna, I. (2010). A comparison of AMSR-E/aqua snow products with in situ observations and MODIS snow cover products in the Mackenzie River basin, Canada. *Remote Sensing*, 2, 2313–2322.
- Venkatesh, T. N., Kulkarni, A. V., & Srinivasan, J. (2013). Relative effect of slope and equilibrium line altitude on the retreat of Himalayan glaciers. *The Cryosphere*, 6, 301–311.
- Walker, D. A., Halfpenny, J. C., Walker, M. D., & Wessman, C. A. (1993). Long-term studies of snow-vegetation interactions. *Bioscience*, 43(5), 287–301.
- Zemp, M., Hoelzle, M., & Haeberli, W. (2009). Six decades of glacier mass-balance observations: A review of the worldwide monitoring network. *Annals of Glaciology*, 50, 101–111.
- Zemp, M., Frey, H., Gärtner-Roer, I., Nussbaumer, S. U., Hoelzle, M., Paul, F., Haeberli, W., Denzinger, F., Ahlström, A. P., Anderson, B., et al. (2015). Historically unprecedented global glacier decline in the early 21st century. *Journal of Glaciology*, 61, 745–762.

**Part III**  
**Remote Sensing and GIScience in Urban**  
**Growth Management**

# Studying the Impact of Urbanization on HYV Rice Fields at a Local Level Using Fine Resolution Temporal RISAT-1 Datasets



Koel Roychowdhury

**Abstract** In 1950, there were around 740 million people living in urban areas, which was predicted to increase to more than 2.5 billion by 2050. One of the most pressing challenges of rapid urbanization lies in providing adequate food to inhabitants. The current research estimates the high-yielding variety of rice fields vulnerable to conversion to non-farm uses around sprawling urban settlements. Rice fields were delineated by polarimetric decomposition on RISAT-1 (FRS-1) datasets. Overlapping the rice fields on hotspot zones, classified using Getis-Ord G statistic, it was observed that 40% of hotspots are rice fields. More fields are vulnerable around municipalities than those around newly declared census towns. Also, rice fields around densely populated settlements are more prone to conversion (more than 50% of hotspots are rice fields) than those around less populated ones (around 35.5%). The research successfully proposes a method to identify areas in need of special attention to prevent unplanned urban expansion negatively affecting rice production and leading to a lack of food security in the region.

**Keywords** RISAT-1 · polarimetry · hot spot analysis · rice · urbanization · conversion of land

## 1 Introduction

Rice is the most important staple food for more than half of the global population, 90% of which are produced in Asia (Hellerstein and Vilorio 2019). India is the second largest producer of rice (Farmers' Portal 2015). After the green revolution during 1960s, high-yielding variety (HYV) seeds were introduced in Indian agriculture (International Rice Research Institute 2014). Use of these varieties not only resulted in higher yields, they produced crops all-round the year with the help of

---

K. Roychowdhury (✉)

Department of Geography, Presidency University, Kolkata, West Bengal, India  
e-mail: [koel.geog@presiuniv.ac.in](mailto:koel.geog@presiuniv.ac.in)

mechanization and irrigation. However, large portions of agricultural lands have become unusable in developed and developing countries under the adverse influence of natural factors including climate change, soil erosion, and salinization (Amundson et al. 2015), especially man-made factors such as urbanization (Martellozzo et al. 2015; Pandey and Seto 2015; Skog and Steinnes 2016; Achhami Abhusan et al. 2019). The impact of settlement expansion on agricultural lands has been widely mapped and monitored using earth observation techniques (Pandey and Seto 2015; Su et al. 2011; Zhong et al. 2014). Images captured by Landsat (Nong et al. 2015; Tang and Di 2019) and MODIS (Pandey et al. 2013) were used to study settlement growth processes and their impacts on farmlands at regional scales. Census data along with night-time light images helped in identifying the effects of urbanization on agricultural lands in India (Gibson et al. 2015; Pandey and Seto 2015). Most recent studies have reported the fragmentation of agricultural lands due to increased urban sprawl (Li et al. 2019a, b; Oueslati et al. 2019). However, not much information on the types of crops affected by urban expansion has been available in previous studies. The aim of this paper is to identify areas under HYV rice cultivation, which are vulnerable to conversion due to expansion of neighboring settlements at a local scale.

## 2 Material and Methodology

### 2.1 Study Area

The research was conducted in the lower alluvial plains of the Bhagirathi Hoogly River (Fig. 1). It extends from 88.16° E, 22.96° N to 88.13° E, 22.37° N covering an area of 93,090 hectares. The area stretches over parts of the districts of Haora, Hugli, and South 24 Parganas of West Bengal in eastern India. Rice is the most dominant food crop of West Bengal, covering more than 70% of the cropped area of the state (Planning Commission 2010). Three varieties of rice are grown in this region: *Aus*, *Aman*, and *Boro*. *Boro* rice is a HYV of rice. It is grown between November and May. This type of rice is cultivated in low-lying areas and requires irrigation for additional supply of water. The district of Haora is one of the largest rice-producing districts of West Bengal, while Hugli and South 24 Parganas are medium producers of rice (Planning Commission, 2010). There are two municipalities (Pujali and Maheshtala) with a total population of more than 30,000 persons and nine census towns (Jagatballavpur, Mansinhapur, Kesabpur, Ramchandrapur, Mallik Bagan, Panchla, Tehatta, Raghudebpur, and Shyampur) with a total population of more than 5000 persons in the study area.

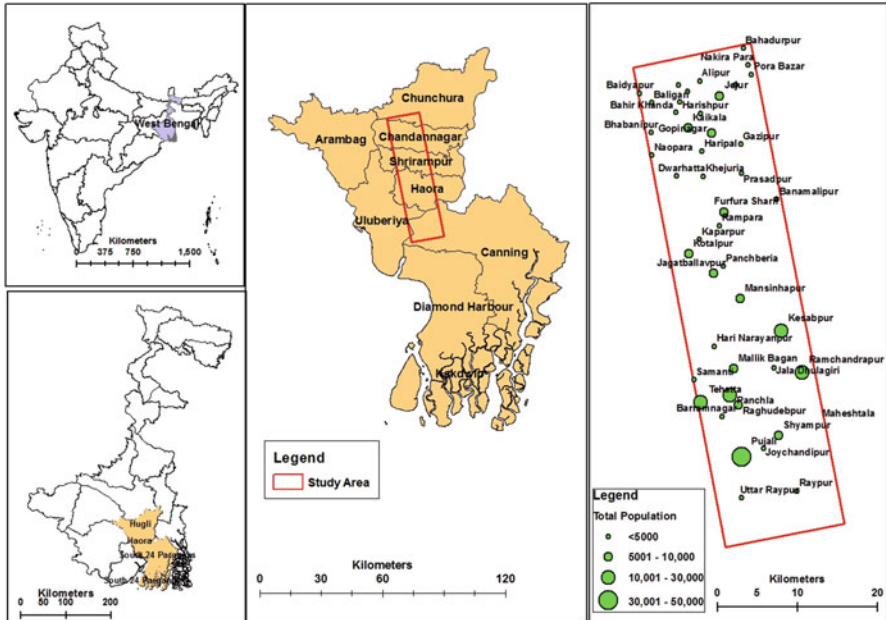


Fig. 1 Study area (a) India; (b) West Bengal; (c) Selected taluks with the case study

## 2.2 Data Used

Since 1990s, microwave remote sensing data have been introduced in rice crop mapping. Images acquired by ERS 1 (Kurosu et al. 1997) and 2 (Liew et al. 1998), RADARSAT 1 and 2 (Choudhury and Chakraborty 2006; Shao et al. 2001), ENVISAT ASAR (Chen et al. 2007), ALOS PALSAR (Zhang et al. 2009), and Sentinel 1 data (Dimov et al. 2016; Guccione et al. 2014; Nguyen et al. 2016; Torbick et al. 2017) have mostly been used for these studies. Since 2012, RISAT-1 hybrid polarimetric data (Halder and Gopalan 2017; Sivasankar et al. 2015a; Uppala et al. 2015) have also proved useful for identification of rice fields in India. Analyses of temporal backscatter during the growing season and polarimetric decomposition of radar images are useful for paddy identification.

This paper uses temporal fine resolution Single Look Complex hybrid polarimetric Radar Imaging Satellite-1 (RISAT-1) data for delineating areas under HYV rice cultivation. Fine Resolution Stripmap Mode-1 (FRS-1) data were used to identify HYV rice fields. FRS-1 data has a swath of 25 km and a 3-m resolution (Kramer 2002). The images are recorded in C-Band of the electromagnetic spectrum with a frequency of 5.44 GHz. A hybrid SAR transmits at circular polarizations and receives at horizontal and vertical polarizations (RH and RV). It is a special case of compact dual-polarization mode. The data used in this research were obtained for the months of December and February. This is the peak HYV rice-growing season in

**Table 1** Specifications of RISAT-1 data used

| Product ID  | Incidence Angle | Polarization           | Node      | Sensor Orientation | Date of Capture |
|-------------|-----------------|------------------------|-----------|--------------------|-----------------|
| 172,805,031 | 32.18           | RH and RV <sup>a</sup> | Ascending | Left               | 24/2/2016       |
| 172,805,041 | 32.17           |                        |           |                    | 11/12/2015      |
| 172,805,071 | 33.72           |                        |           |                    |                 |
| 172,585,081 | 33.72           |                        |           |                    |                 |

<sup>a</sup>RH: Right hand circular polarization, horizontal; RV: Right hand circular polarization, vertical

the region. The details of the RISAT 1 datasets used for the study are presented in Table 1.

To identify rice fields, the overlapping areas of the images were considered for analyses in this study. In the overlapping region, all the parameters associated with identifying the various stages of growth of paddy plants were identifiable for the months of December and February, which helped in proper delineation of the fields. Landsat 8 data collected during the month of December 2015 was used to delineate the extents of settlements in the study area.

## 2.3 Methodology

The method undertaken in this research is broadly divided into three categories including the Processing of RISAT-1 data and identification of rice fields, Processing of Landsat datasets for delineating settlements in the study area, and hotspot analyses for demarcating the most vulnerable rice fields.

### 2.3.1 Processing of RISAT-1 Data

Rice fields were extracted from the RISAT 1 images by means of polarimetric decomposition. The fields were delineated by performing  $m$ - $\delta$  decomposition or Raney decomposition on the images. This method was proposed by Raney (Raney 2006). Raney decomposition method requires Stokes' parameters and Stokes' child parameters as inputs. Stokes' parameters were calculated for all images. These included a set of values that characterize the polarization state of the backscatter signal from two coherent mutually perpendicular receiving signals (Sivasankar et al. 2015b). They were calculated using the formula below:



$$\begin{bmatrix} S_0 \\ S_1 \\ S_2 \\ S_3 \end{bmatrix} = \begin{bmatrix} \langle |E_{RH}|^2 + |E_{RV}|^2 \rangle \\ \langle |E_{RH}|^2 - |E_{RV}|^2 \rangle \\ 2 \operatorname{Re} \langle E_{RH} E_{RV}^* \rangle \\ -2 \operatorname{Im} \langle E_{RH} E_{RV}^* \rangle \end{bmatrix} \tag{1}$$

In each case,  $E_{RH}$  represents complex voltage received by the channel with right-circular transmit and horizontal receive,  $E_{RV}$  represents complex voltage received by the channel of right-circular transmit and vertical polarization receive, \* indicates complex conjugate,  $\langle \dots \rangle$  denotes ensemble average, and Re and Im represent the real or the imaginary value (respectively) of the complex image.

Stokes' child parameters such as degree of polarization, degree of circularity, and relative phase were calculated for this study. They were obtained using the formulas below:

$$m = \frac{\sqrt{s_1^2 + s_2^2 + s_3^2}}{s_0} \quad 0 \leq m \leq 1 \tag{2}$$

$$\delta = \tan^{-1} \left( \frac{s_3}{s_2} \right) \quad -180^\circ \leq \delta \leq 180^\circ \tag{3}$$

$$\sin 2\chi = \frac{-s_3}{ms_0} \tag{4}$$

Stokes' parameters and child parameters were then used for performing  $m$ - $\delta$  decomposition on the images. In this process, the total intensity is first partitioned into completely polarized and un-polarized parts using degree of polarization ( $m$ ). The un-polarized part is considered as volume component and the polarized part is again divided into even and odd bounce component using  $\delta$ . The following are the equations used to estimate the scattering decompositions:

$$f_{\text{odd}} = \sqrt{s_0 X m X \frac{(1 + \sin \delta)}{2}} \tag{5}$$

$$f_{\text{even}} = \sqrt{s_0 X m X \frac{(1 - \sin \delta)}{2}} \tag{6}$$

$$f_{\text{volume}} = \sqrt{s_0 X (1 - m)} \tag{7}$$

In the next step, degree of polarization ( $m$ ); degree of circularity ( $\chi$ ), and relative phase ( $\delta$ ) images for all the months were layer stacked and passed through red, green, and blue channels, respectively. Similar composite images were also created using volume, odd, and double bounce scattering information. A K-means clustering method (Lillesand et al. 2015) was used to identify the various classes from the layer stacked images. Forty clusters were calculated initially with a convergence threshold

of 0.99. The clusters were grouped to four classes, namely rice, other agriculture, settlements, and water bodies. The classification was evaluated using 100 ground control points distributed over the study area. Measures of classification accuracy including overall accuracy, omission, and commission errors were derived using confusion matrices.

### 2.3.2 Processing of Optical Images

In order to identify the nature of settlement expansion in the area, Landsat image captured in December 2015 over the study area was analyzed. The image was classified using the minimum-distance-to-mean method (Lillesand et al. 2015). In this method, the average spectral value in each band is calculated, which comprises the mean vector for each class. Unknown pixels are classified by computing the distance between its value and the mean of each category. Training sample datasets were created. The images were then classified using these training samples. The images were classified into three classes: settlements, agricultural lands, and water bodies (including river and canals). Settlements were extracted from the image for further investigations. The accuracies of the classification for the respective images were tested on 100 random points from Google Earth application.

### 2.3.3 Hotspot Analyses

Hotspot analysis was conducted on the classified Landsat image of 2015. Areas at greatest risk of conversion were identified with the help of this process (Getis and Ord 1992). A nearest neighbor hierarchical clustering method is used in this analysis to identify spatial clusters. These clusters are statistically significant and represent areas of high values (hot spots) and low values (cold spots). The resultant Z scores and p-values represent the areas where features with either high or low values cluster spatially (Qiu et al. 2015). The method of 'fixed distance' was used to define neighbors. Hotspots at threshold values of 250 m were modeled (approximately the distance between two settlements in the area). The impacts of expansion of built-up areas on nearby HYV rice fields were examined up to a distance of 2 km from each settlement. A buffer zone was delineated at a distance of 2 km from each settlement center. Beyond 2 km, the buffer zones of adjacent settlements were intersecting with each other. In order to estimate the impact of individual settlement on its neighboring rice fields, only hotspots within the 2-km buffer zones were considered.

### 3 Results and Discussion

#### 3.1 Identification of Rice Fields from Polarimetric Decomposition

Figures 2a, b show the fields as obtained from layer stacking of m, chi ( $\chi$ ), and delta ( $\delta$ ) images. Volume, odd, and double bounce scattering images were also layer stacked (Fig. 2c, d). The rice fields appear as green patches (Fig. 2a, b) and blue patches (Fig. 2c, d) distributed over the study area. The fields are conspicuously identifiable, especially in the month of February, when the Rabi plants are in the mature stage. In the initial stages of growth, the degrees of polarization over rice

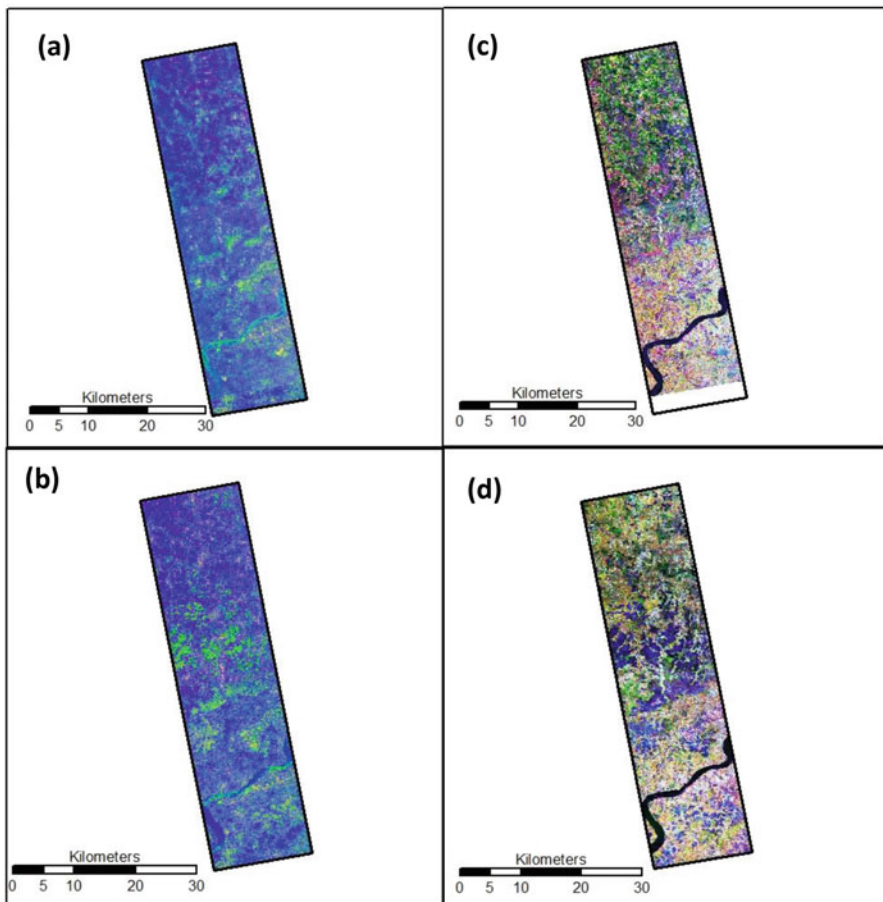


**Fig. 2** Rice fields as identified in the study area from: (a) m-chi-delta for December; (b) m-chi-delta for February; (c) Volume-odd-double bounce scattering for December; (d) Volume-odd-double bounce scattering for February

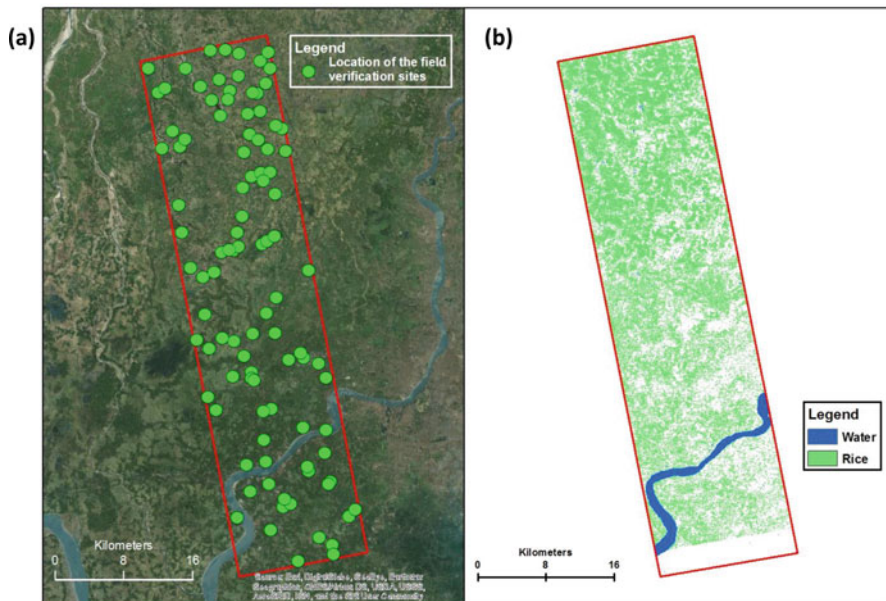


**Fig. 3** (a) Test sites; Rice fields as obtained from (b) classified RISAT-1 data

**Table 2** Results from Accuracy Assessment of classified RISAT-1 data (2015 and 2016)

|             | December        |                     | February        |                     |
|-------------|-----------------|---------------------|-----------------|---------------------|
|             | Users' Accuracy | Producers' Accuracy | Users' Accuracy | Producers' Accuracy |
| Non-Rice    | 80.65           | 60.98               | 52.17           | 60.00               |
| Rice fields | 76.81           | 89.83               | 89.61           | 86.25               |

**Table 3** Results from Accuracy Assessment of classified Landsat data

|                    | December 2015   |                     |
|--------------------|-----------------|---------------------|
|                    | Users' accuracy | Producers' accuracy |
| Settlements        | 100             | 90                  |
| Agricultural lands | 69              | 96                  |
| Water bodies       | 100             | 80                  |

fields are more than 0.2. During this time, high volume scattering (0.3–0.5) was noted over the fields. In February, the values of volume scattering decreased from 0.2 to 0.4. Double bounce is more in the month of February than in the month of December over these areas.

Hundred ground control points (Fig. 3a) randomly distributed over the study area were collected for assessing the accuracy of classification (Table 2). The results are presented in Table 3. Producers' accuracy indicates how well the training set pixels of a given class is classified. Users' accuracy, on the other hand, indicates the probability that a pixel classified into a given class actually belongs to that class on the ground (Bhatta et al. 2010).

The overall accuracies of classification of RISAT-1 data for the months of December and February are 78% and 81%, respectively. The highest users' accuracy for the rice fields was obtained from the classified image of the month of February. During this time, the HYV rice is in the mature stage and the fields can be easily identified from the images (Fig. 3b).

### 3.2 Identification of Settlements from Landsat Images

The accuracies of the classification of Landsat images were tested on 100 random points using Google Earth application (Table 3). The overall accuracies, users' accuracies, and producers' accuracies are presented in Table 3. The overall accuracy of classification was 84% for the image obtained from December 2015. The user's accuracy of settlement class was around 90% in the classified image of 2015. However, relatively high producer's accuracy was obtained for the settlement class, suggesting that omission errors are not significant for this class. Comparatively higher user's accuracies were also noted for the water and agricultural classes. The producer's accuracy for the water class was 100% in the classified image of 2015.

### 3.3 Identifying Settlement Expansion on Adjacent Rice Fields

The impact of settlement expansion on the adjacent rice fields was studied around the urban centers in the study area. It was also observed that the areas of vulnerable rice fields around settlements are strongly correlated with their population density (Table 4). Settlements with high population density (persons per square kilometer) have more rice fields in the hotspot zones around them.

**Table 4** Correlation between areas of rice fields in hotspot zones (hectares) and the areas under hotspot zones (hectares)

| Census Towns   | Rice in hotspots (hectares) | Population density (persons/km <sup>2</sup> ) |
|----------------|-----------------------------|---|
| Jagatballavpur | 58.92                       | 1667  |
| Mansinhapur    | 62.02                       | 3532  |
| Kesabpur       | 290.57                      | 5051  |
| Ramchandrapur  | 409.62                      | 9784  |
| Mallikbagan    | 183.6                       | 2244  |
| Panchla        | 118.73                      | 5861  |
| Tehatta        | 72.97                       | 4916  |
| Raghudebpur    | 151.79                      | 2707  |
| Shyampur       | 140.61                      | 2172  |
| Maheshtala     | 389.17                      | 10,148  |
| Pujali         | 203.44                      | 4453  |

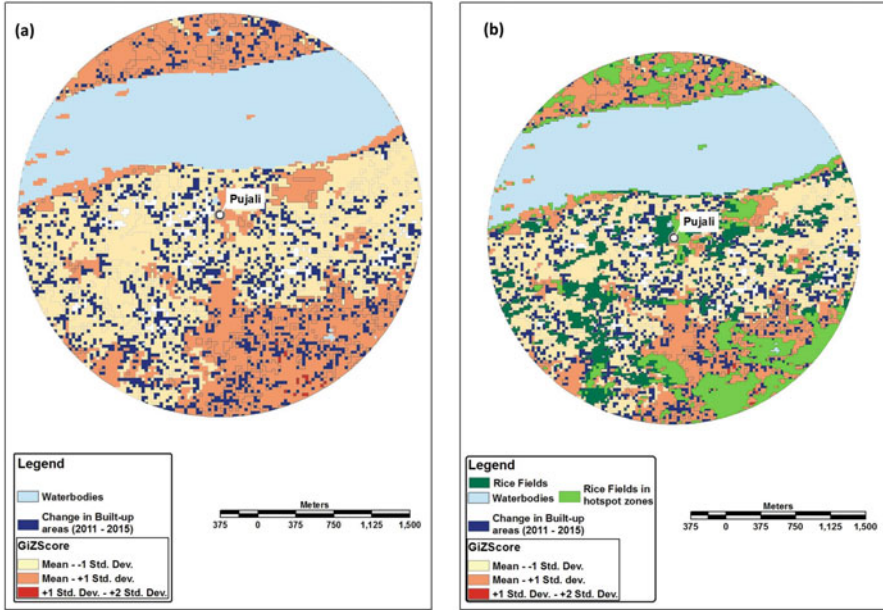


**Fig. 4** (a) Hotspots around Pujali in 2015; (b) Rice fields in the hotspot zones (2015)

Pujali is a small municipality with a population density of 4453 persons per km<sup>2</sup> in 2011. The distribution of hotspots around 2 km from Pujali is shown in Fig. 4. Intersecting the rice fields with the hotspots, it was noted that most of the rice fields coincide with the hotspot zones with z square values between 1 and 2 standard deviations (Fig. 4b). Any expansion of built-up areas in these zones will affect approximately 203.44 hectares of HYV rice fields. The population density of Maheshstala, another municipality in the area, was 10,148 persons per km<sup>2</sup>. Any further expansion of the city in these zones will affect approximately 389.17 hectares of the neighboring HYV rice fields (Fig. 5b).

Hotspots with GiZscore values between mean and 1–2 standard deviations around the new census towns in the area are shown in Fig. 6. In order to identify the vulnerable rice fields, the latter were overlaid on the hotspots around these settlements. Areas under rice fields are least affected around Jagatballavpur (Fig. 6a) with a population density of 1667 persons per km<sup>2</sup>. Only 58.92 hectares of fields are in the hotspot zones within 2 km of this city. The other census towns having less than 100 hectares of rice fields in the hotspot zones around them are Mansinhapur (Fig. 6d) and Tehatta (Fig. 6i), respectively. About 62.02 hectares of rice fields are in the hotspot zones around Mansinhapur and the same is approximately 72.97 hectares around Tehatta. All the other settlements have more than 100 hectares of rice fields in the hotspot zones around them. The areas of rice fields lying in the hotspot zones around Ramchandrapur (population density of 6784

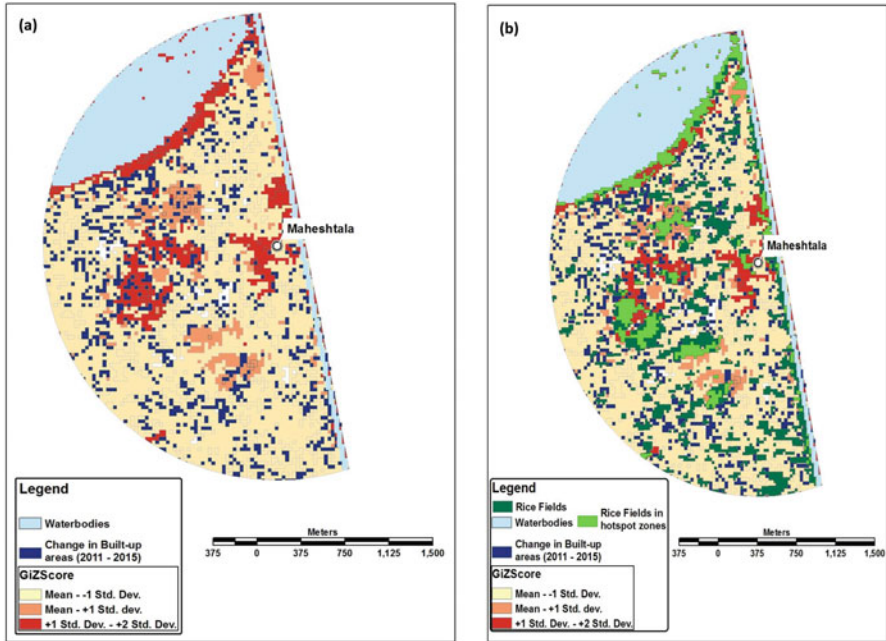


Fig. 5 (a) Hotspot Zones around Maheshtala; (b) Rice in hotspot zones (2015)

persons per km<sup>2</sup>) is 409.62 hectares (Fig. 6g) and Kesabpur (population density of 5051 persons per km<sup>2</sup>) is 290.57 hectares (Fig. 6b).

The rice fields in the hotspot zones around other new census towns in the study area range from 118.73 hectares around Panchla (Fig. 6e), 140.61 hectares around Shyampur (Fig. 6h), 151.79 hectares around Raghudebpur (Fig. 6f), and 183.60 hectares around Mallikbagan (Fig. 6c).

In the study area, approximately 5480 hectares of land has been identified as hotspots around urban centers. These zones indicate clusters of highest vulnerability. Out of these hotspots, around 2081 hectares of lands (i.e., 40%) are under HYV paddy cultivation. Around 35.5% (1489 hectares out of 4192 hectares) of hotspots are under paddy cultivation and more prone to conversion around new and small urban centers, with population density ranging from 1600 to 6000 persons per km<sup>2</sup>. On the other hand, around municipalities and large urban centers in the area with population density of more than 6000 persons per km<sup>2</sup>, 50% of the HYV rice fields are in the hotspot zones. A correlation between areas under rice fields in hotspot zones and the population density of settlements in these areas is shown in Fig. 7. There is a strong positive correlation ( $r = 0.8023$ ,  $p > 0.01$ ) between these two variables. This indicates that with increase of urban sprawl, areas under rice fields will be more affected.

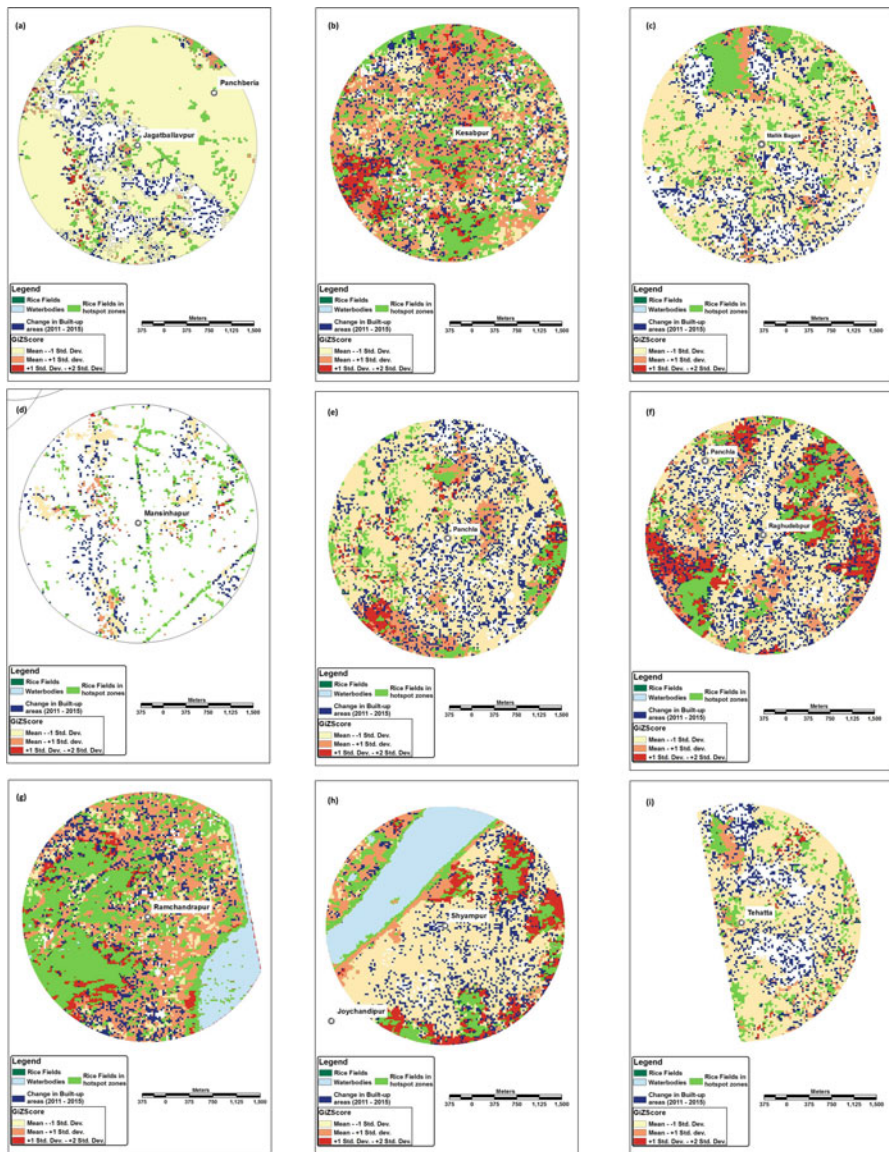
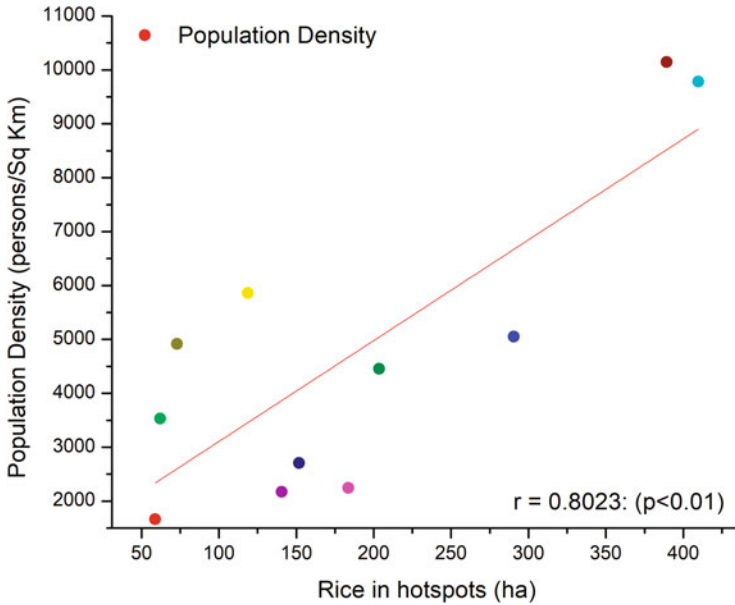


Fig. 6 Rice fields in the hotspot zones around new census towns

### 4 Conclusion

The current study is an attempt to use temporal fine resolution RISAT-I data to identify HYV rice fields and assess their vulnerability around urban areas. Results reveal that around 40% of paddy fields in the area are vulnerable to conversion to





**Fig. 7** Correlation between areas of rice fields in hotspot zones (hectares) and the areas under hotspotzones (hectares)

non-farm uses. Cities with high population density will affect more rice fields compared to the sparsely populated ones. In the last decade (2001–2011), there was an increase in the number of medium-sized towns in West Bengal. Most of these are located away from the big cities (Guin 2016). Studies (Chadchan and Shankar 2012) have indicated that the newly included urban centers lack proper governance and infrastructure. Thereby, it is also probable that these centers will experience unplanned growth. If the current trend of urbanization and population concentration continues in West Bengal, there is a probability that the agricultural lands, which are in immediate proximity of the urban areas, will be affected and converted to non-farm uses in the near future. Since most these agricultural lands are producing HYV rice, the total food crop production in the state might be adversely affected, leading to a lack of food security.

However, a few limitations were encountered in the research. Firstly, fine resolution RISAT-1 data was available only for a few months of the year. This limited its applicability for the complete growing season of HYV rice. Secondly, in order to properly identify the paddy fields, it was necessary to consider only the overlapping part of the images. The temporal variations in the polarimetric parameters of the plants could only be observed in this region. Therefore, the case study area was restricted to 93,100 hectares. Nevertheless, with increased frequency of data availability, fine resolution hybrid polarimetric RISAT-1 data have immense potential in agricultural studies.

The paper presented a method using satellite images that will aid in preparedness by identification of agricultural sites at a risk of irreversible conversion to urban land uses. The research will help in identifying the local environment and assess the land productivity around sprawling urban settlements. In other words, the current research is a useful input to ensure food security to an ever increasing population, especially in third world countries. This will successfully help in future agricultural and urban planning.

**Acknowledgments** The author would like to acknowledge the University Grants Commission (UGC), India, for providing her with a Start-up Grant (UGC-BSR Start-up Grant No. F.30-92/2015) for carrying out this research.

## References

- Abhusan, A., Sajjad, A., Haroon, S. (2019). Relating urbanization and irrigation water demand in Gujranwala District of Pakistan. *World environmental and water resources congress 2019, proceedings*, pp. 1–14. <https://doi.org/10.1061/9780784482339.001>.
- Amundson, R., Berhe, A. A., Hopmans, J. W., Olson, C., Sztein, A. E., & Sparks, D. L. (2015). Soil and human security in the 21st century. *Science*, 348.
- Bhatta, B., Saraswati, S., & Bandyopadhyay, D. (2010). Quantifying the degree-of-freedom, degree-of-sprawl, and degree-of-goodness of urban growth from remote sensing data. *Applied Geography*, 30, 96–111.
- Chadchan, J., & Shankar, R. (2012). An analysis of urban growth trends in the post-economic reforms period in India. *International Journal of Sustainable Built Environment*, 1, 36–49.
- Chen, J., Lin, H., & Pei, Z. (2007). Application of ENVISAT ASAR data in mapping rice crop growth in Southern China. *IEEE Geoscience and Remote Sensing Letters*, 4, 431–435.
- Choudhury, I., & Chakraborty, M. (2006). SAR signature investigation of rice crop using RADA RSAT data. *International Journal of Remote Sensing*, 27, 519–534.
- Dimov, D., Kuhn, J., & Conrad, C. (2016). *Assessment of cropping system diversity in the Fergana Valley through image fusion of Landsat – 8 and sentinel – 1*, in: *ISPRS annals of the photogrammetry, remote sensing and spatial information sciences*. Presented at the XXIII ISPRS Congress, Prague, Czech Republic.
- Farmers' Portal. (2015). *Information on rice*.
- Getis, A., & Ord, J. K. (1992). The analysis of spatial association by use of distance statistics. *Geographical Analysis*, 24, 189–206.
- Gibson, J., Boe-Gibson, G., & Stichbury, G. (2015). Urban land expansion in India 1992–2012. *Food Policy*, 56, 100–113.
- Guccione, P., Lombardi, A., & Giordano, R. (2014). *Assessment of seasonal variations of radar backscattering coefficient using sentinel – 1 data*. Presented at the IEEE international Geoscience and remote sensing symposium, Quebec, Canada.
- Guin, D. (2016). Urban transition in West Bengal, India. *Journal of Asian and African Studies*, 0021909616649211.
- Haldar, D., & Gopalan, R. S. (2017). Assessment of paddy performance under BGREI initiative using RISAT SAR data. *Paddy and Water Environment*, 1–11.
- Hellerstein, D., & Vilorio, D. (2019). Agricultural resources and environmental indicators, 2019 [WWW document]. *AgEcon Search*. <https://doi.org/10.22004/ag.econ.288293>.
- International Rice Research Institute, 2014. *IRRI and the green revolution in India*.
- Kramer, H. J. (2002). *Observation of the earth and its environment: Survey of missions and sensors*.

- Kurosu, T., Fujita, M., & Chiba, K. (1997). The identification of rice fields using multi-temporal ERS-1 C band SAR data. *International Journal of Remote Sensing*, 18, 2953–2965.
- Li, E., Endter-Wada, J., & Li, S. (2019a). Dynamics of Utah's agricultural landscapes in response to urbanization: A comparison between irrigated and non-irrigated agricultural lands. *Applied Geography*, 105, 58–72. <https://doi.org/10.1016/j.apgeog.2019.02.006>.
- Li, W., Wang, D., Liu, S., & Zhu, Y. (2019b). Measuring urbanization-occupation and internal conversion of peri-urban cultivated land to determine changes in the peri-urban agriculture of the black soil region. *Ecological Indicators*, 102, 328–337. <https://doi.org/10.1016/j.ecolind.2019.02.055>.
- Liew, S. C., Kam, S.-P., Tuong, T.-P., Chen, P., Minh, V. Q., & Lim, H. (1998). Application of multitemporal ERS-2 synthetic aperture radar in delineating rice cropping systems in the Mekong River Delta, Vietnam. *IEEE Transactions on Geoscience and Remote Sensing*, 36, 1412–1420.
- Lillesand, T., Kiefer, R. W., & Chipman, J. (2015). *Remote sensing and image interpretation* (7th ed.). Hoboken: Wiley.
- Martellozzo, F., Ramankutty, N., Hall, R. J., Price, D. T., Purdy, B., & Friedl, M. A. (2015). Urbanization and the loss of prime farmland: A case study in the Calgary–Edmonton corridor of Alberta. *Regional Environmental Change*, 15, 881–893.
- Nguyen, D. B., Gruber, A., & Wagner, W. (2016). Mapping rice extent and cropping scheme in the Mekong Delta using sentinel-1A data. *Remote Sensing Letters*, 7, 1209–1218.
- Nong, D. H., Fox, J., Miura, T., & Saksena, S. (2015). Built-up area change analysis in Hanoi using support vector machine classification of Landsat multi-temporal image stacks and population data. *Land*, 4, 1213–1231.
- Oueslati, W., Salanié, J., & Wu, J. (2019). Urbanization and agricultural productivity: Some lessons from European cities. *Journal of Economic Geography*, 19, 225–249. <https://doi.org/10.1093/jeg/lby001>.
- Pandey, B., & Seto, K. C. (2015). Urbanization and agricultural land loss in India: Comparing satellite estimates with census data. *Journal of Environmental Management*, 148, 53–66.
- Pandey, B., Zhang, Q., & Seto, K. C. (2013). An automated algorithm to detect timing of urban conversion of agricultural land with high temporal frequency MODIS NDVI data.
- Planning Commission, G. of I. (2010). *West Bengal development report*. New Delhi.
- Qiu, F., Laliberté, L., Swallow, B., & Jeffrey, S. (2015). Impacts of fragmentation and neighbor influences on farmland conversion: A case study of the Edmonton-Calgary Corridor, Canada. *Land Use Policy*, 48, 482–494.
- Raney, R. K. (2006). Dual-polarized SAR and stokes parameters. *IEEE Geoscience and Remote Sensing Letters*, 3.
- Shao, Y., Fan, X., Liu, H., Xiao, J., Ross, S., Brisco, B., Brown, R., & Staples, G. (2001). Rice monitoring and production estimation using multitemporal RADARSAT. *Remote Sensing of Environment*, 76, 310–325.
- Sivasankar, T., Srivastava, H. S., Sharma, P. K., Kumar, D., & Patel, P. (2015a). Study of hybrid Polarimetric parameters generated from RISAT - 1 SAR data for various land cover targets. *International Journal of Advancement in Remote Sensing, GIS and Geography*, 3, 32–42.
- Sivasankar, T., Srivastava, H. S., Sharma, P. K., Kumar, D., & Patel, P. (2015b). Study of hybrid Polarimetric parameters generated from RISAT - 1 SAR data for various land cover targets. *International Journal of Advancement in Remote Sensing, GIS and Geography*, 3, 32–42.
- Skog, K. L., & Steinnes, M. (2016). How do centrality, population growth and urban sprawl impact farmland conversion in Norway? *Land Use Policy*, 59, 185–196.
- Su, S., Jiang, Z., Zhang, Q., & Zhang, Y. (2011). Transformation of agricultural landscapes under rapid urbanization: A threat to sustainability in hang-Jia-Hu region, China. *Applied Geography*, 31, 439–449.
- Tang, J., & Di, L. (2019). Past and future trajectories of farmland loss due to rapid urbanization using Landsat imagery and the Markov-CA model: A case study of Delhi, India. *Remote Sensing*, 11, 180. <https://doi.org/10.3390/rs11020180>.

- Torbick, N., Chowdhury, D., Salas, W., & Qi, J. (2017). Monitoring Rice agriculture across Myanmar using time series Sentinel-1 assisted by Landsat-8 and PALSAR-2. *Remote Sensing*.
- Uppala, D., Kothapalli, R. V., Polaju, S., Venkata Rama Mullapudi, S. S., & Dadhwal, V. K. (2015). Rice crop discrimination using single date RISAT1 hybrid (RH, RV) polarimetric data. *Photogrammetric Engineering & Remote Sensing*, 81, 557–563.
- Zhang, Y., Wang, C., Wu, J., Qi, J., & Salas, W. A. (2009). Mapping paddy rice with multitemporal ALOS/PALSAR imagery in Southeast China. *International Journal of Remote Sensing*, 30, 6301–6315.
- Zhong, T., Huang, X., Ye, L., & Scott, S. (2014). The impacts on illegal farmland conversion of adopting remote sensing Technology for Land Inspection in China. *Sustainability*, 6, 4426–4451.

# Identification of Impervious Built-Up Surface Features Using ResourceSat-2 LISS-III-Based Novel Optical Built-Up Index



Abhisek Santra, Shreyashi Santra Mitra, Suman Sinha, Shidharth Routh, and Akhilesh Kumar

**Abstract** In the context of urban planning, the increasing urban concentration and growth result in changes from natural landscape to impervious surface features. Remote sensing provides an efficient method in automated identification of land use/cover classes. However, a common challenge is the accurate extraction of built-up features from satellite images. The conventional Normalized Difference Built-up Index (NDBI) has been modified by several researchers in the anticipation of improvement of the built-up area classification. The indices adopted in the study are Index-based Built-up Index (IBI), Built-up Index (BUI), NDBI, and the newly developed Impervious Built-up Index (IBUI). These indices work on automated kernel-based probabilistic thresholding algorithm to group the index values into built-up and non-built-up areas. This study investigates the performance of the abovementioned spectral indices on ResourceSat-2 Linear Imaging Self-Scanner-III (LISS III) imageries of the city of Kolkata, India, and its adjoining areas in the delineation of built-up areas and compares them based on spectral feature space correlation and classification approach. Although all the built-up indices showed high mutual correlation, the performance varied greatly as showed by the accuracy in the classification. Overall accuracy values of built-up feature extraction using IBUI, IBI, BUI, and NDBI are 92.33%, 89%, 86%, and 80.67% respectively.

**Keywords** Built-up · Feature extraction · Spectral indices · Classification · Correlation

---

A. Santra (✉) · S. S. Mitra · S. Sinha · S. Routh · A. Kumar  
Department of Civil Engineering, Haldia Institute of Technology, Haldia, India  
e-mail: [abhisek\\_santra@hithaldia.in](mailto:abhisek_santra@hithaldia.in)

© The Editor(s) (if applicable) and The Author(s), under exclusive license to Springer Nature Switzerland AG 2021  
P. Kumar et al. (eds.), *Remote Sensing and GIScience*,  
[https://doi.org/10.1007/978-3-030-55092-9\\_7](https://doi.org/10.1007/978-3-030-55092-9_7)

## 1 Introduction

The world has witnessed a few natural and anthropogenic pulverizations which had a direct antagonistic impact on sustainable livelihood. The heinous effect of such catastrophe profoundly affects the land cover features; however, the impact proliferates more colossally on the built-up areas, causing alterations in the land cover dynamics. This results in the essential requirement of rapid identification of urban built-up areas, as the maximum economic loss occurs within the urban built-up areas (Varshney and Rajesh 2014). Under such emergency scenario, remote sensing techniques offered complex as well as diverse characteristics of data (Sajjad and Kumar 2019). Therefore, the traditional classification systems detecting specific land use/cover (LULC) changes may yield erroneous results sometimes. The index-based automatic extraction of land features from satellite imagery yields quick and accurate results and thus advantageous for disaster management and spatial mitigation response. However, among all the land cover features, accurate extraction of built-up features is a common challenge from the satellite imagery.

Instigation of the concept began with the development of the Vegetation-Impervious Surface-Soil (VIS) model concept of the urban setup (Ridd 1995). The foundation stone of formulating built-up indices is the Normalized Difference Built-up Index (NDBI) that uses three optical bands, Red (R), Near Infrared (NIR), and Mid-Infrared (MIR) (Zha et al. 2003), targeted in the extraction of urban features with an accuracy of 92.6%; however, mixed with plant noise, hence requiring Normalized Difference Vegetation Index (NDVI) corrections. Subsequently, researchers have made valuable contribution in modifying, improving, and proposing several indices and techniques in this reference. The NDBI has been modified with a thresholding-based algorithm built on difference of continuous images of NDBI and NDVI (HE et al. 2010). This improved the NDBI to attain the overall classification accuracy for automatic segmentation of built-up areas up to 20% higher than the original method. Varshney (2013) also attempted to improve NDBI by implementing an automated kernel-based thresholding algorithm that involved offering higher positive difference values of continuous NDBI and NDVI to built-up regions. Jieli et al. (2010) applied the spectral response characteristics from the red band to augment the built-up area identification, as the spectral reflectance of barren land is more than that of the built-up areas and other land use/cover classes. Soil Adjusted Vegetation Index (SAVI) and Modified Normalized Difference Water Index (MNDWI) were simultaneously used along with NDBI by Xu (2007) to outline urban features using different techniques with an overall classification accuracy ranging from 91.5% to 98.5%. The same three indices were once again used by Xu (2008) to derive a new urban index, Index-based Built-up Index (IBI), to demarcate urban built-up areas by eliminating other LULC features, with an overall classification accuracy as high as 96.7%. Bouhennache et al. (2018) applied the conventional built-up indices and tested newly developed Built-up Land Features Extraction Index (BLFEI), which vigorously distinguishes the built-up land areas from the surrounding areas. Similarly Piyooosh and Ghosh (2018) developed

Normalized Ratio Urban Index (NRUI) and got interesting results in discriminating urban built-up area from its surroundings. Impervious Built-up Index (IBUI), proposed in this study, is a slight modification of IBI, wherein, the vegetation class using NDVI and water class using MNDWI are eliminated from built-up class depicted by NDBI. The formulation of BUI by Lee et al. (2010) helped in the development of a standard city classification method using significant value of the BUI based on values obtained from selected samples to classify built-up lands from images. Maa et al. (2010) combined four built-up indices, namely, NDBI, SAVI, NDISI, and IBI, to formulate exponential percent impervious index on a subtropical city of South China. The index showed positive correlation with the land surface temperature whereas vegetated areas showed negative correlation. Zhou et al. (2014) introduced a new Landsat-8 OLI data index based on the established NDBI. The index initially creates a set of binary images derived from the NDBI and NDVI images. Finally, the resultant image was generated through subtracting the NDVI binary image from the NDBI binary image. The index was applied on Zhengzhou city of Henan province, China, and yielded 91% accuracy in extracting urban built-up areas. However, the index suffers from the inability of discriminating built-up lands from the bare/open surface areas. Wang et al. (2015) proposed and applied the NIR and visible spectral information–dependent Normalized Difference Impervious Index (NDII). The spectral end members were selected using linear spectral mixture analysis. Tian et al. (2018) introduced a novel spectral index Perpendicular Impervious Surface Index (PISI), based on the blue and NIR bands of Landsat data. They have developed the index through selecting the reference line on feature space. The concept of the index development is similar to that of the Perpendicular Vegetation Index (PVI) (Jackson and Huete 1991). The index was tested on four capital cities of China with acceptable accuracy. Thermal Infrared (TIR) information for developing indices has been used for improved built-up classification (Santra 2017; Sinha et al. 2015; Azmi et al. 2016; Kumari et al. 2019); however, most space-borne sensors, specially the high-resolution ones do not have the TIR capabilities. A few thermal image–based indices came into being to extract urban built-up areas in the context of urban heat island. Xu (2010) introduced the concept of Normalized Difference Impervious Surface Index (NDISI) on Landsat ETM+ and ASTER images. The relationship with the land surface temperature was also established. Liu et al. (2013) introduced the modified version of NDISI and gave MNDISI which is a composite index derived from Landsat-5 TM, nighttime ISS photographs, and high-resolution ortho photos. They applied the index over Los Angeles and Las Vegas and successfully extracted the residential, commercial, suburban, airport, harbor areas, and highways. Sun et al. (2017) modified this index and proposed another version of MNDISI, which is the Gaussian automated threshold identification method. The index was applied on Landsat 5–8 datasets with nearly 87% accuracy. Chen et al. (2019) with the enhanced version of NDISI were able to isolate impervious features from bare rock and soil surfaces with almost 94% accuracy. However, the selection criterion was similar to that of the modified version of the index. Garg et al. (2016) compared some of the thermal and optical data–based spectral indices derived from Landsat 8 OLI/TIRS images on Dehradun city and extracted the built-up areas on the

basis of conventional supervised classification and Support Vector Machine (SVM) methods. Sekertekin et al. (2018) also compared four spectral built-up indices to identify impervious surface features in Turkey. They identified that IBI performed best among the four applied indices, whereas Urban Index (UI) (Kawamura et al. 1996) performed least efficiently. Challenges have also been faced by different researchers in distinguishing built-up features and bare soil areas (Benkouider et al. 2019; Rasul et al. 2018). However, the problem is more pronounced in arid and dry climatic areas. Performance of the index-based methods varies with the deviation in scale, image acquisition season/date, and topography; and the thresholding is often observed to be area specific. The present study aims to test the performance of newly developed LISS-III-based IBUI in extraction of impervious urban built-up features. For this a comparative analysis among the indices mentioned above is performed in automatic extraction of built-up areas based on spectral feature space correlation approach.

## 2 Study Area

Kolkata, the capital of West Bengal, India is situated in the bank of the Hugli River. Originally the city was developed on flood plains of the Hugli River. The spatial extent of Kolkata is approximately from  $22^{\circ} 25' N$  to  $22^{\circ} 47' N$  and  $88^{\circ} 12' E$  to  $88^{\circ} 34' E$  with an area approximately  $185 \text{ km}^2$ . The city is surrounded by three districts, namely, Howrah, North 24 Parganas, and South 24 Parganas. The average elevation is around 6 m above MSL. The climate of Kolkata can be considered as a tropical climate with strong southwesterly monsoonal winds during summer. The monthly temperature ranges between  $19^{\circ} C$  and  $30^{\circ} C$ , with a mean temperature of  $27^{\circ} C$ . However, seasonal variation is also striking. Temperature ranges from  $25^{\circ} C$  to  $42^{\circ} C$  and  $8^{\circ} C$  to  $25^{\circ} C$  in summer and winter months, respectively. The average annual rainfall is 1582 mm. In course of time, the city developed and now the built-up structures engulfed almost the administrative boundary of the city. However, some green fields, wetlands, and barren lands are still present in the area. Therefore, it is necessary to clearly isolate the impervious areas from the other land use/cover surfaces for urban sprawl analysis (Fig. 1).

## 3 Database and Methodology

ResourceSat-2 LISS-III imagery of 2011 was considered. The sensor is offering four-band multispectral data at 23.5 m spatial resolution. The spectral bands are green ( $0.52\text{--}0.59 \mu\text{m}$ ), red ( $0.62\text{--}0.68 \mu\text{m}$ ), near infrared ( $0.76\text{--}0.86 \mu\text{m}$ ), and shortwave infrared ( $1.55\text{--}1.70 \mu\text{m}$ ). The ground control points were collected with the help of GPS survey and were tagged on the Survey of India topographical map. The LISS-III data was co-registered with the topographical map under the RMSE



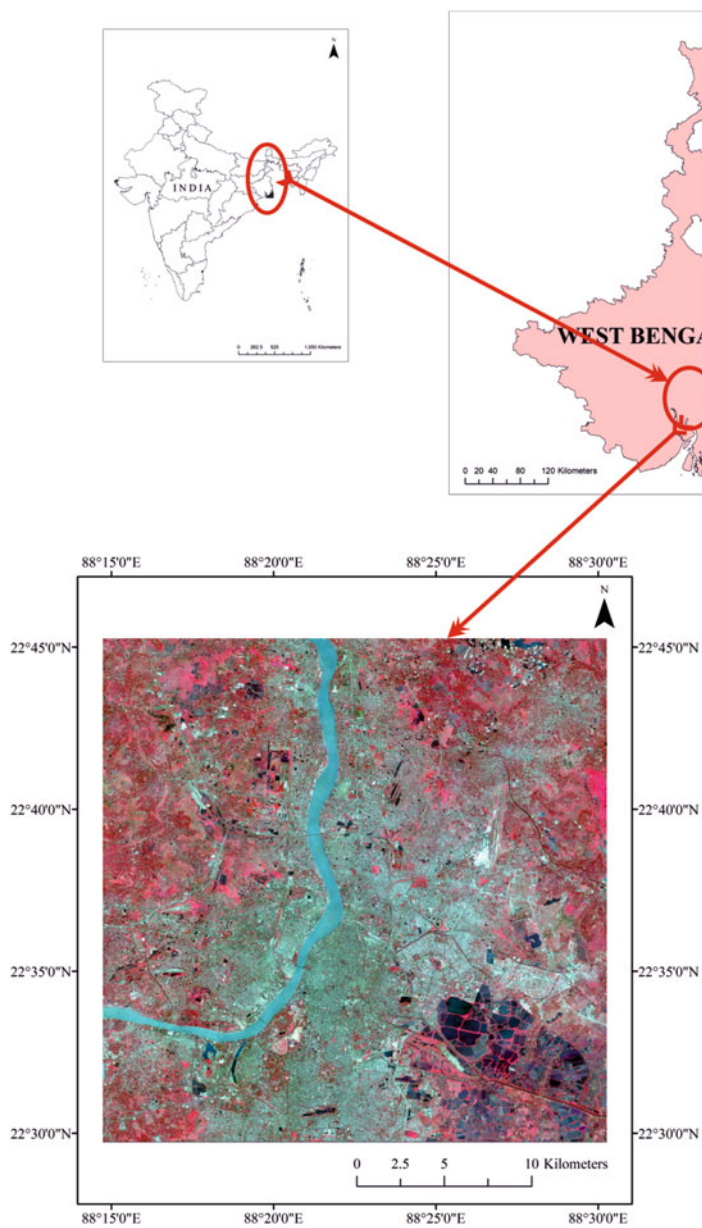


**Fig. 1** Study area

<0.5. The reference system was chosen as UTM Zone-45 with WGS-84 datum. As the radiometric normalization rectify the image from possible atmospheric attenuation effects and solar illumination conditions (Santra et al. 2019), the data was calibrated radiometrically using the FLAASH module available in ENVI. The tool is based on the radiative transfer model used in MODTRAN.

The Digital Numbers (DN) of the four spectral bands (green, red, near infrared, shortwave infrared) of LISS-III data were investigated for each of the four different feature classes, viz. (I) water (WATER), (II) vegetation (VEG), (III) built-up/impervious (BU/I), and (IV) open/bare land (BARE). The variation observed maximum in red and near infrared bands. Three major feature classes, namely, vegetation, water, and built-up, were primarily considered while classifying the land cover classes, using NDVI (Rouse et al. 1973), NDWI (Mcfeeters 1996), and NDBI (Zha et al. 2003) respectively. However, SAVI (Huete 1988), with an additional soil factor, was preferred over NDVI as open/bare land was simultaneously considered. The widely applied spectral built-up indices produce interesting results even on the contemporary Sentinel 2A images (Valdiviezo-n et al. 2018). The use of SWIR in MNDWI (Xu 2006) instead of NIR in NDWI efficiently helps in the suppression and elimination of built-up land vegetation and soil noises in water class. SAVI, MNDWI, and NDBI images were subsequently used as three thematic bands that were mutually negatively correlated to generate IBI that minimizes the redundancy among the original multispectral bands. These same three thematic bands were used to design IBUI (Eq. 8) that showed the ability to separate out the BU/I feature class from the other feature classes. BUI (Eq. 6) was generated from subtracting NDVI from NDBI, however, improved to develop IBUI (Eq. 8) by subtracting the sum of SAVI and MNDWI from NDBI. SAVI identifies the open and bare soil surface, whereas MNDWI helps in the suppression and elimination of built-up land vegetation and soil noises in water class. Therefore, the newly developed IBUI minimizes the redundancy associated with the NDBI in classifying the urban soil, vegetation, and water surfaces along with impervious built-up features. IBI is the normalized form of IBUI. Table 1 documents the equations for the indices used in this study.

## 4 Results and Discussions

### 4.1 Spectral Clusters

The average brightness values of the four spectral bands mentioned above for the major land cover classes, namely, water, vegetation, impervious built-up, and bare land are calculated. The greater inconsistency was observed from the red and near infrared bands. The spectral clusters (Fig. 2) in red and NIR bands for the four classes were separated but with occurrence of spectral mixtures among the classes, especially among the impervious built-up and bare land classes and to some extent in the water class. The open/bare land showed no spectral independence as the class was spectrally merged completely with the built-up class (Fig. 2).

**Table 1** Spectral indices used in this study

| Eq. | Formula  | References          | Remarks  |
|-----|--|---------------------|--|
| 1   | Normalized difference vegetation index $NDVI = \frac{(NIR-R)}{(NIR+R)}$                        | Rouse et al. (1973) | Surface reflectance in near-infrared (NIR) and red (R) spectral bands  |
| 2   | Soil-adjusted vegetation index $SAVI = \frac{(NIR-R) \times (1+L)}{(NIR+R+L)}$                 | Huete (1988)        | L is a constant whose value depends on the soil properties   |
| 3   | Normalized difference water index $NDWI = \frac{(G-NIR)}{(G+NIR)}$                             | Mcfeeters (1996)    | Surface reflectance in near-infrared (NIR) and green (G) spectral bands  |
| 4   | Normalized difference built-up index $NDBI = \frac{(SWIR-NIR)}{(SWIR+NIR)}$                    | Zha et al. (2003)   | Surface reflectance in shortwave infrared (SWIR) or middle infrared (MIR) and near-infrared (NIR) spectral bands |
| 5   | Modified normalized difference water index $MNDWI = \frac{(G-SWIR)}{(G+SWIR)}$                 | Xu (2006)           | Surface reflectance in shortwave infrared (SWIR) or middle infrared (MIR) and green (G) spectral bands           |
| 6   | Built-up index $BUI = NDBI - NDVI$   | Lee et al. (2010)   | NDBI and NDVI from Eqs. 5 and 1, respectively  |
| 7   | Index-based built-up index $IBI = \frac{[NDBI - (SAVI + MNDWI)/2]}{[NDBI + (SAVI + MNDWI)/2]}$ | Xu (2008)           | NDBI, SAVI, and MNDWI from Eqs. 5, 2, and 4, respectively; NDVI from eq. 1 can also be used instead of SAVI      |
| 8   | Impervious built-up index (optical) $IBUI = NDBI - SAVI - MNDWI$                               | In this study       | NDBI, SAVI, and MNDWI from Eqs. 5, 2, and 4, respectively  |

### 4.2 Spectral Index Correlation

NDBI (Zha et al. 2003), BUI (Lee et al. 2010), and IBI (Xu 2008), adapted from previous literatures and IBUI designed in this study, are used to extract built-up regions (Table 1). The spectral feature space of the major classes is illustrated in Fig. 3. Coefficient of determination ( $R^2$ ) values for the aforesaid built-up indices is documented in Table 2 for the study site. The table showed high positive correlation among all the four built-up indices (Fig. 3) that indicates that the new index IBUI follows the same trend as the other already established built-up indices used in the study. Among all the four indices, all except BUI shows extremely high correlation. Thereafter, all the four built-up indices are used to delineate the built-up areas. However, IBUI shows an upper hand in built-up classification among all the built-up indices adopted in this study. The mean values of all the indices used in the study are plotted for the four major land cover classes and the behavior of the indices for land cover classes is depicted in Fig. 4. The figure reveals maximum separability and clearer discrimination of the feature classes for IBI and IBUI, while IBUI showed even better separability than IBI. The next step is to find the accuracy of all the four built-up indices to delineate the built-up/impervious surface features. Index maps for all the indices under consideration are generated (Fig. 5). Classification of index maps generated from the built-up indices is carried out (Fig. 5). The accuracy in delineating the built-up features is documented in Table 3.

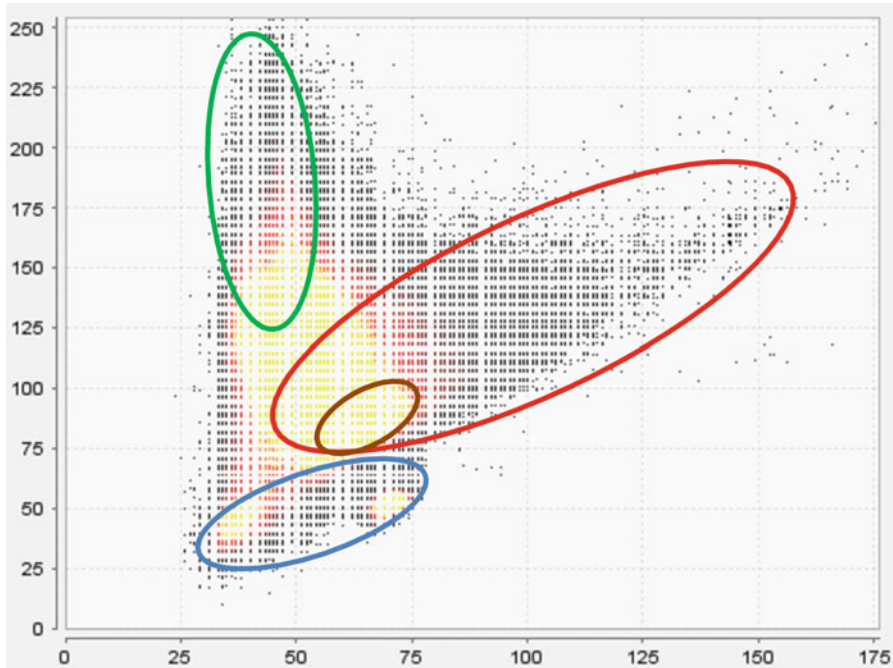


**Fig. 2** Spectral clusters in red (x-axis) and NIR (y-axis) bands for water (blue), vegetation (green), built-up (red), and bare land (brown) classes

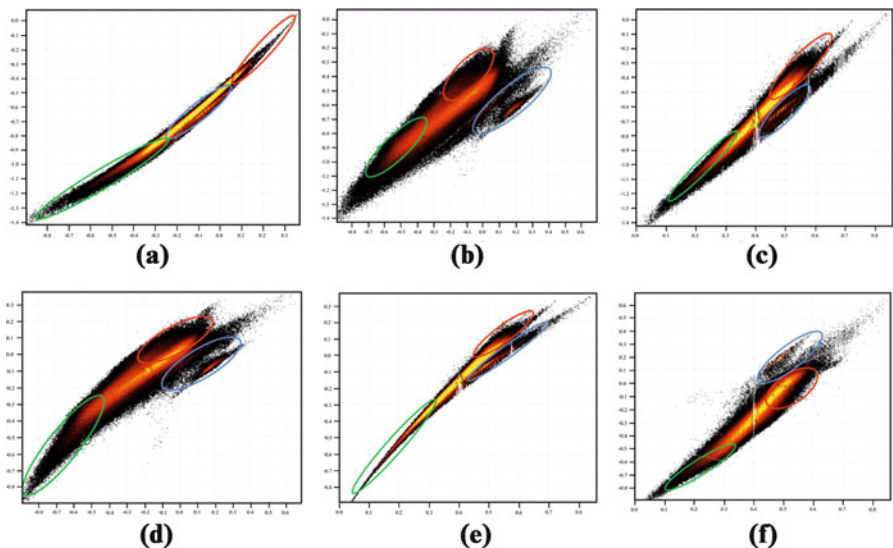


**Fig. 3** Spectral feature space plots of the LISS-III-based index images showing distinctive identification of water (blue), vegetation (green), built-up (red), and open/bare land (brown) land cover classes: (a) IBI (x-axis)–IBUI (y-axis), (b) BUI (x-axis)–IBUI (y-axis), (c) NDBI (x-axis)–IBUI (y-axis), (d) BUI (x-axis)–IBI (y-axis), (e) NDBI (x-axis)–IBI (y-axis), (f) NDBI (x-axis)–BUI (y-axis)

**Table 2** Correlation in terms of coefficient of determination ( $R^2$ ) among spectral indices

|      | IBUI | IBI   | BUI   | NDBI  |
|------|------|-------|-------|-------|
| IBUI |      | 0.971 | 0.742 | 0.92  |
| IBI  |      |       | 0.813 | 0.944 |
| BUI  |      |       |       | 0.876 |
| NDBI |      |       |       |       |

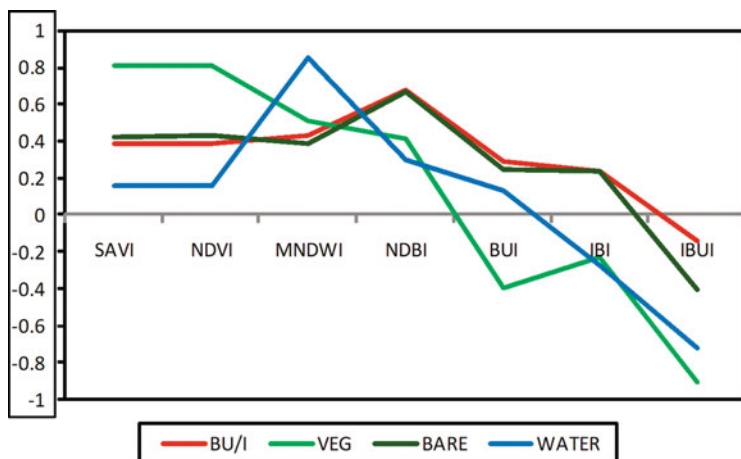


**Fig. 4** Spectral profile of the feature classes: water (blue), vegetation (green), built-up (red), and open/bare land (brown) using spectral indices. (y-axis: index values)

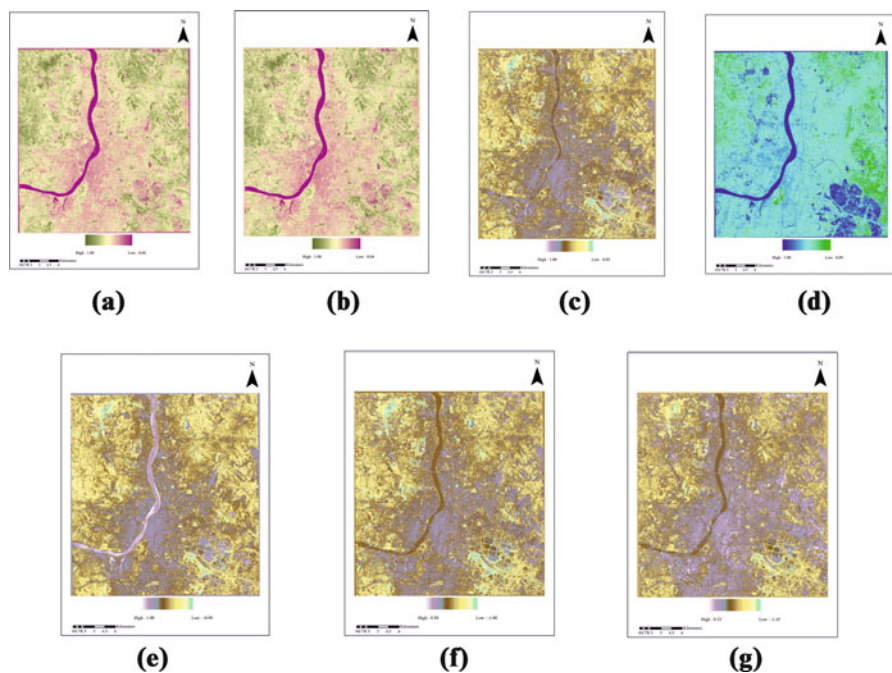


**Fig. 5** Index maps for (a) NDVI (b) SAVI (c) NDBI (d) MNDWI (e) BUI (f) IBI (g) IBUI

**Table 3** Accuracy assessment: Overall accuracy (OA) in percentage and kappa (k) values for built-up (BU) and non-built-up (NBU) area classification

|             | BU  | NBU |     | OA    | K    |             | BU  | NBU |     | OA    | k    |
|-------------|-----|-----|-----|-------|------|-------------|-----|-----|-----|-------|------|
| <b>IBUI</b> |     |     |     |       |      | <b>IBI</b>  |     |     |     |       |      |
| <b>BU</b>   | 192 | 5   | 197 | 92.33 | 0.82 | <b>BU</b>   | 189 | 8   | 197 | 89.00 | 0.75 |
| <b>NBU</b>  | 18  | 85  | 103 |       |      | <b>NBU</b>  | 25  | 78  | 103 |       |      |
| Total       | 210 | 90  | 300 |       |      | Total       | 214 | 86  | 300 |       |      |
| <b>BUI</b>  |     |     |     |       |      | <b>NDBI</b> |     |     |     |       |      |
| <b>BU</b>   | 183 | 14  | 197 | 86.00 | 0.68 | <b>BU</b>   | 181 | 16  | 197 | 80.67 | 0.54 |
| <b>NBU</b>  | 28  | 75  | 103 |       |      | <b>NBU</b>  | 42  | 61  | 103 |       |      |
| Total       | 211 | 89  | 300 |       |      | Total       | 223 | 77  | 300 |       |      |

### 4.3 Accuracy Assessment

Figure 5 shows the qualitative aspect while Table 3 gives the quantitative evaluation of the accuracy of the aforesaid built-up indices for demarcating the built-up areas. The overall accuracy and  $k$  value in the classification shows higher values for IBUI among all the built-up indices revealing its maximum potential for built-up area determination. On comparing the ability of the indices in classifying the built-up areas, IBUI shows the maximum potential, followed by IBI, BUI, and NDBI, respectively. This is also evident from Fig. 4. Spectral feature space correlation between IBUI and IBI in Fig. 3a. shows clear demarcation of the land cover classes; while, in the case of spectral feature space correlation among the other indices, there is a possibility of class overlap. The binary classified maps in Fig. 6 shows that using NDBI as input, there are plenty of occurrences of misclassification of water bodies and vegetation in built-up areas. When BUI is used, this misclassification is somewhat reduced, where instances of misclassification from stagnant water bodies are observed. IBI showed further reduction in the misclassification, while, the use of IBUI showed the maximum accuracy and minimum instances of misclassification in clearly discriminating built-up areas from the other land use/cover, which is also evident from the classification accuracy report mentioned in Table 3. Overall accuracies of built-up feature extraction using IBUI, IBI, BUI, and NDBI are 92.33% ( $k = 0.82$ ), 89% ( $k = 0.75$ ), 86% ( $k = 0.68$ ), and 80.67% ( $k = 0.54$ ), respectively. Hence, the comparative study showed that the IBUI developed in this study has greater potential in identifying impervious built-up land surfaces. The study shows that in dense urban areas like Kolkata, IBUI showed greater variability and better contrast which ultimately facilitates the feature class separability. IBI showed almost similar output as IBUI, however, the dynamic range had been confined. BUI suffered from spectral mixtures of impervious built-up and water classes. Therefore, subtracting water via MNDWI showed improvement in IBUI. Similarly, the soil and vegetation noises are avoided through subtracting SAVI from the IBUI. It is evident from Fig. 4 that IBUI has better capability of distinguishing impervious built-up areas from the bare lands.

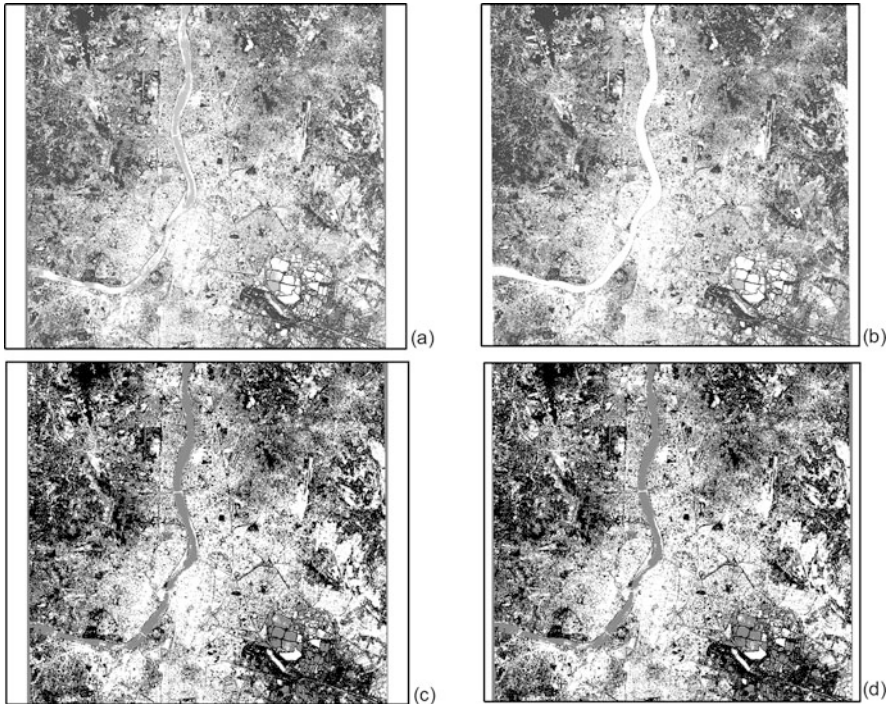


**Fig. 6** Classified binary images distinguishing BU (in black) from NBU (white) using (a) NDVI, (b) BUI, (c) IBI, and (d) IBUI

## 5 Conclusion

Studies throughout the globe showed that the intrinsic heterogeneous characteristics of the impervious built-up lands put difficulty in extraction of impervious surface features through image-derived spectral indices. However, the classification using the built-up indices has varying ranges of accuracy in extracting the built-up areas. The present study revealed the comparative performance of three widely accepted spectral indices and a newly developed LISS-III-based spectral index over the densely populated urban area of Kolkata, India. The work pinpoints the problem of identifying urban impervious built-up feature and distinguishing it from the open bare lands. It offers a plausible solution in precise spatial segregation of the built-up lands among all other surface features. However, due to the time constraints, this chapter only tested the performance of the indices only on ResourceSat-2 LISS-III image and densely overpopulated urban areas. Besides, the limitations of the number of spectral bands of the sensor, only a few indices were applied. The study may be extended in two directions. Firstly, the performance may be tested also in semi-urban and industrial areas. Secondly, other sensor data may be considered if the similar temporal data is available.

The study reveals the potential of IBUI for classifying built-up areas with the maximum accuracy, among the rest, namely, IBI, BUI, and NDBI. However, the findings of this study may be used further to identify the urban impervious features of similar geoclimatic and urban setup. In the context of the present scenario of population explosion, especially in the urban landscape, this kind of study will help the GIScience researchers to recognize the best possible ways to identify the impervious surface areas. This will not only increase the accuracy of urban built-up feature extraction but also enhance the efficiency in understanding urban sprawl. The novelty in this work will endow the GIScience community with an acceptable spectral built-up index that may be applied to any multispectral images to categorize the urban built-up features. Also, the community may widen their scope of research either through applying the index developed in this study or by developing new spectral indices based on the line of the methodology adopted here.

**Acknowledgements** Authors express sincere gratitude to National Remote Sensing Centre (NRSC), Government of India for providing images and Science and Engineering Research Board (SERB), Department of Science and Technology (DST), Government of India, for providing funds under SERB EMR scheme (File Number: EMR/2017/002838).

## References

- Azmi, R., Alami, O. B., Saadane, A. E., Kacimi, I., & Chafiq, T. (2016). A modified and enhanced normalized built-up index using multispectral and thermal bands. *Indian Journal of Science & Technology*, 9, 1–11.
- Benkouider, F., Abdellaoui, A., & Hamami, L. (2019). New and improved built-up index using SPOT imagery: Application to an arid zone (Laghouat and M'Sila, Algeria). *Journal of the Indian Society of Remote Sensing*, 47, 185–192.
- Bouhennache, R., Bouden, T., Taleb-Ahmed, A. & Cheddad, A. (2018). A new spectral index for the extraction of built-up land features from Landsat 8 satellite imagery. *Geocarto International*, 1–21.
- Chen, J., Yang, K., Chen, S., Yang, C., Zhang, S., & He, L. (2019). Enhanced normalized difference index for impervious surface area estimation at the plateau basin scale. *Journal of Applied Remote Sensing*, 13(1–19), 19.
- Garg, A., Pal, D., Singh, H., & Pandey, D. C. (2016, November 18–19). A comparative study of NDBI, NDISI and NDII for extraction of urban impervious surface of Dehradun [Uttarakhand, India] using Landsat 8 imagery. *2016 International Conference on Emerging Trends in Communication Technologies (ETCT)*, pp. 1–5.
- He, C., Shi, P., Xie, D., & Zhao, Y. (2010). Improving the normalized difference built-up index to map urban built-up areas using a semiautomatic segmentation approach. *Remote Sensing Letters*, 1, 213–221.
- Huete, A. R. (1988). A soil-adjusted vegetation index (SAVI). *Remote Sensing of Environment*, 25, 295–309.
- Jackson, R. D., & Huete, A. R. (1991). Interpreting vegetation indices. *Preventive Veterinary Medicine*, 11, 185–200.
- Jieli, C., Manchun, L., Yongxue, L., Chenglei, S. & Wei, H. (2010, June 18–20). Extract residential areas automatically by new built-up Index. 2010 18th International Conference on Geoinformatics, pp. 1–5.



- Kawamura, M., Jayamanna, S., & Tsujiko, Y. (1996). Relation between social and environmental conditions in Colombo Sri Lanka and the urban index estimated by satellite remote sensing data. *International Archives of Photogrammetry and Remote Sensing*, 31, 321–326.
- Kumari, P., Yadav, N. K., Santra, A., & Upadhyay, U. (2019). Identification of urban Heat Islands from multi-temporal Modis land surface temperature data: A case study of the southern part of West Bengal, India. In A. Singh (Ed.), *Wastewater reuse and watershed management: Engineering implications for agriculture, industry, and the environment*. New York: Apple Academic Press.
- Lee, J., Lee, S. S. & Chi, K. H. (2010). Development of an urban classification method using a built-up index. *Selected topics in power systems and remote sensing*. Selected topics in power systems and remote sensing, sixth WSEAS international conference on remote sensing, Iwate Prefectural University, Japan, pp. 39–43.
- Liu, C., Shao, Z., Chen, M., & Luo, H. (2013). MNDISI: A multi-source composition index for impervious surface area estimation at the individual city scale. *Remote Sensing Letters*, 4, 803–812.
- Maa, Y., Kuang, Y., & Huang, N. (2010). Coupling urbanization analyses for studying urban thermal environment and its interplay with biophysical parameters based on TM/ETM+ imagery. *International Journal of Applied Earth Observation and Geoinformation*, 12, 110–118.
- Mcfeters, S. K. (1996). The use of the Normalized Difference Water Index (NDWI) in the delineation of open water features. *International Journal of Remote Sensing*, 17, 1425–1432.
- Piyosh, A. K., & Ghosh, S. K. (2018). Development of a modified bare soil and urban index for Landsat 8 satellite data. *Geocarto International*, 33, 423–442.
- Rasul, A., Balzter, H., Ibrahim, R. F. G., Hameed, M. H., Wheeler, J., Adamu, B., Ibrahim, S. A., & Najmaddin, M. P. (2018). Applying built-up and bare-soil indices from Landsat 8 to cities in dry climates. *Land*, 7.
- Ridd, M. K. (1995). Exploring a V-I-S (vegetation-impervious surface-soil) model for urban ecosystem analysis through remote sensing: Comparative anatomy for cities†. *International Journal of Remote Sensing*, 16, 2165–2185.
- Rouse, J. W., Haas, R. H., Schell, J. A. & Deering, D. W. (1973). Monitoring vegetation systems in the Great Plains with ERTS. *3rd ERTS Symposium, NASA SP-351 I*, pp. 309–317.
- Sajjad, H. & Kumar, P. 2019. Future challenges and perspective of remote sensing technology. In: Kumar, P., Rani, M., Chandra Pandey, P., Sajjad, H. & Chaudhary, B. S. (eds.) *Applications and challenges of geospatial technology: Potential and future trends*. Cham: Springer.
- Santra, A. (2017). Land surface temperature and urban heat island detection: A remote sensing perspective. In A. Santra & S. Santra Mitra (Eds.), *Remote sensing techniques and GIS applications in earth and environmental studies*. New York: IGI Global.
- Santra, A., Santra Mitra, S., Mitra, D., & Sarkar, A. (2019). Relative radiometric normalisation - performance testing of selected techniques and impact analysis on vegetation and water bodies. *Geocarto International*, 34, 98–113.
- Sekertekin, A., Abdikan, S., & Marangoz, A. M. (2018). The acquisition of impervious surface area from LANDSAT 8 satellite sensor data using urban indices: A comparative analysis. *Environmental Monitoring and Assessment*, 190, 381.
- Sinha, S., Sharma, L. K., & Nathawat, M. S. (2015). Improved land-use/land-cover classification of semi-arid deciduous forest landscape using thermal remote sensing. *The Egyptian Journal of Remote Sensing and Space Science*, 18, 217–233.
- Sun, Z., Wang, C., Guo, H. & Shang, R. (2017). A modified normalized difference impervious surface index (MNDISI) for automatic urban mapping from Landsat imagery. *Remote Sensing*, 9(9), 942.
- Tian, Y., Chen, H., Song, Q., & Zheng, K. (2018). A novel index for impervious surface area mapping: Development and validation. *Remote Sensing*, 10.
- Valdiviezo-n, J. C., Téllez-Quiñones, A., Salazar-Garibay, A., & López-Caloca, A. A. (2018). Built-up index methods and their applications for urban extraction from sentinel 2A satellite data: Discussion. *Journal of the Optical Society of America A*, 35, 35–44.

- Varshney, A. (2013). Improved NDBI differencing algorithm for built-up regions change detection from remote-sensing data: An automated approach. *Remote Sensing Letters*, 4, 504–512.
- Varshney, A., & Rajesh, E. (2014). A comparative study of built-up index approaches for automated extraction of built-up regions from remote sensing data. *Journal of the Indian Society of Remote Sensing*, 42, 659–663.
- Wang, Z., Gang, C., li, X., chen, Y., & Li, J. (2015). Application of a normalized difference impervious index (NDII) to extract urban impervious surface features based on Landsat TM images. *International Journal of Remote Sensing*, 36, 1055–1069.
- Xu, H. (2006). Modification of normalised difference water index (NDWI) to enhance open water features in remotely sensed imagery. *International Journal of Remote Sensing*, 27, 3025–3033.
- Xu, H. (2007). Extraction of urban built-up land features from LANDSAT imagery using a thematic-oriented index combination technique. *Photogrammetric Engineering & Remote Sensing*, 73, 1381–1391.
- Xu, H. (2008). A new index for delineating built-up land features in satellite imagery. *International Journal of Remote Sensing*, 29, 4269–4276.
- Xu, H. (2010). Analysis of impervious surface and its impact on urban heat environment using the normalized difference impervious surface index (NDISI). *Photogrammetric Engineering & Remote Sensing*, 76, 557–565.
- Zha, Y., Gao, J., & Ni, S. (2003). Use of normalized difference built-up index in automatically mapping urban areas from TM imagery. *International Journal of Remote Sensing*, 24, 583–594.
- Zhou, Y., Yang, G., Wang, S., Wang, L., Wang, F., & Liu, X. (2014). A new index for mapping built-up and bare land areas from Landsat-8 OLI data. *Remote Sensing Letters*, 5, 862–871.

# Subsidence Assessment of Building Blocks in Hanoi Urban Area from 2011 to 2014 Using TerraSAR-X and COSMO-SkyMed Images and PSInSAR



Van Anh Tran, Quoc Cuong Tran, Duc Anh Nguyen, Tong Minh Dinh Ho, Anh The Hoang, Trung Khien Ha, and Dieu Tien Bui

**Abstract** Covering an area of 3328.9km<sup>2</sup>, Hanoi is the largest city in Vietnam, with a total population of around 8.053 million people in 2019. Due to the economic development, the fast urbanization process, the rapid growth of population, and overexploitation of groundwater, the ground subsidence in the city has become a severe issue, especially in the urban area. This study aims to assess the subsidence of buildings from 2011 to 2014 in the two districts, Ha Dong and Hoang Mai, using the Persistent Scatterer (PS) Interferometric Synthetic Aperture Radar (PSInSAR). For this regard, 19 TerraSAR-X (TSX) and 27 Constellation of Small Satellites for

---

V. A. Tran (✉)

Faculty of Geomatics and Land Administration, Hanoi University of Mining and Geology, Hanoi, Vietnam

e-mail: [tranvananh@humg.edu.vn](mailto:tranvananh@humg.edu.vn)

Q. C. Tran · D. A. Nguyen

Institute of Geological Sciences, Vietnam Academy of Science and Technology, Hanoi, Vietnam

e-mail: [tquong@igs.vn.vast.vn](mailto:tquong@igs.vn.vast.vn)

T. M. D. Ho

IRSTEA/UMR TETIS, Montpellier, France

e-mail: [dinh.ho-tong-minh@irstea.fr](mailto:dinh.ho-tong-minh@irstea.fr)

A. T. Hoang

Department of Geography/Natural Resources Management, Vinh University, Vinh City, Vietnam

School of Geodesy and Geomatics, Wuhan University, Wuhan, Hubei Province, China

T. K. Ha

GIS Group, Department of Business and IT, University of Southeast Norway, Bø i Telemark, Norway

e-mail: [khienht@nuce.edu.vn](mailto:khienht@nuce.edu.vn)

D. T. Bui

Department of Surveying, National University of Civil Engineering, Hanoi, Vietnam

e-mail: [dieu.t.bui@usn.no](mailto:dieu.t.bui@usn.no)

Mediterranean basin Observation (COSMO-SkyMed) high-resolution radar images were collected and used to estimate the ground subsidence at the two districts and then infer the subsidence of buildings in the study area. Besides, the subsidence measured by the geodetic precise leveling technique at three building blocks, CC2 and CQ01 at the Van Quan area (Ha Dong district) and CC7 at the Linh Dam area (Hoang Mai district) were used to validate the results. The result shows that the subsidence derived by the PSInSAR has high accuracy. For CQ01 and CC7, where the PS points were derived from the TerraSAR-X images, the subsidence difference between the PSInSAR method and the leveling technique is 1.6 mm and 2.5 mm, respectively. Whereas, for CC2, where the PS points were taken from the COSMO-SkyMed images, the difference is 5.5 mm. Therefore, it could be concluded that the PSInSAR method and high-resolution radar images are capable of detecting subsidence of building in urban areas.

**Keywords** Building subsidence · InSAR · TerraSAR-X · COSMO-SkyMed · Hanoi · Vietnam

## 1 Introduction

Hanoi is the capital of Vietnam, which has developed rapidly since its expansion in 2008, and now it becomes the largest city in size, 3328,9 km<sup>2</sup> (Phi and Strokova 2015), in Vietnam. The development of Hanoi has resulted in various changes that can be observed, such as upgraded infrastructure systems, new highways, and new urban areas, which change the landscape of the city. However, together with the development, the rapid growth of the population has led to overloads for the city, and among them, housing and freshwater are urgent issues.

During the last decade, the freshwater demand has created high pressures on the water supply of the city, leading to the overexploitation of the groundwater (Tu et al. 2013). Thus, this is the main cause of ground subsidence in the city. In Hanoi, the groundwater resides mainly in aquifers of Quaternary; however, the degradation of these aquifers has reached an alarming rate with the lowering of groundwater levels is around 0.3–0.5 m annually and, consequently, the highest ground subsidence rate can reach to 41 mm/year (Tam and Nga 2018). Among areas, ground subsidence occurs severe in the southern part of the city, including Phap Van, Van Dien, Ha Dong, and Linh Dam, where there is a high concentration of new infrastructure and high buildings.

Although subsidence occurs slowly, they have caused various serious consequences in Hanoi, such as deformation of engineering structures, foundation failures of urban infrastructures, building blocks, and private houses (Dang et al. 2014). Thus, these may generate threats to the sustainable development of the city. Therefore, monitoring and assessing ground subsidence at Hanoi is an important task. In this regard, the precise geodetic leveling and GPS surveys are the most accurate methods because they can estimate the vertical displacement with accuracy from several millimeters to 0.01 mm (Zhang et al. 2011). However, for large areas, radar

remote sensing, that is, Interferometric Synthetic Aperture Radar (InSAR), is the most widely used. This is because it could provide accuracy comparable to GPS (Hu et al. 2019; Motagh et al. 2007).

Among the radar remote sensing techniques used for land subsidence, Interferometric Synthetic Aperture Radar (InSAR) and Differential InSAR (DInSAR) are the most popular used. Herein, the InSAR was first applied to the Seasat image to study small vertical changes over a region of 50 km wide in the Imperial Valley, California, USA (Graham 1974). Then, DInSAR has been developed and deployed in various interdisciplinary domains, such as, tracking the earth's surface movement due to earthquakes, volcano, mineral or water extraction (Peltzer and Rosen 1995; Rott et al. 2000; Yen et al. 2005, 2008), etc. Nevertheless, DInSAR still has some limitations, including atmospheric effects (Zebker et al. 1997), the effect of the baseline (Yang et al. 2013), and topographic features (Anh et al. 2016). For these reasons, new methods, including Persistent Scatterer InSAR (PSInSAR) (Ferretti et al. 2000), which uses a series of images acquired in the same location but at different times to estimate changes in the ground, was introduced.

The first applications of the PSInSAR for the urban subsidence at Pomona California (USA) (Ferretti et al. 2000) and landslide at Ancona (Italy) (Ferretti et al. 2001) showed high accuracy results. Herein, with the use of ERS images, the effects relating to atmosphere, baseline, and topographic features can be minimized when using a series of images at different times. Following these works, Colesanti et al. (2003) evaluated the accuracy of the PSInSAR method for estimating land deformations at Fremont in the Southern Bay Area and San Jose in the Santa Clara Valley with promising results. Since then, several studies using the PSInSAR method for landslides (Ciampalini et al. 2014), land subsidence (Solari et al. 2016), especially for urban subsidence areas (Biswas et al. 2019; Liu et al. 2020; Zhou et al. 2020) have been very effective.

To increase the accuracy of determining land subsidence, the combination of different images, that is, descending and ascending images or different polarizations, that is, VV or HH has been investigated, such as assessing land subsidence in Mexico City (Mexico) from 2002 to 2007 (López-Quiroz et al. 2009). This study addressed the loss of coherence in interferogram pairs and enhanced the accuracy of the subsidence monitoring results. Other studies on urban subsidence areas with promising results include Oslo (Norway) (Dehls and Nordgulen 2003) Shanghai (China) (Damoah-Afari et al. 2007), and Bangkok (Thailand) (Aobpaet et al. 2009). In urban areas, to monitor the subsidence of buildings, the PSInSAR and TerraSAR-X images have been considered to derive both the vertical and the horizontal deformations, that is, at Berlin city (Gernhardt and Bamler 2012). Ciampalini et al. (2014) confirmed that the deformation of human-made structures could be accurately estimated with the use of the PSInSAR, TerraSAR-X images, and COSMO-SkyMed images.

In this study, we aim to assess the subsidence of buildings in Hanoi city using the PSInSAR method, TerraSAR-X images, and COSMO-SkyMed images for the period 2011–2014. It should be noted that the study of the land subsidence in Hanoi by the radar interferometry has been carried out for nearly 20 years ago. In the first study, Raucoules and Carnec (1999) employed the DInSAR and Europe's

ERS-1/2 SAR images; however, due to the limited number of images and lousy interferogram quality, the land subsidence was found even in stable areas. In another study, Tran et al. (2007) used the JERS/1 L band image with the DInSAR method to determine the land subsidence in the period 1995–1998. The land subsidence from the geodetic leveling survey method was used to confirm the result. The result showed that the subsidence rate was high in the southern part of the Hanoi city, from 2 cm to 3 cm per year. However, due to the limited number of images used, the result of this project was also affected by the systematic error. Herein, the subsidence was observed in areas near the Red River and the north of the city, though the geodetic leveling survey result confirmed that no subsidence existed in these areas.

In 2014, Dang et al. (2013) used the SBAS–PSInSAR method to determine the ground subsidence inventories and assess the relationship between the subsidence and the urbanization process for Hanoi. Herein, ALOS PALSAR images for the period 2007–2011 were considered. In a recent study, Le et al. (2016) employed the PSInSAR and TerraSAR-X high-resolution images to detect the land subsidence in the Historical Center of Hanoi in the period 2012–2013. In other projects, Cuong et al. (2015) and Van Anh Tran et al. (2016) estimated ground subsidence for Hanoi for the period 2007–2014 using the PSInSAR. These studies have proven the capability of using the PSInSAR method for ground subsidence at Hanoi.

Nevertheless, exploration of the PSInSAR, TerraSAR-X images, and Cosmo/SkyMed images for determining the subsidence of building blocks in the city has not been carried out. Therefore, in this work, we aim to partially fill this gap with a focus on building blocks at the Ha Dong district and Hoang Mai district in the city.

## 2 Study Area

### 2.1 Description of the Study Area

Hanoi is the capital of Vietnam, located in the northwest of the Red River delta with geographic coordinates from  $20^{\circ}53'$  to  $21^{\circ}23'$  north latitude,  $105^{\circ}44'$  to  $106^{\circ}02'$  east longitude (Fig. 1). The topography of Hanoi is gradually lowered from north to south and from west to east with an average height of 5 to 20 m above sea level. The hills are concentrated in the north and west of the city. Due to the alluvium deposition, three-quarters of the natural area of Hanoi is plain and located on the right bank of the Da River, the two sides of the Red River, and tributaries of other rivers. The mountainous area is mainly in Soc Son, Ba Vi, Quoc Oai, and My Duc districts, with the mountain peaks are in Ba Vi (1281 m), Gia De (707 m), and Chan Chim (462 m).

After the expansion of administrative boundaries in August 2008, Hanoi has an area of 3324.92 square kilometers. The highlight of the urbanization process in Hanoi is the gathering population in urban districts. There were 2.05 million people in 1990, but in 2000, the population increased to 2.67 million people. In 2007, approximately 3.4 million people, and in 2016, the population reached approximately 7.6 million. According to the census of population and housing in 2019, the

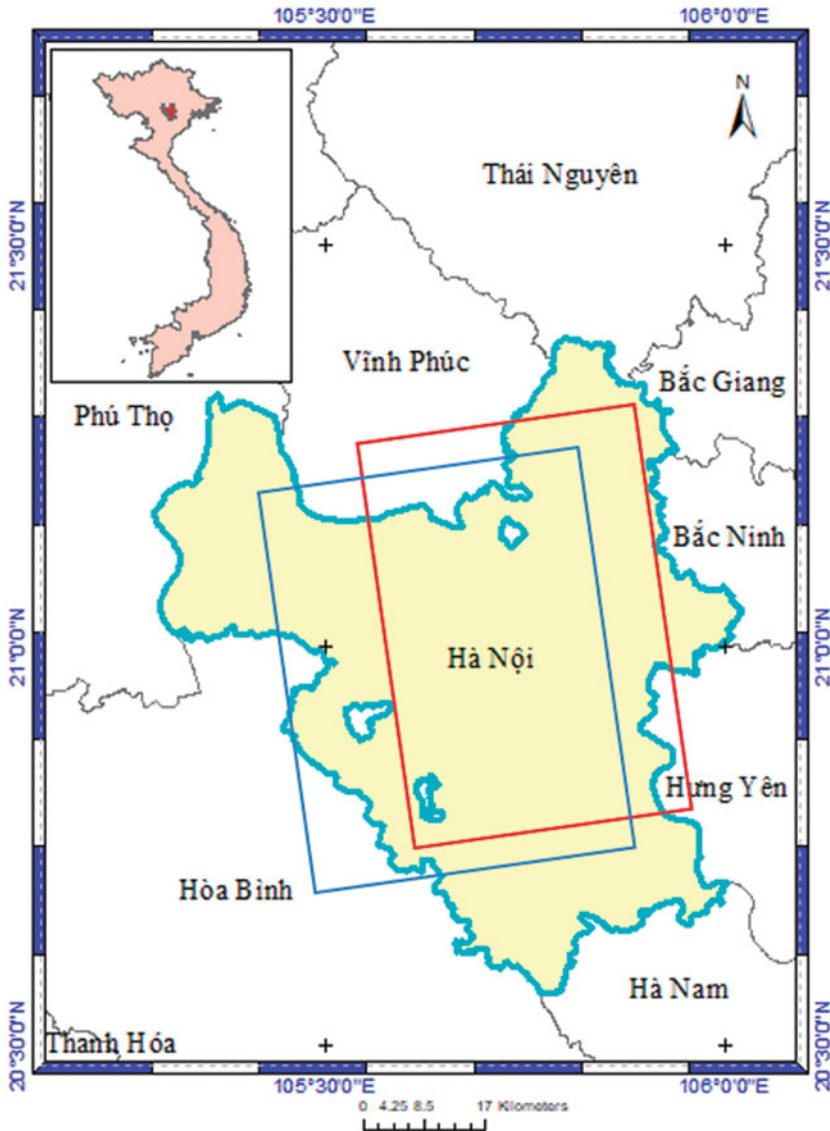


**Fig. 1** Location of the Hanoi urban area. The red rectangles are the frame of TerraSAR-X images, whereas the blue one is the frame of Cosmo/SkyMed images used in this study

total population in the city is 8.053 million people (GSO 2019). The urban population of Hanoi now accounts for about 60% of the city population. In contrast, the rural population tends to decrease. This is due to the urbanization process and the migration of young people from the rural to the urban areas. The expansion of the population size has led to a rapid increase in population density and imbalance.

The land subsidence issue in Hanoi has been recorded since the late 1980s of the last century, especially in areas with the old building blocks. According to the Department of Construction of the Hanoi city, there are about 1516 old building blocks, from two to five floors. They were mostly built between 1960 and the late 1980s; several buildings were built before 1954. Among 1516 building blocks, a total of 935 are located in four old urban districts, Ba Dinh, Hoan Kiem, Dong Da, and Hai Ba Trung. These building blocks can be classified into five groups: (1) prefabricated large panels building, (2) reinforced concrete frame building, (3) frame joints buildings, (4) mixed structures building, and (5) other structures. Due to economic and technological conditions at that time, most of these old building blocks were constructed on shallow foundations, which led to problems of subsidence of building blocks in later years. The most severe subsidence were observed at the E6/E7 Quynh Mai, the A/B Ngoc Khanh, the C1 Thanh Cong, the B7 Thanh Cong, and the B Ngoc Khanh.

In some new residential areas, such as Dong Tau, although building blocks were just used in 2006, the subsidence problem happened just after 1 year (in 2007). So far, subsidence has become more and more serious. Many building blocks have been subsided approximately 30 cm. The leading cause is that these blocks were constructed on the soft soil ground areas in the south of the city. Figure 2 presents the subsidence map (1988–1995) created by the Geological Institute, Vietnam Academy of Science and Technology (VAST). It could be seen that the subsidence mainly distributed in the south of the city, where the highest subsidence rate is the Linh Dam area.

## 2.2 Geological and Hydrological Setting

Geologically, more than 12 formations outcrop in Hanoi, however, their distributions are very different. Quaternary sediments are mainly distributed in the urban area. In contrast, in the northern and western suburbs districts (Dong Anh, Soc Son, Quoc Oai, Chuong My, and My Duc), metamorphic and sedimentary rocks are dominated (Phi and Strokova 2015; Thuan 2006), such as at Na Vang formation ( $P_{2nv}$ ), Yen Duyet formation ( $P_{3yd}$ ), Viet Nam formation ( $T_{1vn}$ ), Tan Lac formation ( $T_{1tl}$ ), Khon Lang Formation ( $T_{2kl}$ ), Na Khuat Formation ( $T_{2nk}$ ), Dong Giao Formation ( $T_{2ađg}$ ), Nam Tham Formation ( $T_{2nt}$ ), Song Boi Formation ( $T_{2-3sb}$ ), Ha Coi Formation ( $J_{1-2hc}$ ), and Tam Đảo formation ( $J-K_{1td}$ ).

Hydrogeologically, most of the groundwater at the Hanoi urban area resides in the quaternary formations, which can be separated into two aquifers, Holocene aquifer ( $QH$ ) and Pleistocene aquifer ( $QP$ ) (Tam and Nga 2018). The first aquifer has a mean thickness of 18.9 m, whereas, in the second one, the average thickness is 59.5 m. The average hydraulic conductivity is 12.5 m/day and 31.9 m/day for the  $QH$  aquifer and the  $QP$  aquifer, respectively.



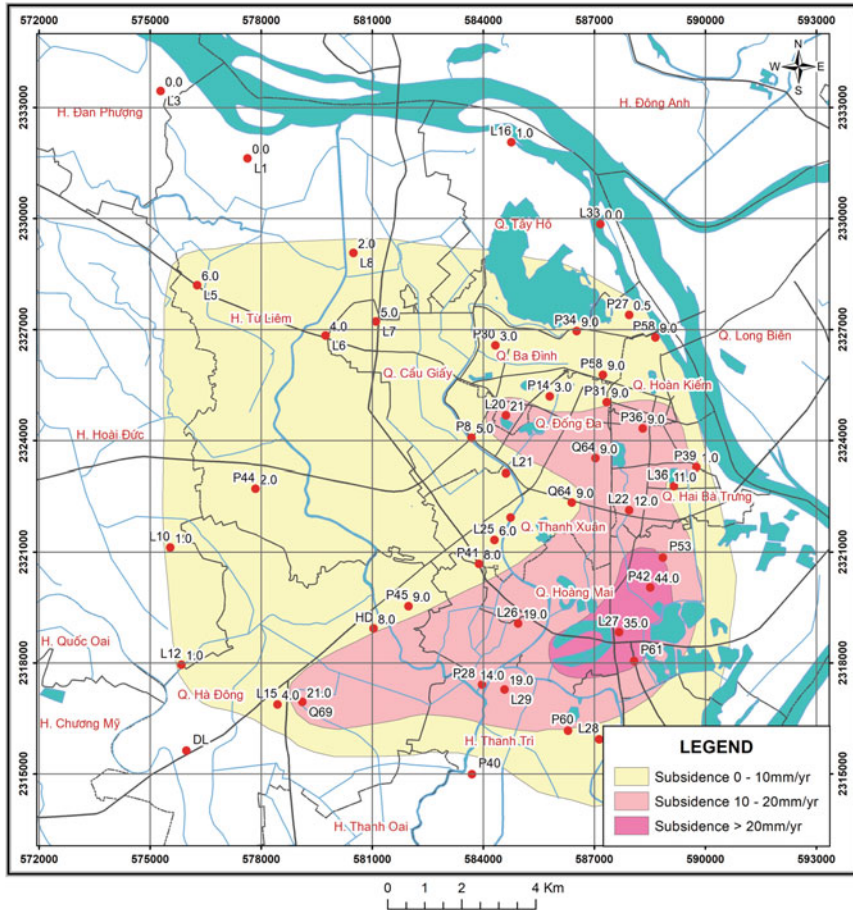


Fig. 2 Distribution of the subsidence at the Hanoi city derived from the geodetic leveling method

### 3 Data Used

#### 3.1 TerraSAR-X and Cosmo-SkyMed Data

In order to derive the subsidence of building blocks in this project, a total of 19 TerraSAR-X images (X-band with 3.1 cm wavelength, the StripMap mode) and 27 Cosmo-SkyMed images (X-band with 3.1 cm wavelength, the StripMap HI MAGE mode) for the period 2011–2014 were acquired. The reason for both the TerraSAR-X images and the Cosmo-SkyMed images were employed is that we want to verify the ability for the subsidence detection of the two types. The detailed information of these images is presented in Table 1.

**Table 1** Characteristics of the SAR data used (TSX: TerraSAR-X; CSM: Cosmo-SkyMed)

| TerraSAR-X (TSX)<br>Orbit (ascending) |                             |                    | COSMO SkyMed (CSK)<br>Orbit (ascending) |                             |                    |
|---------------------------------------|-----------------------------|--------------------|---|-----------------------------|--------------------|
| ID                                    | Acquisition Time<br>(D-M-Y) | Baseline Bn<br>[m] | ID                                      | Acquisition Time<br>(D-M-Y) | Baseline Bn<br>[m] |
| 1                                     | 10-04-2012                  | -42                | 1                                       | 27-05-2011                  | -601               |
| 2                                     | 21-04-2012                  | -24                | 2                                       | 05-07-2011                  | -213               |
| 3                                     | 26-06-2012                  | -133               | 3                                       | 15-08-2011                  | 644                |
| 4                                     | 11-09-2012                  | -384               | 4                                       | 22-08-2011                  | 1036               |
| 5                                     | 30-04-2013                  | 5                  | 5                                       | 23-09-2011                  | 1083               |
| 6                                     | 05-07-2013                  | -138               | 6                                       | 10-11-2011                  | 1283               |
| 7                                     | 20-09-2013                  | 60                 | 7                                       | 21-12-2011                  | -295               |
| 8                                     | <b>12-10-2013</b>           | 0                  | 8                                       | 22-01-2012                  | -95                |
| 9                                     | 23-10-2013                  | -120               | 9                                       | 10-03-2012                  | -19                |
| 10                                    | 25-11-2013                  | -63                | 10                                      | 05-06-2012                  | -66                |
| 11                                    | 11-06-2014                  | 137                | 11                                      | 16-07-2012                  | 810                |
| 12                                    | 22-06-2014                  | -89                | 12                                      | 24-08-2012                  | 294                |
| 13                                    | 25-07-2014                  | -179               | 13                                      | 21-11-2012                  | 758                |
| 14                                    | 07-09-2014                  | 215                | 14                                      | 30-12-2012                  | -247               |
| 15                                    | 29-09-2014                  | 45                 | 15                                      | 20-03-2013                  | 941                |
| 16                                    | 10-10-2014                  | 90                 | 16                                      | <b>08-06-2013</b>           | <b>0</b>           |
| 17                                    | 21-10-2014                  | 10                 | 17                                      | 27-08-2013                  | 108                |
| 18                                    | 01-11-2014                  | -91                | 18                                      | 14-10-2013                  | -298               |
| 19                                    | 23-11-2014                  | -54                | 19                                      | 15-11-2013                  | 1118               |
|                                       |                             |                    | 20                                      | 17-12-2013                  | 767                |
|                                       |                             |                    | 21                                      | 19-02-2014                  | 149                |
|                                       |                             |                    | 22                                      | 27-06-2014                  | -301               |
|                                       |                             |                    | 23                                      | 29-07-2014                  | -180               |
|                                       |                             |                    | 24                                      | 30-08-2014                  | 846                |
|                                       |                             |                    | 25                                      | 01-10-2014                  | 351                |
|                                       |                             |                    | 26                                      | 02-11-2014                  | 655                |
|                                       |                             |                    | 27                                      | 04-12-2014                  | 242                |

Figure 1 show two frames of TSX and CSK. It could be seen that the Hanoi area is fully covered by the TSX frame, but the CSK frame was slight to the left. Therefore, a part of the Red River was stayed outside of the CSK frame. By using the PSInSAR method, the TSX images were processed to derive 810,000 Persistent Scatterer (PS) points and 420,000 PS points for the study area, with the LOS angle of  $34.4^\circ$  and  $25.2^\circ$ , respectively. Figures 4 and 5 represent the result of the land subsidence distribution using the CSK and TSX images in the study area.

### 3.2 Geodetic Leveling Data

To verify the detected subsidence results using the PSInSAR in the study area, the subsidence at three building blocks, which were measured by the precise geodetic leveling method, were used. They include two building blocks, namely CC2 and CQ01 at the Van Quan area, Ha Dong district, and one building block of CC7 at the Linh Dam area, Hoang Mai district. These building blocks were selected because they have experienced a high level of subsidence. Herein, with the CC2, the measurement was conducted in 18 months, from April 2013 to November 2014. Whereas, for the CQ01, the survey was conducted in 30 months, from May 2012 to November 2014. For the case of the CC7, the precise geodetic leveling task was conducted in 41 months, from July 2011 to December 2014.

Tables 2, 3, and 4 show the displacement results of these building blocks measured by the precise geodetic leveling method. It should be noted that the measurement was conducted after the construction of these blocks was completed 1 year (Fig. 3).

## 4 Methodology

### 4.1 PSInSAR Method

Because the description of the PSInSAR method is well described in the literature, such as in Ferretti et al. (2000), therefore, in this section, only salient features of this method are provided. Herein, we focus on the distinction of different phases at a given location of a sequence of images. Thus, all images are co-registered together

**Table 2** Displacement results (mm) of the CQ01 building block at the Van Quan area

| Time (D/M/Y) | Subsidence |
|--------------|------------|
| 1/5/2012     | -2.25      |
| 1/7/2012     | -2.58      |
| 1/9/2012     | -2.94      |
| 11/10/2012   | -3.21      |
| 1/4/2013     | -3.41      |
| 1/5/2013     | -3.61      |
| 5/7/2013     | -4.4007    |
| 20/9/2013    | -4.8165    |
| 23/10/2013   | -4.9947    |
| 25/11/2013   | -5.1729    |
| 22/6/2014    | -6.3015    |
| 25/7/2014    | -6.4797    |
| 29/9/2014    | -6.8361    |
| 21/10/2014   | -6.9549    |
| 23/11/2014   | -7.1331    |

**Table 3** Displacement results (mm) of the CC7 building block at the Linh Dam area

| Time (D/M/Y) | Subsidence |
|--------------|------------|
| 30/7/2011    | -0.59      |
| 30/8/2011    | -1.17      |
| 30/9/2011    | -1.52      |
| 23/11/2011   | -2.16      |
| 21/12/2011   | -3.408     |
| 22/1/2012    | -3.9872    |
| 10/3/2012    | -4.856     |
| 5/6/2012     | -6.4307    |
| 16/7/2012    | -7.1728    |
| 24/8/2012    | -7.8787    |
| 21/11/2012   | -9.4896    |
| 30/12/2012   | -10.1955   |
| 20/3/2013    | -11.6435   |
| 8/6/2013     | -13.0915   |
| 27/8/2013    | -14.5395   |
| 14/10/2013   | -15.4083   |
| 15/11/2013   | -15.9875   |
| 17/12/2013   | -16.5667   |
| 19/2/2014    | -17.7251   |
| 27/6/2014    | -20.0419   |
| 29/7/2014    | -20.6211   |
| 30/8/2014    | -21.2003   |
| 1/10/2014    | -21.7795   |
| 2/11/2014    | -22.3587   |
| 4/12/2014    | -22.9379   |

**Table 4** Displacement results (mm) of the CC2 building block at the Van Quan area

| Time (D/M/Y) | Subsidence |
|--------------|------------|
| 10/4/2013    | -2.47      |
| 2/7/2013     | -4.82      |
| 8/9/2014     | -6.46      |
| 14/11/2014   | -7.12      |

by choosing one image as the master and the other as slave images. This will result in multiple pairs of images with different baselines. Figure 4 depicts the PSInSAR method, and Eq. (1) represents the synthetic phase of image pairs.

As depicted in Fig. 4, the point  $P$  is observed by  $N$  times in different scanning tracks, where  $N$  is the repetition of the same sensor. Each observation acquired an image of the whole scene. Two complex images can be combined to calculate the interferogram presented in Eq. (1) (Bamler and Hartl 1998).

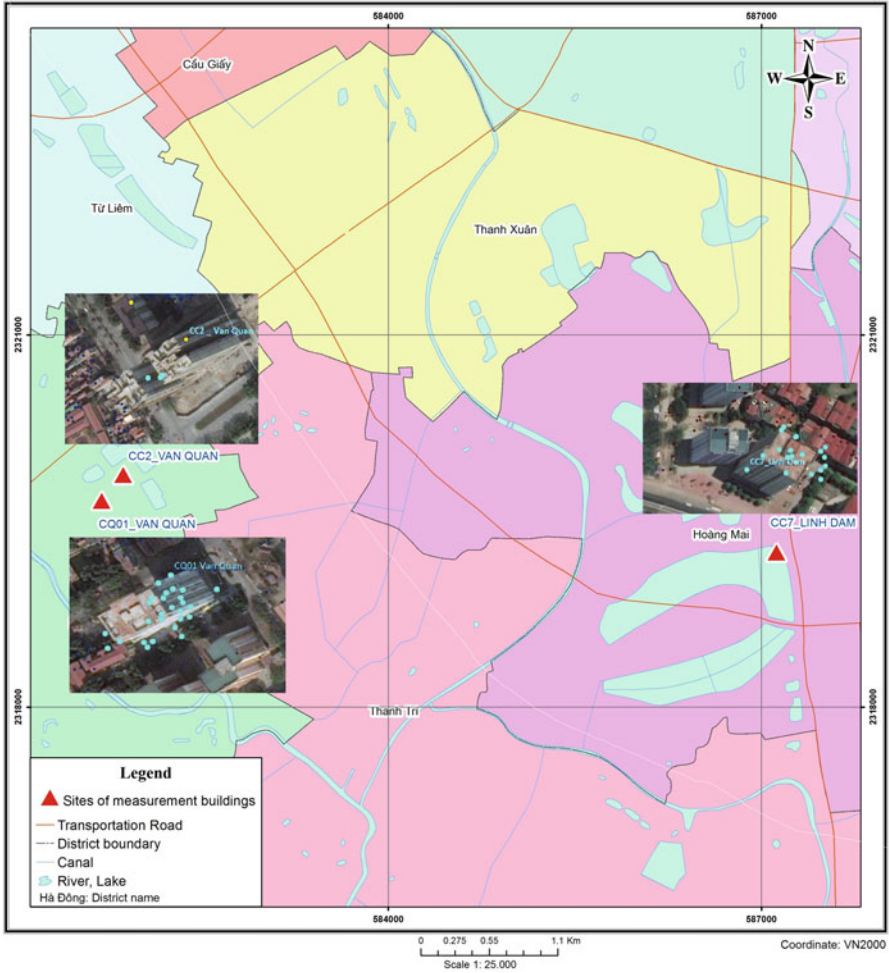


Fig. 3 Locations and photos of these building blocks, CQ01, CC7, and CC2

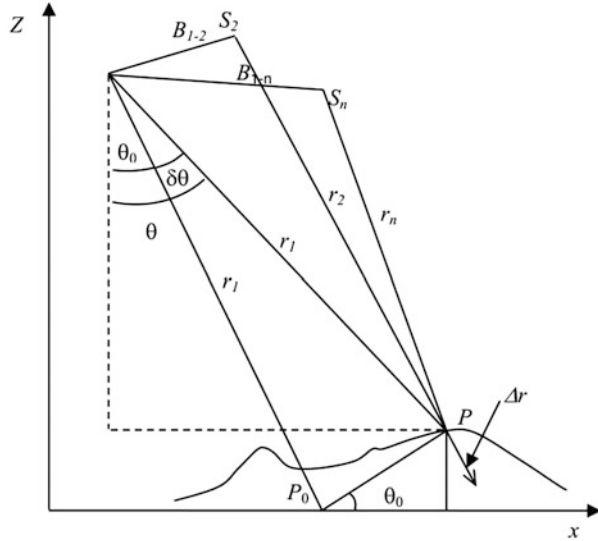
$$\varphi_{nm} = \varphi_n - \varphi_m = \left( \frac{4\pi}{\lambda} R_n(P) + \alpha(n) \right) - \left( \frac{4\pi}{\lambda} R_m(P) + \alpha(m) \right) \quad (1)$$

where  $R_n(P)$  and  $R_m(P)$  are the slant range from the  $n$ -th and  $m$ -th antenna to the  $P$  point on the earth surface, and  $\alpha(n)$  and  $\alpha(m)$  are the phase errors due to atmospheric propagation of the two times of acquisitions.

If there are terrain displacement, Eq. (1) can be written as follows:

$$R_n(P) = R_{n0} + v(P) \cdot t_n \quad (2)$$

**Fig. 4** InSAR geometry:  $N$  sensors, the displacement is Line of Sight direction



where  $v(P)$  is the Linear Deformation Rate;  $t_n$  is the time of the acquisition of the  $n$  pass.

The interferometric phases will store information about the geometry of the system, including the topographic phase and the displacement phase between the two acquisitions of the target (Ferretti et al. 2007).

The following is the explanation of the single-target model for the determination of deformations. First, we assume that each pixel in the SAR image is a target to be determined so that the value of each pixel is the sum of multiple scattering responses. The result is a realization of a stochastic process, in which the pdf conditioned on the interferometric phases may be regarded as being a zero-mean, multivariate circular normal distribution (Bamler and Hartl 1998). Therefore, the ensemble of the second-order moments represents sufficient statistics to infer information from the image data. With reference to a particular location in the slant range–azimuth plane, the expression of the second-order moment for the  $nm$ -th interferometric pair may be expressed, under the assumption of phase triangularity, as follows:

$$E[y_n y_m^*] = \gamma_{nm} \exp(j(\varphi_n - \varphi_m)) \tag{3}$$

where  $y_n$  is a pixel in the  $n$ -th SAR image at the considered slant range–azimuth location,  $y_m$  is a pixel in the  $m$ -th SAR image at the considered slant range–azimuth location,  $\gamma_{nm}$  is the coherence of the  $nm$ -th interferometric pair, and  $\varphi_n$  is the interferometric phase for the  $n$ -th acquisition.

It should be noted that the images are supposed to be normalized, such that  $E[|y_n|^2] = 1 \forall n$ , the interferometric phases can be expressed in vectors as follows:

$$\varphi = \psi(\theta) + \alpha \tag{4}$$

where  $\varphi = [\varphi_0 \dots \varphi_{N-1}]^T$  is the vector of the interferometric phases,  $\theta$  is the vector of the unknown parameters which describe the LDF and residual topography to be estimated,  $\psi(\theta) = [\psi_0(\theta) \dots \psi_{N-1}(\theta)]^T$  represents a vector of known functions of  $\theta$ , and  $\alpha = [\alpha_0 \dots \alpha_{N-1}]^T$  is the atmospheric field or atmospheric phase screen (APS), affecting the  $N$  acquisitions.

APS can be modeled according to a random process, spatially correlated, and not correlated with multiple image acquisitions with repetition intervals longer than 1 day (Guarnieri 2010). In this case, APS is modeled as a normal and zero mean stochastic process with variance  $\sigma_\alpha^2$ :

$$\alpha \sim N(0, R_\alpha); R_\alpha = \sigma_\alpha^2 I_n \tag{5}$$

where  $I_n$  is the  $N \times N$  identity matrix.

The full description of APS can be found in Guarnieri (2010).

The set of coherence,  $\gamma_{nm}$ , of each pair of the interferogram, which determines the correlation and the lost correlation of the pixels due to different causes such as superficial, volumetric, and temporal, is proposed by Zebker and Villasenor (1992) in Eq. (6) below:

$$\gamma_{nm} = \gamma_0 \gamma_{nm}^{sup} \gamma_{nm}^{vol} \gamma_{nm}^{temp} \tag{6}$$

From Eq. (3), we could derive the following equation:

$$R^{def} = E[yy^H] = \phi \Gamma \phi^H \tag{7}$$

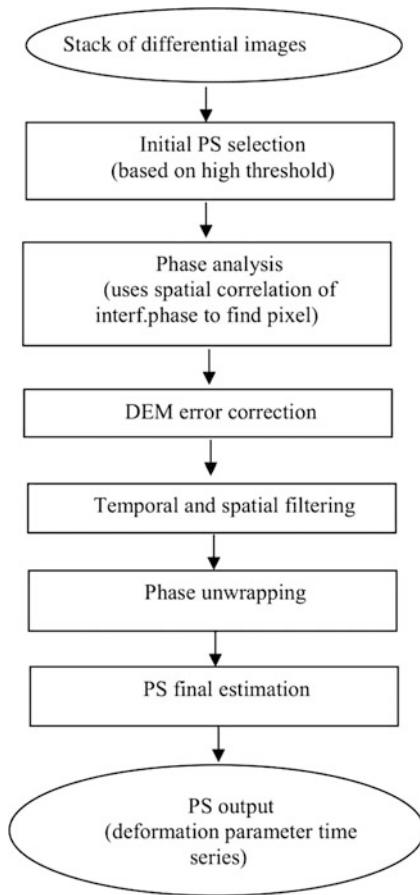
where  $R$  is the data covariance matrix;  $y = [y_0 \dots y_{N-1}]^T$  is the stack of the SLC images at a given location,  $(r, x)$ , in the slant range, azimuth plane;  $\Gamma$  represents an  $N \times N$  symmetric matrix, whose elements are given by the interferometric coherences  $[\Gamma]_{nm} = \gamma_{nm}$ ; and  $\phi$  is an  $N \times N$  diagonal matrix whose elements are given by the interferometric phases:

$$\phi = diag\{ \exp(j\varphi_0) \dots \exp(j\varphi_{N-1}) \} \tag{8}$$

With the use of the PSInSAR method, our goal is to separate the deformation phase from general phases. The separation of these phases requires the use of an accurate digital topography model and selection of permanent scattering (PS) points, which are selected based on the high scattering points above all image pairs. The processing procedure is shown in Fig. 5, which is the implementation process to detect the subsidence at PS scattering points with the StaMPS software (Hooper et al. 2010).

According to Ferretti et al. (2001), the selection of permanent scattering points based on amplitude stability. As we already know, the observation signal of the SAR image is the set:  $s_i = 1 + n_i$  for  $i = 0, 1, \dots, N$ , therefore, the scattered amplitude points are:

**Fig. 5** Flow chart of the SAR image processing in this research



$$DA = \sigma_{|s|} / M_{|s|} \tag{9}$$

Stable amplitude points will be used to determine the stability phase. Determining these permanent scattering points is relatively easy with the set of SLC images that have been co-registration. In urban areas where there is much angular scattering, various permanent scattering points can be derived, so this approach is well suited for structure monitoring.

## 4.2 Accuracy Assessment

In this project, the accuracy assessment is carried out by comparing the subsidence results derived from the TerraSAR-X and 27 COSMO-SkyMed images with the



PSInSAR method and those from the precise geodetic leveling technique, which described in Tables 2, 3, and 4. Herein, Root Mean Squared Error (RMSE) in Eq. (10) was used.

$$\text{RMSE} = \sqrt{\frac{(d_{\text{PSI}} - d_{\text{lev}})^2}{n}} \quad (10)$$

where  $d_{\text{PSI}}$  is the subsidence derived from the PSInSAR method;  $d_{\text{lev}}$  is the subsidence obtained from the precise geodetic leveling method; and  $n$  is the number of the measurement points used.

## 5 Results and Discussion

The results of the subsidence in this research are shown in Figs. 6, 7, and 8. With the PSInSAR method, the TSX images show 810,000 PS points and the LOS angle is  $34.4^\circ$ , whereas with the LOS angle of  $25.2^\circ$  a total of 420,000 PS points is derived.

As shown in Figs. 6 and 7, it is found that the distributions of subsidence made by these two types of images are quite similar, especially in the south of the city. However, for the result of the Cosmo-SkyMed images, the number of the PS points is less than that of the TerraSAR-X images. Thus, this result leads to more holes in the subsidence image, where the coherences are low or less permanent scatters are at these locations.

After determining the land subsidence by the two types of data, we randomly selected 18 points spread over the entire study area to compare the subsidence values from the TerraSAR-X images and the Cosmo-SkyMed images. The correlation of the two subsidence results is shown in Fig. 8 with  $R^2$  of 0.91, indicating that the subsidence values are similar in almost positions, and they can be used to complement each other in places where the image loses coherence.

In order to validate the subsidence result deriving from the TerraSAR-X images and the Cosmo-SkyMed images, the subsidence results at the three building blocks, CC2, CQ01, and CC7 obtained from the precise geodetic leveling method, mentioned in Sect. 3.2, were used. The locations of the surveyed buildings are shown above in Fig. 3, which are marked by a red triangle. At these locations, the CC7 can identify the PS subsidence points with the Cosmo-SkyMed images, while at the CC2 and CQ01 the PS subsidence points are from the TerraSAR-X images. These PS points were overlaid over the 3D imagery of the study area to extract PS points on the three building blocks above. Then, the coordinates of each PS point can be expressed in values  $(x, y, z)$ . Herein, we extract only PS points that match the time with the precise geodetic leveling. It could be observed that each building block has different measured values, the CC2 has the least leveling values (measured only in four periods), whereas the CQ01 and CC7 were measured in a long time series and nearly

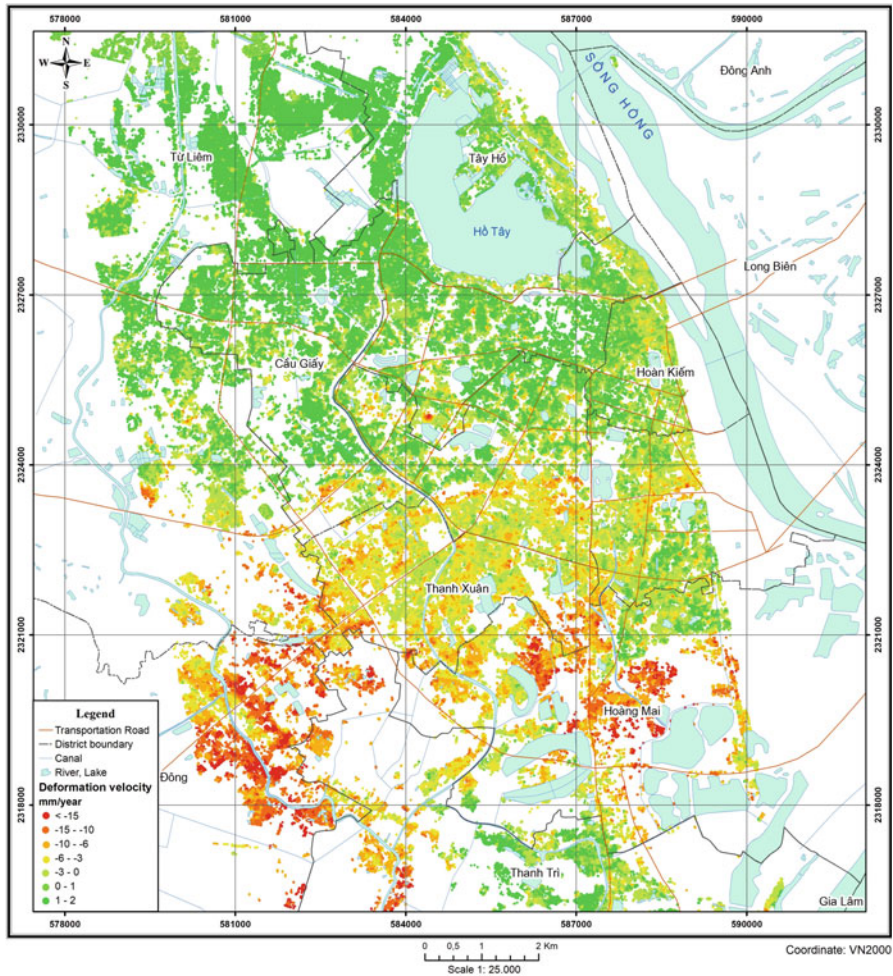


**Fig. 6** Land subsidence map for the study area in the period 2011–2014 using the Cosmo-SkyMed

coincided with the image acquisition time (see Tables 2, 3, and 4). The result is shown in Figs. 9, 10, and 11.

For the chart in Figs. 9, 10, and 11, the x-axis represents the subsidence calculated from the PSInSAR and the y-axis represents the subsidence measured by the leveling method. The black line represents the linear regression line. Blue points are subsidence points determined by the two methods at different times.

In the CQ01 building block, there are 15 PS points, whereas the CC7 has 24 PS points and the CC2 has PS 4 points. The regression equation shows the degree of coherence of these two data types. The result shows that all correlations between the two methods are higher than 0.85, indicating that the subsidence of the building blocks derived from the PSInSAR method is in line with those from the precise

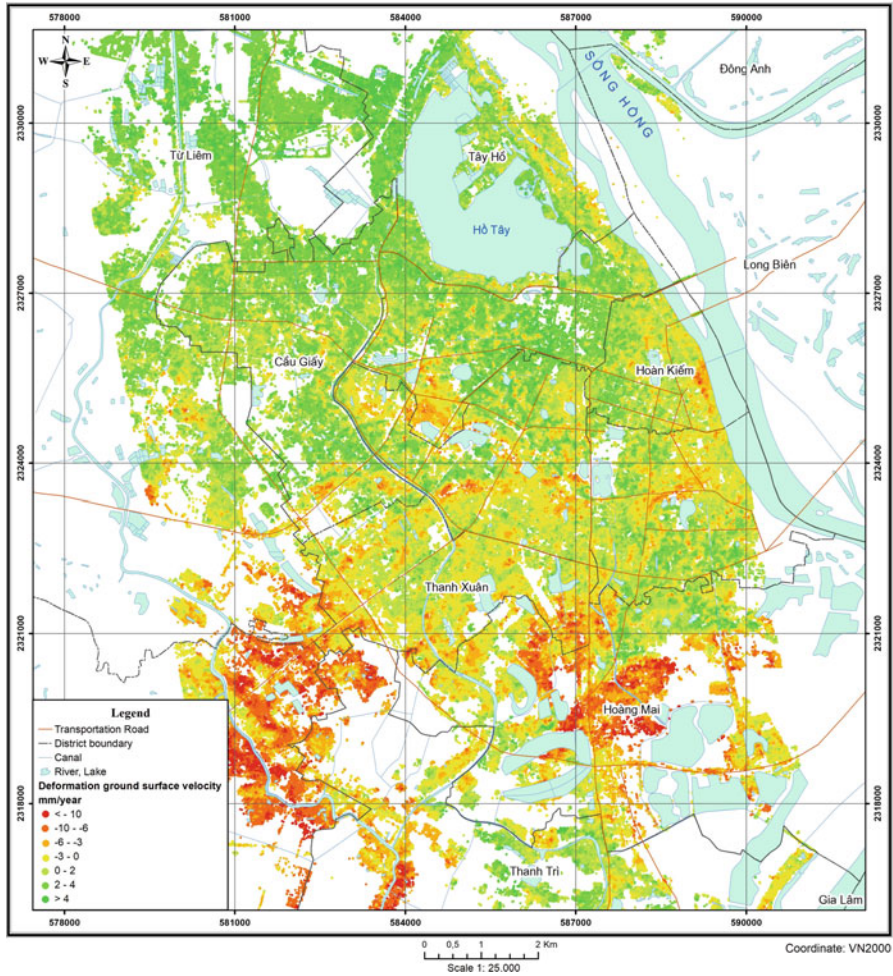


**Fig. 7** Land subsidence map for the study area in the period 2012–2014 using the TerraSAR-X

geodetic leveling. For a better understanding of the subsidence differences between the PSInSAR and the precise geodetic leveling, diagrams of subsidence in time series were produced, and the results are shown in Figs. 12, 13, and 14.

In Figs. 12, 13, and 14, the blue points are subsidence points from the PSInSAR method, and the brown points are subsidence points from the leveling method. The vertical axis is the subsidence, and the horizontal axis is the times of building measurement. The solid black regression line is the regression line of subsidence values from the images, and the dashed regression line is the regression line of the subsidence values measured by the leveling method. It could be observed that the subsidence derived from the two types of the TerraSAR-X images and the Cosmo-SkyMed images with the PSInSAR method are higher than the values measured by

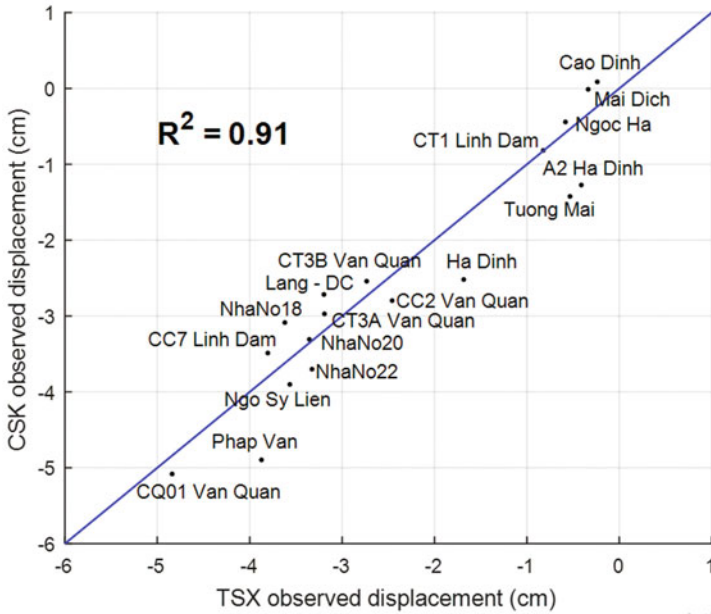


**Fig. 8** Correlation between land subsidence results in the period of 2011–2014 using the TerraSAR-X images and the Cosmo-SkyMed images

Correlation between subsidences by TSX and leveling survey at CQ01

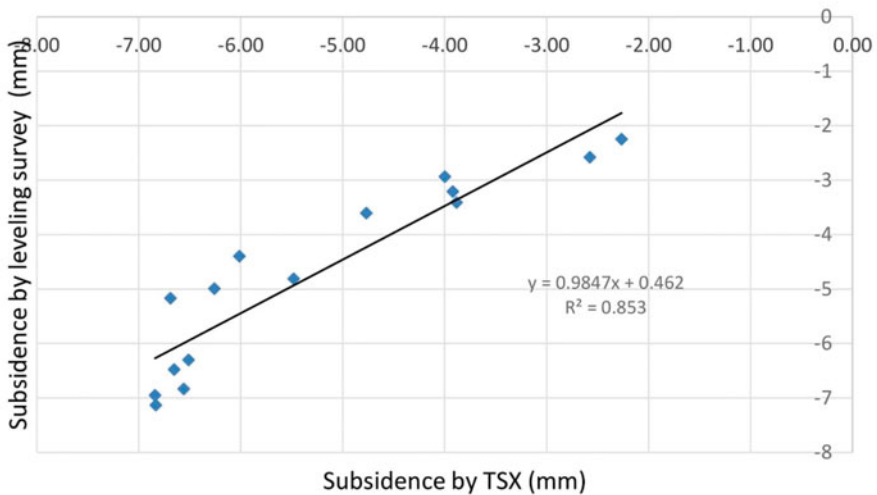


**Fig. 9** Correlation between subsidence rate values by the precise geodetic leveling method at CQ01 Van Quan and those calculated from TerraSAR-X images for the period of 2012–2014

Correlation between subsidences by TSX and leveling survey at CC7

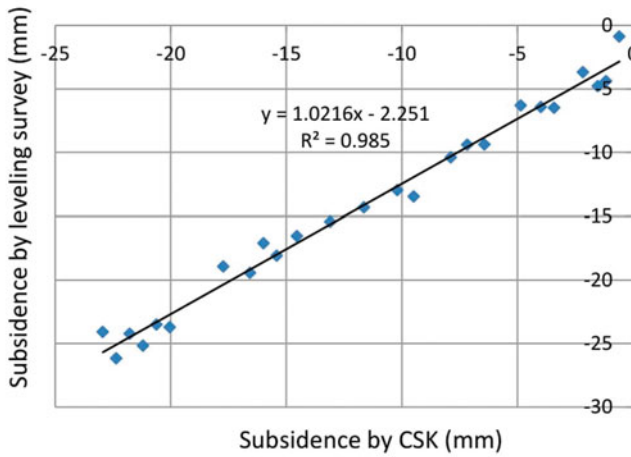


**Fig. 10** Correlation between subsidence rate values by the precise geodetic leveling method at the CC7 Linh Dam and that calculated from the Cosmo-SkyMed images for the period of 2012–2014

Correlation between subsidences by TSX and leveling survey at CC2

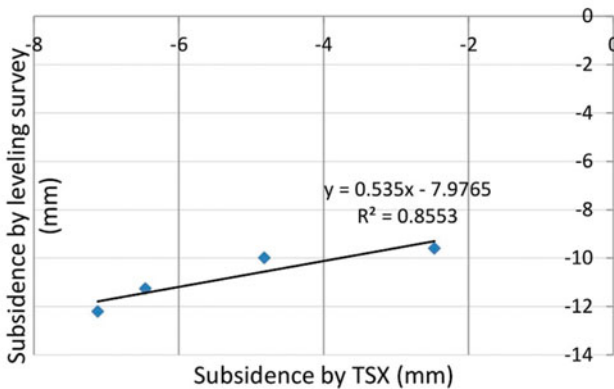


**Fig. 11** Correlation between subsidence rate values by the precise geodetic leveling method at CC2 Van Quan and those calculated from the Cosmo-SkyMed images for the period of 2013–2014

the leveling method. The difference between the two regression lines shows the accuracy of the PSInSAR measurement. At the CC2 building block, the measurement time for this building was just over 1 year, from 2012 to 2013; therefore, the error at this building is quite high, RMSE is about 5.5 mm/year. For the CQ01 building block, the surveying time was longer, from 2012 to 2014; therefore, the number of the PS points were also higher; so RMSE here is about 1.6 mm/year.

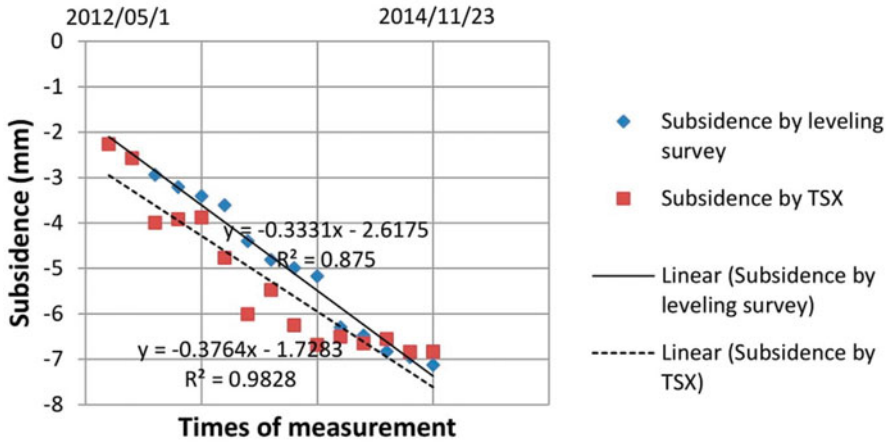


**Fig. 12** Validation between subsidence values by the precise geodetic leveling at the CQ01 Van Quan and land subsidence calculated from the TerraSAR-X images by the PSInSAR method for the period of 2012–2014

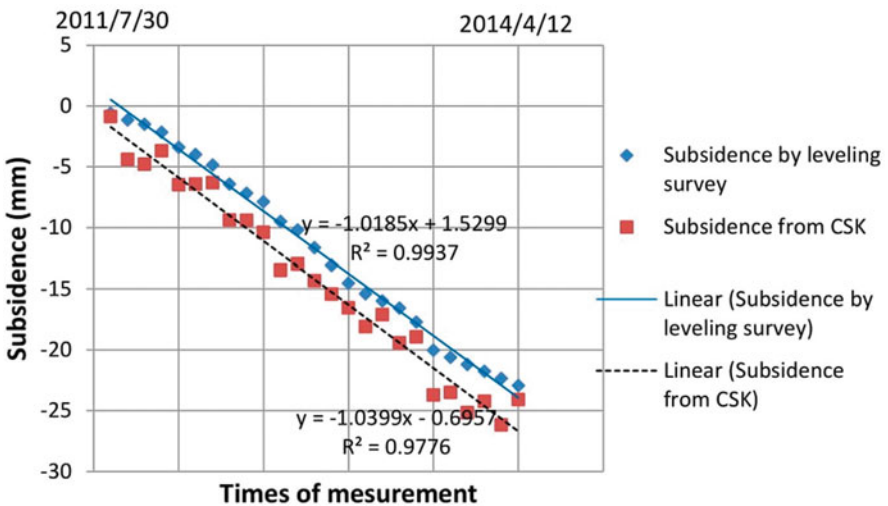


**Fig. 13** Validation between subsidence values by the precise geodetic leveling at the CC7 Linh Dam and land subsidence calculated from Cosmo-SkyMed images by the PSInSAR method for the period of 2011–2014

Regarding the CC7 building block, the survey time was the longest, from 2011 to 2014. RMSE of the subsidence between the PSInSAR and the leveling method is about 2.5 mm/year.

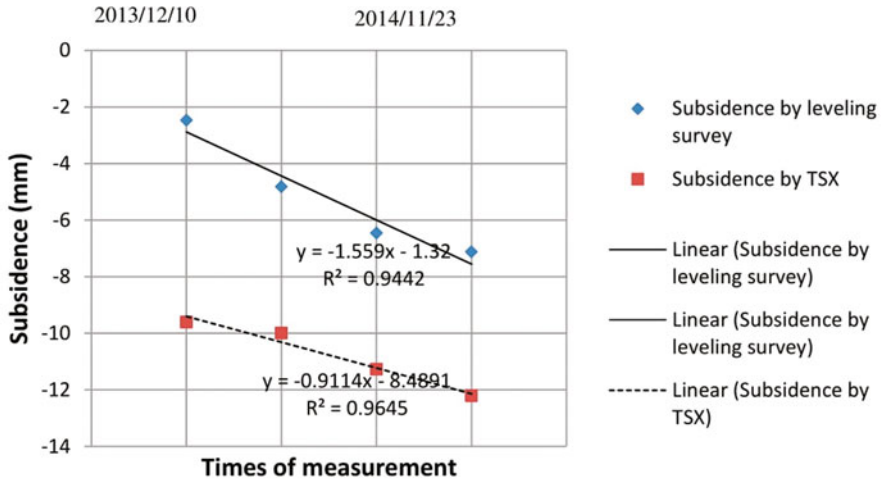


**Fig. 14** Validation between subsidence values by the precise geodetic leveling at the CC2 Van Quan and land subsidence calculated from the TerraSAR-X images by the PSInSAR method for the period of 2012–2014

## 6 Conclusions

In this research, we assessed the subsidence of the building blocks in the southern part of the Hanoi urban area using the TerraSAR-X images and the Cosmo-SkyMed images with the PSInSAR method. The subsidence result was validated by comparing it to those measured by the precise geodetic leveling method. Based on the RMSE and  $R^2$  of the subsidence between the two methods, it could be concluded that the PSInSAR method produced a good result. Thus, these methods can be used to complement each other.

The limitation of this research is that only the subsidence at three building blocks was validated; therefore, it is impossible to confirm which of the image, the TerraSAR-X or the Cosmo-SkyMed, is better for the detection of the building subsidence. The amount of the PS points derived from the TerraSAR-X is more massive than those of the Cosmo-SkyMed, because the TerraSAR-X image covers a larger area than that of the Cosmo-SkyMed.

The subsidence velocities measured from the precise geodetic leveling method tends to be lower than those obtained from the PSInSAR. However, when the length of the measurement time of the leveling method is longer, the subsidence difference between the two methods is narrowed. The error is high (5.5 mm/year) at the CC2 building block with a short surveying time. Whereas with the other building blocks, the CC7 and the CQ01, the error is less than 2.5 mm/year.

Overall, this work also showed that the PSInSAR method with the TerraSAR-X images and the Cosmo-SkyMed images for detecting the subsidence of building blocks in urban areas is promising, which can help in monitoring the subsidence of

buildings in large areas. The subsidence information from the PSInSAR method is also easily converted and integrated into GIS for further analysis.

**Acknowledgments** The research was supported by the Viet Nam National Science Project (the project code is DTDL.2012-T/28). The authors would like to thank the Geographical Institute and the Remote Sensing Center of Vietnam for supporting the material facilities.

## References

- Anh, T. V., Cuong, T. Q., Anh, N. D., & Khac, D. V. (2016). Study of subsidence detection by DinSAR and evaluation of some factors to the outcome. *Vietnam Journal of Earth Sciences*, 37, 344–354.
- Aobpaet, A., Cuenca, M. C., Hooper, A., & Trisirisatayawong, I. (2009). Land subsidence evaluation using. In Lacoste-Francis, H (Ed.), *SAR time series analysis in Bangkok metropolitan area: Fringe 2009 workshop*, Frascati, Italy.
- Bamler, R., & Hartl, P. (1998). Synthetic aperture radar interferometry: Inverse problems, v. 14, p. R1.
- Biswas, K., Chakravarty, D., Mitra, P., & Misra, A. (2019). Investigation of ground deformation with PSInSAR approach in an unstable urban area Naples, Italy using X-band SAR images: Active and Passive Microwave. *Remote Sensing for Environmental Monitoring, III*, 111540J.
- Ciampalini, A., Bardi, F., Bianchini, S., Frodella, W., Del Ventisette, C., Moretti, S., & Casagli, N. (2014). Analysis of building deformation in landslide area using multisensor PSInSAR™ technique. *International Journal of Applied Earth Observation and Geoinformation*, 33, 166–180.
- Colesanti, C., Ferretti, A., Novali, F., Prati, C., & Rocca, F. (2003). SAR monitoring of progressive and seasonal ground deformation using the permanent scatterers technique. *IEEE Transactions on Geoscience and Remote Sensing*, 41, 1685–1701.
- Cuong, T. Q., Minh, D. H. T., & Le Toan, T. (2015). Ground subsidence monitoring in Vietnam by multi-temporal InSAR technique: *Geoscience and Remote Sensing Symposium (IGARSS), 2015 IEEE International*, pp. 3540–3543.
- Damoah-Afari, P., Ding, X.-L., Li, Z., Lu, Z., & Omura, M. (2007). Six years of land subsidence in Shanghai revealed by JERS-1 SAR data: *Geoscience and Remote Sensing Symposium, 2007. IGARSS 2007. IEEE International*, pp. 2093–2097.
- Dang, V., Doubre, C., Weber, C., Masson, F., & Gourmelen, N. (2013). Recent land subsidence caused by the rapid urban development in the Hanoi urban region (Vietnam) using ALOS InSAR data. *Natural Hazards and Earth System Sciences Discussions*, 1, 6155–6197.
- Dang, V. K., Doubre, C., Weber, C., Gourmelen, N., & Masson, F. (2014). Recent land subsidence caused by the rapid urban development in the Hanoi region (Vietnam) using ALOS InSAR data. *Natural Hazards and Earth System Sciences*, 14, 657.
- Dehls, J., & Nordgulen, Ø. (2003). *Evaluation of the use of PSInSAR for the monitoring of subsidence in Oslo region*: Geological Survey of Norway Report 2003.105.
- Ferretti, A., Prati, C., & Rocca, F. (2000). Nonlinear subsidence rate estimation using permanent scatterers in differential SAR interferometry. *IEEE Transactions on Geoscience and Remote Sensing*, 38, 2202–2212.
- Ferretti, A., Prati, C., & Rocca, F. (2001). Permanent scatterers in SAR interferometry. *IEEE Transactions on Geoscience and Remote Sensing*, 39, 8–20.
- Ferretti, A., Monti-Guarnieri, A., Prati, C., Rocca, F., & Massonet, D. (2007). *InSAR principles-guidelines for SAR interferometry processing and interpretation*, TM-19. Retrieved from The Netherlands.



- Gernhardt, S., & Bamler, R. (2012). Deformation monitoring of single buildings using meter-resolution SAR data in PSI. *ISPRS Journal of Photogrammetry and Remote Sensing*, 73, 68–79.
- Graham, L. C. (1974). Synthetic interferometer radar for topographic mapping. *Proceedings of the IEEE*, 62, 763–768.
- GSO. (2019). *General statistics office of Vietnam*. <https://www.gso.gov.vn>
- Guarnieri, S. T. a. A. M. (2010). *Methods and performances for multi-pass SAR interferometry*. Geoscience and Remote Sensing New Achievements Intech Open.
- Hooper, A., Spaans, K., Bekaert, D., Cuenca, M. C., Ankan, M., & Oyen, A. (2010). StaMPS/MTI manual: Delft Institute of Earth Observation and Space Systems Delft University of technology. *Kluyverweg*, 1, 2629.
- Hu, L., Dai, K., Xing, C., Li, Z., Tomás, R., Clark, B., Shi, X., Chen, M., Zhang, R., & Qiu, Q. (2019). Land subsidence in Beijing and its relationship with geological faults revealed by Sentinel-1 InSAR observations. *International Journal of Applied Earth Observation and Geoinformation*, 82, 101886.
- Le, T. S., Chang, C.-P., Nguyen, X. T., & Yhokha, A. (2016). TerraSAR-X data for high-precision land Subsidence monitoring: A case study in the historical Centre of Hanoi, Vietnam. *Remote Sensing*, 8, 338.
- Liu, L., J. Yu, B. Chen, and Y. Wang, 2020, Urban subsidence monitoring by SBAS-InSAR technique with multi-platform SAR images: A case study of Beijing plain, China. : European Journal of Remote Sensing, p. 1–13.
- López-Quiroz, P., Doin, M.-P., Tupin, F., Briole, P., & Nicolas, J.-M. (2009). Time series analysis of Mexico City subsidence constrained by radar interferometry. *Journal of Applied Geophysics*, 69, 1–15.
- Motagh, M., Djamour, Y., Walter, T. R., Wetzel, H.-U., Zschau, J., & Arabi, S. (2007). Land subsidence in Mashhad Valley, northeast Iran: results from InSAR, levelling and GPS. *Geophysical Journal International*, 168, 518–526.
- Peltzer, G., & Rosen, P. (1995). Surface displacement of the 17 May 1993 Eureka Valley, California, earthquake observed by SAR interferometry. *Science*, 268, 1333.
- Phi, T. H., & Strokova, L. A. (2015). Prediction maps of land subsidence caused by groundwater exploitation in Hanoi, Vietnam. *Resource-Efficient Technologies*, 1, 80–89.
- Raucoules, D., & Carnec, C. (1999). DEM derivation and subsidence detection on Hanoi from ERS SAR interferometry. In *Proceedings of 2nd international workshop on ERS SAR interferometry: Fringe*.
- Rott, H., Mayer, C., & Siegel, A. (2000). *On the operational potential of SAR interferometry for monitoring mass movements in alpine areas: EUSAR 2000*, pp. 43–46.
- Solari, L., Ciampalini, A., Raspini, F., Bianchini, S., & Moretti, S. (2016). PSInSAR analysis in the Pisa urban area (Italy): A case study of subsidence related to stratigraphical factors and urbanization. *Remote Sensing*, 8, 120.
- Tam, V. T., & Nga, T. T. V. (2018). Assessment of urbanization impact on groundwater resources in Hanoi, Vietnam. *Journal of Environmental Management*, 227, 107–116.
- Thuan, D., (2006). *Results of palynological analysis of the Neogene deposits from the northern part of Vietnam* (12 p). Hanoi: Vietnamese Academy of Science and Technology, Institute of Geological Sciences.
- Tran, V. A., Masumoto, S., Raghavan, V., & Shiono, K. (2007). Spatial distribution of subsidence in Hanoi detected by JERS-1 SAR interferometry. *Geoinformatics*, 18, 3–13.
- Tu, T. V., Anh, H. N., Duc, D. M., & Tung, N. M. (2013). Prediction of the ground subsidence at ha dong area due to urbanization and ground water exploitation. *Journal of Sciences of the Earth*, 35, 29–35.
- Van Anh Tran, Q. C. T., Nguyen, D. A., & Nguyen, N. H. (2016). Application of PSInSAR method for determining of land subsidence in Hanoi city by Cosmo-Skymed imagery. *GIS IDEAS*, 2016.
- Yang, Y., Pepe, A., Manzo, M., Bonano, M., Liang, D., & Lanari, R. (2013). A simple solution to mitigate noise effects in time-redundant sequences of small baseline multi-look DInSAR interferograms. *Remote Sensing Letters*, 4, 609–618.

- Yen, J.-Y., Chen, K.-S., Chang, C.-P., & Wang, C.-T. (2005). *Temporal and spatial pattern of the 1997 Manyi earthquake using differential InSAR: geoscience and remote sensing symposium, 2005. IGARSS'05. Proceedings. 2005 IEEE International*, pp. 5308–5311.
- Yen, J.-Y., Chen, K.-S., Chang, C.-P., & Boerner, W.-M. (2008). Evaluation of earthquake potential and surface deformation by differential interferometry. *Remote Sensing of Environment*, 112, 782–795.
- Zebker, H. A., & Villasenor, J. (1992). Decorrelation in interferometric radar echoes. *IEEE Transactions on Geoscience and Remote Sensing*, 30, 950–959.
- Zebker, H. A., Rosen, P. A., & Hensley, S. (1997). Atmospheric effects in interferometric synthetic aperture radar surface deformation and topographic maps. *Journal of Geophysical Research: Solid Earth*, 102, 7547–7563.
- Zhang, Y., Zhang, J., Wu, H., Lu, Z., & Guangtong, S. (2011). Monitoring of urban subsidence with SAR interferometric point target analysis: A case study in Suzhou, China. *International Journal of Applied Earth Observation and Geoinformation*, 13, 812–818.
- Zhou, C., Lan, H., Gong, H., Zhang, Y., Warner, T. A., Clague, J. J., & Wu, Y. (2020). Reduced rate of land subsidence since 2016 in Beijing, China: Evidence from Tomo-PSInSAR using RadarSAT-2 and Sentinel-1 datasets. *International Journal of Remote Sensing*, 41, 1259–1285.

# Analysis of Land Use/Land Cover Mapping for Sustainable Land Resources Development of Hisar District, Haryana, India



B. S. Chaudhary, Reeta Rani, Sanjeev Kumar, Y. P. Sundriyal, and Pavan Kumar 

**Abstract** Natural resources on the earth are being continuously stressed to meet the demands of increasing population. The increasing population requires enhanced production of food, energy, and water. To ensure reasonable civic amenities for quality life, there is need for the development of more infrastructure, more areas under habitation, and enhanced per capita expenditure. Land resources, being finite, need to be prudently used to meet the ever-increasing demand. This requires the study of land use/land cover (LU/LC) and its monitoring to understand the changing dynamics and optimal utilization of the resources. Geoinformation technologies are helpful to a great extent for not only creation of baseline information but also to monitor such changes. The present study has been carried out for Hisar district of Haryana state, India, over a period of 10 years to understand the change in the land use/land cover pattern. The district has a total geographical area of 4174.52 sq. km. Digital image processing with selected ground truth has been carried out for generating the information from satellite data. IRS/LANDSAT data have been used for the purpose. This information has been analyzed in the light of various land resources constraints by taking collateral information on soil types, groundwater quality, and depth along with geomorphological constraints. This information has been used for suggesting land resources development plan for the region which will ensure optimum and prudent use of land resources.

**Keywords** Land use/land cover · Hisar · India · Land resources and sustainable development

---

B. S. Chaudhary  
Department of Geophysics, Kurukshetra University, Kurukshetra, Haryana, India  
e-mail: [bschaudhary@kuk.ac.in](mailto:bschaudhary@kuk.ac.in)

R. Rani · S. Kumar · Y. P. Sundriyal  
Department of Geology, HNB Garhwal Central University, Srinagar, Uttarakhand, India

P. Kumar (✉)  
College of Horticulture and Forestry, Rani Lakshmi Bai Central Agricultural University, Jhansi, Uttar Pradesh, India

## 1 Introduction

Land use refers to human use of an area of the earth. Generally, the land is divided into sections, such as forest land, agricultural land, fallow land, pasture etc., informing the economic activity that takes place on the land. Land use and changes in it have a very important impact on the environment and ecology of an area (Anderson 1971; Arya et al. 1999; Chaudhary and Kumar 2017; Chaudhary et al. 2008). Among the issues related to natural resource conservation are the points related to land use conservation: soil erosion and conservation, soil quality enhancement, water quality and availability, vegetation protection, wildlife habitat, etc. Land use and land cover have different significance in their own ways and is the basis for Natural Resources Census. Land use is defined as a land which is used by different human activities like farms, industry, etc., or how land is utilized; land cover is slightly different (Xiubin 1996; Turner et al. 1994; Falcucci et al. 2007). Land cover is that land on which physical material is present at the surface of earth, like trees, bare land, etc. Land classification refers to different land types based on similar character. Land can be classified based on physical determinants such as soil profile, soil texture, and many different conditions, as well the purpose for which it is being used. Land Cover Classification considers biophysical individuality. Land Use Classification considers the serviceable use of land associated with human activities (Anderson et al. 1976).

Remote sensing application technology provides reliable information on natural resources and proper data acquisition system, both quantitative and qualitative. It is useful for planners and natural resources persons. This technology proved to be a boon to land use planners. Land comprises all elements of the physical environment to the extent that these influence potential for land use. The growing pressure of population coupled with increasing multiple requirements – environmental, social, and land use problems – have necessitated the optimum utilization of land of an area. Information on existing land use is essential for planning optimal utilization of land (Chaudhary 2003; Clevers et al. 1999; Dhawan 2017; Gupta and Roy 2012; Hooda et al. 1992; Hussin and Shaker 1995). Land use is a dynamic phenomenon and controlled by several factors such as climate, geomorphology, soils, water availability, socioeconomic and cultural factors, etc. The physical results of past human activity, such as vegetation clearance, etc., are included within the concept of land use changes. Unfavorable consequences from past use, such as eroded soils, degraded vegetation, and salt-affected soils, must also be included.

Land and soil are precious natural resources and are nature's gift to the human-kind. The prosperity of a country depends on the richness of these resources. In a country like India, where the population pressure on land is high, rational utilization of the land resources assumes great importance for the optimal and sustained production with minimum hazards. Essentially, this will mean proper utilization of land and soil. These resources, however, have been most recklessly used by humans in the past to extract more and more from them. This has caused rapid deterioration and degradation of lands. Land is the basic and most important resource in Haryana,

as it is true for nearly all other states of the country (Kumar 2017; Kushwaha and Oesten 1995; Ram and Singh 1995; Rani 2017; Toleti 1995).

The land resources are limited, as the total geographical area is fixed. Land is, therefore, scarce in supply. It is irreplaceable and not reproducible. While the land is finite, the population dependent on land and its needs are infinite (Narumalani et al. 2004; Reid et al. 2000; Kuemmerle et al. 2006). These have been increasing with time. Per capita availability of the resources, therefore, has been declining. One of the prime requisites for better land use is information on existing land use and the distribution of settlement, forest, agricultural land, barren land, etc., and they are important to determine land use policy, planning of transportation, and communication services, etc. The present land use is the result of different causes which are related to landforms, soil conditions, irrigation facilities, marketing, communication and transport, and socioeconomic conditions (Yang and Liu 2005; Yonas et al. 2013; Meyfroidt and Lambin 2008).

Remote sensing technology implies observation of an object from a distance, without being in actual contact with it. Remote sensing of the earth or any other planetary body involves collection of information like topography, natural resources, and natural phenomena such as volcanic eruptions, forest fires, floods, droughts, etc., with the help of sensors like cameras, scanners, radiometers on board platforms like airplanes, rockets, balloons, etc. The study reveals the land use/land cover changes from 1988–1989 to 1999–2000.

## 2 Materials and Methods

### 2.1 Study Area

The study area which comprises of Hisar district extends from 28°53'45" to 29°49'15" N latitudes and 75°13'15" to 76°18'15" E longitudes, and covers an area of 4174 sq. km. The district is bordered by Fatehabad district and Rajasthan state in the west, Rohtak district in the east, Bhiwani district in the south, and Jind district in the north. The location map of the study area is shown in Fig. 1. The southwest monsoon season lasts from the interim week of June to the middle of September. The weather here is almost dry from October month to the following June. Occasionally, light disturbances occur with lightning due to western disturbances. Only 75–80% annual rainfall is received in the four rainy months of June to September. Here also the average annual rainfall is 450 mm and 133.4 mm in July, 116.2 mm in August, 54.5 mm from September, and 49.8 mm average annual rainfall since June. The average rainfall season is 354 mm. The maximum rainfall ever measured was 793.6 mm in 1976. The minimum rainfall was recorded in the year 2000, which is 145.2 mm. Here, 10–15% of the total rainfall is in the winter season due to southern disturbances. The maximum days of the rainy season are in the months of July and August and the minimum days are in November and December. The lands in the district are Aeolian plains, older alluvial plains, and Chautang flood plains, which further have sand dunes, plains, old channels, and

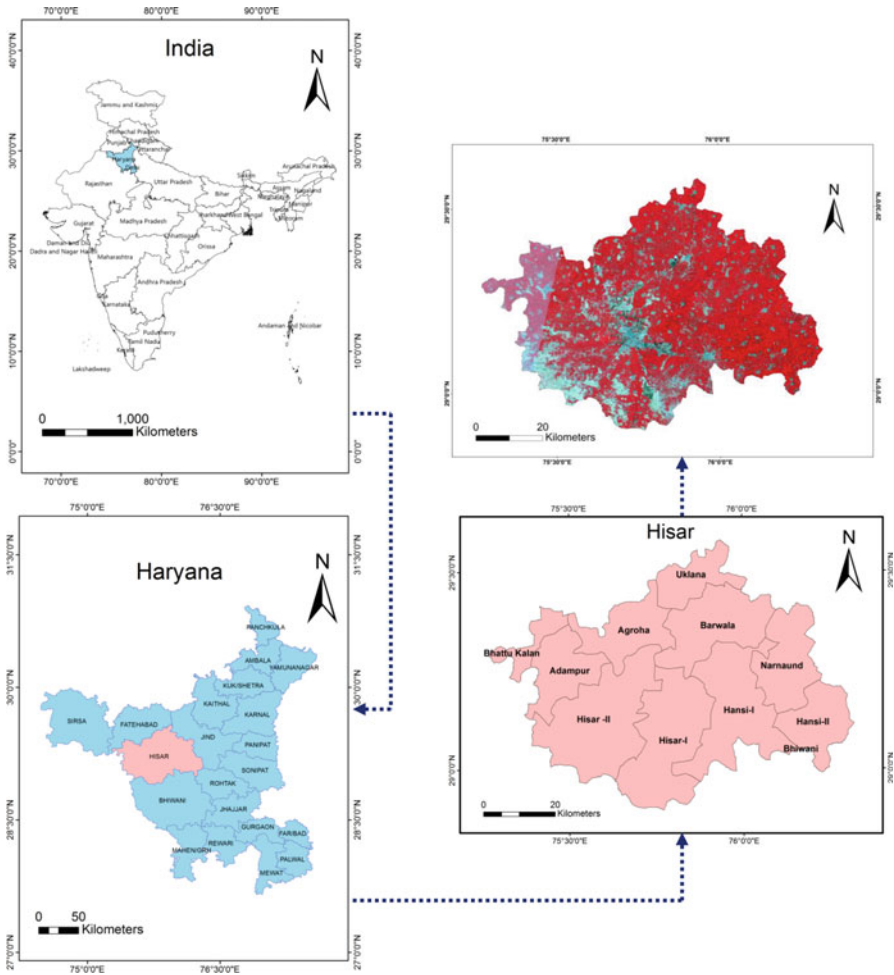


**Fig. 1** Location map of Hisar district, Haryana

basin as subunits. Aeolian activities are dominant in west and southwest parts of district, having presence of sand dunes, sandy plains, and interdunal areas. As a part of the Indo-Gangetic alluvial plain, the study area owes its genesis contemporaneously with the uplift of the Himalayas. This sag has since been filled up by sediments derived from the rivers and channels of northern Himalayas and southern Aravalli hills from Pleistocene to recent times (Rani 2017).

## 2.2 Data Used

The study area is covered by Survey of India Toposheet Nos.: H43P-7, 8, 10–12, 14–16 H43Q-03, 04, 08, H43V-09, 13 on 1:50,000 scales. These were used for the

preparation of digital base map, demarcation of district boundary, and other collateral information. Landsat TM+ data of October 1999, February 2000, October 2014, and February 2015 (A, B, C, and D in Fig. 3) are used to prepare LU/LC maps of study area. In the preparation of LU/LC map of area, ancillary data in the form of topographic maps and other published relevant material were used as reference information.

Landsat TM and ETM+ images were selected as the remotely sensed data for this study. The Landsat's temporal resolution is 16 days and its spatial resolution is 30 m, meaning that images for a specific path and row are available every 16 days. Landsat being sun-synchronous, it generates day images only (Rani et al. 2018; Kumar et al. 2014, 2018a, b; Mandal et al. 2014; Yadav et al. 2014). These images are available for download upon request from United States Geological Survey (USGS)–specified websites such as [earthexplorer.usgs.gov](http://earthexplorer.usgs.gov) and [glovis.usgs.gov](http://glovis.usgs.gov). For acquiring Landsat TM and ETM+ data from its historical data archives, [earthexplorer.usgs.gov](http://earthexplorer.usgs.gov) was chosen. USGS offers open access to Level 1C product to users; L1C is a radiometrically and geometrically corrected. The correction algorithms used the spacecraft model and sensor, using images generated by in-flight computers during data acquisition events. Operational Land Imager (OLI) on board Landsat TM and ETM+ makes available the opportunity to estimate SSC in Gaula River. Orthorectified and terrain-corrected level-1 data that overpass on 28 October 2017 was acquired from USGS Earth Explorer site to synchronize with collected ground truth data from three sites. Data was provided in Geo TIFF format with UTM projection and WGS84 datum.

Landsat TM and ETM+ satellite has two main sensors. There are the Landsat TM and ETM+ using nine spectral bands in different wavelengths of visible thermal infrared sensor (TIRS). OLI which collects and captures visible bands, near-infrared and shortwave light to observe a 185 km (115 mile) wide swath of the earth in 15–30 m resolution covering wide areas of earth's landscape while providing sufficient resolution to distinguish feature like urban centers, farms, forests, etc., corresponding image was selected by inputting Path and Row numbers of 194 and 56 respectively. This TILE covers the entire length of the Gaula River basin. After selecting the desired date and type of product an order was placed for processed L1C product. It is to be noted that the best monsoon seen month of October was considered for the present study.

### 2.2.1 Georeferencing of Satellite Images

Satellite data of both the years were loaded through EXPORT/IMPORT function of ERDAS/IMAGINE as generic binary file or directly in GEOMATICA. From the original data sets Area of Interest (AOI) was extracted and subsequently mosaicking of images was performed. Raw satellite images do not orient with respect to ground. In order to correct them, ground coordinates of any coordinate system has to be assigned (Bisht et al. 2014; Kumar et al. 2012, 2013; Rani et al. 2011; Sharma et al. 2011). Image rectification/georeferencing includes assigning map coordinates to image data. Georeferencing/rectification may be carried out by two techniques.

In forest technique, it is image-to-image registration, and this process involves assigning coordinates of already geo-rectified image to raw image; and second technique is assigning coordinates to known points in raw image collected from ground by means of GPS. For this study, Landsat ETM+ satellite data, which are freely available, were downloaded from website (GLCF data product). These satellite images are already geo-referenced and used to geo-reference IRS 1D LISS III satellite images of the study area using image-to-image georectification process in ERDAS Imagine (Murthy et al. 2017; Kumar et al. 2016; Pandey et al. 2015).

A flowchart of the methodology used and satellite images are given in Fig. 2. Scanning, georeferencing, and mosaicking of the toposheets were carried out for using these as reference sources for georeferencing of different digital satellite data of 1999–2000 and 2014–2015 after that supervised and unsupervised classification was carried out. Also, various LU/LC categories were identified on the basis of standard image interpretation keys like tone, texture, shape, size, pattern, and association, etc. The built-up area gave doubtful signature in the supervised/unsupervised classification, and hence on-screen digitization was also carried out for removing the doubt in built-up land (Fig. 3).

### 3 Result and Discussion

For various land resource studies, regional planning and management, land use/land cover mapping is very important. In case of land degradation status mapping and monitoring, the land use/land cover study is proved to be very much helpful. In this study, land use/land cover mapping was carried out to achieve the ultimate objective of this research. The detailed methodology to generate land use/land cover map has been discussed.

#### 3.1 Land Use/Land Cover

The LU/LC map was generated using supervised classification approach using two seasons satellite imageries, and five broad land categories were identified. These land categories are as follows:

- Built-up (Built-up Compact, Built-up, Sparse Vegetated/Open Area, Rural, Industrial Area, Ash/Cooling, Pond/Effluent and other Waste)
- Agricultural Land (Kharif, Rabi, Cropped in Two Seasons, Cropped in More than Two Seasons, Fallow Land, Agriculture, Plantation)
- Forest (Open, Deciduous, Open Tree, Clad Area)
- Grass/Grazing Land (Alpine/ Sub-Alpine)
- Wastelands (Salt-Affected Land, Open Scrub Land, Desertic Sandy Area)
- Wetlands (Manmade, i.e., Water-logged, Saltpans, Inland, etc.)
- Water Bodies (Canal/Drain Permanent and Seasonal Lake/Ponds)



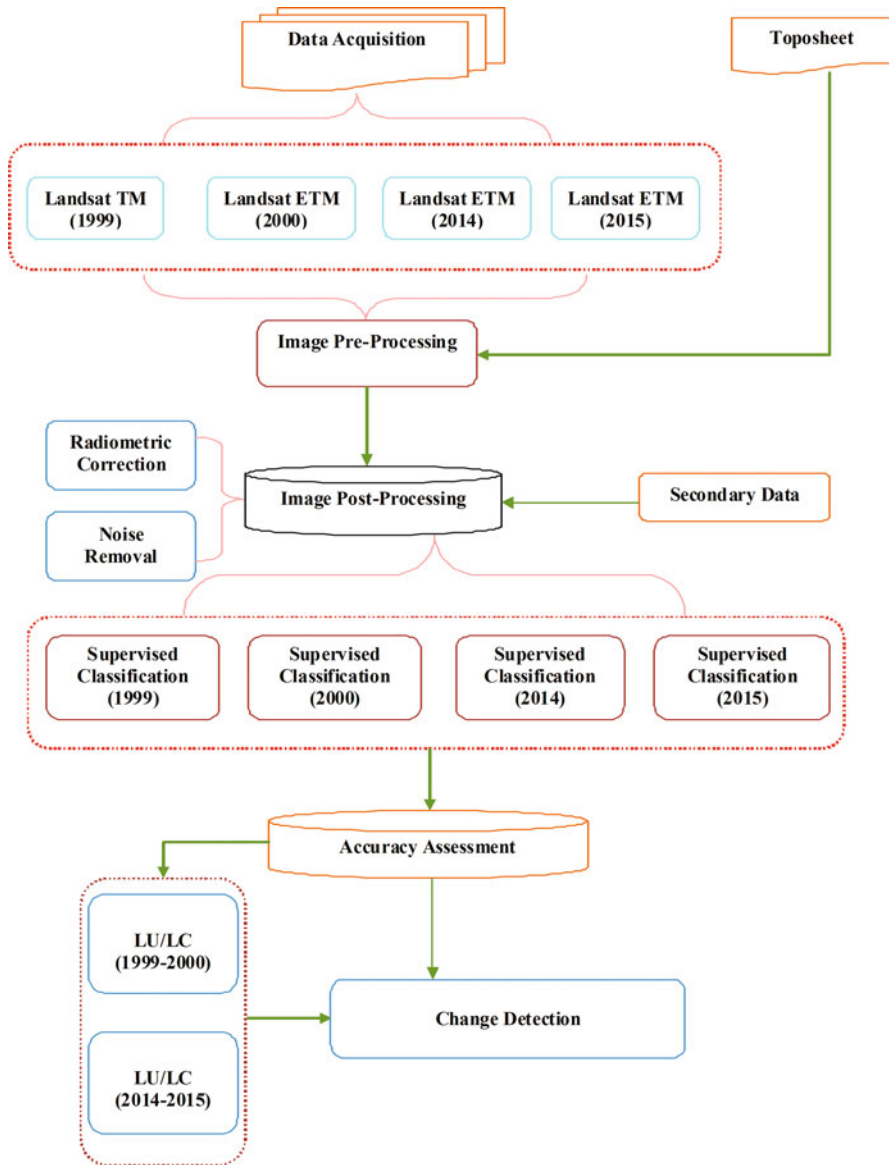
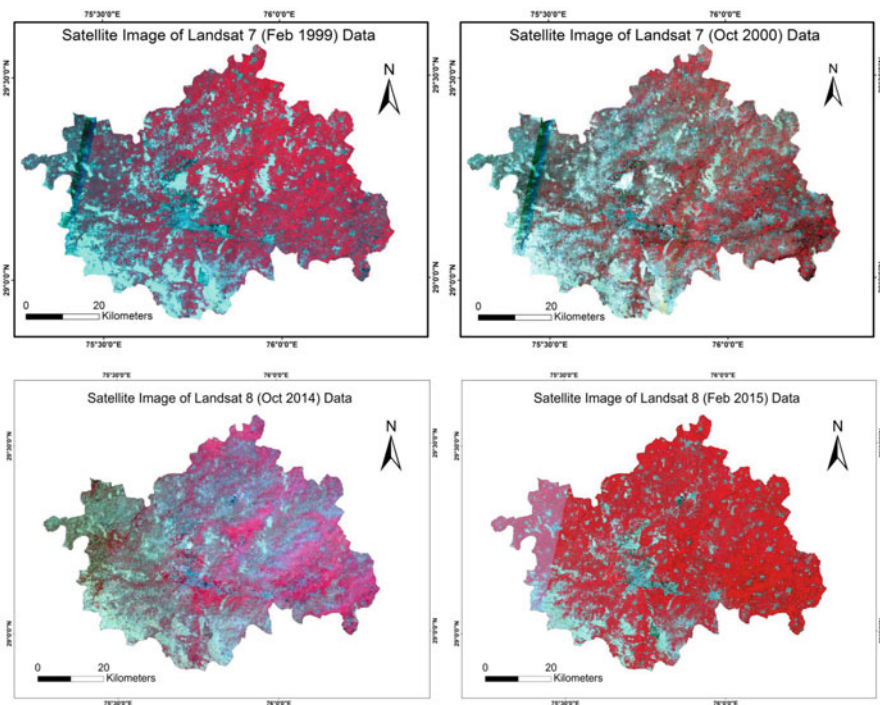


Fig. 2 Flowchart of methodology

The classes interpreted were subsequently verified in the field by conducting an extensive field survey. Area statistics for different land use/land cover categories was generated and are given in Tables 1 and 2. Characteristics and spatial distribution of each of the land class have been discussed in the following sections. In present study, the district divides in to 7 major categories and 21 subcategories according to world standards (Natural Resources Information System (NRIS)), as follows.



**Fig. 3** Satellite images (a-October 1999, b-February 2000, c-October 2014, and d-February 2015)

### 3.1.1 Built-Up Land

It is characterized by intensive land use where the site has been altered by human actions. Level-II classifications under Built-up land category are Built-up Compact, Built-up Sparse, Vegetated/Open Area, Rural, Industrial Area, Ash/Cooling Pond, and other Waste. Total area under this category is 127.5 sq. km in year 1999–2000, and it increased by 28.40 sq. km in year 2014–2015.

### 3.1.2 Agricultural Land

The land which is used for farming and production of food and crops. In this category, land covered under Kharif, Rabi, Cropped in 2 Seasons and Cropped in More than 2 Seasons, Fallow Land, and Agriculture Plantation. Area covered under this category is 3829.68 sq. km in year 1999–2000, which decreased by 8.37 sq. km in year 2014–2015.

**Table 1** Showing area statistics of different land use/land cover classes of Hisar district for year 1999–2000

| Area of land use/land cover categories in year 1999–2000 |   |                |
|--|---|----------------|
| Category   | Subcategory (level-III)                         | Area (sq. km)  |
| Built-up   | Built-up compact                                | 21.08          |
|  | Built-up sparse                                 | 5.59           |
|  | Vegetated/open area                             | 6.64           |
|  | Rural   | 57.05          |
|  | Industrial area                                 | 36.57          |
|  | Ash/cooling, pond/effluent, and other wastes    | 0.59           |
| Agricultural land  | Kharif  | 187.85         |
|  | Rabi  | 189.95         |
|  | Cropped in 2 seasons                            | 3284.75        |
|  | Cropped in more than 2 seasons                  | 0.37           |
|  | Fallow land                                     | 162.75         |
|  | Agriculture plantation                          | 3.79           |
| Forest   | Open deciduous (dry/moist/thorn)                | 5.49           |
|  | Open tree clad area                             | 23.46          |
| Grass/grazing land                                       | Alpine/sub-Alpine                               | 134.73         |
| Wastelands   | Salt-affected land                              | 0.58           |
|  | Open scrub land                                 | 18.07          |
|  | Desertic sandy area                             | 5.46           |
| Wetlands   | Manmade (water logged, salt pans, etc.), inland | 0.64           |
| Water bodies   | Canal/drain                                     | 13.83          |
|  | Permanent and seasonal lakes/ponds              | 15.27          |
|  | <b>Total area</b>                               | <b>4174.52</b> |

**Table 2** Showing area statistics of different land use/land cover classes of Hisar district for year 2014–15

| Category           | Area in 1999–2000 | Area in 2014–2015 | Change in area |
|--------------------|-------------------|-------------------|----------------|
| Built-up           | 127.52            | 155.93            | 28.40          |
| Agricultural land  | 3829.68           | 3821.31           | –8.37          |
| Forest             | 28.92             | 39.43             | 10.51          |
| Grass/grazing land | 134.73            | 113.02            | –21.71         |
| Wasteland          | 24.11             | 15.23             | –8.88          |
| Wetland            | 0.66              | 0.40              | –0.25          |
| Water bodies       | 28.89             | 29.20             | 0.31           |
| <b>Total area</b>  | <b>4174.52</b>    | <b>4174.52</b>    | <b>0.00</b>    |

### 3.1.3 Forest Land

Forest land use is a function of the social and economic purposes for which land is managed, while forest land cover is a human definition of the biological cover observed on the land (Watson et al. 2000). In this category, land covered under

Open Deciduous (Dry/Moist/Thorn), Open Tree Clad Area. Area covered under this category is 28.92 sq. km in year 1999–2000, which increased by 10.51 sq. km in year 2014–2015.

### **3.1.4 Grass/Grazing Land**

Land covered by grass/crops and suitable for grazing by animals is known as Grass/Grazing Land. Alpine/Sub-Alpine are type of grasslands present in study area. Area covered under this category is 134.73 sq. km in year 1999–2000, which decreased by 21.71 sq. km in year 2014–2015.

### **3.1.5 Wasteland**

Wasteland is a barren or uncultivated land which may be barren due to flood or any other natural activities. In this category, land covered include Salt-Affected Land, Open Scrub Land, Desertic Sandy Area, etc. Area covered under this category is 24.11 sq. km in year 1999–2000, which decreased by 8.88 sq. km in year 2014–2015. The various wasteland categories identified in the study area are scrubland, land without scrub, sand (desertic and riverine) stony land, and gully or ravine land.

### **3.1.6 Wetland**

Wetlands are areas where water covers the soil or is present either at or near the surface of the soil all year or for varying periods of time during the year, including during the growing season. In this category, land covered under manmade (waterlogged, salt pans, etc.) and inland. Area covered under this category is 0.66 sq. km in year 1999–2000, which decreased by 0.25 sq. km in year 2014–2015.

### **3.1.7 Water Bodies**

It is an area which is covered water and by flow of water. In this category, land covered under Canal/Drain and Permanent and Seasonal Lake/Ponds. Area covered under this category is 28.89 sq. km in year 1999–2000 (Table 3), which increased by 0.31 sq. km in year 2014–2015. Ephemeral rivers/streams are major contributors in this category of land. Tank or ponds are associated with settlement areas, whereas other natural water bodies exist in east of Aravalli hills.

Land use/land cover map of study area for year 1999–2000 and 2014–15 is shown in figures 4 and 5. Land use/land cover map of Hisar district prepared using online digitization technique of satellite imageries Landsat 7 and Landsat 8 for year 1999–2000 and 2014–15. Area covered under different categories shown in Tables 1 and 2. Change in area is also in Table 3 (Figs. 4 and 5).

**Table 3** Change in area of LU/LC under different category from 1999–2000 to 2014–2015

| Category           | Area in 1999–2000 | Area in 2014–2015 | Change in area |
|--------------------|-------------------|-------------------|----------------|
| Built-up           | 127.52            | 155.93            | 28.40          |
| Agricultural land  | 3829.68           | 3821.31           | -8.37          |
| Forest             | 28.92             | 39.43             | 10.51          |
| Grass/grazing land | 134.73            | 113.02            | -21.71         |
| Wasteland          | 24.11             | 15.23             | -8.88          |
| Wetland            | 0.66              | 0.40              | -0.25          |
| Water bodies       | 28.89             | 29.20             | 0.31           |
| <b>Total area</b>  | <b>4174.52</b>    | <b>4174.52</b>    | <b>0.00</b>    |

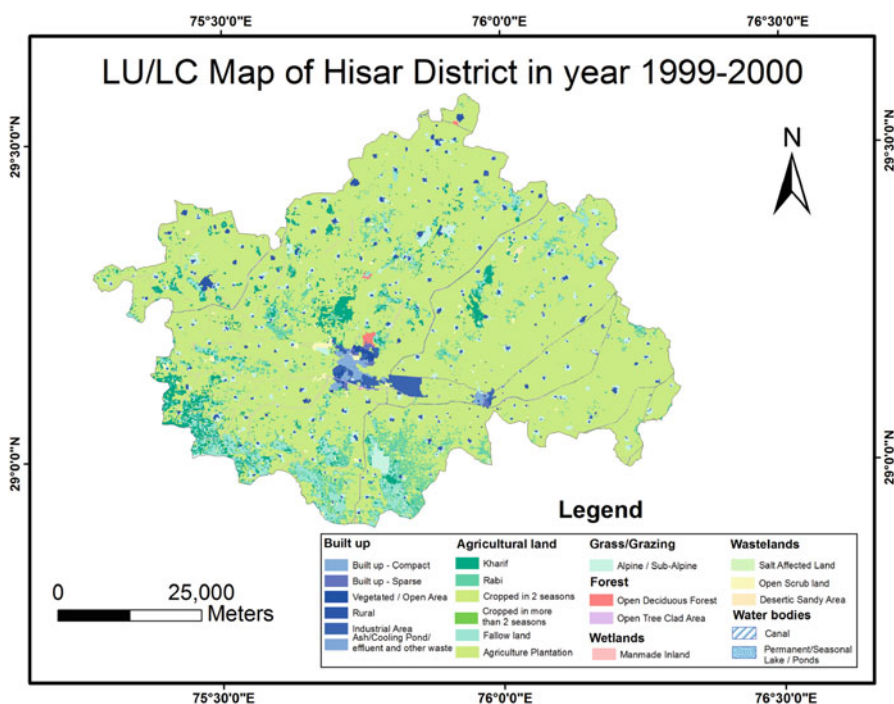


**Fig. 4** Land use/land cover map of Hisar district for year 1999–2000

## 4 Conclusions

The study indicates maximum increase of 28.40 sq. km under built-up land over last 15 years. This is due to the conversion of agriculture land and grass land to built-up land due to increasing pressure of population and migration of the people from other states to the area. There is negligible increase in the area under water body, which is not commensurate with the population increase in these 15 years as the area is

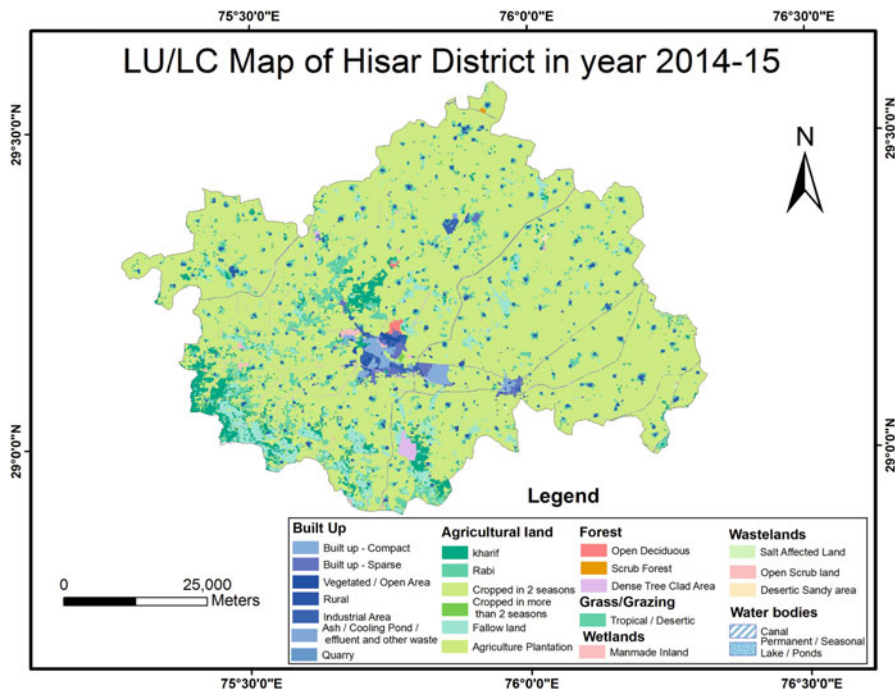


Fig. 5 Land use/land cover map of Hisar district for year 2014–15

predominantly deserts and groundwater conditions including quality and availability are not so good. Hence there is a need of some water harvesting planning in the district. Grass/ grazing land is increasingly being converted into forest land which is a healthy sign. There is remarkable reduction in the area under wastelands which has been converted to built-up and forests. The study demonstrates the subtle role of geospatial technology in LU/LC mapping and monitoring for the use of planners/ decisions makers.

**Acknowledgements** The authors are thankful to University Grant Commission, New Delhi, for the funding provided under Major Research Project wide reference F. No. 41-883/ 2012 (SR).

## References

Anderson, J. R. (1971). Land use classification schemes used in selected recent geographic applications of remote sensing. *PE and RS*, 37(4), 379–387.

Anderson, J. R., Hardy, E. E., Roach, J. T., & Witmer, R. E. (1976). *A land use and land cover classification system for use with remote sensor data*. Geological Survey Professional Paper, U. S. Govt. Printing Office, Washington, 964.

- Arya, V. S., Sultan, S., Chaudhary, B. S., Kumar, A., & Toleti, B. V. M. R. (1999). *Mapping of soil and water resources of Mewat area: Problems and their management using remote sensing techniques*. Technical Report, HARSAC/TR/ 25/99.
- Bisht, P., Kumar, P., Yadav, M., Ravat, J. S., Sharma, M. P., & Hooda, R. S. (2014). Spatial dynamics for relative contribution of cropping pattern analysis on environment by integrating remote sensing and GIS. *International Journal of Plant Production*, 4(3), 299–304.
- Chaudhary, B. S. (2003). *Integrated land and water resources Management in Southern Part of Haryana using remote sensing and geographical information (GIS)*. PhD thesis. Unpublished, University of Rajasthan, Jaipur.
- Chaudhary, B. S., & Kumar, S. (2017). Use of RS and GIS for land use/land cover mapping of K-J watershed, India. *International Journal of Advances in Remote Sensing and GIS*, 5, 85–92.
- Chaudhary, B. S., Saroha, G. P., & Yadav, M. (2008). Human induced land use/ land cover changes in northern part of Gurgaon District, Haryana, India: Natural resources census concept. *Journal of Human Ecology*, 23(3), 243–252.
- Clevers, J. G. P. W., Muecher, C. A., Popov, V. P. Vandysheva, N. M., & Vassilenko, G. I. (1999). Agriculture land cover monitoring over Russia using remote sensing. *EARSeL Symposium ITC, Enschede, the Netherlands*. A. A. Balkema, Publishers Rotterdam, p. 18.
- Dhawan, V. (2017). *Water and agriculture in India: Background paper for the South Asia expert panel during the global forum for food and agriculture*. German Bundestag: Federal Ministry of Food and Agriculture.
- Falcucci, A., Maiorano, L., & Boitani, L. (2007). Changes in land-use/land-cover patterns in Italy and their implications for biodiversity conservation. *Landscape Ecology*, 22(4), 617–631.
- Gupta, S., & Roy, M. (2012). Land use/land cover classification of an urban area – A case study of Burdwan Municipality, India. *International Journal of Geomatics and Geosciences*, 2 (IV), 1014–1026.
- Hooda, R. S., Manchanda, M. L., & Sharma, J. R. (1992). Digital analysis of IRS – 1A LISS I data for land use/ land cover mapping in Haryana state. In R. L. Karale (Ed.), *NNRMS – A new perspective*. Bangalore: ISRO-NNRMS.
- Hussin, Y. A., & Shaker, S. R. (1995). *Monitoring the changes in the tropical forest land use by remote sensing and GIS*. World Congress, Tampere/Finland, August, 6 to12, Proceedings IUFRO XX.
- Kuemmerle, T., Radeloff, V. C., Perzanowski, K., & Hostert, P. (2006). Cross-border comparison of land cover and landscape pattern in Eastern Europe using a hybrid classification technique. *Remote Sensing of Environment*, 103, 449–464.
- Kumar, S. (2017). *Remote Sensing and GIS Based Watershed Studies in Koshalya-Jhajhara Watershed in North India*. Shodhganga, Ph.D. Thesis, Kurukshetra University Kurukshetra, Haryana.
- Kumar, P., Kumar, D., Mandal, V. P., Pandey, P. C., Rani, M., & Tomar, V. (2012). Settlement risk zone recognition using high resolution satellite data in Jharia coal field, Dhanbad, India. *Life Science Journal*, 9(1s), 1–6.
- Kumar, P., Singh, B., & Rani, M. (2013). An efficient hybrid classification approach for land use / land cover analysis in Semi-Desert area using ETM+ and LISS-III sensor. *Sensors Journal, IEEE*, 13(6), 2161–2165.
- Kumar, P., Pandey, P. C., Kumar, V., Singh, B. K., Tomar, V., & Rani, M. (2014). Efficient recognition of Forest species biodiversity by inventory based geospatial approach using LISS IV. *Sensors Journal, IEEE*, 13(6), 2161–2165.
- Kumar, P., Pandey, P. C., Singh, B. K., Katiyar, S., Mandal, V. P., Rani, M., Tomar, V., & Patairiya, S. (2016). Estimation of accumulated soil organic carbon stock in tropical forest using geospatial strategy. *The Egyptian Journal of Remote Sensing and Space Science*, 19(1), 109–123.
- Kumar, P., Sajjad, H., Tripathy, B. R., Ahmed, R., & Mandal, V. P. (2018a). Prediction of spatial soil organic carbon distribution using sentinel-2A and field inventory data in Sariska Tiger Reserve. *Natural Hazards*, 90(2), 693–704.

- Kumar, P., Sajjad, H., Mohanto, K. K., Ahmed, R., & Mandal, V. P. (2018b). Assessing suitability of Allometric models for predicting stem volume of *Anogeissus pendula* Edgew in Sariska Tiger Reserve. *India Remote Sensing Applications: Society and Environment*, 10, 47–55.
- Kushwaha, S. P. S., & Oesten, G. (1995). A rule based system for forests land use planning. *Photonirvachak*, 23(3), 115–125.
- Mandal, V. P., Shutrana, S., Pandey, P. C., Patariya, S., Shamim, M., & Sharma, S. (2014). Appraisal of suitability for urban planning and expansion analysis using quick bird satellite data. *ARNP Journal of Engineering and Applied Sciences*, 9(12), 2716–2722.
- Meyfroidt, P., & Lambin, E. F. (2008). The causes of the reforestation in Vietnam. *Land Use Policy*, 25, 182–197.
- Murthy, C. S., Singh, J., Kumar, P., & Sai, M. V. R. S. (2017). A composite index for drought hazard assessment using CPC rainfall time series data. *International Journal of Environmental Science and Technology*, 14(9), 1981–1988.
- Narumalani, S., Mishra, D. R., & Rothwell, R. G. (2004). Change detection and landscape metrics for inferring anthropogenic processes in the greater EFMO area. *Remote Sensing of Environment*, 91, 478–489.
- Pandey, P. C., Kumar, P., Tomar, V., Rani, M., Katiyar, S., & Nathawat, M. S. (2015). Modelling spatial variation of fluoride pollutant using geospatial approach in the surrounding environment of an aluminium industries. *Environmental Earth Sciences*, 1–12.
- Ram, B., & Singh, S. (1995). Remote sensing in sustainable land use planning. *National Symposium on Remote Sensing of Environment at Punjab Remote sensing Application Centre in PAU, Ludhiana*, pp. 189–195.
- Rani, R. (2017). *Groundwater studies in Hisar district of Haryana using Geoinformatics and Geophysical Resistivity Techniques*. Shodhganga, PhD thesis, Kurukshetra University Kurukshetra, Haryana.
- Rani, M., Kumar, P., Yadav, M., & Hooda, R. S. (2011). Wetland assessment and monitoring using image processing techniques: A case study of Ranchi, India. *Journal of Geographic Information System*, 3, 345–350.
- Rani, M., Kumar, P., Pandey, P. C., Srivastava, P. K., Chaudhary, B. S., Tomar, V., & Mandal, V. P. (2018). Multi-temporal NDVI and surface temperature analysis for urban heat Island inbuilt surrounding of sub-humid region: A case study of two geographical regions. *Remote Sensing Applications: Society and Environment*, 10, 163–172.
- Reid, R. S., Kruska, R. L., Muthui, N., Taye, A., Wotton, S., Wilson, C. J., & Mulatu, W. (2000). Land-use and land-cover dynamics in response to changes in climatic, biological and socio-political forces: The case of southwestern Ethiopia. *Landscape Ecology*, 15, 339–355.
- Sharma, M. P., Yadav, M., Yadav, K., Prawasi, R., Kumar, P., & Hooda, R. S. (2011). Cropping system analysis using remote sensing & GIS: A block level study of Kurukshetra District. *Journal of Agricultural and Biological Science*, 6(10), 45–61.
- Toleti, B.V.M. R. (1995). *A study on impact of coal mining on land use and land cover in Jharia Coalfield (Dhanbad) India through remote sensing technique*. PhD thesis (Unpublished), Indian School of Mines, Dhanbad, India.
- Turner, B., Meyer, W. B., & Skole, D. L. (1994). Global land-use/land-cover change: Towards an integrated study. *Ambio Stockholm*, 23(1), 91–95.
- Watson, R. T., Noble, I. R., Bolin, B., Ravindranath, N. H., Verardo, D. J., & Dokken, D. J. (2000). *Land use, land-use change and forestry: A special report of the intergovernmental panel on climate change*. Cambridge University Press.
- Xiubin, L., (1996). A review of the international researches on land use/land cover change. *Acta Geographica Sinica*, 6.
- Yadav, M., Sharma, M. P., Prawasi, P., Khichi, R., Kumar, P., Mandal, V. P., Salim, A., & Hooda, R. S. (2014). Estimation of wheat/rice residue burning areas in major districts of Haryana, India, using remote sensing data. *Journal of the Indian Society of Remote Sensing*, 42(2), 343–352.



- Yang, X., & Liu, Z. H. I. (2005). Quantifying landscape pattern and its change in an estuarine watershed using satellite imagery and landscape metrics. *International Journal of Remote Sensing*, 26, 5297–5323.
- Yonas, B., Beyene, F., Negatu, L., & Angassa, A. (2013). Influence of resettlement on pastoral land use and local livelihoods in Southwest Ethiopia. *Tropical and Subtropical Agroecosystems*, 16, 103–117.

**Part IV**  
**Challenges and Future Directions in**  
**GIScience**

# A Spatial Investigation of the Feasibility of Solar Resource Energy Potential in Planning the Solar Cities of India



Koel Roychowdhury and Radhika Bhanja

**Abstract** India is experiencing large-scale urbanization, and the key component leading to such demographic growth and increasing GDP in these urban spaces is an uninterrupted energy supply. The energy generated from nonconventional energy resources consequently leads to resource scarcity and environment pollution. The renewable energy generation and its optimum utilization is the key to the sustainable growth of cities and its hinterland. Although India is in the fifth position among the leading countries to harness renewable energy, in order to suffice the growing energy requirements, it will still require thrice the energy than the total energy consumed today. The Ministry of New and Renewable Energy has undertaken the “Development of Solar Cities” program to boost renewable energy usage in urban sectors. Around 60 cities are participating in this program. However, the viability of the program in these cities still needs to be established. The current study, therefore, focuses on identifying solar hotspots of India and how the spatial distribution of solar energy resources accentuates or hinders the performance of the solar cities. A technoeconomic feasibility study has been conducted using solar resource datasets derived from high-resolution satellites. Further, the Technique for Order of Preference by Similarity to Ideal Solution (TOPSIS) method was applied to identify the cities with the maximum potential to successfully fulfil the ambitious solar city project. The statistical analysis reveals that cities lying in western India are best for harnessing solar energy in large scale. The power will be generated through Concentrated Solar Power (CSP) systems or in residential and commercial sectors using Solar Photovoltaic (SPV) systems. The study explores the feasibility of site selection for the ambitious solar city project, focusing on existing policies, technology, and economic capacity of the selected cities to meet the project targets.

**Keywords** Urbanization · Energy consumption · Renewable energy · Solar city · Renewable energy funding

---

K. Roychowdhury (✉) · R. Bhanja  
Department of Geography, Presidency University, Kolkata, West Bengal, India  
e-mail: [koel.geog@presiuniv.ac.in](mailto:koel.geog@presiuniv.ac.in)

## 1 Introduction

Cities are moving forward to achieve the global goals of combating climate change and adapting all possible measures for a sustainable low carbon future. India, too, has undertaken a giant leap in achieving a massive project of installing 175 GW of renewable energy by 2020, where 100 GW of power will be generated from solar energy, 60 GW from wind energy, 10 GW from biopower, and 5 GW from small hydropower plants (Press Information Bureau 2018). In order to accomplish such ambitious goals, the country's energy systems are being subjected to sustainable transformations. Indian cities are equally participating in different renewable energy programs, thereby substantially reducing the use of conventional sources of energy to meet the growing energy demands. The Solar City Mission (SCM) program is such an initiative by the Ministry of New and Renewable Energy (MNRE) to address the energy demands of Indian cities in a holistic manner. SCM program aims to reduce around 10% of the projected demand of conventional energy in the cities, through its combination with renewable energy sources, thereby promoting energy efficiency measures and energy-inclusive development of the selected cities. The program was introduced to motivate the Urban Local Bodies (ULBs) adopting renewable energy-based projects like solar, wind, biomass, small hydro, and waste to energy based on the need and resource availability in the city (Ministry of New and Renewable Energy, 2018).

India is a tropical country and its geographic location is favorable to tap solar energy by employing large-scale solar plants and solar photovoltaic systems in rooftops, water heating, and irrigation purposes and many more. India has already installed 25 GW of grid-connected solar power capacity. The unplanned compact cities of India are willing to benefit from renewable energy and therefore, a technoeconomic feasibility assessment of potential cities is a prerequisite prior to cost-intensive renewable energy investment in these cities. The application of geographic information system (GIS) in the field of renewable energy planning has been extensively used for efficient resource utilization and planned production, generation, and storage of renewable energy (Alhamwi et al. 2017; Chow et al. 2014; Firozjaei et al. 2019; Gastli and Charabi 2010; Piragnolo et al. 2015). Non-geospatial methods like mathematical models (Eldin et al. 2016; Shehzad et al. 2016; Xiang et al. 2018) and economic models (Byrne et al. 2017; Okoye et al. 2016; Wegertseder et al. 2016) are mostly used to calculate the optimum generation of electricity from renewables, but they lack the ability to determine the variation over space and time. The geospatial models employ land use, buildings, rooftops, and infrastructure data to map the potential of a region to harvest renewable energy successfully. Geospatial awareness is crucial for sustainable energy infrastructure planning (Resch et al. 2014). This research opens up a new horizon for a national-level assessment of the feasibility of solar energy planning by utilizing high-resolution data and geospatial modelling tools.

Resource assessment is a fundamental approach for investors and renewable energy planners to determine appropriate geographical locations with abundant

and consistent resources. There are studies which spatially assess the solar energy potential at local, regional, and global scales. Solar hotspots are regions of greater solar energy potential than their surrounding regions, suitable for commercialization of solar energy (Ramachandra et al. 2011). The procedure of site selection for solar energy can be tedious at times. Large-scale solar power projects require vast land areas to capture a large amount of solar irradiation. One of the hindrances faced in developing such projects is the variability of solar irradiation in different geographical locations. Other factors that determine the location of solar PV plants include identification of physical constraints like the presence of hilly areas, protected areas, forests, and water bodies (Anwarzai and Nagasaka 2017); installation and operation cost; incentives from the government; and the proximity to the site for energy consumption, which may be either rural or urban. Considering the massive potential of India to harness solar energy, determining the suitable location to develop solar plants by investors is a challenging task. The use of remote sensing and GIS for decision-making can improve the accuracy of site selection procedure.

Open-source data from World Bank, National Aeronautics and Space Administration (NASA), and National Renewable Energy Laboratory (NREL) are frequently used to assess the solar energy potential of countries (Asumadu-Sarkodie and Owusu 2016; Chandler et al. 2015; Jahangiri et al. 2016; Watson et al. 2019). GIS tools have proven to be beneficial in assessing the solar energy potential for different cities in India (D. Kumar 2018; K. E. Kumar and Kumari 2019; Ramachandra and Shruthi 2007). The study considers two main solar irradiation datasets: global horizontal irradiation (GHI) to map potential areas of solar photovoltaic (SPV) and direct normal irradiation (DNI) to identify suitable areas for large-scale solar plants like Concentrated Solar Plants (CSP). The areas suitable for harnessing solar energy are mainly delineated using solar irradiation datasets and then GIS is further used to classify and segregate regions of the basis of resource availability and other socio-economic attributes (Freitas et al. 2015). Most of the studies have not considered the effectiveness of battery backup of solar systems, which is mainly calculated in terms of days with no sunshine.

Numerous methodologies have been adopted in recent studies to increase the accuracy of predicting the most feasible locations to tap solar energy resources. One such method involves modelling the spatial feasibility of solar energy resources using GIS-based multicriteria decision analysis (MCDA). This method uses spatial information, decision-making attributes, and criteria weights to conduct the spatial assessment of renewable energy resource potential (Greene et al. 2011). Site suitability analysis using a weighted sum model was applied to identify consumer suitable and economically viable regions for utility-scale solar projects in the countries across southwestern United States (Brewer et al. 2015). A combination of GIS and analytical hierarchical process (AHP) was used to compute a land suitability index in Saudi Arabia and the most suitable location to construct solar power plants were identified (Al Garni and Awasthi 2017). Wu et al. (2017) designed a geospatial multicriteria analysis model (MapRE) to estimate the renewable energy potential of a specific site with the help of ArcGIS, Python, and R programming languages. This method has also been used to locate regions with

greater investment opportunities for renewable energy in Bangladesh (Shiraishi et al. 2019). Moreover, different levels of hindrances require flexible results, and therefore, GIS-based ordered weighted averaging approach can also be applied to determine the optimal location for developing solar projects in Iran (Firozjaei et al. 2019).

The solar hotspots of India were first characterized by Ramachandra et al. (2011) using NASA SSE Global insolation datasets superimposed on agroclimatic zones of India. The potential zones were segregated for SPV and CSP systems, and it was observed that around 58% of the country could meet the power requirements of large-scale solar plants in a sustainable manner. The same methodology was used to locate renewable energy potential taluks in Karnataka, India (Ramachandra and Shruthi 2007). The study concludes that the coastal areas of the state received more solar irradiation than its surrounding areas and were ideal for tapping solar energy. GIS-based MCDA are also applied to assess the feasibility of solar energy resources in Indian context. Numerous criteria are applicable to determine the feasible areas to tap solar energy. Reshma et al. (2018) used criteria such as distance from road and water bodies, availability of barren lands, slope map, direction of sun radiation, and existing built-up area to conduct the solar site assessment of the Thiruvannamalai district, Tamil Nadu. In the same manner, AHP was used to rank areas in Sikkim according to the technoeconomic feasibility of solar energy resources and GIS was used to generate a technology-aided suitability map for medium-scale solar energy plant installations in the state of Sikkim (Ghose et al. 2019).

This research attempts to identify the solar hotspots of India and how the spatial distribution of solar energy resources accentuates or hinders the performance of the solar cities. The study is novel as it considers different aspects of technoeconomic feasibility, which previously had not been considered in the Indian context. In addition to a detailed analysis of solar radiation aspect and economic feasibility of Indian states, the study also aims to justify the viability of the Solar Cities Mission program, for which 60 cities have been selected to encourage the renewable energy usage in urban areas. The study explores the feasibility of site selection for the ambitious solar city project, focusing on existing policies, technology, and economic capacity of the selected cities to meet the project targets.

## 2 Material and Method

### 2.1 Study Area

A technoeconomic feasibility of solar energy resource potential in 60 selected solar cities of India has been studied here. For the implementation of solar city projects, a sum of up to Rs. 50 lakhs per city would be provided to the ULBs, depending upon population and initiatives taken by the city council or administration body. The program provides a framework to prepare a Master Plan of the solar city to establish sector-wise strategies and targets for implementation of renewable energy projects in

the city. Till date 36 solar cities have compiled their Master Plans, while only 4 cities have received more than 50% of the allotted amount for successful implementation of their Master Plans (MNRE 2018). SCM is mainly a capacity-building program for the stakeholders involved in the planning and implementation of green energy strategies in the selected solar cities of India. Therefore, a spatial investigation into the feasibility of renewable energy resources in the remaining cities must be conducted, prior to the dissemination of further funds to these cities.

## 2.2 Data Used

To identify the solar hotspots of India, three relevant solar irradiation datasets were considered, i.e. Global horizontal irradiation (GHI), Direct normal irradiation (DNI) and Photovoltaic power potential (PVOUT). These datasets were acquired from Global Solar Atlas, a web platform funded by the World Bank and Energy Sector Management Assistance Program (ESMAP) to provide quick access to solar resource data globally. These datasets for India can be downloaded in two formats of raster data: GeoTIFF and AAIGRID (Esri ASCII Grid). The data layers are provided in a geographic spatial reference (EPSG:4326) and the resolution of the pixels is adjusted to 30 arcsec (nominally 1 km) (World Bank Group 2018). The solar irradiation datasets for India is available from 1999 to 2018, and the solar data are available in terms of long-term yearly average of daily totals and as long-term average of yearly summaries. Here, long-term average of yearly summaries was used.

Solar radiation datasets consider both irradiance and irradiation values for analysis. GHI (kWh/m<sup>2</sup>) is the total amount of direct and diffuse components of radiation from the sun falling on a flat surface. GHI is considered relevant for generating energy from SPV and other solar heating technologies such as solar water heaters, solar water pumps, and many more. On the other hand, DNI (kWh/m<sup>2</sup>) is the amount of solar radiation that reaches the earth's surface in a straight line from the sun at a particular position in the sky. DNI is useful for tapping solar energy by the CSPs. Both variables were processed using different solar radiation models. GHI was derived from the SOLIS clear-sky model coupled with the cloud index with the help of three geostationary satellites, mainly National Oceanic and Atmospheric Administration (NOAA), European Organisation for the Exploitation of Meteorological Satellites (EUMETSAT), and Japanese Meteorological Agency (Cebecauer et al. 2010). DNI was calculated from DirIndex, coupled with high-resolution DEM data, to avoid inconsistency of solar radiation and removal of aerosol contents (Ruiz-Arias et al. 2010; Šúri et al. 2010). Moreover, PVOUT (kWh/kWp) was also considered in this study to identify the regions with the highest energy-capturing potential by PV technologies. It is defined as the amount of electricity (in kWh) that can be generated by a DC power of a PV system with 1 kW peak installed capacity. Higher values of PVOUT indicate an effective operation of PV systems (Solargis 2019). PVOUT is a viable option for investors to

identify locations where better-quality solar panels with high grade silicon cells and improved temperature coefficient performance (N-type silicon cells) with slower degradation rate can be installed. The GHI, DNI, and PVOOUT data are available worldwide between 60°N and 45°S. The datasets are available at 1-km spatial resolution, from 1999 to 2018 for North and South America, and part of Asia (up to 100° longitude).

The PV system penetration in the Indian market requires huge investments from both public and private enterprises. MNRE reports that the average cost required to install a rooftop solar system with on-grid connection is Rs 75 per watt. Renewable energy becomes lucrative when they lower the electricity bill of consumers at a lesser installation cost; therefore, the central government, as well as the state governments of India have designed policies to provide different types of incentives to eligible producers to tap solar energy through SPVs and CSPs (MNRE 2019). The policies were examined, and the incentives were categorized and coded to determine the type of economic benefits provided by each state government to its investors to expertly install solar PV systems in their frontiers. The policies can be accessed from the MNRE website.

### 2.3 Methodology

The solar resources distribution was depicted using GHI and DNI values and the potential zones with high energy yield capacity were depicted through PVOOUT data. Each parameter was classified into seven groups of solar potential and the areas were extracted and measured. The classification of the individual potential zones was done based on natural breaks or the Jenks method. The Jenks method groups value based on their similarity by minimizing the variance within classes and maximizing the difference between classes (Jenks 1977). The method first generated random classes, then the class boundaries of each class are adjusted by assigning the boundary values of each class its next class. This iterative process halts when the variance within classes reaches to its lowest possible value while the variance between classes has reached its maximal limit (de Smith et al. 2018). This method of classification has been previously used by (Prävālie et al. (2019) to delineate solar resource potential zones using 7-point Likert scale of significance.

To delineate the economically feasible zones, the solar energy policies for each state were examined and required information was extracted and coded to determine the type of economic benefits provided by each state government to its investors. Four categories were selected to represent the economic viability of solar projects state-wise, namely number of eligible producers, provision for land allotment, provision for banking of power, and monetary incentives, which include interest subsidy in the form of lower interests and fixed capital investment, waiver from electricity duty and stamp duty, exemption or concession in land premium, project report subsidy, and technical patent subsidy. The total number of benefits provided by the governments determines the economic potential of each state for effective



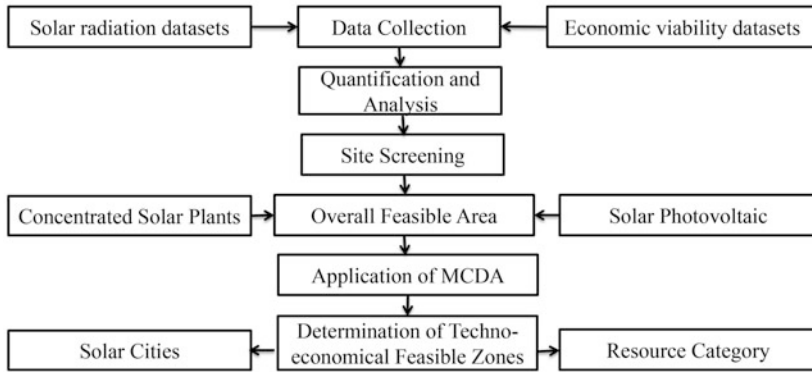


**Fig. 1** Overview of the methodology used in the study

installation of the solar PV systems. To classify the states into economic potential zones, the above-mentioned methodology to delineate solar resource potential zones was applied.

Finally, after the overall feasible areas were delineated, the data from all layers of solar resource potential zones and economic potential zones was extracted to solar city point vector layer and a GIS-based MCDA method was applied to identify the cities with the maximum potential to successfully fulfil the ambitious solar city project. The detailed methodology is explained in Fig. 1. The TOPSIS method, developed by Yoon and Hwang (1981), was used to find the solar cities with ideal conditions to harness solar energy. The method presumes that each criterion leads toward an increasing or decreasing utility, through which positive and negative ideal solution are defined. The Euclidean distance approach is used to calculate the distance between each criteria and the ideal point (Eq. 1 and 2).

$$S_+ = \left[ \sum_{c=1}^n (W_{ck} - W_{+c})^2 \right]^{0.5} \tag{1}$$

$$S_- = \left[ \sum_{c=1}^n (W_{ck} - W_{-c})^2 \right]^{0.5} \tag{2}$$

The relative closeness to the ideal point can be calculated by (Eq. 3)

$$CI = \frac{S_{k-}}{S_{k+} + S_{k-}} \tag{3}$$

Where  $W_{ck}$  is the weighted standardized criterion value of the  $k$ th alternative, calculated by multiplying standardized criterion value by the corresponding weight, and  $W_{+c}$  is the ideal value and  $W_{-c}$  is the negative ideal value for the  $k$ th criterion (Malczewski 1999; Ozturk and Batuk 2011).

### 3 Results and Discussion

#### 3.1 Solar Resource Potential in India

India, on an average, receives 1500–2000 sunshine hours per year (Sunwatt-India 2013). The solar radiation maps generated from the GHI and DNI datasets (Fig. 2) reveal a large geographical area of India is suitable to harness solar energy. The classification of GHI data reveals that 19% of the geographical area (0.744 mil km<sup>2</sup>), mainly Gujarat, half of Rajasthan and Karnataka, and parts of Tamil Nadu and Andhra Pradesh receives GHI more than 1965.00 kWh/m<sup>2</sup>, and can be considered as the ideal locations to tap solar energy with the help of SPVs in the future. Madhya Pradesh, Maharashtra, Chhattisgarh, Andhra Pradesh, and parts of Rajasthan, Karnataka, and Tamil Nadu and the eastern part of Kashmir occupy the next major class with a higher potential area to capture solar energy (more than 1800 kWh/m<sup>2</sup> and less than 1965 kWh/m<sup>2</sup>). This zone covers around 1.3 mil km<sup>2</sup> of India’s geographical area.

On the other hand, only a significant part of eastern Kashmir exhibits maximum DNI values (> 2000 kWh/m<sup>2</sup>). Gujarat and 50% of Rajasthan’s geographical area lie in the second belt of the very high solar potential zone and occupy a minimal area of 0.44 mil m<sup>2</sup>. Madhya Pradesh, Chhattisgarh, parts of Maharashtra and Karnataka, western Andhra Pradesh, and the remaining area of Rajasthan receive DNI ranging between 1470.00 kWh/m<sup>2</sup> and 1660.00 kWh/m<sup>2</sup> and are also suitable to harness solar energy in large quantities. These three regions, covering around 1.6 mil km<sup>2</sup> of

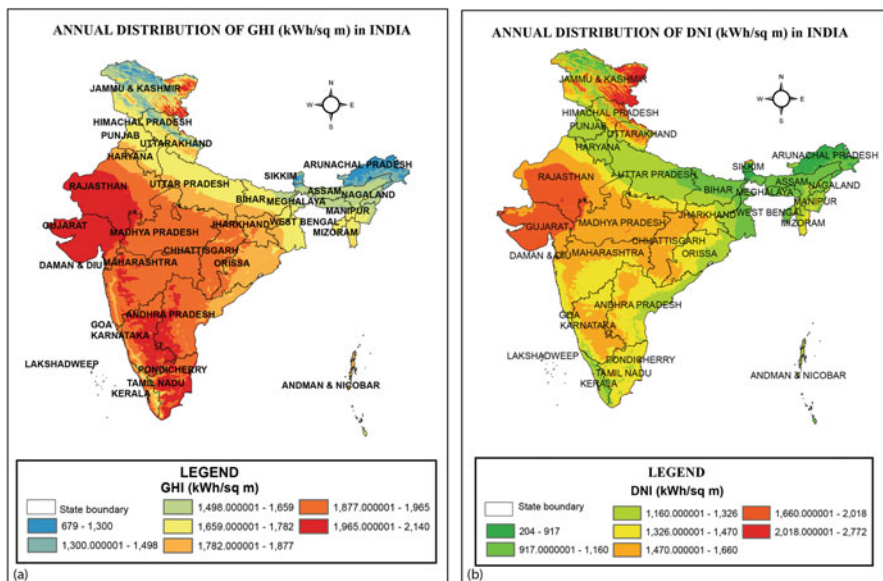


Fig. 2 Spatial representation of GHI (a) and DNI (b) values in the states of India

India's geographical area, are most favorable for CSP systems. Although the distribution of DNI and GHI in India show vast difference, the homogeneous distribution of the high, very high, and maximum solar potential zones, except that of Kashmir, may enable them to conduct interstate electricity distribution from solar power plants installed in the neighboring states.

The distribution of GHI and DNI values for regions with lesser potential to tap solar energy were almost similar. The states of Himachal Pradesh, Haryana, Punjab, Mizoram, northern parts of Uttar Pradesh and Bihar, and the alluvial plain and deltaic region of West Bengal receive average solar radiation when compared to the remaining states of India. These regions cannot solely depend on solar energy power plants as their future electricity suppliers. Here, a combination of thermal and solar power plants may suffice the need to generate electricity from renewable energy resources, without jeopardizing the electricity demand of the growing population and urban infrastructure. The remaining state of northeast India and western and central part of Jammu and Kashmir have poor ability to tap solar energy, and therefore these states can consider different renewable energy options to meet their energy needs sustainably.

### ***3.2 Technological Advantage in Solar Sites***

The photovoltaic power potential (PVOUT) of solar sites combines solar irradiation and air temperature datasets to obtain the maximum power out when the input power adheres to the Standard Test Conditions (STC) of 1000 W/m<sup>2</sup> global insolation, 25° C module temperature, and 1.5 air-mass (AM). The SPVs are an array of photovoltaic cells which convert solar energy to direct current (DC) electricity. These solar cells are composed of a thin layer of N-type silicon above a thick layer of P-type silicon. When the sunrays fall on the cells, the light simulated electrons gain momentum and electricity is generated at the P–N junction. The efficiency of the SPVs varies with the purity of silicon used in the solar cells. Around 90% of the world's SPVs use either monocrystalline or polycrystalline silicon cells to achieve 12–20% cell efficiencies. The purity level of monocrystalline silicon cells is higher than polycrystalline silicon cells, and therefore monocrystalline cells are more expensive.

The classification of PVOUT (Fig. 3) is nearly similar in characteristics to the categorization of DNI. The east part of Kashmir exhibits maximum PVOUT values (>1800 kWh/kWp). Gujarat and 50% of Rajasthan's geographical area form a very high technologically potential zone to generate a greater amount of solar energy using efficient SPVs. This region occupies an area of 0.51 mil m<sup>2</sup>. Madhya Pradesh, Chhattisgarh, Maharashtra and Karnataka, western and southern Andhra Pradesh, west Jharkhand, and the remaining area of Rajasthan have the photovoltaic power potential ranging between 1533.00 kWh/kWp and 1630.00 kWh/kWp and are also suitable to harness solar energy in large quantities. The combination of these three potential zones covers an area of 2.08 km<sup>2</sup> and they overlap with regions having

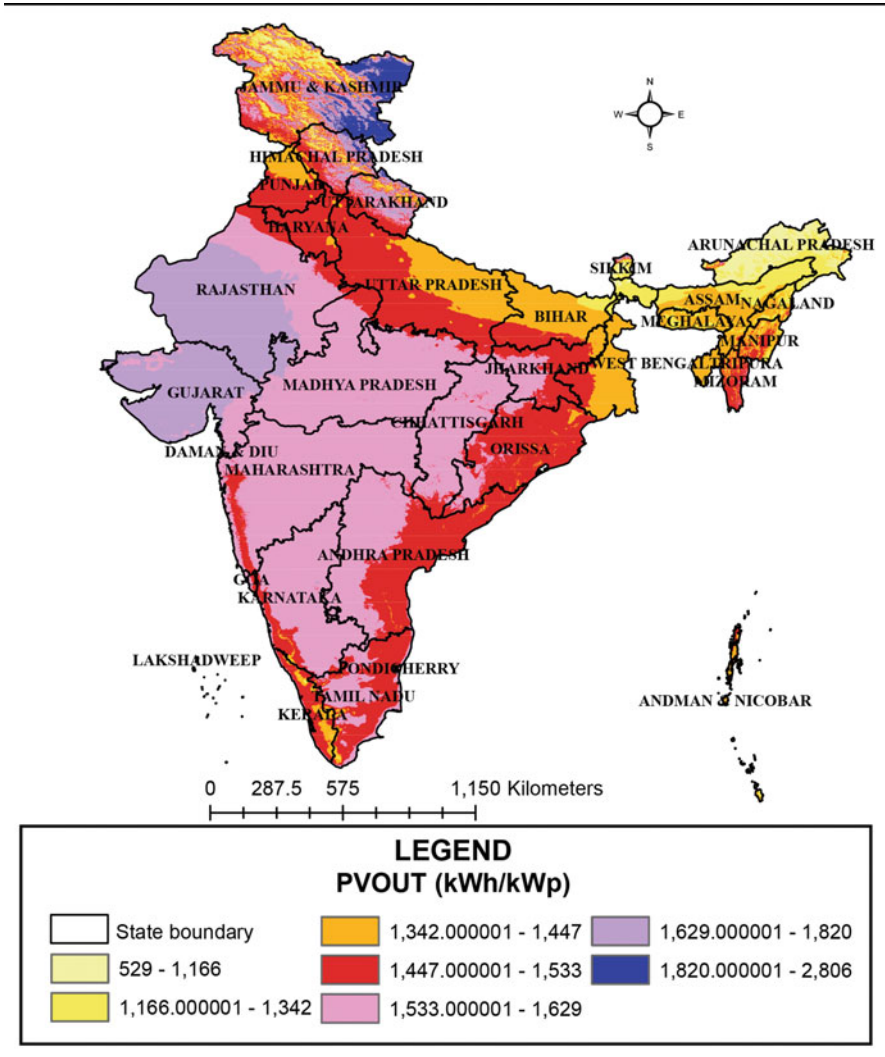


Fig. 3 State-wise distribution of PVOUT in India

greater DNI values. Therefore, investing in large-scale utility solar plants like CSPs will be of greater advantage to the government in shifting the power sector towards renewables sustainably. The initial cost of installation and production may be high, but will bring forth massive long-term benefit monetarily and through environment protection and conservation.

### ***3.3 Solar Economic Potential Zones of India***

In this study, the solar economic potential zones were delimited on the basis of the different types of economic benefits provided by each state government to its investors, mainly in terms of the number of eligible producers, provision for land allotment, provision for banking of power, and monetary incentives. It is believed that a greater number of eligible producers will invite a variety of solar projects in a city or the state. Most of the governments restrict their policies to registered companies who are eligible through bidding system conducted by the respective governments. On the other hand, it is observed that the policies which allow more number of producers to tap solar energy usually provide more monetary incentives to the investors, and therefore they attract funds and investments easily from different parts of the state. If land incentives are provided by the government, then the project developer can invest extra money into solar-efficient technologies. The banking of electricity refers to the process by which the power generated from electricity generating station is supplied to the grid and often sold to a third party. In such a situation, the generating station has the authority to draw back the electricity supplied from the grid for its own use. As the number of years for banking of electricity increases, the receiving station gets ample time to generate the required fund to repay the generating station. In this way, energy-deficit regions can make use of renewable energy to lighten their areas in a sustainable manner. Other monetary incentives include subsidies provided by the government to promote the development of solar power systems in their jurisdiction.

The economic feasible zone can be easily identified in Fig. 4. The solar policies of Rajasthan, Gujarat, Jammu and Kashmir, Karnataka, Chhattisgarh, Jharkhand, Bihar, Meghalaya, and Mizoram provide maximum number of economic incentives by allowing maximum number of producers to be eligible to tap solar energy; these governments are ready to provide necessary land to project developers with the lowest bid in solar energy generation tenders. These states also provide maximum number of subsidies to its investors. The average performing states include Punjab, Himachal Pradesh, Haryana, Uttar Pradesh, Kerala, Karnataka, and Assam. Their average performance is a result of lower number of banking facilities and monetary incentives provided by the government. The remaining states like West Bengal, Uttarakhand, Tamil Nadu, Sikkim, and Arunachal Pradesh have very little contribution toward an effective solar energy policy, and therefore have performed very poorly in the solar economic feasibility section of the study.

### ***3.4 Viability of Solar Cities Mission***

The concept of the solar city is manifold as it embraces definitions oscillating from a decentralized solar approach to a reduction in conventional sources of energy and meeting sustainable energy needs (Byrne et al. 2015; Kim et al. 2006). The global

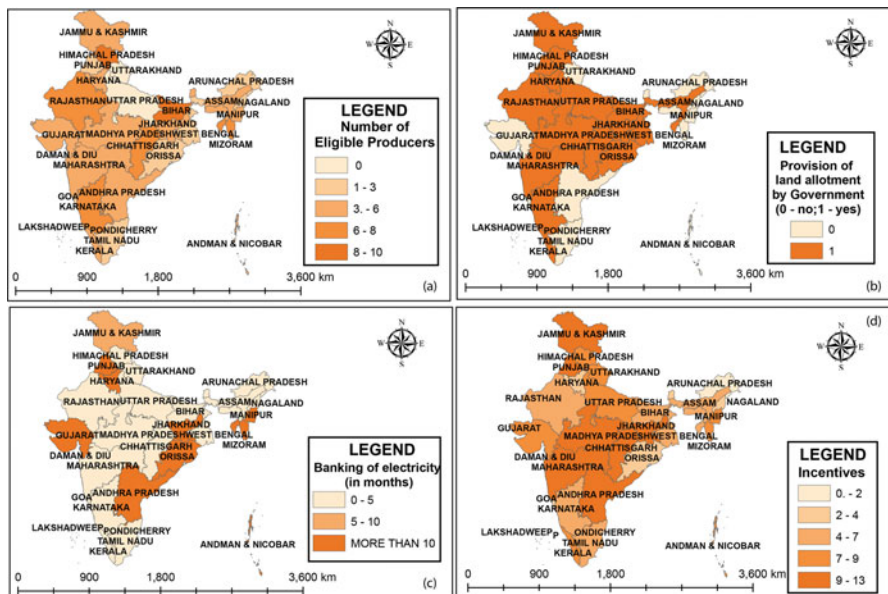


**Fig. 4** Total number of economic benefits provided by each state government to its investors, mainly in terms of the number of eligible producers (a), provision for land allotment (b), provision for banking of power (c), and monetary incentives (d)

cities located in high solar potential areas are involved in deployment of rooftop solar PV technologies in urban environment (Byrne and Taminau 2018; Peng and Lu 2013). These studies mainly concentrate on the estimation of PV-suitable roof area as a means to address the dual-energy challenges within their city boundaries. The Indian cities are rarely planned and architecturally aesthetic to comply with the international standards in addressing solar energy accessibility challenges. Therefore, there is a need to delineate areas that are not only suitable for PV installations in rooftop areas but also construction of large-scale solar parks with CSP facilities. Therefore, in this study, a GIS-based MCDA method was applied to identify the cities with the maximum potential to successfully fulfil the ambitious solar city project.

In order to deploy SPVs in the solar cities, the conditions that were considered necessary are as follows: high GHI, maximum PVOU, and the highest number of economic benefits that will be provided by the government. Similarly, the best cities to tap solar energy from CSPs include the same options, except the higher GHI values are replaced with higher DNI values. TOPSIS method was used to determine which cities have the best potential to invest in SPVs and CSPs for the renewable energy generation within and surrounding their administrative boundaries. It was observed that (Fig. 5) for the deployment of SPVs, Rajkot, Gandhinagar, and Shirdi from west India and Mahbubnagar and Vijayawada from southeast India have the highest technoeconomic potential for the deployment of SPVs within their urban

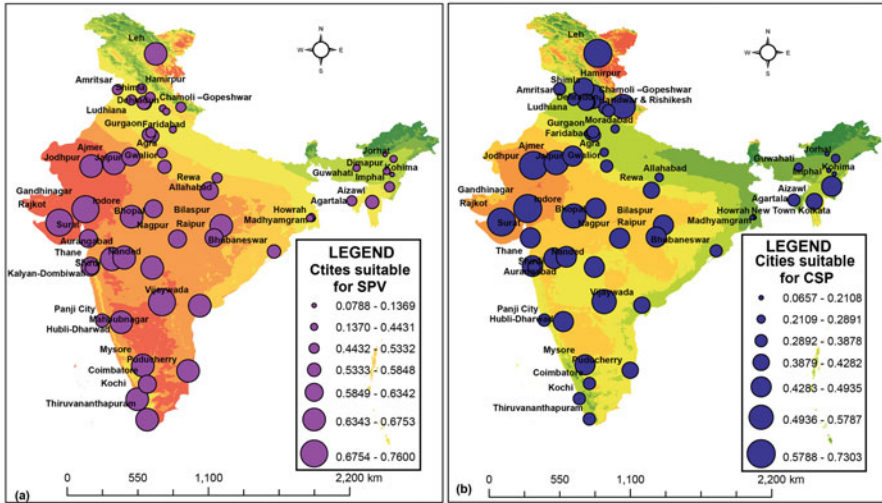


**Fig. 5** Solar City suitability analysis using TOPSIS method for determination of cities suitable for harnessing solar from SPVs (a) and CSPs (b)

boundaries. Around 15 cities fall in the second-best technoeconomic feasible zone, mainly all the cities of Maharashtra and Kerala as well as the cities of Ajmer, Jodhpur, Raipur, Mysore, Leh, and the Union Territory of Puducherry. The solar cities of Gujarat, Maharashtra, and Kerala, which show a higher technologically and economically solar energy resource potential have already set ambitious targets to achieve the SCM by 2022. The Gujarat government is ready to install 8 lakh rooftop solar PV in residences by 2022 and the surplus electricity generated through such systems will be bought at Rs 2.25 per unit (The Indian Express 2019). Such initiatives further boost the urbanites to install the cost intensive SPVs in their urban rooftops. These cities are also ideal to develop large-scale solar plants in their vicinity to fulfil the cities’ energy demand.

The cities which have the potential to generate solar energy without much risk include the remaining cities falling in west India, Chandigarh, Mohali, and the solar cities of Central India. Although Chandigarh falls in this category, but has substantially progressed in achieving the targets set in their SCM Master Plan. Chandigarh and its surrounding solar cities have the potential to generate electricity from large-scale CSPs as they have a higher technoeconomic potential for the deployment of CSPs than SPVs. The solar cities falling in central and east India have lower technoeconomic potential for the deployment of SPVs and CSPs, and therefore the government administering these cities should be prepared to take the risk before developing the SCM Master Plans and setting SCM targets. MNRE has achieved 25% of its ambitious target till date, and aims to achieve the remaining 75% of the target by 2022. However, achieving such ambitious projects do not depend only on financial incentives; other factors like lack of knowledge about energy systems,

inconsistent pricing structure, technical and market barriers, and socioeconomic constraints can hinder the success rates of these projects (Painuly 2001).

## 4 Conclusion

The renewable energy infrastructure planning and energy system modelling from centralized generation of electricity to a decentralized one is very challenging. The future energy landscapes may generate optimum amount of electricity when their effectiveness is studied spatially. The integration of GIS science with the planning and modelling of renewable energy systems incorporates a space and time factor in the modelling process. Although the application GIS in energy system modelling is in the infant stage, the integration of GIS and decision-making approaches in renewable energy studies will enhance the future research avenues in this field.

This study open new horizons for “spatial awareness” from freely available data sources of solar energy resources, and thus this study examines the viability of technoeconomic potential of solar energy resources in different solar cities of India as a means to assess the viability of the Solar Cities Mission program in all these cities. Here, for the first time, a multivariate approach to exploring the technoeconomic feasibility of solar cities using the TOPSIS approach was conducted to study the spatial allocation of solar energy resources all over India. The cities located in the west and south India have the highest potential to tap solar energy in the form of SPVs and CSPs and, therefore, maximum investment should be directed in electrifying these cities from solar energy. The National Solar Mission and the SCM are smart initiatives by the Indian government to mandate the use of renewable energy in the Indian cities. A gradual shift to renewable energy is mandatory for India to secure citizens from the perils of climate change and global warming.

## References

- Al Garni, H. Z., & Awasthi, A. (2017). Solar PV power plant site selection using a GIS-AHP based approach with application in Saudi Arabia. *Applied Energy*, 206, 1225–1240.
- Alhamwi, A., Medjroubi, W., Vogt, T., & Agert, C. (2017). GIS-based urban energy systems models and tools: Introducing a model for the optimisation of flexibilisation technologies in urban areas. *Applied Energy*, 191, 1–9.
- Anwarzai, M. A., & Nagasaka, K. (2017). Utility-scale implementable potential of wind and solar energies for Afghanistan using GIS multi-criteria decision analysis. *Renewable and Sustainable Energy Reviews*, 71, 150–160.
- Asumadu-Sarkodie, S., & Owusu, P. A. (2016). The potential and economic viability of solar photovoltaic power in Ghana. *Energy Sources, Part A: Recovery, Utilization, and Environmental Effects*, 38(5), 709–716.
- Brewer, J., Ames, D. P., Solan, D., Lee, R., & Carlisle, J. (2015). Using GIS analytics and social preference data to evaluate utility-scale solar power site suitability. *Renewable Energy*, 81, 825–836.



- Byrne, J., & Taminiau, J. (2018). Utilizing the urban fabric as the solar power plant of the future. In *Urban energy transition* (pp. 31–49). Amsterdam: Elsevier.
- Byrne, J., Taminiau, J., Kurdgelashvili, L., & Kim, K. N. (2015). A review of the solar city concept and methods to assess rooftop solar electric potential, with an illustrative application to the city of Seoul. *Renewable and Sustainable Energy Reviews*, *41*, 830–844.
- Byrne, J., Taminiau, J., Kim, K. N., Lee, J., & Seo, J. (2017). Multivariate analysis of solar city economics: Impact of energy prices, policy, finance, and cost on urban photovoltaic power plant implementation. *Wiley Interdisciplinary Reviews: Energy and Environment*, *6*(4), e241.
- Cebecauer, T., Šúri, M., & Perez, R. (2010). High performance MSG satellite model for operational solar energy applications. In *ASES National Solar Conference*, Phoenix, USA.
- Chandler, W. S., Stackhouse Jr, P. W., Barnett, A. J., Hoell, J. M., Westberg, D. J., & Ross, A. I. (2015). *Enhancing the NASA prediction of worldwide energy resource web data delivery system with geographic information system (GIS) capabilities*.
- Chow, A., Fung, A., & Li, S. (2014). GIS modeling of solar neighborhood potential at a fine spatiotemporal resolution. *Buildings*, *4*(2), 195–206.
- de Smith, M. J., Goodchild, M., & Longley, P. (2018). *Geospatial analysis* (6th edn), Retrieved October 1, 2019, from <https://arxiv.org/pdf/1902.06672.pdf>
- Eldin, S. A. S., Abd-Elhady, M. S., & Kandil, H. A. (2016). Feasibility of solar tracking systems for PV panels in hot and cold regions. *Renewable Energy*, *85*, 228–233.
- Firozjaei, M. K., Nematollahi, O., Mijani, N., Shorabeh, S. N., Firozjaei, H. K., & Toomanian, A. (2019). An integrated GIS-based ordered weighted averaging analysis for solar energy evaluation in Iran: Current conditions and future planning. *Renewable Energy*, *136*, 1130–1146.
- Freitas, S., Catita, C., Redweik, P., & Brito, M. C. (2015). Modelling solar potential in the urban environment: State-of-the-art review. *Renewable and Sustainable Energy Reviews*, *41*, 915–931.
- Gastli, A., & Charabi, Y. (2010). Solar electricity prospects in Oman using GIS-based solar radiation maps. *Renewable and Sustainable Energy Reviews*, *14*(2), 790–797.
- Ghose, D., Naskar, S., & Roy, A. K. (2019). An open source software: Q-GIS based analysis for solar potential of Sikkim (India). *International Journal of Open Source Software and Processes (IJOSSP)*, *10*(1), 49–68.
- Greene, R., Devillers, R., Luther, J. E., & Eddy, B. G. (2011). GIS-based multiple-criteria decision analysis. *Geography Compass*, *5*(6), 412–432.
- Jahangiri, M., Ghaderi, R., Haghani, A., & Nematollahi, O. (2016). Finding the best locations for establishment of solar-wind power stations in Middle-East using GIS: A review. *Renewable and Sustainable Energy Reviews*, *66*, 38–52.
- Jenks, G. F. (1977). *Optimal data classification for choropleth maps*. Department of Geography: University of Kansas Occasional Paper.
- Kim, J., Han, D., & Na, J. (2006). The solar city Daegu 2050 project: Visions for a sustainable city. *Bulletin of Science, Technology & Society*, *26*(2), 96–104.
- Kumar, D. (2018). Mapping solar energy potential of southern India through geospatial technology. *Geocarto International*, 1–19.
- Kumar, K. E., & Kumari, N. (2019). Estimation of photovoltaic energy potential and reduced carbon emission through geo-spatial technology—a case study of Karnal City, Haryana (India).
- Malczewski, J. (1999). *GIS and multicriteria decision analysis*. New York: Wiley.
- MNRE. (2018). *Solar/Green cities*. Retrieved November 21, 2018, from <https://mnre.gov.in/solar-cities>
- MNRE. (2019). *Solar Rooftop- Grid Connected*. Retrieved October 1, 2019, from <https://mnre.gov.in/solar-rooftop-grid-connected>
- Okoye, C. O., Taylan, O., & Baker, D. K. (2016). Solar energy potentials in strategically located cities in Nigeria: Review, resource assessment and PV system design. *Renewable and Sustainable Energy Reviews*, *55*, 550–566.
- Ozturk, D., & Batuk, F. (2011). Technique for order preference by similarity to ideal solution (TOPSIS) for spatial decision problems. In *Proceedings ISPRS*.

- Painuly, J. P. (2001). Barriers to renewable energy penetration; a framework for analysis. *Renewable Energy*, 24(1), 73–89.
- Peng, J., & Lu, L. (2013). Investigation on the development potential of rooftop PV system in Hong Kong and its environmental benefits. *Renewable and Sustainable Energy Reviews*, 27, 149–162. <https://doi.org/10.1016/j.rser.2013.06.030>.
- Piragnolo, M., Masiero, A., Fissore, F., & Pirotti, F. (2015). Solar irradiance modelling with NASA WW GIS environment. *ISPRS International Journal of Geo-Information*, 4(2), 711–724.
- Präválie, R., Patriche, C., & Bandoc, G. (2019). Spatial assessment of solar energy potential at global scale. A geographical approach. *Journal of Cleaner Production*, 209, 692–721.
- Press Information Bureau. (2018). *The Government is promoting development of solar energy in the country by providing various fiscal and promotional incentives*. Retrieved November 23, 2018, from <http://pib.nic.in/newsite/PrintRelease.aspx?relid=180728>
- Ramachandra, T. V., & Shruthi, B. V. (2007). Spatial mapping of renewable energy potential. *Renewable and Sustainable Energy Reviews*, 11(7), 1460–1480. <https://doi.org/10.1016/j.rser.2005.12.002>.
- Ramachandra, T. V., Jain, R., & Krishnadas, G. (2011). Hotspots of solar potential in India. *Renewable and Sustainable Energy Reviews*, 15(6), 3178–3186.
- Resch, B., Sagl, G., Törmros, T., Bachmaier, A., Eggers, J.-B., Herkel, S., . . . Gündra, H. (2014). GIS-based planning and modeling for renewable energy: Challenges and future research avenues. *ISPRS International Journal of Geo-Information*. v3 n2662-692
- Reshma, R., Ramesh, M., Jayaseelan, S., & Jaganathan, R. (2018). GIS based site suitability MO DELLING for locating solar power park in Thiruvannamalai district, Tamil Nadu. *Journal on Electrical Engineering*, 11(4), 43.
- Ruiz-Arias, J. A., Cebecauer, T., Tovar-Pescador, J., & Šúri, M. (2010). Spatial disaggregation of satellite-derived irradiance using a high-resolution digital elevation model. *Solar Energy*, 84(9), 1644–1657.
- Shehzad, S. A., Hayat, T., Alsaedi, A., & Chen, B. (2016). A useful model for solar radiation. *Energy, Ecology and Environment*, 1(1), 30–38.
- Shiraishi, K., Shirley, R. G., & Kammen, D. M. (2019). Geospatial multi-criteria analysis for identifying high priority clean energy investment opportunities: A case study on land-use conflict in Bangladesh. *Applied Energy*, 235, 1457–1467.
- SolarGIS. (2019). Solar resource atlas.
- Sunwatt-India. (2013). *Why solar*. Retrieved October 1, 2019, from <http://www.sunwattindia.com/whysolar.html>
- Šúri, M., Cebecauer, T., & Perez, R. (2010). Quality procedures of SolarGIS for provision site-specific solar resource information. *Proceeding of the SolarPACES*.
- The Indian Express. (2019, August 9). Gujarat government to buy solar power from homes at Rs 2.25 per unit. Retrieved from
- Watson, A. C., Jacobson, M. D., & Cox, S. L. (2019). *Renewable energy data, analysis, and decisions viewed through a case study in Bangladesh*. Golden: National Renewable Energy Lab (NREL).
- Wegertseder, P., Lund, P., Mikkola, J., & García Alvarado, R. (2016). Combining solar resource mapping and energy system integration methods for realistic valuation of urban solar energy potential. *Solar Energy*, 135, 325–336.
- World Bank Group. (2018). Global solar atlas. *World Bank Group [US]*, 9.
- Wu, G. C., Deshmukh, R., Ndhlukula, K., Radojicic, T., Reilly-Moman, J., Phadke, A., et al. (2017). Strategic siting and regional grid interconnections key to low-carbon futures in African countries. *Proceedings of the National Academy of Sciences*, 114(15), E3004–E3012.
- Xiang, B., Cao, X., Yuan, Y., Sun, L., Wu, H., & Haghghat, F. (2018). A novel hybrid energy system combined with solar-road and soil-regenerator: Dynamic model and operational performance. *Energy Conversion and Management*, 156, 376–387.
- Yoon, K., & Hwang, C. L. (1981). *TOPSIS (technique for order preference by similarity to ideal solution)—a multiple attribute decision making, w: Multiple attribute decision making—methods and applications, a state-of-the-at survey*. Berlin: Springer.

# Mapping Rice Growth Stages Employing MODIS NDVI and ALOS AVNIR-2



Dyah R. Panuju, David J. Paull, Amy L. Griffin, and Bambang H. Trisasongko

**Abstract** Rice, a staple food of most Asian inhabitants, is broadly cultivated and has attracted substantial research interest in the past few decades. Monitoring rice production areas is important due to the growing global demand for the crop. Since cropping systems vary across time and space, frequent monitoring over broad areas is required. This research exploits Moderate Resolution Imaging Spectroradiometer (MODIS) data to identify the stage of rice growth, and Advanced Land Observing Satellite–Advanced Visible and Near Infrared Radiometer Type 2 (ALOS AVNIR-2) to map the stages. Exploiting X12-ARIMA to decompose Normalized Difference Vegetation Index (NDVI) time-series for growth-stage indication and five classifiers for mapping the growth stages, the framework was tested in Indonesia’s “paddy basket,” namely the North Coastal Region of West Java. A conventional classifier, Maximum Likelihood, was compared with some decision tree algorithms, namely Classification Rule with Unbiased Interaction Selection (CRUISE) and Quick, Unbiased, Efficient, Statistical Tree (QUEST); neural network (NN); and support vector machine (SVM) for mapping the growth stages. The seasonal component of time-series decomposition assisted in indicating the stages. Meanwhile, decision tree

---

D. R. Panuju (✉)

Department of Soil Science and Land Resource, Bogor Agricultural University, Bogor, Indonesia

e-mail: [panuju@apps.ipb.ac.id](mailto:panuju@apps.ipb.ac.id)

D. J. Paull

School of Science, The University of New South Wales, Canberra, Australia

e-mail: [d.paull@adfa.edu.au](mailto:d.paull@adfa.edu.au)

A. L. Griffin

Geospatial Science Discipline, School of Science, RMIT University, Melbourne, Australia

e-mail: [amy.griffin@rmit.edu.au](mailto:amy.griffin@rmit.edu.au)

B. H. Trisasongko

Department of Soil Science and Land Resource, Bogor Agricultural University, Bogor, Indonesia

e-mail: [trisasongko@apps.ipb.ac.id](mailto:trisasongko@apps.ipb.ac.id)

© The Editor(s) (if applicable) and The Author(s), under exclusive license to Springer Nature Switzerland AG 2021

P. Kumar et al. (eds.), *Remote Sensing and GIScience*,

[https://doi.org/10.1007/978-3-030-55092-9\\_11](https://doi.org/10.1007/978-3-030-55092-9_11)

algorithms produced interpretable rules for rice growth stages while the spatial representation of SVM and NN was closer to the ground truth.

**Keywords** ALOS AVNIR-2 · X12-ARIMA · MODIS · pixel-based classifier · rice · growth stages

## 1 Introduction

Rice is a staple food for over half the global human population, and provides more than 20% of energy and 15% of protein being ingested (FAO 2014b). About 700 million tons have been produced annually (FAO 2014a) and sold at a median cost of US\$412 per ton in the last 2 years (FAO 2015), placing it among the most valuable agricultural commodities in the world. Increasing demand for rice and its international trade mean that production must increase at a commensurate rate; yet human population expansion and urbanization are consuming prime agricultural lands (Azadi et al. 2011; Phuc et al. 2014). Therefore, monitoring the world's major rice growing areas is of immediate concern.

Remote sensing offers the technology to obtain environmental information over broad areas and monitoring at a frequent revisit times and at various spatial scales (Lu et al. 2003). Since paddy has a relatively short growth cycle (100–160 days) (International Rice Research Institute 2013) and its cultivation varies between farmers, frequent monitoring is required for assessing farming practices and for allowing valid estimation of the area under cultivation and in different growth stages.

Temporal-based growth stages exploration using optical images mostly employs vegetation indices (VIs). They, however, are affected by seasonality (Verbesselt et al. 2010), which is defined as the periodic cycle of vegetative growth or natural events, affected by seasonal and interannual climate variability (Zhao et al. 2013; Pezzulli et al. 2005). Monitoring land surfaces, including rice growth phases by using VIs therefore needs to account for seasonal variation (Verbesselt et al. 2010; Panuju et al. 2010). The growth stages of vegetation have been studied by exploring phenological pattern of plants facilitated by time series analysis (Zhao et al. 2013).

Meanwhile, decomposing a univariate time series of a vegetation index has allowed the differentiation of vegetation types (Lu et al. 2003) and identification of cropping intensities (Chen et al. 2012a, b). The present research is focused specifically on decomposition techniques that assist in differentiating rice growth stages. Mapping agriculture extent, especially of rice fields, has been achieved using numerous remote sensing platforms, including synthetic-aperture radar (SAR) (Toan et al. 1997; Trisasongko 2019) or optical imageries (Panuju and Trisasongko 2008; Trisasongko et al. 2012).

Mapping of farmland has been facilitated by image classification techniques (Wu et al. 2014; Ozdarici-Ok et al. 2015). Decision tree classification, a nonparametric technique, is currently attracting a substantial amount of research in remote sensing (Yang et al. 2003; Zhao et al. 2011). The fact that these methods make no

statistical assumptions, their explicit structure, and ease of interpretability, particularly in the identification of discriminating factors between classes are among possible reasons for their popularity (Pal and Mather 2003).

Multiple algorithms in decision tree techniques are available to optimize classification, for instance, the Classification Rule with Unbiased Interaction Selection (CRUISE) and Quick, Unbiased, Efficient, Statistical Tree (QUEST). Loh (2011) concluded that QUEST and CRUISE generated better accuracy compared with other algorithms tested. Nonetheless, various experiments and applications comparing multiple classifiers demonstrated inconsistent accuracies. For instance, Pal and Mather (2003) showed that both Maxlike and NN outperformed decision tree classification of hyperspectral imagery on two environmental settings, but other research demonstrated that SVM generated more stable accuracy for different numbers of variables and sizes of training pixels than Maxlike, NN, and decision tree classifiers (Huang et al. 2002). It seems, therefore, that the comparisons yield different results under different settings. Thus, to have an optimal result in a given environmental setting, comparison of multiple algorithms is warranted.

The present study explores the use of seasonal time series analysis and several classifiers employing MODIS and ALOS AVNIR for mapping growth stages. The goal is to investigate the potential of time-series decomposition of VIs for indicating growth phases and to compare the performance of five classifiers for mapping paddy growth stages. The classification accuracy and resulting crop maps were then assessed.

## 2 Study Area

In Indonesia, rice production areas are distributed throughout almost all islands, with Java having the largest planted area and the most productive one (Panuju et al. 2013). The North Coastal Region (NCR) of West Java is one of the most important rice-basket areas, sharing 35% of West Java province's production (Kementerian Pertanian Republik Indonesia 2015). Nonetheless, NCR's proximity to Jakarta has put the paddy fields in this region under land development pressure. Therefore, monitoring the spatial dynamics of these paddy fields is critical in the region. This study was conducted in the NCR area, which is located between  $107^{\circ} 31' - 107^{\circ} 54' E$  and  $6^{\circ} 11' - 6^{\circ} 49' S$  and it comprises 205,177 ha, or 6.34% of West Java's area.

The site concentrated on PT Sang Hyang Seri's (PT SHS) area. PT SHS is a seed producer having fields located in various parts of Indonesia including the site. Rice plots were clearly mapped, and had appropriate sizes for medium-coarse resolution image analyses that allowed identification of homogeneous samples. Access to such data is often difficult to obtain for remote sensing applications since small-scale farmers dominate paddy cultivation in the region.

### 3 Materials and Method

This research employed optical imagery, including MODIS and ALOS AVNIR. MOD13Q1 datasets from the sinusoidal grid of H28V09, having 250 m spatial resolution, were accessed freely from the United States Geological Survey (USGS) and used to develop the time-series VIs. The MODIS data spanned from Julian Day-1 of 2004 until Day-353 of 2010. MOD13Q1 of Collection 5 comprises 12 bands including blue, red, near infrared, and mid-infrared reflectance, and the Normalized Difference Vegetation Index (NDVI), Enhanced Vegetation Index (EVI), vegetation index quality, and pixel reliability. A new equation of EVI called EVI2 has been implemented to derive EVI layers to account for atmospheric disturbances in cloudy or hazy pixels (Didan et al. 2015).

The time-series of NDVI and EVI (including EVI2) were compared to help identify the beginning and end of growing seasons as well as the identification of rice phenology and cropping intensity. Furthermore, an ALOS AVNIR image dated June 30, 2009, matching with the available ground truth, was used to map rice areas based on their growth phases. Ancillary information about planting management provided by PT SHS for the years 2006–2009 was used to evaluate time-series analysis and to assist the identification of rice growth cycles.

The flow of analyses is described in Fig. 1. The figure shows three main parts, including data preparation, identification of growth stages, and mapping rice stages.

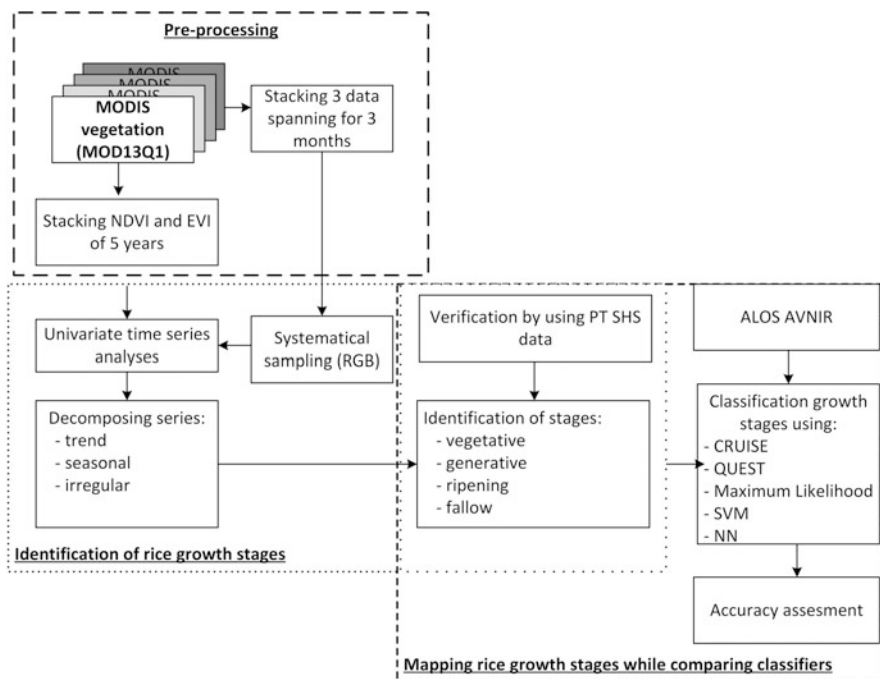


Fig. 1 The flow of analyses

Data preparation involved MODIS acquisition, stacking, and sampling. The next steps are explained in detail in the following subsections.

### 3.1 Identifying Rice Growth Stages

Seasonality has been discussed in previous research employing vegetation indices (Jonsson and Eklundh 2002). Seasonal adjustment was used in the present study to correct and smooth the time-series of VIs while decomposing time-series into trend, seasonal, and irregular components for indicating the growth stages.

In this research, X-12-ARIMA, a combination of a seasonal adjustment procedure (X) and an autoregressive, integrated moving average (ARIMA) technique was used to analyze time-series VIs. The procedure is the extension of X-11, the standard statistical technique to analyze univariate time-series data (Shiskin et al. 1965). Homogeneity of variances across time or written as  $\text{Var}(Y_t) = \text{Var}(Y_{t+k}) = \gamma_0$  and a constant mean with no trend are expected in X12-ARIMA (Chatfield 1996). When the stationarity assumption is not met, then differencing should be employed (Box and Jenkins 1968). Assuming that original series of vegetation index ( $Y_t$ ) follows a particular seasonal ARIMA model, as explained by Wei (2006), the parameter for series data having (p,d,q)x(P,D,Q) order can be estimated by using:

$$\phi_p(B)\Phi_p(B^s)(1-B)^d(1-B^s)^D Y_t = \theta_q(B)\Theta_Q(B^s)a_t \quad (1)$$

Lowercase letters represent nonseasonal orders, while uppercase letters denote seasonal ones. Letters p, d, and q represent orders for autoregressive, difference, and moving average components, respectively, while  $\phi$  symbolizes an autoregressive function and  $\theta$  stands for the autoregressive process. Moreover, B is a backshift operator in which

$$\begin{aligned} \phi_p(B) &= 1 - \phi_1 B - \phi_2 B^2 \dots - \phi_p B^p \quad \text{and} \quad \theta_p(B) \\ &= 1 - \theta_1 B - \theta_2 B^2 \dots - \theta_p B^p \end{aligned} \quad (2)$$

Further discussion regarding X-12-ARIMA is provided by Findley et al. (1998). If seasonality is indicated by the order of seasonal components being  $>1$ , then seasonal adjustment analysis is performed to transform VIs and decompose them into components. The technique was performed on both the NDVI and EVI series based on Time-series Regression with ARIMA noise, Missing values, and Outliers (TRAMO) and Signal Extraction in ARIMA Time-Series (SEATS) (Gómez and Maravall 1996, 2001). Before decomposing the time series, following the work of Jia et al. (2002), all VIs were summarized into monthly datasets using maximum and average values. The original series data was decomposed by using an additive

model, which can be written as  $Y_t = T_t + S_t + I_t$ , where  $Y$  is the original value, subscript  $t$  refers to time,  $T$  denotes the trend component,  $S$  stands for the seasonal component, and  $I$  symbolizes the irregular component. In the present research, a seasonality test was used to indicate seasonal times of planting and sowing. The count of peaks from a smooth pattern can be used to estimate the intensity.

PT SHS cultivates various strains of rice, which vary across seasons. In order to correspond with image data acquisition dates, only cultivation for the year 2009 was graphed, and there were three cultivars being grown at that time, that is, hybrid, Ciherang, and Situ Bagendit. The local cultivar Ciherang was selected in this research since it is popular for farmers. For each sowing and planting time, one plot was taken as a sample, with each plot covering a minimum area of 12 ha. There are distinct stages of paddy growth (Vergara 1992), and this research attempted to observe four of them: vegetative, reproductive, ripening, and fallow.

### ***3.2 Training, Testing, and Classification of Paddy Growth Stages***

In this research, all algorithms were executed on atmospherically uncorrected ALOS AVNIR-2 imagery dated June 30, 2009. AVNIR consists of four spectral bands, has 10 m spatial resolution (at nadir), and 70 km swath width. The range of wavelengths for each band is Band 1: 0.42–0.50, Band 2: 0.52–0.60, Band 3: 0.61–0.69, and Band 4: 0.76–0.89 (Tadono et al. 2004). The ground truth data were taken from plots of PT SHS (Fig. 2). The size of every plot was 50 m wide, with various lengths depending on irrigation networks and micro relief.

We identified training and testing sites from the result of time-series decomposition analysis verified by PT SHS ancillary data. Plots of training and testing samples were taken separately to avoid overfitting. All five classifiers, CRUISE, QUEST, Maxlike, NN, and SVM, were employed to classify paddy areas using three, four, and five classes. The classes included four paddy stages of vegetative, reproductive, ripening, and fallow, as well as built-up areas.

Verification of paddy growth stages for training samples was made based on its age as recorded in the PT SHS data. Different rice cultivars have growth phases with different durations. Ciherang normally takes 120 days for the entire growth cycle and its vegetative stage extends from 0 (seedlings) to 55 days. In this research, three-class analysis consisted of vegetative ( $X < 55$  days), reproductive ( $55 \text{ days} < X < 90$  days), and ripening ( $X > 90$  days), where  $X$  represented the age of the plants on June 30, 2009; four-class analysis added fallow; and five-class analysis added the category built-up area, which occurred in the surroundings. Figure 3 shows images taken from the fieldwork, including fields that had just been cultivated with hybrid and Ciherang cultivars.



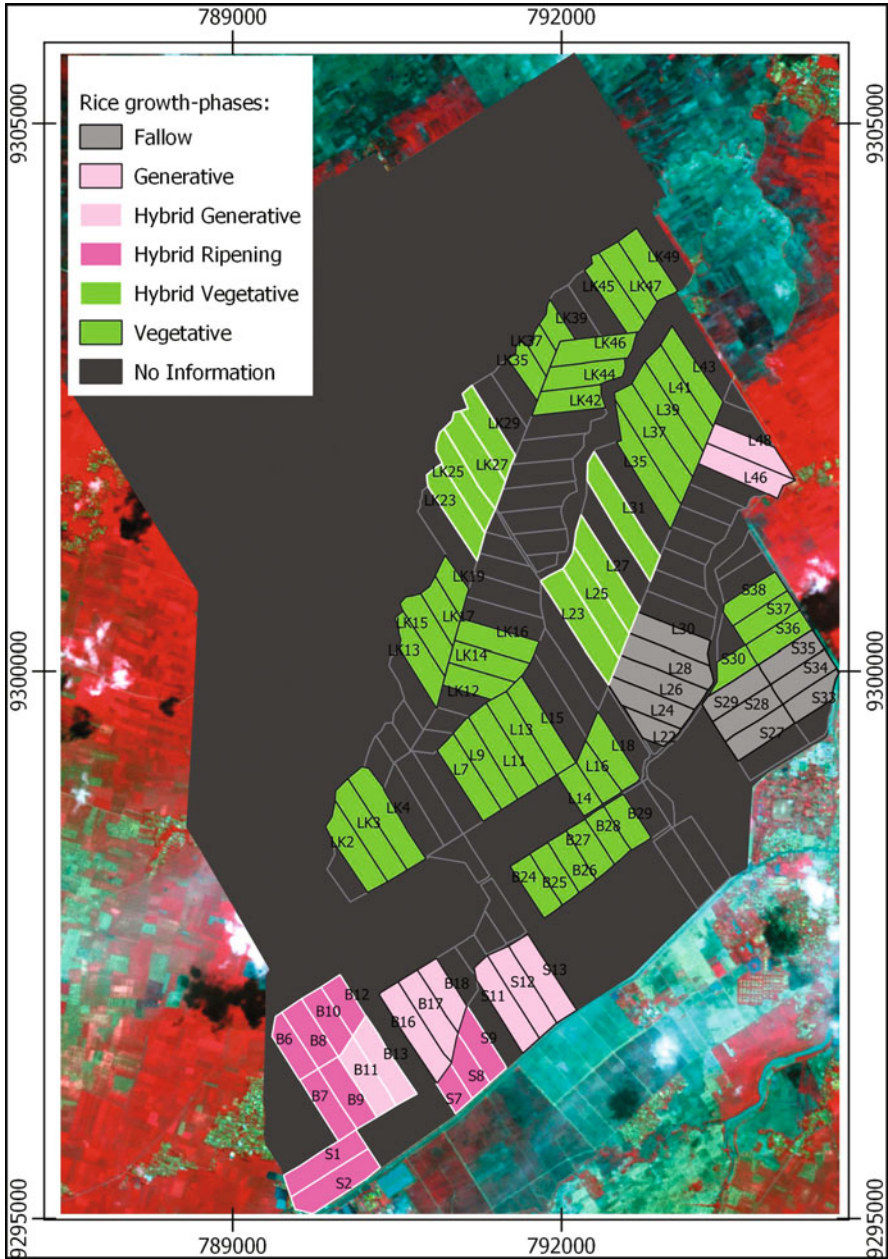


**Fig. 2** Field plots of PT SHS overlaid on AVNIR-2 false color RGB (4–3–2) imagery. Letters and numbers denote the name of plots. Color represents paddies growth-phases on June 30, 2009 AVNIR-2 image copyright JAXA

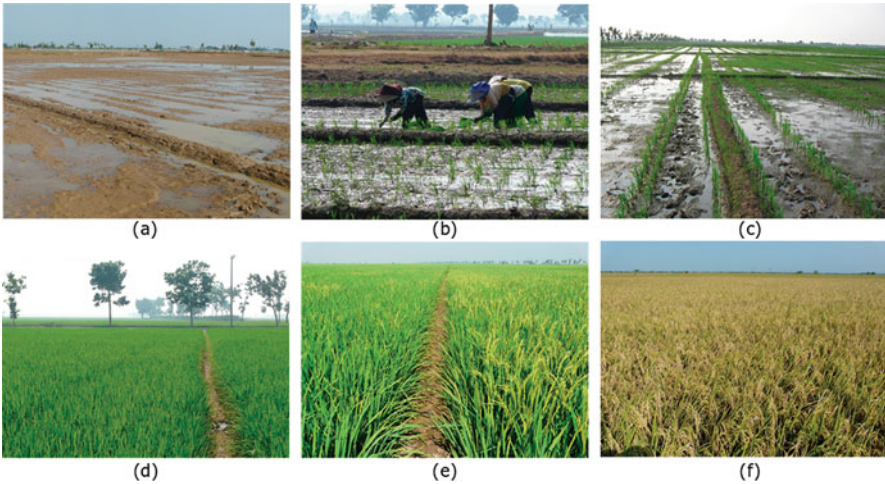


**Fig. 3** (a) Fallow fields, (b) just planted with Ciherang cultivar, (c) just planted with hybrid cultivar, (d) vegetative, (e) reproductive, and (f) ripening paddy stages

### 3.3 Accuracy Assessment of the Five Classifiers

The performance of classifiers was evaluated based on training data for building the rules, then assessing the accuracy based on testing samples. Theoretically, the accuracy assessment will sufficiently describe the proportion of correctly classified pixels compared to the ground truth when sampling scheme, size, classification scheme, and spatial autocorrelation were considered (Congalton 1991). In this case, training and testing samples size for every class was about 620 pixels. Overall accuracy, Kappa, and confusion matrices were then assessed. All plots were observed, while detailed records, including photographs, were taken randomly at about five points for each class to represent vegetative and nonvegetative conditions, guided by information from field managers.

## 4 Results and Discussion

### 4.1 Identifying Rice Growth Stages

Raw time-series of selected paddy fields are presented in Fig. 4. In general, the values of NDVI range and mean (0.1–0.7; 0.4) were greater than those of EVI (0.1–0.5; 0.3), since there was correction of the values of EVI by the blue channel. Nevertheless, both indices generally indicated similar patterns. By comparing two indices on sample locations coupled with in situ information about sowing and transplanting, an indicative pattern of the various growth phases emerged.

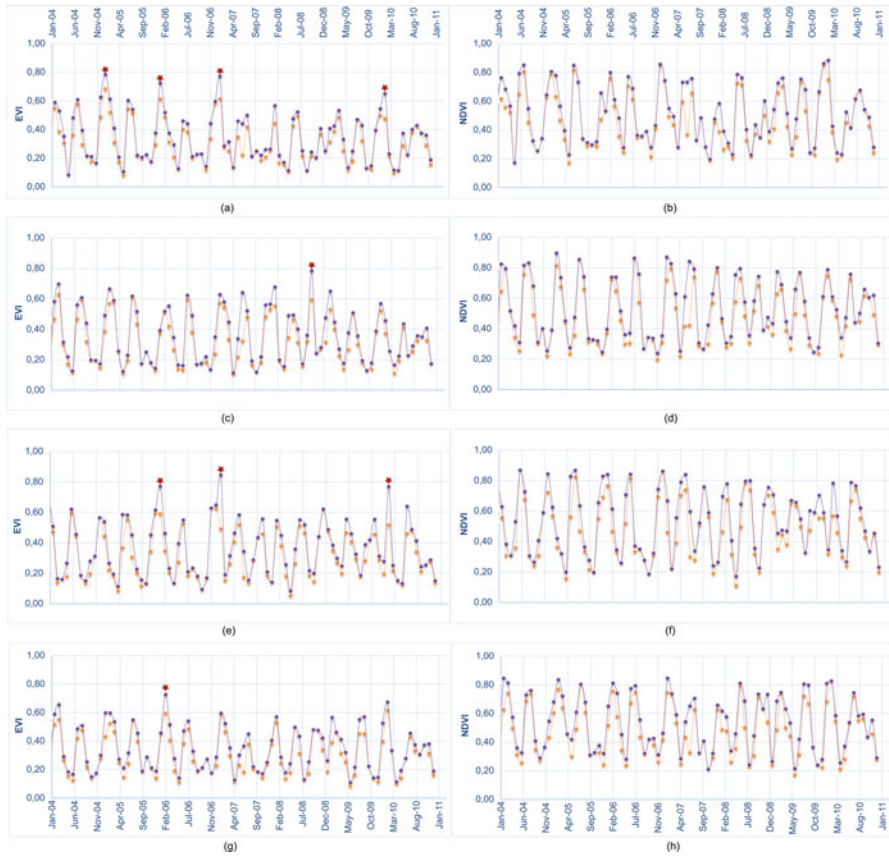


**Fig. 4** The original time-series of (left) EVI and (right) NDVI for 7 years of average plot samples, from top to bottom: (a,b) vegetative L17, (c,d) reproductive L43, (e,f) ripening S11, and (g,h) fallow L28. Dashed lines represent monthly average values and solid lines correspond to monthly maximum values. Red stars indicate unusual spikes

NDVI and EVI plots showed different patterns across periods (Fig. 4). Unusual observations shown by spikes (see stars) were more likely to be detected by using maximum EVI values than averages. On the other hand, the graphs of maximum NDVI seemed to be smoother than the average values and had smaller differences between peaks. About 16 peaks were found from 7 consecutive years of NDVI or EVI datasets (Fig. 4). This suggests that most rice fields at the test site experienced a cropping intensity of 2.25–2.5 crop cycles per year. This intensity is considered relatively high for most rice fields in Indonesia at this moment, and is likely due to the extensive irrigation network across the NCR, including the test site.

Figure 5 shows the decomposition series of average EVI and NDVI, and maximum EVI and NDVI. Both series were selected to account for designated growing phases (March–August 2009) that could be related to the AVNIR acquisition dates. The trend component of NDVI decomposition depicted a similar pattern to EVI,

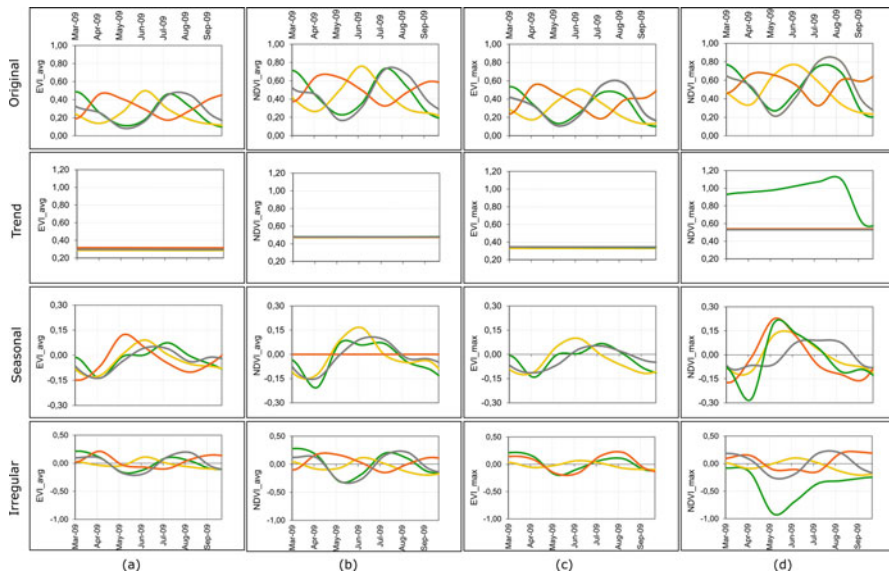


**Fig. 5** Decomposition series of average (a) EVI and (b) NDVI, and maximum (c) EVI and (d) NDVI from (O) their original observation series into (T) trend, (S) seasonal, and (I) irregular components for four samples over the year 2009. Green lines represent vegetative L17, yellow lines stand for reproductive L43, brown lines denote ripening S11 and gray lines follow L28

being constant over the period of analysis for average and maximum values, except for vegetative plot L17 and maximum NDVI. L17 was planted with the hybrid cultivar, which tends to have heterogeneous stages within plots during the early vegetative stage until the end of their productive stage at “heading” substage (the end of reproductive stage) (Fig. 4). An increasing trend followed by a decrease after pollination indicated the heterogeneity of stages within plot L17. Different vegetation cover within the plot is then less observable after pollination, resulting in the more homogeneous value of indices within the hybrid-cultivated plot after the phase.

The seasonal component of the series showed an oscillating pattern that could be associated with growing stages. Phenological patterns shown in Fig. 5 row S reflect crop calendars available for the test site. The sequence of growing seasons for four parcels obtained from SHS planting calendar matches relatively well with Fig. 4. The calendar differed across plots (see Fig. 1). The S11 plot, for instance, which in June was in a heading–ripening phase, corresponds to the pattern. S11 peaked first, followed by L43, which was in reproductive stage. These were trailed by the L17 plot, which was in a vegetative phase at that time, and lastly by L28, hosting hybrid cultivar in an early vegetative phase.

The irregular component differed somewhat between EVI and NDVI. Since the magnitude of EVI was relatively smaller than NDVI, the regular component of EVI for average and maximum values was also lower. The irregular component of maximum NDVI of L17 was curvier than other plots, as was the trend component.

Patterns of maximum EVI and NDVI were therefore reasonably similar to the average values of both indices. Even though decomposition of the maximum value of EVI on the fallow plot L28 was approximated due to an inadequate model for seasonal adjustment, the information was still useful for representing the cropping calendar.

### 4.2 Map of Paddy Growth Stages

All algorithms including the decision tree were designed to differentiate paddy growth phases in the controlled areas. As explained by Friedl and Brodley (1997), decision tree classification provides a rule structure that eases interpretation by identifying spectral bands that could separate classes. Figure 6 compares classification rules constructed by CRUISE and QUEST with 3 and 4 classes. Tree structure for five classes is not presented, nevertheless, the summary is provided in Table 1. In general, CRUISE generated a more complicated structure than QUEST. For instance,

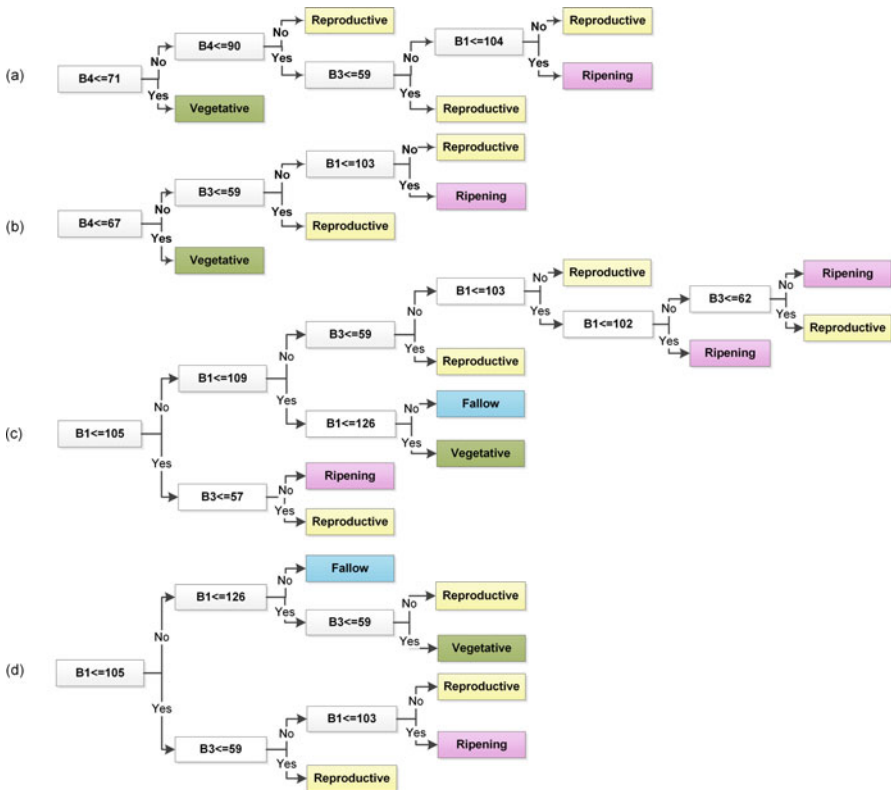


**Fig. 6** Decision trees for three (a,b) and four (c,d) classes using the CRUISE and QUEST algorithms respectively

**Table 1** Number of rules for QUEST and CRUISE algorithms for 3, 4, and 5 classes of paddy stages and built-up land

| Classes      | Cruise    |           |           | Quest     |           |           |
|--------------|-----------|-----------|-----------|-----------|-----------|-----------|
|              | 3 classes | 4 classes | 5 classes | 3 classes | 4 classes | 5 classes |
| Fallow       |           | 1         | 4         |           | 1         | 2         |
| Vegetative   | 1         | 1         | 2         | 1         | 1         | 5         |
| Reproductive | 3         | 4         | 3         | 2         | 3         | 3         |
| Ripening     | 1         | 3         | 1         | 1         | 1         | 1         |
| Built-up     |           |           | 9         |           |           | 9         |
| Total rules  | 5         | 9         | 19        | 4         | 6         | 20        |

when QUEST produced four rules for three classes, CRUISE created five rules. The result also suggests that adding classes creates more complicated branches. Of the decision trees produced by CRUISE, the three-class tree consisted of five rules, the four-class tree consisted of nine rules, and the five-class tree consisted of 19 elements. It appears that the number of classes was an important factor dictating tree structure.

Moreover, tree structures show that the most important spectral band differs throughout different numbers of classes. For instance, AVNIR-2 Band 4 was the most important channel for discriminating paddy growth phases without fallow and built-up classes; its wavelength (0.76–0.89  $\mu\text{m}$ ) corresponds to the near infrared (NIR) portion of the electromagnetic spectrum. Band 4 (NIR) distinguished vegetative phase from reproductive phase. Other channels that contributed to discriminating three classes were the red channel (0.61–0.69  $\mu\text{m}$ ) and the blue channel (0.42–0.5  $\mu\text{m}$ ). These two channels differentiated the reproductive from the ripening stage. Those channels discriminated different concentrations of chlorophyll in the different stages of paddy. This result is similar to a previous test using Landsat- and LOSAT-simulated data (Trisasongko et al. 2010) that found that the NIR channel had substantial utility for rice monitoring.

However, when the fallow class was added, the discriminator was not the same. For four classes, the first and second discriminators were the blue and red channels, while NIR was not important. During growing seasons, rice fields are mostly waterlogged, except shortly before ripening. According to Chuvieco and Huete (2010), absorption on water bodies increases with longer wavelengths, thus the highest reflectance occurs in the blue band, it decreases in NIR, and approaches zero in SWIR. The blue portion of the spectrum was, therefore, useful for discriminating paddy fields in this phase. Using Band 1 (blue), fallow lands that were waterlogged could be distinguished from the vegetative phase. In all cases, Band 2 was seen to be the least important for this task. Indeed, although tree structures generated by CRUISE and QUEST were different, the discriminator was the same.

### 4.3 The Accuracy of Classifications and their Spatial Configuration

Accuracy assessment through overall accuracy, Kappa and their spatial configuration revealed some important features. Increasing the number of land cover classes did not always reduce classification accuracies (Fig. 7). Classifications using four classes produced the highest accuracy for all algorithms except maximum likelihood, which generated the same accuracy both for three and four classes. In this case, maximum likelihood outperformed other algorithms by producing overall accuracy and Kappa at 99.2% and 0.984, respectively. The next highest accuracy of three-class classification was generated by CRUISE and SVM at 94.6% and 94.0%, respectively. Maximum likelihood maintained the same accuracy as three-class classification when adding one class, but then drastically decreased to 78.4% when a fifth class was added. The other three classifiers, namely QUEST, NN, and SVM, produced even higher accuracies when one class was added, from 87.3%, 91.8%, and 94.0%, respectively, to 90.7%, 93.2%, and 95.5%, respectively. Of the two decision tree classifiers, QUEST produced a slightly lower accuracy using three land cover classes compared to CRUISE. However, for five land cover classes, the reduction of the accuracy of QUEST was less than CRUISE, with QUEST (82.4%) producing higher accuracy than CRUISE (80.4%). This is consistent with the findings of Trisasongko et al. (2012), although that study used different datasets, that is, Worldview-2, which has nine spectral bands with additional coastal, yellow, and red-edge channels. That research produced accuracies of 77% and 89% for CRUISE and QUEST, respectively. In the most complex classes, SVM outperformed other classifiers in producing accuracy at 87.9%, while maximum likelihood seemed to generate the lowest accuracy.

As shown by Pal and Mather (2003), using more spectral bands would likely generate higher accuracy. This suggests that several tests ought to be undertaken to determine optimal approaches under different settings including datasets. Another issue seen in this research is declining accuracy for complex classification. For some classifiers including SVM, NN, and the QUEST, rising error was trivial at certain

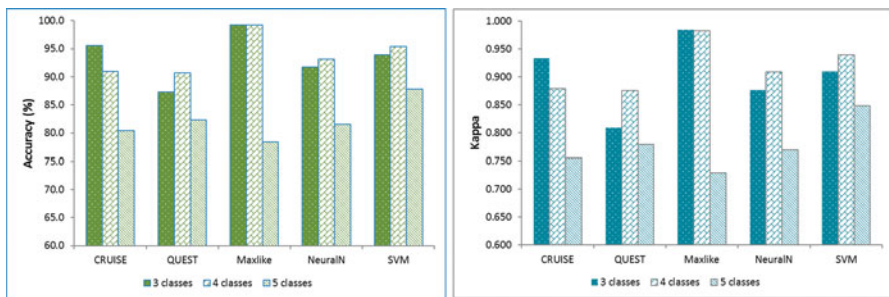


Fig. 7 The comparison of overall accuracy and Kappa value of five classifiers for three, four, and five classes of paddy growth stages and built-up use

**Table 2** The confusion matrix for five algorithms when differentiating five classes including three paddy growth stages, fallow, and built-up land

| Class              | Fallow | Vegetative | Reproductive | Ripening | Built-up |
|--------------------|--------|------------|--------------|----------|----------|
| CRUISE             |        |            |              |          |          |
| Unclassified       | 0.0    | 0.0        | 0.0          | 0.0      | 0.0      |
| Fallow             | 100.0  | 0.0        | 0.0          | 0.0      | 0.2      |
| Vegetative         | 0.0    | 97.0       | 0.0          | 0.0      | 7.3      |
| Reproductive       | 0.0    | 0.0        | 91.7         | 27.6     | 0.0      |
| Ripening           | 0.0    | 0.0        | 1.9          | 20.8     | 0.0      |
| Built-up           | 0.0    | 3.0        | 6.4          | 51.6     | 92.5     |
| QUEST              |        |            |              |          |          |
| Unclassified       | 0.0    | 0.0        | 0.0          | 0.0      | 0.0      |
| Fallow             | 100.0  | 0.0        | 0.0          | 0.0      | 0.0      |
| Vegetative         | 0.0    | 97.3       | 0.0          | 0.0      | 2.7      |
| Reproductive       | 0.0    | 0.0        | 88.1         | 22.4     | 0.0      |
| Ripening           | 0.0    | 0.0        | 1.9          | 28.9     | 0.0      |
| Built-up           | 0.0    | 2.7        | 10.0         | 48.7     | 97.3     |
| Maximum likelihood |        |            |              |          |          |
| Unclassified       | 0.0    | 0.0        | 0.0          | 0.0      | 0.0      |
| Fallow             | 100.0  | 0.0        | 0.0          | 0.0      | 0.0      |
| Vegetative         | 0.0    | 83.9       | 0.0          | 0.0      | 1.1      |
| Reproductive       | 0.0    | 0.0        | 78.1         | 0.0      | 0.0      |
| Ripening           | 0.0    | 0.0        | 0.2          | 30.4     | 0.0      |
| Built-up           | 0.0    | 16.1       | 21.7         | 69.6     | 98.9     |
| Neural network     |        |            |              |          |          |
| Unclassified       | 0.0    | 0.0        | 0.0          | 0.0      | 0.0      |
| Fallow             | 100.0  | 0.0        | 0.0          | 0.0      | 0.0      |
| Vegetative         | 0.0    | 99.2       | 0.0          | 0.0      | 27.3     |
| Reproductive       | 0.0    | 0.0        | 83.1         | 0.0      | 0.0      |
| Ripening           | 0.0    | 0.0        | 15.6         | 53.3     | 0.0      |
| Built-up           | 0.0    | 0.8        | 1.3          | 46.7     | 72.7     |
| SVM                |        |            |              |          |          |
| Unclassified       | 0.0    | 0.0        | 0.0          | 0.0      | 0.0      |
| Fallow             | 100.0  | 0.0        | 0.0          | 0.0      | 0.2      |
| Vegetative         | 0.0    | 97.6       | 0.0          | 0.0      | 2.1      |
| Reproductive       | 0.0    | 0.0        | 81.9         | 0.0      | 0.0      |
| Ripening           | 0.0    | 0.0        | 17.2         | 62.0     | 0.0      |
| Built-up           | 0.0    | 2.4        | 0.9          | 38.0     | 97.7     |

levels; however, this issue could be interesting for maximum likelihood and CRUISE. Despite the highest accuracies of Maxlike and CRUISE for small numbers of classes, accuracies produced by these two algorithms decreased substantially when classifying numerous categories.

In order to understand misclassification and possible mixtures among classes, an accuracy matrix using testing datasets was generated for the five classes (Table 2).



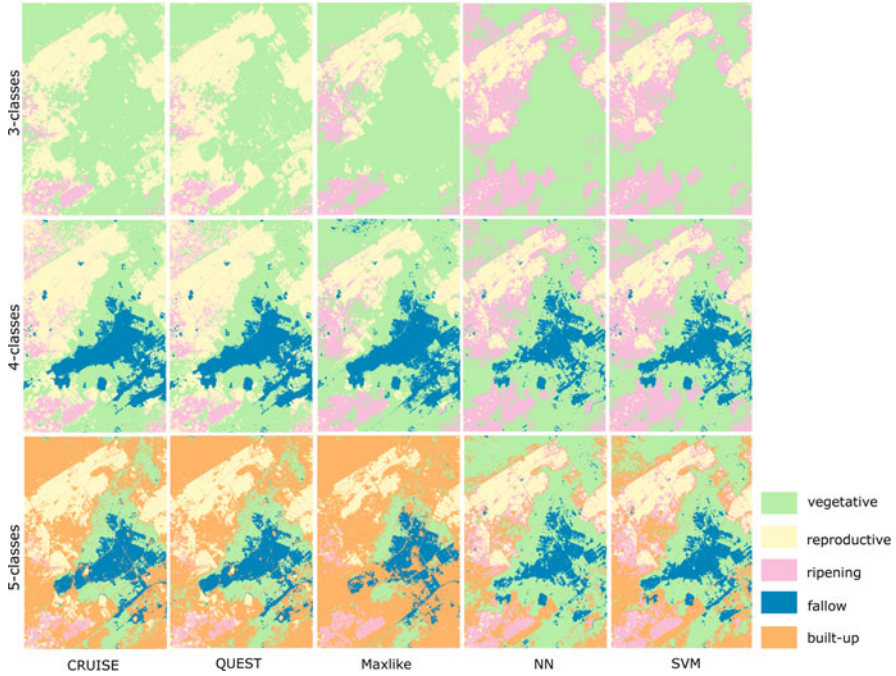


**Fig. 8** The map of classification of ALOS-2 using CRUISE, QUEST, Maximum Likelihood (Maxlike), Neural Networks (NN), and Support Vector Machine (SVM) for three (top), four (middle), and five (bottom) classes of paddy growth stage and built-up land

It shows that the easiest class to separate was fallow. The result was consistent for all classifiers. The conclusion is easily interpretable due to nonexistence of vegetative cover on fallow land.

The ripening paddy class was the hardest class to split. Testing data showed that some ripening paddy areas could be misclassified as being in the reproductive stage or built-up areas due to their spectral mixture or similarity. It is apparent that all classifiers were more or less unable to classify ripening rice properly. Hybrid cultivar taken as samples for the ripening class indicated a spectral mixture with reproductive plants and at the same time with built-up lands. Non-simultaneous planting across an entire plot applied for the hybrid cultivar; rather, there are different dates of planting between the edge and middle parts of the plot. In ripening stage, chlorophyll contents decreased substantially from their productive stage, which resulted in similarity to, and thus confusion with, built-up lands. Moreover, in built-up areas, most settlements were surrounded by small gardens planted with various trees, shrubs, or crops that result in a spectral mixture in between vegetative and built-up classes. Therefore, there is difficulty in separating ripening and built-up areas. Reproductive stages were seen to mix as well with other classes such as ripening or built-up land.

The resulting classifications are presented in Fig. 8. CRUISE and QUEST produced similar spatial patterns, as did NN and SVM, while Maxlike performed

in a distinctly different way to the other classifiers. It seems that although overall accuracy produced by NN and SVM was lower than Maxlike (for three classes), the spatial pattern of NN and SVM was closer to the spatial pattern of the ground truth. As the number of classes became larger, CRUISE, QUEST, and Maxlike overestimated built-up areas as did SVM, but to a lesser degree. This result is not entirely consistent with the accuracy produced by using training and testing data where SVM had the highest accuracy followed by NN. Overall, NN and SVM respectively generated the most accurate spatial pattern.

## 5 Conclusions

Time-series analyses are invaluable to assess advantages and disadvantages of using VIs. EVI is likely to be a better candidate for rice monitoring compared to NDVI. The research also found that averaged values of monthly data produced suitable information to assist the identification of crop calendars. The results suggested that crop calendars, which traditionally have been limited in availability, can be reconstructed from time-series analysis. Moreover, analyses using ground truth data suggest the importance of considering cultivars when mapping rice areas, particularly when hybrid and nonhybrid types are planted in closed proximity.

This research showed that all algorithms exposed their advantages in classification. CRUISE and QUEST, like other decision trees algorithms, were somewhat robust and interpretable due to their capability to visualize rule development during classification. In the present research, CRUISE was more suitable for discriminating a small number of classes. Nonetheless, CRUISE's error rates rose substantially when more classes were targeted. QUEST, in contrast, provided lower accuracy, yet was able to prevent the declining overall accuracy with an increasing number of classes. This suggests that in the future a thorough performance test to compare these algorithms with other algorithms (e.g., C5 or Random Forest) is necessary to develop a better picture of their respective strengths and weaknesses.

Accuracy assessment is an important tool to evaluate the performance of classifiers. Nevertheless, this research indicates that merely having high overall accuracy does not necessarily result in a map that resembles the ground truth data, particularly when the accuracy assessment is based on training and testing samples. As stated by Congalton (1991), sample size or sampling scheme (randomized, stratified, or systematic) may still be an unresolved question. Comparing spatial patterns produced by a classifier qualitatively (visually) and quantitatively with higher spatial resolution data would provide better information on the robustness of the classifier.

**Acknowledgements** The authors are indebted to the United States Geological Survey (USGS), PT Sang Hyang Seri, the Japan Aerospace Exploration Agency (JAXA) for data access, Australia Awards scholarship, and UNSW Canberra for research facilities. The MOD13Q1 data product was retrieved from the online Data Pool, courtesy of the NASA Land Processes Distributed Active Archive Center (LP DAAC), USGS/Earth Resources Observation and Science (EROS) Center,

Sioux Falls, South Dakota, ([https://lpaac.usgs.gov/data\\_access/data\\_pool](https://lpaac.usgs.gov/data_access/data_pool)). ALOS AVNIR was provided by JAXA under grant number RA6-3040. Thanks to Julie Kesby (previously with PEMS, UNSW, Canberra) for providing editorial advice.

## References

- Azadi, H., Ho, P., & Hasfiati, L. (2011). Agricultural land conversion drivers: A comparison between less developed, developing and developed countries. *Land Degradation & Development*, 22(6), 596–604. <https://doi.org/10.1002/ldr.1037>.
- Box, G. E. P., & Jenkins, G. M. (1968). Some recent advances in forecasting and control. *The Royal Statistical Society Series C-Applied Statistics*, 17(2), 91–109.
- Chatfield, C. (1996). *The analysis of time series : An introduction* (5th ed.). London: Chapman and Hall.
- Chen, C. F., Chen, C. R., & Son, N. T. (2012a). Investigating rice cropping practices and growing areas from MODIS data using empirical mode decomposition and support vector machines. *GIScience & Remote Sensing*, 49(1), 117–138. <https://doi.org/10.2747/1548-1603.49.1.117>.
- Chen, C. F., Son, N. T., & Chang, L. Y. (2012b). Monitoring of rice cropping intensity in the upper Mekong Delta, Vietnam using time-series MODIS data. *Advances in Space Research*, 49(2), 292–301. <https://doi.org/10.1016/j.asr.2011.09.011>.
- Chuvieco, E., & Huete, A. (2010). *Fundamentals of satellite remote sensing*. Boca Raton: CRC Press.
- Congalton, R. G. (1991). A review of assessing the accuracy of classifications of remotely sensed data. *Remote Sensing of Environment*, 37(1), 35–46. [https://doi.org/10.1016/0034-4257\(91\)90048-B](https://doi.org/10.1016/0034-4257(91)90048-B).
- Didan, K., Munoz, A. B., Solano, R., & Huete, A. (2015). *MODIS vegetation index user's guide (MOD13 series), version 3*. Arizona: Vegetation Index and Phenology Lab, The University of Arizona.
- FAO. (2014a). *FAO statistical year book: Asia and the Pacific food and agriculture*. Bangkok: Food and Agriculture Organization of the United Nations, Regional Office for Asia and the Pacific.
- FAO. (2014b). *A regional strategy for sustainable hybrid rice development in Asia*. Bangkok: Food and Agriculture Organization of the United Nations, Regional Office for Asia and the Pacific.
- FAO. (2015). Global information and early warning system on food and agriculture. In *Crop Prospects and Food Situation: Global Information and Early Warning System on Food and Agriculture (GIEWS), Trade and Markets Division (EST), Food and Agriculture Organization of the United Nations*. FAO.
- Findley, D. F., B. C. Monsell, W. R. Bell, M. C. Otto, and B-C. Chen. 1998. "New capabilities and methods of the X-12-ARIMA seasonal-adjustment program." *Journal of Business & Economic Statistics* 16 (2):127–152. doi: <https://doi.org/10.1080/07350015.1998.10524743>.
- Friedl, M. A., & Brodley, C. E. (1997). Decision tree classification of land cover from remotely sensed data. *Remote Sensing of Environment*, 61(3), 399–409. [https://doi.org/10.1016/S0034-4257\(97\)00049-7](https://doi.org/10.1016/S0034-4257(97)00049-7).
- Gómez, V., & Maravall, A. (1996). Program TRAMO(\*) and SEATS(\*\*): Instructions for the user, (Beta version, September 1996). In *Banco de Espana - Servicio de Estudios*. Gomez and Maravall: Banco de Espana, Madrid.
- Gómez, V., & Maravall, A. (2001). Automatic modelling methods for univariate series. In Peña, D., Tiao, G. C., & Tsay R.S. (Eds.), *A course in time series analysis* (pp. 171–201). New York: Wiley.
- Huang, C., Davis, L. S., & Townshend, J. R. G. (2002). An assessment of support vector machines for land cover classification. *International Journal of Remote Sensing*, 23(4), 725–749. <https://doi.org/10.1080/01431160110040323>.

- International Rice Research Institute. (2013). How to develop a crop calendar. In *Learn about best practices in rice farming*. <http://www.knowledgebank.irri.org/step-by-step-production/pre-planting/crop-calendar>.
- Jia, G. J., Epstein, H. E., & Walker, D. A. (2002). Spatial characteristics of AVHRR-NDVI along latitudinal transects in northern Alaska. *Journal of Vegetation Science*, 13(3), 315–326. <https://doi.org/10.1111/j.1654-1103.2002.tb02056.x>.
- Jonsson, P., & Eklundh, L. (2002). Seasonality extraction by function fitting to time-series of satellite sensor data. *IEEE Transactions on Geoscience and Remote Sensing*, 40(8), 1824–1832. <https://doi.org/10.1109/Tgrs.2002.802519>.
- Kementerian Pertanian Republik Indonesia. (2015). Basis Data Statistik Pertanian. <http://aplikasi.pertanian.go.id/bdsp/newlok.asp>
- Loh, W. Y. (2011). Classification and regression trees. *Wiley Interdisciplinary Reviews-Data Mining and Knowledge Discovery*, 1(1), 14–23. <https://doi.org/10.1002/Widm.8>.
- Lu, H., Raupach, M. R., McVicar, T. R., & Barrett, D. J. (2003). Decomposition of vegetation cover into woody and herbaceous components using AVHRR NDVI time series. *Remote Sensing of Environment*, 86(1), 1–18. [https://doi.org/10.1016/S0034-4257\(03\)00054-3](https://doi.org/10.1016/S0034-4257(03)00054-3).
- Ozdarici-Ok, A., Ok, A. O., & Schindler, K. (2015). Mapping of agricultural crops from single high-resolution multispectral images-data-driven smoothing vs. parcel-based smoothing. *Remote Sensing*, 7(5), 5611–5638. <https://doi.org/10.3390/rs70505611>.
- Pal, M., & Mather, P. M. (2003). An assessment of the effectiveness of decision tree methods for land cover classification. *Remote Sensing of Environment*, 86(4), 554–565. [https://doi.org/10.1016/S0034-4257\(03\)00132-9](https://doi.org/10.1016/S0034-4257(03)00132-9).
- Panuju, D. R., & Trisasonoko, B. H. (2008). The use of statistical tree methods on rice field mapping. *Jurnal Ilmiah Geomatika*, 14(2), 75–84.
- Panuju, D. R., Trisasonoko, B. H., Susetyo, B., Raimadoya, M. A., & Lees, B. (2010). Historical fire detection of tropical forest from NDVI time series data: Case study on Jambi, Indonesia. *ITB Journal of Science*, 42(1), 47–64. <https://doi.org/10.5614/itbj.sci.2010.42.1.5>.
- Panuju, D. R., Mizuno, K., & Trisasonoko, B. H. (2013). The dynamics of rice production in Indonesia 1961–2009. *Journal of the Saudi Society of Agricultural Sciences*, 12(1), 27–37. <https://doi.org/10.1016/j.jssas.2012.05.002>.
- Pezzulli, S., Stephenson, D. B., & Hannachi, A. (2005). The variability of seasonality. *Journal of Climate*, 18(1), 71–88. <https://doi.org/10.1175/Jcli-3256.1>.
- Phuc, N. Q., van Westen, A. C. M., & Zoomers, A. (2014). Agricultural land for urban development: The process of land conversion in Central Vietnam. *Habitat International*, 41, 1–7. <https://doi.org/10.1016/j.habitatint.2013.06.004>.
- Shiskin, J., Young, A. H., & Musgrave, J. C. (1965). *The X-11 variant of the census method II seasonal adjustment program*: US Department of Commerce, Bureau of the Census.
- Tadono, T., Shimada, M., Watanabe, M., Rosenqvist, A., & Furuta, R. (2004). Overview of ALOS research and science program. In *Sensors, systems, and next-generation satellites VIII* (Vol. 5570, pp. 10–21). International Society for Optics and Photonics.
- Toan, T. L., Ribbes, F., Wang, L.-F., Floury, N., Ding, K.-H., Kong, J. A., Fujita, M., & Kurosu, T. (1997). Rice crop mapping and monitoring using ERS-1 data based on experiment and modeling results. *IEEE Transactions on Geoscience and Remote Sensing*, 35(1), 41–56. <https://doi.org/10.1109/36.551933>.
- Trisasonoko, B. H. (2019). Hybrid polarimetric synthetic aperture radar for the detection of waterlogged rice fields *Applications and Challenges of Geospatial Technology*, 241–255. Springer.
- Trisasonoko, B. H., Panuju, D. R., Tjahjono, B., Barus, B., Wijayanto, H., Raimadoya, M. A., & Irzaman. (2010). Simulasi Pemanfaatan Data LOSAT untuk Pemetaan Padi. *Makara Seri Teknologi*, 14(2), 116. <https://doi.org/10.7454/mst.v14i2.703>.
- Trisasonoko, B. H., Panuju, D. R., & Iman, L. S. (2012). Satellite monitoring of small-scale farming systems in Subang, Indonesia. *Journal of Mathematical and Fundamental Sciences*, 44(1), 67–78. <https://doi.org/10.5614/itbj.sci.2012.44.1.6>

- Verbesselt, J., Hyndman, R., Newnham, G., & Culvenor, D. (2010). Detecting trend and seasonal changes in satellite image time series. *Remote Sensing of Environment*, 114(1), 106–115. <https://doi.org/10.1016/j.rse.2009.08.014>.
- Vergara, B. S. (1992). *A farmer's primer on growing rice*. Manila: International Rice Research Institute.
- Wei, WWS. 2006. *Time Series Analysis: Univariate and Multivariate Methods*: Addison-Wesley publishing company, Inc.
- Wu, Z., Thenkabail, P. S., Mueller, R., Zakzeski, A., Melton, F., Johnson, L., Rosevelt, C., Dwyer, J., Jones, J., & Verdin, J. P. (2014). Seasonal cultivated and fallow cropland mapping using MODIS-based automated cropland classification algorithm. *Journal of Applied Remote Sensing*, 8(1). <https://doi.org/10.1117/1.JRS.8.083685>.
- Yang, C. C., Prasher, S. O., Enright, P., Madramootoo, C., Burgess, M., Goel, P. K., & Callum, I. (2003). Application of decision tree technology for image classification using remote sensing data. *Agricultural Systems*, 76(3), 1101–1117. [https://doi.org/10.1016/S0308-521X\(02\)00051-3](https://doi.org/10.1016/S0308-521X(02)00051-3).
- Zhao, J., Zhang, D., Wang, D., & Huang, W. (2011). *Integrating Landsat TM Imagery and See5 Decision-tree Software for Identifying Croplands: A Case Study in Shunyi District, Beijing*. Paper presented at the WISM 2011, Part I, LNCS 6987.
- Zhao, M., Peng, C., Xiang, W., Deng, X., Tian, D., Zhou, X., Yu, G., He, H., & Zhao, Z. (2013). Plant phenological modeling and its application in global climate change research: Overview and future challenges. *Environmental Reviews*, 21(1), 1–14. <https://doi.org/10.1139/er-2012-0036>.

# Habitat Suitability Mapping of Sloth Bear (*Melursus ursinus*) in the Sariska Tiger Reserve (India) Using a GIS-Based Fuzzy Analytical Hierarchy Process



Purva Jain, Raihan Ahmed, Haroon Sajjad, Meheboob Sahana, Abolfazl Jaafari, Jie Dou, and Haoyuan Hong

**Abstract** This chapter presents a habitat suitability mapping of sloth bear using fuzzy analytical hierarchy process that relies on geographical information system (GIS)–automated techniques. We selected nine parameters for assessing sloth bear habitat suitability: food availability, distance to waterholes, canopy density, slope, elevation, grazing, human disturbance, and distance to villages and roads. All the weighted parameter layers were integrated to obtain suitability classes. Of the total area of the Reserve, 44% area was found under moderate suitability class and 34% area under high suitability class. Within three core areas of the Reserve, the concentration of high suitability was observed in Core-I area. The habitat suitability classes were validated by analyzing their relationship with the zonal statistics of beat-wise habitat-use intensity data of sloth bear in the Reserve. This analysis revealed that the beat-wise habitat-use intensity coincides with suitability zones. Our study may prove to be beneficial for managing and formulating guidelines for the self-sustenance of the reintroduced bears in the Reserve. The model adopted in this study can also be applied for assessing habitat suitability of other bear species in different geographical regions at various scales.

---

P. Jain  
Sehgal Foundation, Gurugram, Haryana, India

R. Ahmed · H. Sajjad (✉) · M. Sahana  
Department of Geography, Faculty of Natural Science, Jamia Millia Islamia, New Delhi, Delhi, India

A. Jaafari  
Tarbiat Modares University, Tehran, Iran

J. Dou  
Public Works Research Institute (PWRI), Tsukuba, Japan

H. Hong  
Cartography and Geographical Information System, School of Geographic Science, Nanjing, China

**Keywords** Sloth bear · Habitat suitability factors · Reintroduction · Geospatial techniques · Habitat use intensity · Sariska Tiger Reserve

## 1 Introduction

The sloth bear (*Melursus ursinus*) is endemic and patchily distributed in the Indian subcontinent (Erdbrink 1953; Sathyakumar et al. 2012). Over the past years, sloth bear has experienced unparalleled threat primarily due to poaching and habitat loss (Akhtar et al. 2004; Yoganand et al. 2006). The root cause of the problem is primarily related to deteriorating and shrinking habitat that lead to the increase in human and bear conflicts (Akhtar et al. 2004; Bargali et al. 2005; Garshelis et al. 1999; Johnsingh 2003). The species is vulnerable to extinction (IUCN 2013) and has led to its inclusion in Schedule I of the Indian Wildlife (Protection) Act as amended in 2003 (GOI 1972; GOR 2014). Moreover, the International Union for Conservation of Nature (IUCN) has listed sloth bears as “vulnerable,” considering the rapid loss in their natural habitat (Garshelis et al. 2008).

The conservation of sloth bear is challenging, since it requires large areas to meet their requirement, making it necessary to have landscape-level management (Sinha et al. 2017). The primary issue for the successful application of conservation plans is to properly identify and delineate the priority habitats for the conservation and reintroduction programs (Clevenger et al. 2002; Felix et al. 2004; Gerrard et al. 2001; Kaminski et al. 2013). Different methodologies such as radio telemetry (Joshi et al. 1995, 1999a, b; Ratnayake et al. 2007a, b) or bear sign (Akhtar et al. 2004; Chauhan et al. 2003) have been adopted to study sloth bear–habitat interactions. However, the absence of the target species makes it challenging for wildlife manager to identify priority habitats required for reintroduction and future monitoring purpose (Didier and Porter 1999;; Mackenzie 2005; Hirzel et al. 2006; Lobo et al. 2010).

Reintroduction process is defined as the deliberate release of some species into an area with the aim of reestablishing a viable and self-sustained population of that species in the long term (Stanley Price 1991). It is crucial to restore the species which are vulnerable to loss or reduction to a nonviable level locally (Stuart 1991). However, before initiating any reintroduction program, it is crucial to understand the role of different geo-environmental factors that are supposed to directly and/or indirectly exert effect on a reintroduction program. Various studies have suggested the limitations and procedures to enhance the reintroduction programs of bears (e.g., May 1991; Smith et al. 1991; van Manen and Pelton 1997; Clark et al. 2002; De Barba et al. 2010; Converse et al. 2013; Reading et al. 2013). Cost and time in reintroduction programs are the major hindrances that, in many cases, dramatically decreased the success rate of the conservation measures (Earnhardt 1999; Helmstedt and Possingham 2017). Hence, scientific principles and methodologies are required to adopt successful and timely reintroduction programs (Pullin 2002).

Since the 1980s, habitat suitability index (HSI) models have emerged and proven to be very effective for identifying and protecting critical habitats of the threatened species (Lauria et al. 2015), assessing ecological impacts on wildlife populations and

facilitating management plans (Brooks & Temple 1990; Kaminski and Comer 2011). Further, the HSI models have frequently been suggested and used to predict and estimate the sloth bear habitat suitability (e.g., Kaminski and Comer 2011; Nawaz et al. 2014). The prediction of habitat suitability of species depends on an adequate knowledge and information of their different habitat characteristics, such as food habits, shelter, mating behavior, and so on (Bargali et al. 2012; Porwal et al. 1996). Previous studies (e.g., Akhtar et al. 2004; Clevenger et al. 2002; Joshi et al. 1995; Clevenger et al. 2006; Mitchell et al. 2002; Smith 1985) have found food availability as a crucial factor in distribution of the bear populations. Sloth bear is the only species of bear adapted as myrmecophagy, whose diets are largely or exclusively composed of termites or ants (Sacco and Van Valkenburgh 2004). In India, sloth bears mostly supplement their diets with fruit and plant matter (e.g., Chauhan et al. 2003; Akhtar et al. 2004). The historical records of elevation and slope preferences are confusing. While, in Western Ghats of India, sloth bear is observed up to 2000 m elevation (Dharaiya et al. 2016), some studies in Sri Lanka (e.g., Phillips 1984; Ratnayeke et al. 2007a, b; Santiapillai and Santiapillai 1990; Bargali et al. 2004), India (Johnsingh 2003), and Nepal (Garshelis et al. 1999) have found out sloth bear as a lowland species, occurring in habitat below 1000 m. However, Ratnayeke et al. (2007b) has found out 98% of the range was below 300 m in Sri Lanka. Sloth bears also prefer the areas covered by forests (Puri et al. 2015), presumably because these areas are more productive in fruit and provides more shelter. However, In the Wasgamuwa National Park of Sri Lanka, bears have rarely been observed at lowland sparse forest, as these areas are more prone to human activities (Ratnayeke et al. 2007a, b). The agricultural activities in the reserve can result in crop damage by bear that, in turn, increase the probability of human–bear conflict (Bargali et al. 2004; Karamanlidis et al. 2011; Rigg et al. 2011; Can et al. 2014).

The presence of substantial literature regarding sloth bear habitat preferences across the globe and the historical presence of sloth bear and suitable habitat in the Sariska Tiger Reserve (STR) provides a case where priority areas can be identified in the absence of a target species with the help of GIS tools and the use of site-specific habitat data. Therefore, we have attempted to identify suitable habitat for the reintroduction of bear through an understanding of requirement of the species with respect to feeding, shelter, and other requisites for their better management and conservation.

## 2 Study Area

This study was conducted in the Sariska Tiger Reserve located in the Alwar district of Rajasthan state in India. The area extends from 27°05' N to 27° 33'N latitudes and 76°17' E to 76° 34'E longitudes. The study area lies in the Aravalli, the oldest mountain range of India, and its elevation ranges from 540 to 777 m. The area is characterized by dry deciduous and tropical thorn forests (Champion and Seth 1968). The Reserve covers approximately 1200 km<sup>2</sup>. Out of the Reserve area, 881.11 km<sup>2</sup> is



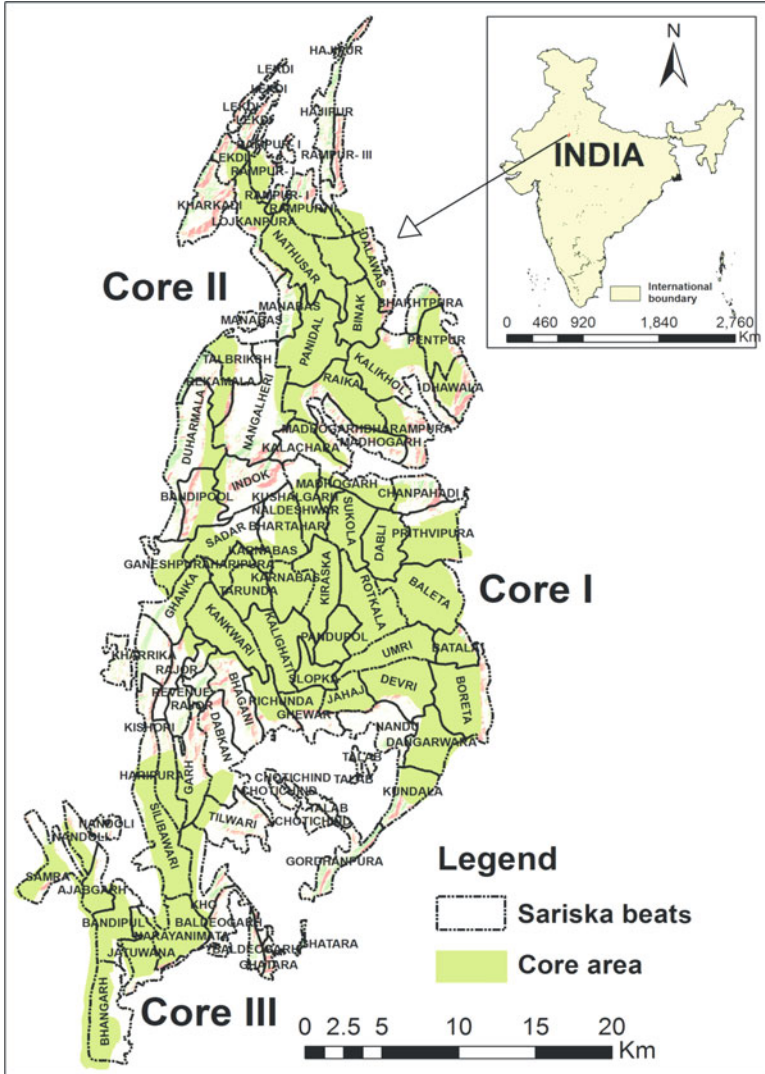


**Fig. 1** Location of the Sariska Tiger Reserve in Rajasthan state, India. The Reserve is divided into 84 beats and three core areas named as core I, core II, and core III

under Critical Tiger Habitat (CTH) area and the remaining is buffer zone. The CTH is further divided into core I (273.8 km<sup>2</sup>), II (126 km<sup>2</sup>), and III (97.5 km<sup>2</sup>) (GOR 2014). Sariska Tiger Reserve has six ranges: Sariska, Akbarpur, Talvriksh, Tehla, Alwar buffer, and Ajabgarh range. These ranges are further divided into 84 beats: Talvriksh range (13 beats), Akbarpur range(17 beats), Sariska range (19 beats), Tehla range (20 beats), Alwar Buffer (15 beats), and Ajabgarh (13 beats) (See Fig. 1).

Although there is still a place called “Rich-unda” that means “Bear is there,” sloth bears disappeared from the Reserve in early twentieth century. Although the reason for the disappearance of sloth bear from the Reserve is not clearly known, poaching and bear–human conflict are considered as the main possible reasons (GOR 2014). The area has high abundance of various fruit trees and shrubs such as *Ziziphus*, *Ficus*, *Phoenix*, *Diospyros*, *Anogeissus*, *Boswellia*, and *Butea*, and large numbers of termite mounds that can very well sustain a large population of sloth bear in the Reserve. However, the Reserve is currently highly burdened with anthropogenic activities due to many villages and hamlets (Jain and Sajjad 2016a; Jain and Sajjad 2016b). Further, the state highways (SH-13 AND 29A) which pass through the sanctuary (GOR 2014) have resulted in a serious habitat fragmentation in the Reserve (Jain et al. 2016). The Reserve also consists of several pilgrimage sites, where attract millions of devotees over the year.

The sloth bear was rescued and relocated in the Core I of the Reserve in the year 2013 and since then the male sloth bear has survived on wild food resources without being involved in any conflict. However, during field visit it was found that the current status of sloth bear is unknown, and the authorities have proposed a reintroduction program of sloth bear according to the National Tiger Conservation Authority (NTCA).

### 3 Methodology

Since recently, only one bear has been reported in the Reserve. This bear has been rescued from the nearby area and relocated in the Core I of the Reserve, therefore, we have attempted to find conducive habitat for this sloth bear and other bears which are reintroduced in the near future. For this purpose, an integrated geospatial approach that rely on analytical hierarchical process (AHP), fuzzy logic, and GIS-automated techniques was proposed. In the first step of the study, the most effective parameters on the assessment of habitat suitability of sloth bear were identified following a preliminary analysis that used available data, potential relationships between characteristics of the Reserve and sloth bears, and suggestions given in the literature (e.g., Akhtar et al. 2004; Kaminski et al. 2013; Nawaz et al. 2014; Bargali et al. 2012; Mitchell et al. 2002; Ratnayeke et al. 2007a, b; Akhtar et al. 2007; Das et al. 2014; Larson 2003; Palei et al. 2014; Sinha et al. 2017). The map layer related to each factor were collected from the forest department of the Sariska and satellite data. These data were further informed in the second step of study using several field surveys and screening processes. The third and final step included post-field surveys, database creation, and geospatial modeling. The methodology adopted in this study is shown in Fig. 2 and explicitly described as follows:

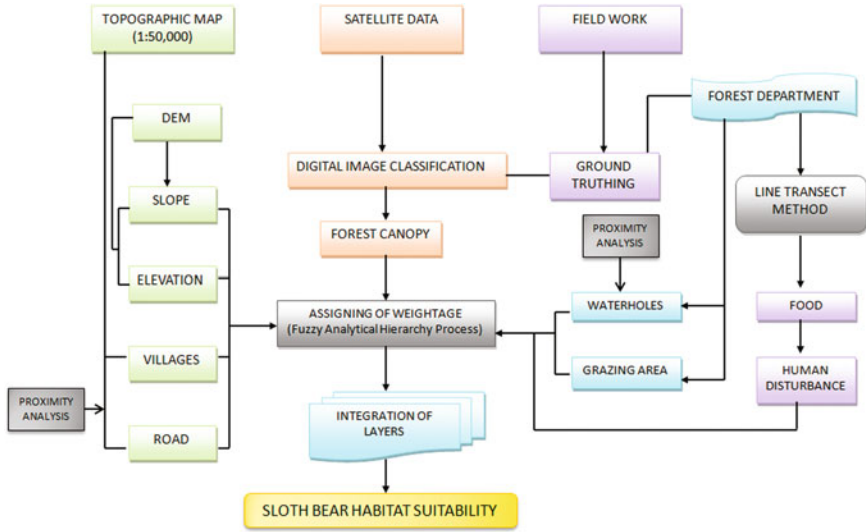


Fig. 2 Flowchart of the methodology adopted for habitat suitability analysis of sloth bear

### 3.1 Data Processing

Landsat TM (Thematic Mapper) image of September 28, 2014, was used for the evaluation of habitat suitability in the study area. Image were geometrically registered to 1:50,000 scale survey topographic maps of the study area. It was followed by atmospheric correction and radiometric calibration. Due to the mountainous nature of the study area, topographic normalization was performed to correct the solar illumination differences. The layer maps of slope and elevation were extracted from a shuttle radar topographic machine digital elevation model (SRTM DEM) with 30 m resolution using the Arc Map software.

### 3.2 Fieldwork

Topographical sheets, survey of India of 1:50,000 scale were used for identifying geographical locations of villages, pilgrimage sites, and roads in STR. Extensive investigations by the forest department of the Sariska on the Reserve have been the major source of data associated with number of trees cut, branches lopped, grasses and bamboo cut, livestock sighted, and density of tree species and shrubs used in the present study. The distance sampling technique (Buckland et al. 2001) was used to calculate plants density in the study area. According to the Phase IV Report (2015), 194 linear transects of 1.6 km to 5 km each were placed within the study area of 1200 km<sup>2</sup> in such a way that every beat is covered by two transects lines. These

transects were walked two times in the early morning hours, in April and May 2015. A global positioning system (GPS) was used to define the coordinates (i.e., latitude and longitude) of the beginning and ending points of each transect (Phase IV Report 2016). Field survey for ground truthing and validation of the presence of shrubs and fruit trees was carried out during September 2016.

### 3.3 Post Fieldwork

The ultimate database was created using the remote sensing and GIS-automated techniques. Following the work of Rikimaru (1996), forest canopy density maps were prepared and categorized. The locations of water holes of the study area were acquired from the Sariska management report and topographical sheets (GOR 2014). The area faces water scarcity issue despite receiving a good amount of rain primarily due to the geological structure and the absence of inflow in the area. Few natural water holes existed in the study area. Majority of the water points have been artificially constructed (GOR 2014).

The distance of 1.6 km and 0.8 km was taken from the roads and villages present in the Reserve assuming bears avoid area within it (Clevenger et al. 2006). There are contrasting views regarding the impact of roads on habitat quality of bear. While some studies reported the negative effects of road networks on habitat suitability (Ratnayeke et al. 2007a, b; van Manen 1991), other studies showed positive effect of road networks (Carr and Pelton 1984; Fecske et al. 2002; Reynolds-Hogland and Mitchell 2007). In this study, we followed van Manen (1991), assuming that roads exert a negative influence on habitat suitability due to continuous traffic flow, accidents, and increased chances of legal and illegal killing.

Food availability, human disturbance, and grazing layers were prepared from the beat-wise data provided by the forest department using the line transect method (Phase IV Report 2015). The food availability layer indicates the density of fruit trees and shrubs available in the respective beat. Those shrubs (*Ziziphus nummularia*), herbs (*Cassia fistula*), and fruit trees (*Phoenix*, *Ziziphus*, *Ficus*, *Diospyros*, *Aegle*) that are palatable for sloth bear were included in this study. Grazing layer was prepared based on the number of cattle sighted. Similarly, human disturbance layer was prepared using the beat-wise data on grasses, bamboo, and tree cutting and lopping. In the Reserve, the areas located in higher altitudes and flat surfaces are more susceptible to human disturbances (Jain et al. 2016). Therefore, we considered elevation and slope as other influencing factors for the assessment of habitat suitability. The factors considered for the assessment of habitat suitability were food availability, water, elevation, slope, canopy density, distance to villages and road, grazing activity, and human disturbance (see Fig. 3). Based on the weighting the importance of these factors using the Fuzzy Analytical Hierarchy Process (FAHP), assessment of habitat suitability was performed (see Fig. 2). The beat-wise data on sloth bear availability during the years 2015–2016 was collected from the Sariska forest department.

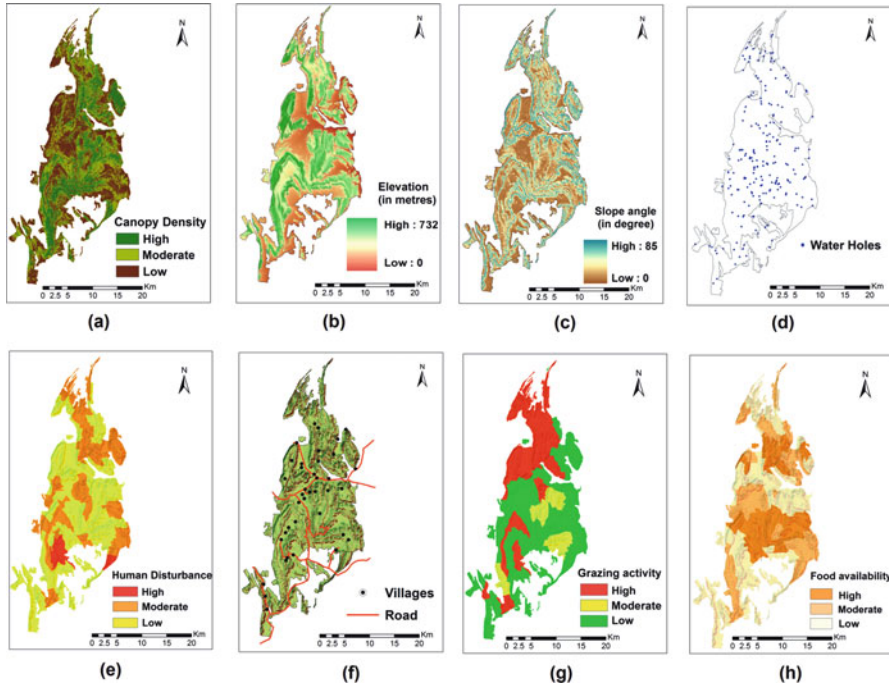


**Fig. 3** GIS maps representing (a) canopy density map, (b) elevation (in meters), (c) slope angle (in degree), (d) waterholes, (e) human disturbance, (f) villages and road, (g) grazing activity, and (h) food availability in the STR

### 3.4 Identifying Sloth Bear Habitat Suitability Using Fuzzy Analytical Hierarchy Process (FAHP)

An integrated approach of GIS-automated techniques, fuzzy logic, AHP, and statistical algorithm was adopted to weight the effective factors in habitat suitability and its potential mapping. The FAHP has an advantage over analytical hierarchy process for handling vagueness, uncertainty, fuzziness associated with decision-making process, and mapping (Ahmed et al. 2017; Deng 1999; Jamil et al. 2017). The priority vector through FAHP was obtained through triangular fuzzy comparison matrix for sloth bear habitat suitability.

For applying FAHP, “E” value was obtained based on hierarchy using following notation:

$$E_{gi}^1, E_{gi}^2, E_{gi}^3, E_{gi}^4, E_{gi}^n$$

where for each criteria the goal set of  $gi$  is ( $i = 1, 2, 3, 4, \dots, n$ ).

All value of  $E_{gi}^j$  are triangular fuzzy number ( $j = 1, 2, 3, 4, \dots, m$ ).

The stepwise description of FAHP given by Chang (1996) is as follows:  
 For *i*th criteria the synthetic extent value of Fuzzy ( $S_1$ ) is expressed as:

$$S_1 = \sum_{j=1}^m E_{gi}^j \otimes \left[ \sum_{i=1}^n \sum_{j=1}^m E_{gi}^j \right]^{-1} \tag{1}$$

Computation of this involves

$$\sum_{j=1}^m E_{gi}^j \tag{2}$$

Addition operation of fuzzy for *E* extent value of a particular matrix is expressed in Eq. (3), and finally a new set is obtained for further use, that is (*x, y, z*).

$$\sum_{j=1}^m E_{gi}^j = \left( \sum_{j=1}^m x_j, \sum_{j=1}^m y_j, \sum_{j=1}^m z_j \right) \tag{3}$$

where

- x* = lower limit value
- y* = middle limit value
- z* = upper limit value

From *x, y, and z* set we have Eq. (4):

$$\left[ \sum_{i=1}^n \sum_{j=1}^m E_{gi}^j \right]^{-1} \tag{4}$$

Addition operation of fuzzy for  $E_{gi}^j$  (*j* = 1, 2, 3, 4, ..... *m*) values, inverse vector is computed through Eq. (5).

$$\sum_{i=1}^n \sum_{j=1}^m E_{gi}^j = \left( \sum_{j=1}^m x_j, \sum_{j=1}^m y_j, \sum_{j=1}^m z_j \right) \tag{5}$$

By inverting vector, we have:

$$\left[ \sum_{i=1}^n \sum_{j=1}^m E_{gi}^j \right]^{-1} = \left[ 1/\sum_{i=1}^n x_i, 1/\sum_{i=1}^n y_i, 1/\sum_{i=1}^n z_i \right] \tag{6}$$

Degree of possibility for  $E_1 \geq E_2$  is calculated as

$$V(E_1 \geq E_2) = \sup_{x \geq y} [\min(\mu_{E_1}(p), \mu_{E_2}(q))] \tag{7}$$

where  $p$  and  $q$  are the membership function values of each criterion and  $V(E_1 \geq E_2) = 1$ . Since  $E_1$  and  $E_2$  are convex fuzzy numbers, we have:

$$V(E_1 \geq E_2) = 1 \text{ iff } y_1 \geq y_2$$

$$V(E_2 \geq E_1) = \text{hgt}(E_1 \cap E_2) = \mu_{y_1}(d) \tag{8}$$

where point of highest intersection ( $d$ ) is between  $(\mu_{E_1})$  and  $(\mu_{E_2})$ .

when

$$E_1 = (x_1, y_1, z_1) \text{ and } E_2 = (x_2, y_2, z_2).$$

The ordination of  $d$  is expressed as below:

$$V(E_2 \geq E_1) = \text{hgt}(E_1 \cap E_2) = \frac{x_1 - r_2}{(y_2 - z_2) - (y_1 - x_1)} \tag{9}$$

Convex fuzzy number and its degree of possibility to be greater than  $k$  convex fuzzy number  $E_i$  ( $i = 1, 2, 3, 4, \dots, k$ ) can be expressed as:

$$\begin{aligned} V(E \geq E_1, E_2, \dots, E_k) &= V[(E \geq E_1) \text{ and } (E \geq E_2) \text{ and } \dots \text{ and } (E \geq E_k)] \\ &= \min V(E \geq E_i), i = 1, 2, 3, \dots, k \end{aligned} \tag{10}$$

The Eq. (10) is supported by the following:

$$d(C_1) = \min V(S_i \geq S_k)$$

where  $k = 1, 2, 3, \dots, n; k \neq i$ .

The weight vectors are expressed through the Eq. (11)

$$W_1 = [d(C_1), d(C_2), d(C_3), \dots, d(C_n)]^T \tag{11}$$

where  $C_i$  ( $i = 1, 2, 3, \dots, n$ )

Process of normalization for weight vectors are performed using following equation:

$$W = [d(C_1), d(C_2), d(C_3), \dots, d(C_n)]^T \tag{12}$$

where  $W$  represents non fuzzy number.

### 3.5 *Habitat Suitable Classes (HSC)*

To determine the HSC of the study area, weighted factors were integrated using weighted linear combination in a GIS environment as follows:

$$\begin{aligned} \text{HSC} = & [(CD_w CD_{nr}) + (R_w R_{nr}) + (El_w El_{nr}) + (FA_w FA_{nr}) + (SI_w SI_{nr}) \\ & + (GA_w GA_{nr}) + (WH_w WH_{nr}) + (V_w V_{nr}) + (HD_w HD_{nr})] \end{aligned} \quad (13)$$

where CD is canopy density, R is road, El is elevation, FA is food availability, GA is grazing activity, WH is water holes, V is villages, and HD is human disturbance. Subscripts of w and nr represent weights and normalized value of all the factors influencing habitat suitability.

### 3.6 *Validation*

It is difficult to validate the results of a habitat suitability prediction in the absence of target species. In this study, the known we have attempted to validate the HSC by analyzing its relationship with the beat-wise habitat use intensity data (2015–2016) of the only sloth bear present in the STR. Zonal statistics of sloth bear habitat suitability and beat-wise habitat use intensity of sloth bear in STR were calculated to characterize the influencing factors for habitat suitability analysis.

## 4 *Result and Discussion*

The habitat suitability of sloth bear provides insight of priority areas for conservation and effective decision making for reintroducing sloth bear into the study area. To overcome the uncertainty in assigning the priority to the habitat suitability parameters, triangular fuzzy numbers (TFN) were assigned on the basis of literature review (Akhtar et al. 2004; Kaminski et al. 2013; Nawaz et al. 2014; Bargali et al. 2012; Mitchell et al. 2002; Ratnayeke et al. 2007a, b; Akhtar et al. 2007; Das et al. 2014; Larson 2003; Palei et al. 2014) and field research on habitat suitability of sloth bear in our study area. The selected factors were assigned four triangular fuzzy numbers to assign weights, that is, very strong importance (VSI –2, 5/2, 3), strong importance (SI –3/2, 2, 5/2), weak importance (WI –1, 3/2, 2), and equal (E –1, 1, 1). Factors like distance to villages, road, grazing activity, and human disturbance have inverse relationship with sloth bear habitat suitability (Garshelis et al. 1999; Clevenger et al. 2006; Yoganand et al. 2006; Kaminski et al. 2013; Bargali et al. 2012). Many studies have focused on the effect of human activities on bears. The negative effects of human activity on sloth bears in India has been reported by Garshelis et al. (1999) and Yoganand et al. (2006). In the Terai region some large patches of



remnant forests seemingly sufficient to sustain sloth bears have no evidence of bears since they are severely degraded from grazing, cutting, lopping, and other human activities (Garshelis et al. 1999). Likewise a study on the threats on sloth bear in India by Yoganand et al. (2006) reported habitat loss or degradation, overgrazing, over-extraction of minor forest produce and related human disturbances, fire damage, and conflict with humans, as the major threats to the sloth bear are from poaching and its habitat. In Wasgomuwa National Park, Sri Lanka, the major threats to sloth bears are poaching and human activity. Raiding of agricultural fields leads to higher human–bear conflicts and eventually killing of bear by villagers in rage (Ratnayeke et al. 2006). The studies done on black and brown bears have also similar findings (Clevenger et al. 2006; Elgmork 1978 Reynolds-Hogland and Mitchell 2007). A temporal study of 40 years' period conducted in Norway found out a negative correlation between the rate of cabin and road construction and the growth rate of the local bear population (Elgmork 1978). Human–bear conflicts had a negative impact on conservation of bears to an extreme extent and therefore it is necessary for the bear to stay away from human habitation (Can et al. 2014). Hence, these parameters were inversed in habitat suitability matrix table. Based on the alternative weights obtained through normalizing the values of suitability parameters, habitat suitability areas were prioritized (Table 1) and criterion weights were obtained through FAHP (Table 2). Each habitat suitability parameter was multiplied with criterion weight on the basis of their habitat suitability for sloth bear (See Eq. 13).

Food availability, waterholes presence, and distance to village parameters were found to be the most significant determining factors for sloth bear habitat suitability (Table 2). Nearly 44% area was under moderate suitability class, which is followed by high suitability (34%), and low suitability (22%) (see Table 3, Fig. 4). High food availability, proximity to waterholes, and less human interference were the prospective factors for the ideal habitat. Areas with low availability of food and water as well as presence of villages and roads are less suitable locations for the sloth bear habitat. The slope does not have significant influence on sloth bear habitat suitability. Higher elevation areas (up to 500 m) were found to be most suitable habitat. The higher elevations of STR are less prone to human disturbances (Jain et al. 2016). The bear prefers high canopy density areas for resting place. This finding is in agreement with Akhtar et al. (2007), who observed dense vegetation beyond 10 m radius around the sloth bear den. However, the STR has dry deciduous forest and thus only 22% of the total area of the Reserve comprised of high canopy density (Fig3a). Within the three core areas of STR, core I area has the largest area (47%) under high suitable habitat followed by medium habitat (37%) and low suitable habitat (16%). Cores II and III was found to have moderate habitat suitability for sloth bear where 47% and 46% of their respective areas were under moderate suitability class. Only 47% area of Core I and 26% of Core III was found highly suitable for sloth bear habitat. Low suitability was observed in those areas that were located in the vicinity of the villages and roads of the Reserve.

Sloth bear habitat suitability was validated with the beat-wise habitat-use intensity data of sloth in the STR (see Fig. 5). The high beat habitat-use intensity was observed in areas of high suitability (77%) followed by moderate suitability (17%)

**Table 1** Normalized rank of parameters of sloth bear habitat suitability

| Factor                 | Class     | Assigned rank | Normalized rank |
|------------------------|-----------|---------------|-----------------|
| Villages (V)           | 800 m     | 1             | 0.11            |
|                        | 1600 m    | 3             | 0.33            |
|                        | >1600 m   | 5             | 0.56            |
| Road (R)               | 800 m     | 1             | 0.11            |
|                        | 1600 m    | 3             | 0.33            |
|                        | >1600 m   | 5             | 0.56            |
| Grazing (GA)           | High      | 2             | 0.22            |
|                        | Moderate  | 3             | 0.33            |
|                        | Low       | 4             | 0.44            |
| Food availability (FA) | High      | 5             | 0.42            |
|                        | Moderate  | 4             | 0.33            |
|                        | Low       | 3             | 0.25            |
| Canopy density (CD)    | 0–27%     | 2             | 0.22            |
|                        | 28–38%    | 3             | 0.33            |
|                        | 39–100%   | 4             | 0.44            |
| Slope (SI)             | 0°–11°    | 3             | 0.27            |
|                        | 11°–24°   | 4             | 0.36            |
|                        | 24°–86°   | 4             | 0.36            |
| Elevation (E)          | 0–400 m   | 3             | 0.21            |
|                        | 400–500 m | 4             | 0.29            |
|                        | 500–600 m | 4             | 0.29            |
|                        | 600–750 m | 3             | 0.21            |
| Water holes (WH)       | 800 m     | 5             | 0.42            |
|                        | 1600 m    | 4             | 0.33            |
|                        | >1600 m   | 3             | 0.25            |
| Human disturbance (HD) | High      | 2             | 0.20            |
|                        | Moderate  | 3             | 0.30            |
|                        | Low       | 4             | 0.40            |

and low suitability (7%). The high beat habitat-use intensity was characterized by high food availability, nearness to waterholes, high canopy density, and less human interference (see Table 4). The abiotic parameters (slope and elevation) did not figure in generating influence on sloth bear beat habitat-use intensity. The studies conducted by Larson (2003) and Akhtar et al. (2004) have shown the similar results. Moderate beat habitat-use intensity was found in areas of moderate habitat suitability (47%) followed by high suitability (30%) and low suitability (23%). The medium and low beat habitat-use intensity was found in areas with moderate habitat suitability. From this analysis it can be inferred that the sloth bear preferred to occupy mostly the high suitability area in the Reserve. Beats with medium habitat-use intensity covered human disturbance area (55%) followed by area in proximity to human settlements (33%), whereas beats with low habitat-use intensity has only 25% of area with human disturbance and 26% area lies in the proximity to the

**Table 2** Pair-wise matrix for habitat suitability on the basis of suitability parameters

|                   | Canopy density | Road         | Elevation      | Food availability | Slope          | Grazing activity | Water holes  | Villages       | Human disturbance | Wc*  |
|-------------------|----------------|--------------|----------------|-------------------|----------------|------------------|--------------|----------------|-------------------|------|
| Canopy density    | 1, 1, 1        | 2, 2.5, 3    | 0.4, 0.5, 0.67 | 0.5, 0.67, 1      | 2, 2.5, 3      | 0.33, 0.4, 0.5   | 1, 1.5, 2    | 0.33, 0.4, 0.5 | 1, 1.5, 2         | 0.11 |
| Road              | 0.33, 0.4, 0.5 | 1, 1, 1      | 0.5, 0.67, 1   | 0.33, 0.4, 0.5    | 0.4, 0.5, 0.67 | 1, 1.5, 2        | 1, 1, 1      | 0.33, 0.4, 0.5 | 0.33, 0.4, 0.5    | 0.11 |
| Elevation         | 1.5, 2, 2.5    | 1, 1.5, 2    | 1, 1, 1        | 0.4, 0.5, 0.67    | 0.33, 0.4, 0.5 | 0.5, 0.67, 1     | 1, 1.5, 2    | 0.33, 0.4, 0.5 | 1, 1, 1           | 0.08 |
| Food availability | 1, 1.5, 2      | 2, 2.5, 3    | 1.5, 2, 2.5    | 1, 1, 1           | 1.5, 2, 2.5    | 0.4, 0.5, 0.67   | 1.5, 2, 2.5  | 1, 1.5, 2      | 2, 2.5, 3         | 0.17 |
| Slope             | 0.33, 0.4, 0.5 | 1.5, 2, 2.5  | 2, 2.5, 3      | 0.4, 0.5, 0.67    | 1, 1, 1        | 0.5, 0.67, 1     | 1, 1.5, 2    | 0.5, 0.67, 1   | 1.5, 2, 2.5       | 0.08 |
| Grazing activity  | 2, 2.5, 3      | 0.5, 0.67, 1 | 1, 1.5, 2      | 1.5, 2, 2.5       | 1, 1.5, 2      | 1, 1, 1          | 0.5, 0.67, 1 | 1.5, 2, 2.5    | 1.5, 2, 2.5       | 0.08 |
| Water holes       | 0.5, 0.67, 1   | 1, 1, 1      | 0.5, 0.67, 1   | 0.4, 0.5, 0.67    | 0.5, 0.67, 1   | 1, 1.5, 2        | 1, 1, 1      | 1, 1.5, 2      | 0.5, 0.67, 1      | 0.14 |
| Villages          | 2, 2.5, 3      | 2, 2.5, 3    | 2, 2.5, 3      | 0.5, 0.67, 1      | 1, 1.5, 2      | 0.4, 0.5, 0.67   | 0.5, 0.67, 1 | 1, 1, 1        | 0.5, 0.67, 1      | 0.12 |
| Human disturbance | 0.5, 0.67, 1   | 2, 2.5, 3    | 1, 1, 1        | 0.33, 0.4, 0.5    | 0.4, 0.5, 0.67 | 0.4, 0.5, 0.67   | 1, 1.5, 2    | 1, 1.5, 2      | 1, 1, 1           | 0.11 |

\*Weighted criteria

**Table 3** Habitat suitability of sloth bear and characteristics of influencing factors

| Habitat suitability                  | Food availability (in %) |        |     | Waterholes' buffer (in %) | Canopy density (In %) | Slope (in degree) | Elevation (in meters) | Grazing area (in %) |        |     | Human disturbance (in %) |        |     | Villages (in %) | Roads (in %) |
|--------------------------------------|--------------------------|--------|-----|---------------------------|-----------------------|-------------------|-----------------------|---------------------|--------|-----|--------------------------|--------|-----|-----------------|--------------|
|                                      | High                     | Medium | Low |                           |                       |                   |                       | High                | Medium | Low | High                     | Medium | Low |                 |              |
| High area (279.28km <sup>2</sup> )   | 53                       | 26     | 21  | 67                        | 37                    | 14                | 515                   | 24                  | 13     | 63  | 0.5                      | 26     | 74  | 0.02            | 0.02         |
| Medium area = (363 km <sup>2</sup> ) | 16                       | 33     | 51  | 45                        | 31                    | 14                | 490                   | 37                  | 10     | 53  | 4                        | 44     | 52  | 19              | 29           |
| Low area = (183.53 km <sup>2</sup> ) | 5                        | 29     | 65  | 43                        | 26                    | 10                | 450                   | 39                  | 9      | 52  | 10                       | 35     | 55  | 78              | 67           |

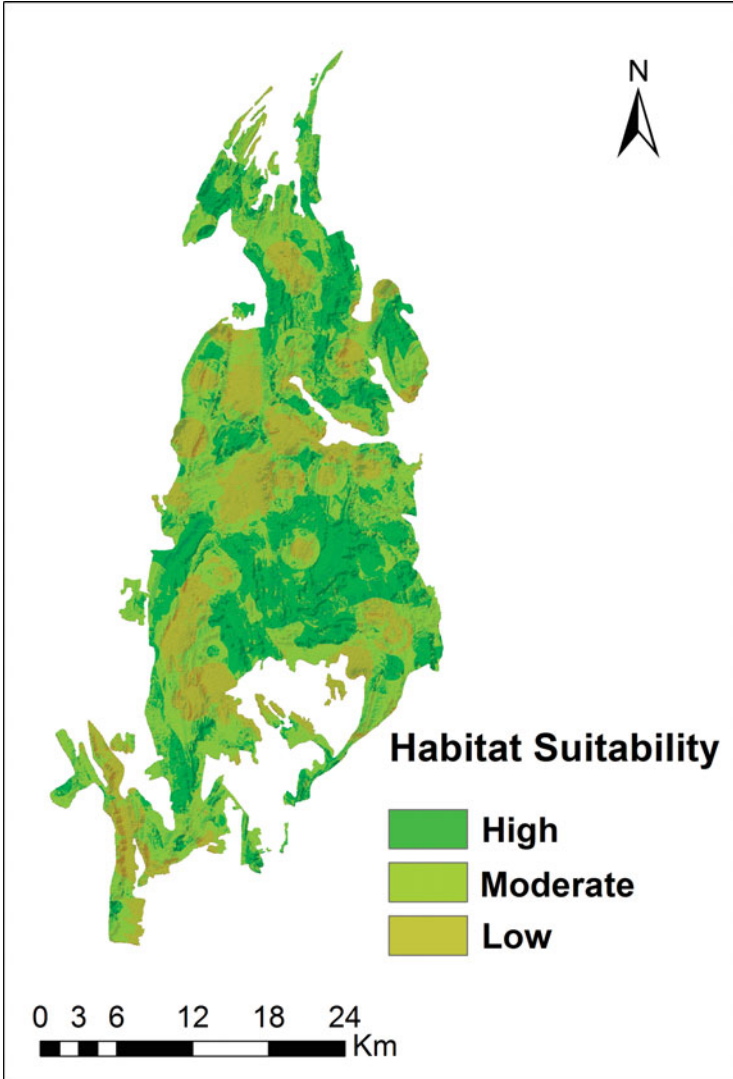


**Fig. 4** Habitat suitability map for sloth bear in Sariska Tiger Reserve, India

villages. This shows that beats with medium habitat use intensity exposed to higher human interference than the beats with low habitat-use intensity. Food availability in these areas could be the factor for medium beat habitat-use intensity in human disturbance areas. Resource availability could be a decisive variable for analyzing habitat quality for bears. The study by Larson (2003) also is in conformity with our

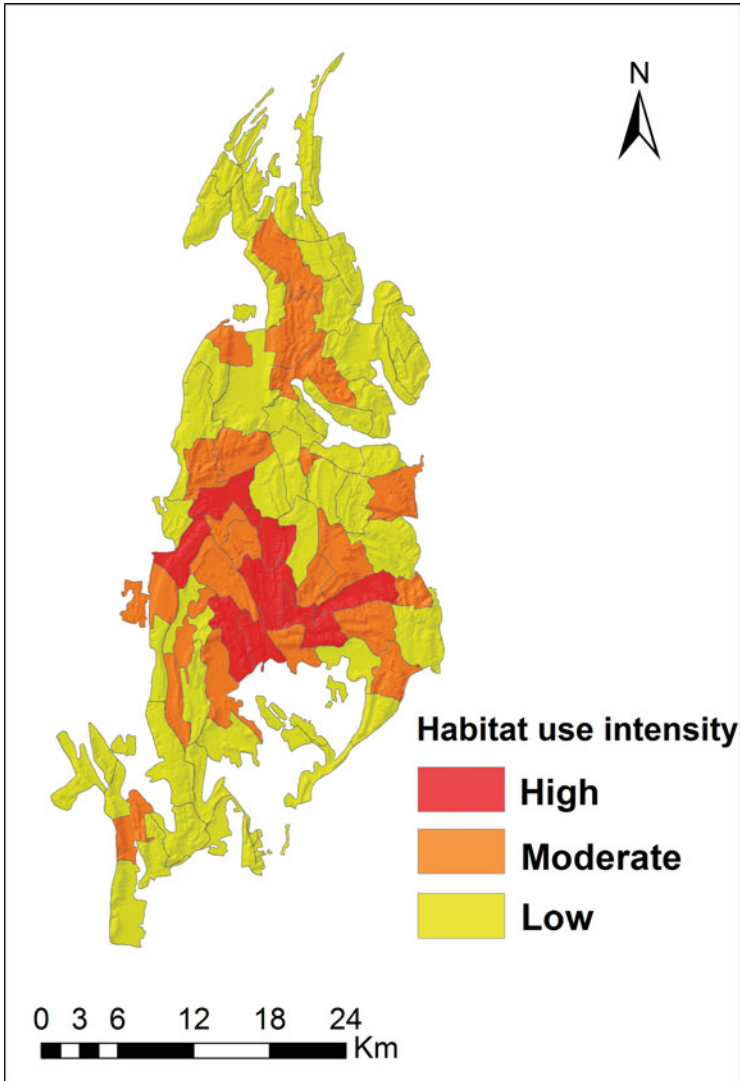


**Fig. 5** Sloth bear habitat-use intensity in Sariska Tiger Reserve, India

findings. The beats with high and medium habitat-use intensity were seen in the areas of road interference. Thus, influence of roads was not seen in bear habitat-use intensity while tree cutting and lopping, villages, and grazing activities can be a major hindrance in the success of sloth bear reintroduction program.

**Table 4** Sloth bear habitat use intensity and characteristics of influencing factors

| Sloth bear habitat-use intensity        | Beats occupied | Food availability (in %) | Waterholes' buffer (in %) | Canopy density (in %) | Slope (in degree) | Elevation (in meters) | Grazing (in %) | Human disturbance (in %) | Villages' buffer (in %) | Roads' buffer (in %) | Habitat suitability (in %) |        |     |
|---|----------------|--------------------------|---------------------------|-----------------------|-------------------|-----------------------|----------------|--------------------------|-------------------------|----------------------|----------------------------|--------|-----|
|   |                |                          |                           |                       |                   |                       |                |                          |                         |                      | High                       | Medium | Low |
| High<br>(area = 91 km <sup>2</sup> )    | 10             | 100                      | 75                        | 88                    | 12                | 490                   | 20             | 30                       | 13                      | 21                   | 77                         | 17     | 7   |
| Medium<br>(area = 240 km <sup>2</sup> ) | 22             | 68                       | 46                        | 28                    | 12                | 500                   | 41             | 55                       | 33                      | 19                   | 30                         | 47     | 23  |
| Low<br>(area = 497 km <sup>2</sup> )    | 52             | 40                       | 50                        | 25                    | 13                | 480                   | 46             | 25                       | 26                      | 11                   | 24                         | 48     | 28  |

## 5 Conclusion

The study analyzed the site-specific factors of sloth bear habitat suitability for identification of potential areas. The factors selected for identifying habitat suitability were food availability, water, elevation, slope, canopy density distance to villages and road, grazing activity, and human disturbance. Weights of these factors were obtained using Fuzzy analytical hierarchy process (FAHP). Comparison matrix of influencing factors revealed that food availability, water, and villages have higher weightage contrary to the other influencing factors in the study area. Food availability was found to be the most dominant factor in determining the habitat suitability of sloth bear. The weighted factors were integrated to produce high, medium, and low habitat suitability classes using weighted linear combination in GIS environment. Habitat suitability analysis revealed that largest area (44%) was found under moderate suitability followed by high (34%) and low (22%) suitability categories. These suitability classes were validated with the beat habitat-use intensity data of the sloth bear in the study area. Food availability (100%), canopy density (88%), and nearness to the waterholes (75%) have shown high habitat-use intensity. The bear avoided areas with human settlements; however, intermediate distance from the settlement areas was preferred, especially with food sources. Therefore, areas with human disturbance recorded medium beat habitat-use intensity. Mertzanis (1992) also presented similar results. Besides resource availability and disturbance free areas, high canopy density also played a crucial role in bear habitat-use intensity in STR. Core I has the largest area under high habitat suitability class (47%). The high suitability was found in areas having high beat habitat-use intensity by sloth bear. Hence, it validated our habitat suitability model and therefore helped us to identify areas in the STR with the potential to support sloth bear population. Human interference was found to have profound impact on habitat suitability. The successful reintroduction requires a human disturbance free contiguous area in the Reserve. Therefore, the habitat quality conducive for sloth bear could be increased if the priority is accorded for restricting human activities. Some bears could be introduced on experimental basis in the STR for deeper understanding of the biological, social, economic, and political aspects for the successful implementation of the reintroduction program of sloth bears.

**Acknowledgments** The authors would like to thank the Sariska Forest Department for their constant cooperation. We would like to extend our gratitude to Sariska Field Director, R.S. Shekhawat, for providing valuable suggestions and secondary data that enabled successful completion of this project. We would also like to extend our special thanks to Botanical Survey of India team under M. Singhadia for assisting us in conducting the fieldwork.

**Disclosure Statement** No potential conflict of interest was reported by the authors.



## References

- Ahmed, R., Sajjad, H., & Husain I (2017). Morphometric parameters-based prioritization of sub-watersheds using fuzzy analytical hierarchy process: A Case Study of Lower Barpani Watershed, India. *Natural Resources Research*, 1–9.
- Akhtar, N., Singh Bargali, H., & Chauhan, N. P. S. (2004). Sloth bear habitat use in disturbed and unprotected areas of Madhya Pradesh, India. *Ursus*, 15(2), 203–211.
- Akhtar, N., Bargali, H. S., & Chauhan, N. P. S. (2007). Characteristics of sloth bear day dens and use in disturbed and unprotected habitat of North Bilaspur Forest Division, Chhattisgarh, Central India. *Ursus*, 18(2), 203–208.
- Bargali, H. S., Akhtar, N., & Chauhan, N. P. S. (2004). Feeding ecology of sloth bears in a disturbed area in Central India. *Ursus*, 15(2), 212–217.
- Bargali, H. S., Akhtar, N., & Chauhan, N. P. S. (2005). Characteristics of sloth bear attacks and human casualties in North Bilaspur Forest Division, Chhattisgarh, India. *Ursus*, 16(2), 263–267.
- Bargali, H. S., Akhtar, N., & Chauhan, N. P. S. (2012). Sloth bear (*Melursus ursinus*) habitat in the forests of North Bilaspur Forest Division, Chhattisgarh. *Indian Forester*, 138(10), 876.
- Brooks, B. L., & Temple, S. A. (1990). Habitat availability and suitability for loggerhead shrikes in the upper Midwest. *American Midland Naturalist*, 75–83.
- Buckland, S. T., Anderson, D. R., Burnham, K. P., Laake, J. L., Borchers, D. L., & Thomas, L. (2001). *Introduction to distance sampling estimating abundance of biological populations*. Can, Ö. E., D’Cruze, N., Garshelis, D. L., Beecham, J., & Macdonald, D. W. (2014). Resolving human-bear conflict: A global survey of countries, experts, and key factors. *Conservation Letters*, 7(6), 501–513.
- Carr, P. C., & Pelton, M. R. (1984). Proximity of adult female black bears to limited access roads. In *Proceedings of the Annual Conference of the Southeastern Association of Fish and Wildlife Agencies* (Vol. 38, pp. 70–77).
- Champion, H. G., & Seth, S. K. (1968). A revised survey of forest types of India. Government of India, New Delhi. Reprinted, 2005.
- Chang, D. Y. (1996). Applications of the extent analysis method on fuzzy AHP. *European Journal of Operational Research*, 95(3), 649–655.
- Chauhan, N. P. S., Bargali, H. S., & Akhtar, N. (2003). *Ecology and management of problematic Sloth Bear (Melursus ursinus) in the North Bilaspur Forest Division, Madhya Pradesh*. Dehra Dun: Wildlife Institute of India.
- Clark, J. D., Huber, D., & Servheen, C. (2002). Bear reintroductions: Lessons and challenges. *Ursus*, 335–345.
- Clevenger, A. P., Wierzchowski, J., Chruszcz, B., & Gunson, K. (2002). GIS-generated, expert-based models for identifying wildlife habitat linkages and planning mitigation passages. *Conservation Biology*, 16(2), 503–514.
- Clevenger, A. P., Purroy, F. J., & Pelton, M. R. (2006). Brown bear (*Ursus arctos* L.) habitat use in the Cantabrian Mountains, Spain. *Mammalia*, 56(2), 203–214.
- Converse, S. J., Moore, C. T., & Armstrong, D. P. (2013). Demographics of reintroduced populations: Estimation, modeling, and decision analysis. *The Journal of Wildlife Management*, 77(6), 1081–1093.
- Das, S., Dutta, S., Sen, S., Babu, S., Kumara, H. N., & Singh, M. (2014). Identifying regions for conservation of sloth bears through occupancy modelling in North-Eastern Karnataka, India. *Ursus*, 25(2), 111–120.
- De Barba, M., Waits, L. P., Garton, E. O., Genovesi, P., Randi, E., Mustoni, A., & Groff, C. (2010). The power of genetic monitoring for studying demography, ecology and genetics of a reintroduced brown bear population. *Molecular Ecology*, 19(18), 3938–3951.
- Deng, H. (1999). Multicriteria analysis with fuzzy pairwise comparison. *International Journal of Approximate Reasoning*, 21(3), 215–231.

- Dharaiya, N., Bargali, H. S., & Sharp, T. (2016). *Melursus ursinus*. The IUCN red list of threatened species 2016: e.T13143A45033815. <https://doi.org/10.2305/IUCN.UK.2016-3.RLTS.T13143A45033815.en>
- Didier, K. A., & Porter, W. F. (1999). Large-scale assessment of potential habitat to restore elk to New York State. *Wildlife Society Bulletin*, 409–418.
- Earnhardt, J. M. (1999, November). Reintroduction programmes: Genetic trade-offs for populations. In *Animal conservation forum* (Vol. 2, No. 4, pp. 279–286). Cambridge: Cambridge University Press.
- Elgmork, K. (1978). Human impact on a brown bear population (*Ursus arctos* L.). *Biological Conservation*, 13(2), 81–103.
- Erdbrink, D. P. (1953). *A review of fossil and recent bears of the old world. Vol. I–II*. Doctoral dissertation, thesis, University of Utrecht. De Lange, Deventer, pp. 1–597.
- Fecske, D. M., Barry, R. E., Precht, F. L., Quigley, H. B., Bittner, S. L., & Webster, T. (2002). Habitat use by female black bears in western Maryland. *Southeastern Naturalist*, 1(1), 77–92.
- Felix, A. B., Campa, H., Millenbah, K. F., Winterstein, S. R., & Moritz, W. E. (2004). Development of landscape-scale habitat-potential models for forest wildlife planning and management. *Wildlife Society Bulletin*, 32(3), 795–806.
- Garshelis, D. L., Joshi, A. R., Smith, J. L., & Rice, C. G. (1999). *Sloth bear conservation action plan* (p. 309). Bears: Status Survey and Conservation Action Plan.
- Garshelis, D. L., Ratnayeke, S., & Chauhan, N. P. S. (2008). *Melursus ursinus*. In: IUCN 2012. IUCN red list of threatened species. Version 2012.2. [www.iucnredlist.org](http://www.iucnredlist.org). Accessed 3 Mar 2016.
- Gerrard, R., Stine, P., Church, R., & Gilpin, M. (2001). Habitat evaluation using GIS: A case study applied to the San Joaquin Kit Fox. *Landscape and Urban Planning*, 52(4), 239–255.
- Government of India (GOI). (1972). The wildlife (protection act). Natraj Publication, Dehradun, India. 2003. Page 218 in the wildlife (protection act). Natraj Publication, Dehradun.
- Government of Rajasthan (GOR). (2014). *Management plan for Sariska Tiger Reserve (2014–2024)*. Sariska: Project Tiger.
- Helmstedt, K. J., & Possingham, H. P. (2017). Costs are key when reintroducing threatened species to multiple release sites. *Animal Conservation*, 20(4), 331–340.
- Hirzel, A. H., Le Lay, G., Helfer, V., Randin, C., & Guisan, A. (2006). Evaluating the ability of habitat suitability models to predict species presences. *Ecological Modelling*, 199(2), 142–152.
- International Union for Conservation (IUCN) (2013). IUCN red list of threatened species. Assessed from: <https://www.iucnredlist.org/>
- Jain, P., & Sajjad, H. (2016a). Analysis of willingness for relocation of the local communities living in the critical Tiger habitat of the Sariska Tiger Reserve, India. *Local Environment*, 21(11), 1409–1419.
- Jain, P., & Sajjad, H. (2016b). Household dependency on forest resources in the Sariska Tiger Reserve (STR), India: Implications for management. *Journal of Sustainable Forestry*, 35(1), 60–74.
- Jain, P., Ahmed, R., & Sajjad, H. (2016). Assessing and monitoring forest health using a forest fragmentation approach in Sariska Tiger Reserve, India. *Norsk Geografisk Tidsskrift-Norwegian Journal of Geography*, 70(5), 306–315.
- Jamil, M., Ahmed, R., & Sajjad, H. 2017 Land suitability assessment for sugarcane cultivation in Bijnor district, India using geographic information system and fuzzy analytical hierarchy process. *GeoJournal*, 1–17.
- Johnsingh, A. J. T. (2003). Bear conservation in India. *Journal of the Bombay Natural History Society*, 100(2&3), 190–201.
- Joshi, A. R., Garshelis, D. L., & Smith, J. L. (1995). Home ranges of sloth bears in Nepal: Implications for conservation. *The Journal of Wildlife Management*, 204–214.
- Joshi, A. R., Smith, J. L. D., & Rice, C. G. (1999a). Sloth bear conservation action plan (*Melursus ursinus*). C. Servheen, S. Herrero, and B. Peyton, compilers. *Bears. Status survey and*

- conservation action plan. *IUCN/SSC Bear and Polar Bear Specialist Groups, IUCN-The World Conservation Union, Gland, Switzerland*, pp. 225–240.
- Joshi, A. R., Smith, J. L., & Garshelis, D. L. (1999b). Sociobiology of the myrmecophagous sloth bear in Nepal. *Canadian Journal of Zoology*, 77(11), 1690–1704.
- Kaminski, D. J., & Comer, C. E. (2011). A landscape-scale approach for modeling habitat suitability for the Louisiana Black Bear (*Ursus americanus luteolus*) in East Texas. Faculty Publications. Paper 293. <http://scholarworks.sfasu.edu/forestry/293>
- Kaminski, D. J., Comer, C. E., Garner, N. P., Hung, I., & Calkins, G. E. (2013). Using GIS-based, regional extent habitat suitability modeling to identify conservation priority areas: A case study of the Louisiana black bear in East Texas. *The Journal of Wildlife Management*, 77(8), 1639–1649.
- Karamanlidis, A. A., Sanopoulos, A., Georgiadis, L., & Zedrosser, A. (2011). Structural and economic aspects of human-bear conflicts in Greece. *Ursus*, 22, 141–151.
- Larson, M. A. (2003). *Landscape-level habitat suitability models for twelve wildlife species in southern Missouri* (U.S Forest Service General Technical Report NC- 233). St. Paul: North Central Research Station.
- Lauria, V., Gristina, M., Attrill, M. J., Fiorentino, F., & Garofalo, G. (2015). Predictive habitat suitability models to aid conservation of elasmobranch diversity in the Central Mediterranean Sea. *Scientific Reports*, 5, 13245.
- Lobo, J. M., Jiménez-Valverde, A., & Hortal, J. (2010). The uncertain nature of absences and their importance in species distribution modelling. *Ecography*, 33(1), 103–114.
- Mackenzie, D. I. (2005). What are the issues with presence-absence data for wildlife managers? *Journal of Wildlife Management*, 69(3), 849–860.
- May, R. M. (1991). The role of ecological theory in planning re-introduction of endangered species. In *Symposium of the Zoological Society of London* (Vol. 62, pp. 145–163).
- Mertzanis, G. (1992). Aspects biogéographiques et écologiques des populations helléniques d'ours brun (*Ursus arctos* L.). Cas d'une sous-population du Pinde: application à la conservation de l'espèce et de son habitat.; These, Université de Montpellier II, France, 220pp.
- Mitchell, M. S., Zimmerman, J. W., & Powell, R. A. (2002). Test of a habitat suitability index for black bears in the southern Appalachians. *Wildlife Society Bulletin*, 794–808.
- Nawaz, M. A., Martin, J., & Swenson, J. E. (2014). Identifying key habitats to conserve the threatened brown bear in the Himalaya. *Biological Conservation*, 170, 198–206.
- Palei, H. S., Mohapatra, P. P., & Sahu, H. K. (2014, June). Dry season diet of the sloth bear (*Melursus ursinus*) in Hadagarh wildlife sanctuary, eastern India. In *Proceedings of the Zoological Society* (Vol. 67, no. 1, pp. 67–71). Springer India.
- Phase IV Report. (2015). *Monitoring of tigers, co-predators & their prey*. Rajasthan: Sariska Tiger Reserve.
- Phillips, W. W. A. (1984). The sloth bear. Pages 290–296 in wildlife and nature protection Society of Sri Lanka, manual of mammals of Sri Lanka. Colombo, Sri Lanka.
- Porwal, M. C., Roy, P. S., & Chellamuthu, V. (1996). Wildlife habitat analysis for 'sambar' (*Cervus unicolor*) in Kanha National Park using remote sensing. *International Journal of Remote Sensing*, 17(14), 2683–2697.
- Pullin, A. S. (2002). Protecting species through ex-situ conservation and reintroduction. *Conservation Biology*, 227–251.
- Puri, M., Srivathsa, A., Karanth, K. K., Kumar, N., & Karanth, K. U. (2015). Multiscale distribution models for conserving widespread species: The case of sloth bear *Melursus ursinus* in India. *Diversity and Distributions*, 21(9), 1087–1100.
- Ratnayake, S., Wijeyamohan, S., & Santiapillai, C. (2006). *The status of sloth bears in Sri Lanka. Understanding bears to secure their future* (pp. 35–40). Gifu, Japan: Japan Bear Network.
- Ratnayake, S., Van Manen, F. T., & Padmalal, U. K. G. K. (2007a). Home ranges and habitat use of sloth bears *Melursus ursinus inornatus* in Wasgomuwa National Park, Sri Lanka. *Wildlife Biology*, 13(3), 272–284.

- Ratnayeke, S., Van Manen, F. T., Pieris, R., & Pragash, V. S. J. (2007b). Landscape characteristics of sloth bear range in Sri Lanka. *Ursus*, 18(2), 189–202.
- Reading, R. P., Miller, B., & Shepherdson, D. (2013). The value of enrichment to reintroduction success. *Zoo Biology*, 32(3), 332–341.
- Reynolds-Hogland, M. J., & Mitchell, M. S. (2007). Effects of roads on habitat quality for bears in the southern Appalachians: A long-term study. *Journal of Mammalogy*, 88(4), 1050–1061.
- Rigg, R., Findo, S., Wechselberger, M., Gorman, M. L., Sillero-Zubiri, C., & Macdonald, D. W. (2011). Mitigating carnivore-livestock conflict in Europe: Lessons from Slovakia. *Oryx*, 45, 272–280.
- Rikimaru, A. (1996). *LAMDSAT TM Data Processing Guide for forest Canopy Density Mapping and Monitoring Model*. In ITTO workshop on utilization of remote sensing in site assessment and planning for rehabilitation of logged-over Forest. July 30-August 1, Bangkok, Thailand.
- Sacco, T., & Van Valkenburgh, B. (2004). Ecomorphological indicators of feeding behaviour in the bears (Carnivora: Ursidae). *Journal of Zoology*, 263(1), 41–54.
- Santiapillai, A., & Santiapillai, C. (1990). Status, distribution and conservation of the sloth bear (*Melursus ursinus*) in Sri Lanka (Tigerpaper) (FAO).
- Sathyakumar, S., Kaul, R., Ashraf, N. V. K., Mookerjee, A., & Menon, V. (2012). *National bear conservation and welfare action plan*. Ministry of Environment and Forests. Delhi: Wildlife Institute of India and Wildlife Trust of India.
- Sinha, D., Goparaju, L., Upadhyaya, S.K., Kumar, M. & Rexwal, O. (2017). Report on sloth bear habitats, assessment of human-bear conflict and identification of suitable corridors for Wildlife Conservation in District Mirzapur of Uttar Pradesh (India). World Wide Fund for Nature-India and Vindhyan Ecology and Natural History Foundation.
- Smith, T. R. (1985). *Ecology of black bears in a bottomland hardwood forest in Arkansas*. Doctoral dissertation, University of Tennessee, Knoxville.
- Smith, K. G., Clark, J. D., & Gipson, P. S. (1991). History of black bears in Arkansas: Over-exploitation, near elimination, and successful reintroduction. In *Eastern Workshop on Black Bear Research and Management* (Vol. 10, pp. 5–13).
- Stanley Price, M. R. (1991). A review of mammal re-introductions, and the role of the reintroduction specialist group of IUCN/SSC. In *Beyond captive breeding: Re-introducing endangered mammals to the wild*. *Symposium of the Zoological Society of London* (Vol. 62, pp. 9-25).
- Stuart, S. N. (1991). Re-introductions: to what extent are they needed? Beyond Captive Breeding. Re-introducing Endangered Mammals to the Wild. In *Proceedings of a symposium held at the Zoological Society of London*, London, UK, 24–25 November 1989, 62: 27–37.
- van Manen, F. T. (1991). *A feasibility study for the potential reintroduction of black bears into the Big South Fork Area of Kentucky and Tennessee*. Tennessee Wildlife Resources Agency.
- van Manen, F. T., & Pelton, M. R. (1997). *Procedures to enhance the success of a black bear reintroduction program* (pp. 67–77). Their Biology and Management: Bears.
- Yoganand, K., Rice, C. G., Johnsingh, A. J. T., & Seidensticker, J. (2006). Is the sloth bear in India secure? A preliminary report on distribution, threats and conservation requirements. *Journal-Bombay Natural History Society*, 103(2/3), 172–181.

# Estimation of Air Pollution Using Regression Modelling Approach for Mumbai Region, Maharashtra, India



Maya Kumari, Shivangi S. Somvanshi, and Syed Zubair

**Abstract** Timely information concerning variations in the levels of air pollutants in urban regions is needed for implementing appropriate preventive actions. In this regard, an attempt has been made to develop statistical models using remote sensing data that can be beneficial in obtaining direct information on air quality using remotely sensed data easily and quickly. The present research is an integrated approach to attain the spatiotemporal attributes of air pollution index of particulate matter (PM<sub>10</sub> and PM<sub>2.5</sub>) and traces gases (O<sub>3</sub>, NO<sub>2</sub>, and CO) pollutants in Mumbai city of India. Radiance values of different bands, vegetation indices, and urbanization index resulting from Landsat 8 Operational Land Imager (OLI) and Thermal Infrared Sensor (TIRS) images were employed to create regression-based models with air pollution indices (APIs), which were intended from field-based air pollution data. The spatial variation of API for different air pollutants was simulated using the inverse distance weighted (IDW) method of interpolation. It was observed that among all the image-based parameters, the highest correlation of pollutants was with near infrared (NIR) and normalized difference vegetation index (NDVI). The correlation between APIs, vegetation/urbanization based, and land surface temperature (LST) indices suggest that areas with low vegetation, dense urbanization, and high LST are consistently pertaining to elevated concentrations of air pollutants. The high correlation coefficient, 0.965 between overall API and API (PM<sub>10</sub>), indicates that PM<sub>10</sub> has a significant effect on the overall air quality of the study area, followed by PM<sub>2.5</sub>. Correlation results also revealed a positive relation of air pollutants with urban settlement density and satellite-derived LST, respectively. The multivariate regression model with the two most correlated variables (NIR and NDVI) gave the most accurate air pollution image with R square (R<sup>2</sup>) value of 0.69, 0.55, and 0.52 for API (PM<sub>10</sub>), API (NO<sub>2</sub>), and overall API, respectively. Regression model for API

---

M. Kumari (✉) · S. Zubair

Amity School of Natural Resources & Sustainable Development, Amity University Uttar Pradesh, Noida, Uttar Pradesh, India

S. S. Somvanshi

Amity Institute of Environment Science, Amity University Uttar Pradesh, Noida, Uttar Pradesh, India

(PM<sub>2.5</sub>) with a least R<sup>2</sup> value of 0.34 seems inadequate for the prediction of API (PM<sub>2.5</sub>). On comparing among the APIs-modeled and APIs-interpolated images, 72.27% accuracy was obtained for API (PM<sub>10</sub>), 66.01% accuracy was obtained for API (NO<sub>2</sub>), and 79.89% accuracy was obtained in the case of overall API. The developed regression models were validated using February 12, 2019, in situ and satellite data.

**Keywords** Air pollution index (API) · Landsat 8 OLI & TIRS · Regression technique · Vegetation Indices · Built-up index · Land surface temperature (LST)

## 1 Introduction

Atmospheric pollution is the main issue hindering growth in developing countries, including India. An increase in the air pollutant concentration with a rise in the built-up land use denseness is a significant concern (Weng and Yang 2006). Consequently, to maintain the quality of the air within the permissible limits as per standards, it is required to gather information timely and frequently concerning variations in air pollution levels in urban communities (Vashisht et al. 2018). Significant use of remote sensing expertise in ambient air pollution monitoring began in the 1970s, followed by the enhancement in technology, as stated by the variation in reflectance of ground entities on satellite-based imagery (Ruru and Shouping 2005). Although due to the comparatively weak and fuzzy border, caused by the blending of this data with the ground truth data, the delineation of information with respect to air pollution, from remotely detected satellite images is troublesome. A portion of studies about explorations in this field has exposed the connection between land use/land cover (LULC) through satellite-based reflectance and air pollution (Ahmad et al. 2006; Ruru and Shouping 2005). Among the unique components, it was likewise discovered that vegetation cover could be contemplated as a controlling attribute for air toxins; therefore, vegetation indices are assessed as indicators for built-up regulated pollution (Hogda et al. 1995; Manawadu and Samarakoon 2005).

It is observable that Mumbai is experiencing exponential urbanization, which resulted in environmental degradation–related scenarios such as elevated environmental pollution and LST (Kumari and Sarma 2017). Urban land-use pattern has a considerable effect on the air pollutants concentration. With an increase in the greenhouse gases concentration in air, it significantly affects temperature of the area (Zheng et al. 2017). Peng et al. (2010) work indicated a positive relationship between land-use change and degraded air quality in urban areas. Increase in air pollution and LST affect the climate of the country, especially for those who are driven by monsoon like India, which ultimately leads to erratic patterns of rainfall.

To study the spatial distribution of air contaminants, interpolation strategies of GIS are generally put in use by modifying point data to surface data (Wong et al. 2004 and Bell 2006). Among various interpolation methods, the most widely used

techniques for air quality predictions are Kriging and IDW (Bell 2006). It likewise aids in managing the huge database in a primary and speedy way. This study is an effort to derive a relation between different air pollutants with vegetation/urbanization indices and other image-based characteristics. The ambient air contamination parameters used are in the form of pollution index in accordance with  $PM_{2.5}$ ,  $PM_{10}$ , CO,  $NO_2$ , and  $O_3$  along with overall API, which can be characterized as a numeric pollution indicator that can be calculated using weighted estimations of individual pollutant ( $PM_{2.5}$ ,  $PM_{10}$ , CO,  $NO_2$ , and  $O_3$ ) (Rao and Rao 2001). The image specifications taken into consideration are four vegetation indices: Enhanced Vegetation Index (EVI), Normalized Difference Vegetation Index (NDVI), Soil-Adjusted Vegetation Index (SAVI), Atmospherically Resistant Vegetation Index (ARVI), and one urbanization index Normalized Difference Urbanization/Built-up Index (NDBI), LST along with all other 11 bands of Landsat OLI and TIRS satellite data.

## 2 Study Area

Mumbai is the capital city of Maharashtra. It falls between latitude  $18^{\circ}30'$  to  $19^{\circ}20'$  N and Longitude  $72^{\circ}45'$  to  $73^{\circ}00'$  E. Mumbai consists of two districts, one is the island city, made up of seven islands and the other is suburbs (Fig. 1). In 2016,

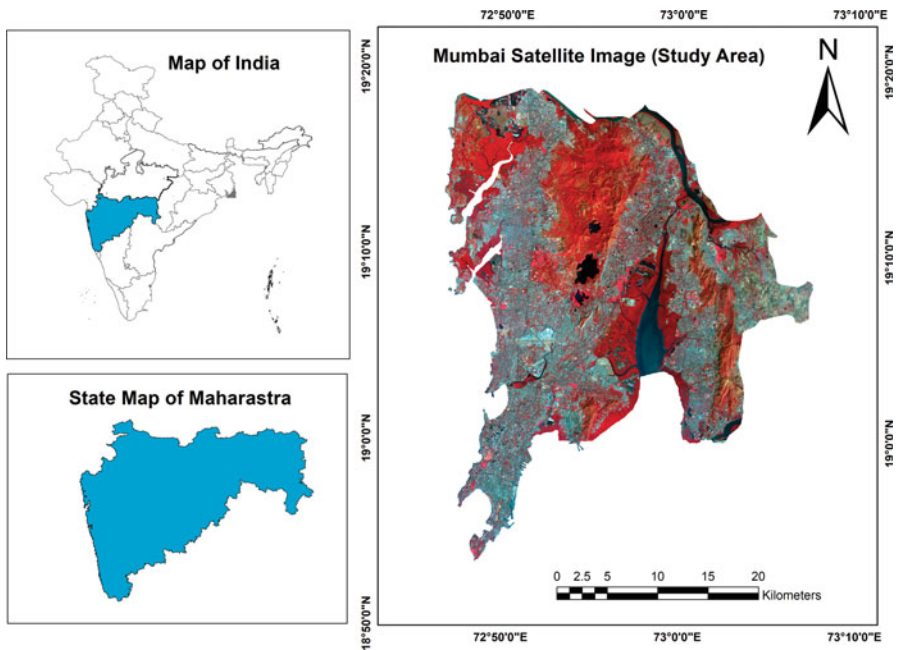


Fig. 1 Location map of study area

Mumbai is categorized as the second most crowded metropolitan zone in India with the population of 21.3 million. The whole territory of Mumbai is 603.4 km<sup>2</sup>, of this 67.79 km<sup>2</sup> is of the island city, while the rural region covers 370 km<sup>2</sup>. The Arabian Sea surrounds Mumbai to the west. Most of the areas of the city lie just above the mean sea level, with an average elevation of 14 m. The climate of the city is tropical dry and wet. The months from June to the end of September comprises of the southwest monsoon season, and months of October and November structure the post-monsoon season. The average total yearly precipitation is 2146.6 mm for the island city, and 2457 mm for the suburbs. The average annual temperature recorded is 27.2 °C.

### 3 Field Data Collection

Computation of the formula for Air Pollution Index (API) is dependent upon the type of prime contaminants of the study region. In this study, the API was computed using the value of PM<sub>10</sub>, PM<sub>2.5</sub>, NO<sub>2</sub>, CO, and O<sub>3</sub> with the help of the following formula (Rao et al. 2004):

$$API = \frac{1}{4} * \left( \frac{PM_{10}}{S_{PM_{10}}} + \frac{PM_{2.5}}{S_{PM_{2.5}}} + \frac{NO_2}{S_{NO_2}} + \frac{CO}{S_{CO}} + \frac{O_3}{S_{O_3}} \right) \quad (1)$$

Where, PM<sub>10</sub>, PM<sub>2.5</sub>, NO<sub>2</sub>, CO, and O<sub>3</sub> stand for individual values of particulate matter of diameter less than 10 µm and 2.5 µm respectively. Nitrogen dioxide, carbon monoxide and ozone, and S<sub>PM10</sub>, S<sub>PM2.5</sub>, S<sub>NO2</sub>, S<sub>CO</sub>, and S<sub>O3</sub> stand for standard values of the respective pollutants, as stated by Central Pollution Control Board (CPCB). The API concerning each pollutant was also evaluated and used in the present study. The formula employed to compute the API of the single contaminants was as written below (Rao and Rao 2001):

$$API_{Pollutant} = \left( \frac{Pollutant}{S_{Pollutant}} \right) * 100 \quad (2)$$

wherein, Pollutant and S<sub>Pollutant</sub> represent individual values and standardized values of each pollutant (PM<sub>10</sub>, PM<sub>2.5</sub>, NO<sub>2</sub>, CO, and O<sub>3</sub>). The ground-based ambient air pollutant data of Mumbai needed for the study was gathered from the website of System of Air Quality and Weather Forecasting and Research (SAFAR) developed by Ministry of Earth Science, Government of India and Indian Institute of Tropical Meteorology, Pune ([http://safar.tropmet.res.in/map\\_data.php?city\\_id=3&for=current](http://safar.tropmet.res.in/map_data.php?city_id=3&for=current)). Information was gathered from 10 monitoring locations, as mentioned in SAFAR.



### 3.1 Spatial Interpolation of APIs

With respect to quantitative analysis of the interrelation among air pollutants and land use, APIs were interpolated from 10 monitoring sites of Mumbai city by the IDW interpolation method. IDW nonlinear interpolation method was used to convert discrete data of these 10 sampling locations into continuous data over the entire study area. Values of different parameters were extracted using interpolated maps from 50 random locations, which were used for the development of the model and quantitative analysis. Data of similar sample points of the different dates were used for validation purposes.

## 4 Satellite Data

The data used in the present study are Landsat 8 OLI and TIRS satellite data acquired on February 5, 2019, and February 12, 2019 was obtained from the United States Geological Survey (USGS). Different bands along with the spatial resolution of the Landsat 8 OLI and TIRS satellite image, are as mentioned in Table 1. Landsat 8 has two sensors onboard, the Operational Land Imager (OLI) with nine bands, and the Thermal Infrared Sensor (TIRS) with two bands (Somvanshi et al. 2018).

**Table 1** Different bands of Landsat 8 OLI & TIRS satellite data

| Bands                        | Wavelength ( $\mu\text{m}$ ) | Resolution (m) |
|------------------------------|------------------------------|----------------|
| Band 1 (coastal/aerosol): B1 | 0.435–0.451                  | 30             |
| Band 2 (blue): B2            | 0.452–0.512                  | 30             |
| Band 3 (green): B3           | 0.533–0.590                  | 30             |
| Band 4 (red): B4             | 0.636–0.673                  | 30             |
| Band 5 (NIR): B5             | 0.851–0.879                  | 30             |
| Band 6 (shortwave IR-1): B6  | 1.566–1.651                  | 30             |
| Band 7 (shortwave IR-2): B7  | 2.107–2.294                  | 30             |
| Band 8 (PAN): B8             | 0.503–0.676                  | 15             |
| Band 9 (cirrus): B9          | 1.363–1.384                  | 30             |
| Band 10 (TIR – 1): B10       | 10.60–11.19                  | 100            |
| Band 11 (TIR – 2): B11       | 11.50–12.51                  | 100            |

## 5 Data Analysis and Model Generation

### 5.1 Conversion of Digital Number (DN) to Radiance

The DN values of Landsat images were transformed to radiance values to remove the systematic glitches and improvise the attributes. The transformation depends on a calibration curve of DN (Chander and Markham 2003; Negi et al. 2009).

### 5.2 Image Processing (Spectral Enhancement)

Since the time satellite recording of spectral radiance of ground objects in visible and near-infrared bands became possible, many others have developed various indices based on the certain combinations (sum, difference, ratio, linear-additional) of bands (Somvanshi et al. 2017). These indices are used to identify and monitor the temporal variation of the object. Moreover, these combinations have the advantage of reducing the effect of external factors, such as solar irradiance, atmospheric influence, etc. (Girard and Girard 2003). Four vegetation-based indices, Normalized Difference Vegetation Index (NDVI), Soil-Adjusted Vegetation Index (SAVI), Enhanced Vegetation Index (EVI), and Atmospherically Resistant Vegetation Index (ARVI) and one urbanization-based index, Normalized Differential Built-up Index (NDBI), as shown in Table 2, were used for the present study. All the images produced after spectral enhancement were used for the development of models for monitoring air pollution parameters over the study area.

**Table 2** List of spectral indices used in the study

| Indices   | Formula   | Date                |
|---|---|---------------------|
| Normalized Differential Vegetation Index (NDVI)   | $(\text{NIR} - \text{Red}) / (\text{NIR} + \text{red})$   | Rouse et al. (1973) |
| Soil-Adjusted Vegetation Index (SAVI)             | $[(\text{NIR} - \text{Red}) / (\text{NIR} + \text{red} + 0.5)] * (1 + 0.5)$   | Huete (1988)        |
| Atmospherically Resistant Vegetation Index (ARVI) | $(\text{NIR} - (\text{red} - 1 * (\text{blue} - \text{red}))) / (\text{NIR} + (\text{red} - 1 * (\text{blue} - \text{red})))$ | Tanre et al. (1992) |
| Enhanced Vegetation Index (EVI)                   | $2.5 * ((\text{NIR} - \text{red}) / ((\text{NIR} + 6 * \text{red} - 7.5 * \text{blue}) + 1))$                                 | Huete et al. (2002) |
| Normalized Differential Built-up Index (NDBI)     | $(\text{NIR} - \text{SWIR}) / (\text{NIR} + \text{SWIR})$   | Zha et al. (2003)   |

### 5.3 Model Generation

The statistical analysis was done using SPSS 20. Pearson correlation and multiple linear regression (MLR) were employed to discover the association between APIs (dependent variables) and pixel values of different bands and the indices developed through the satellite image (independent variables). Correlation analysis helped us in evaluating the effectiveness of these parameters in predicting the air quality of the study area. This statistical tool assisted in exclusion of irrelevant independent variables; only those with a high correlation coefficient with dependent variables were selected (Somvanshi et al. 2019).

Further, MLR models were employed to measure the associations within the various APIs and shortlisted bands and indices of the satellite data. To generate the regression formula for prediction of API (PM<sub>10</sub>), API (NO<sub>2</sub>), and overall API of the study area, coefficients of the selected variables were put in use. After analyzing the regression coefficients (R<sup>2</sup>), the standard error of the mean Y estimate (SE(Y)), and P-value at 95% confidence level, the developed regression model was used for developing a unique class simulated maps for air quality of the study area.

### 5.4 Model Validation

The developed regression model on the satellite data of February 5, 2019, was validated and quantified using the ground truth data and satellite image of February 12, 2019, to certify that they are not only applicable on a specific data set but also generated precise results on several data sets. To validate the models, two quantitative criteria R square (R<sup>2</sup>) and Root Mean Square Error (RMSE) were calculated between the calculated and predicted values. R<sup>2</sup> values specify the preciseness of the linear statistical relationship between two values, and RMSE indicates absolute estimation errors (Moriassi et al. 2007).

## 6 Land Surface Temperature (LST)

The LST was measured using Landsat 8 dataset. The methodology for the derivation of LST was taken from *Landsat Data Users Handbook* Science Data. Transformation of DN values in thermal infrared wavelength to spectral radiance ( $L_\lambda$ ) was done employing the equation given below:

$$L_\lambda = \text{gain} \times DN + \text{offset} \quad (3)$$

Where  $L_\lambda$  is spectral radiance; gain is the slope of the radiance/DN conversion function; DN is the digital number of a given pixel; offset is the intercept of the

radiance/DN conversion function (Landsat Project Science Office 2002). The metadata file linked with every Landsat image contains the offset and gain-related information. ERDAS Imagine and ArcGIS 10.5 software were used for image processing and analysis.

Afterward, the surface temperature was computed by using the acquired spectral radiance (Lk) values. The formula for the conversion is as follows:

$$T_B = K_2 / \left( \ln \left( \frac{K_1}{L_\lambda} \right) + 1 \right) \quad (4)$$

Where  $T_B$  represents surface temperature in kelvin,  $K_1$  with a value of 666.09 is the calibration constant 1,  $K_2$  with a value of 1282.71 is the calibration constant 2, and  $L_\lambda$  is the thermal band pixel's spectral radiance.

Values of temperature acquired using the above equation were referenced to a black body. Spectral emissivity ( $\epsilon$ ) corrections were applied in accordance to land cover. The content, chemical composition, structure, and roughness of the surface of land are the parameters that affect the emissivity of an area. For vegetative covers, emissivity can differ considerably with the type of plant species, areal density, and growth stage (Snyder et al. 1998).

Depending upon the land surface type, the rectifications in the emissivity were applied. Vegetative and nonvegetative regions were assigned a value of 0.95 and 0.92, respectively (Nichol 1994). The LST (emissivity-corrected) was calculated by employing the following formula (Artis and Carnahan 1982 and Weng et al. 2004).

$$\text{LST} = \frac{T_B}{1 + \left( \frac{\lambda T_B}{\rho} \right) \ln \epsilon} \quad (5)$$

where  $\lambda$  represents emitted radiance's wavelength;  $\rho = h^* c / \sigma$  ( $1.4389 \times 10^{-2}$  Mk);  $\sigma$  is Boltzmann's constant ( $1.389 \times 10^{-23}$  JK<sup>-1</sup>);  $h$  is Planck's constant ( $6.6269 \times 10^{-34}$  Js), and  $c$  is the velocity of light ( $2.9989108 \times 10^8$  ms<sup>-1</sup>).

Further, the Pearson correlation was employed to discover the relation between LST, air quality, and land use.

## 7 Results

### 7.1 Correlation between APIs, Radiance Values, and LST

Satellite-driven data gives an upper hand for acquiring data spatially as well as over time. The LST was predicted using the radiance values of thermal bands of Landsat data during February 2019; the temperature ranged from 21.54 to 36.53 °C with a mean temperature of 27.58 °C (Fig. 2).

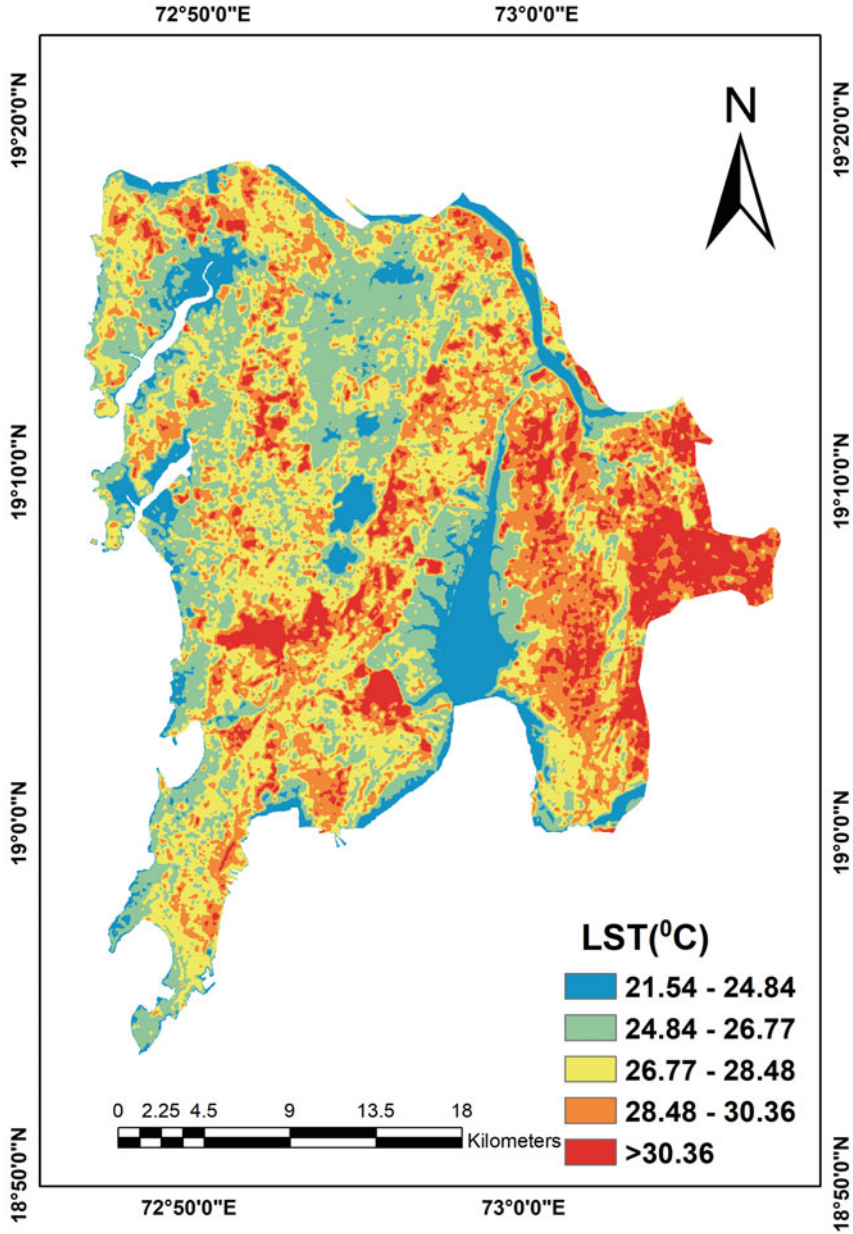


Fig. 2 Land surface temperature of the study area for February 2019

**Table 3** Correlation matrix between APIs and radiance values

|      | API    | API (PM <sub>10</sub> ) | API (PM <sub>2.5</sub> ) | API (NO <sub>2</sub> ) | API (CO) | API (O <sub>3</sub> ) |
|------|--------|-------------------------|--------------------------|------------------------|----------|-----------------------|
| API  | 1      | 0.965                   | 0.668                    | 0.555                  | 0.291    | -0.167                |
| B1   | 0.263  | 0.071                   | 0.253                    | 0.086                  | 0.400    | -0.087                |
| B2   | 0.228  | 0.028                   | 0.220                    | 0.094                  | 0.427    | -0.110                |
| B3   | 0.166  | -0.061                  | 0.181                    | 0.030                  | 0.387    | -0.078                |
| B4   | 0.104  | -0.068                  | 0.114                    | 0.016                  | 0.310    | -0.063                |
| B5   | -0.692 | -0.833                  | -0.548                   | -0.740                 | -0.103   | 0.415                 |
| B6   | -0.240 | -0.364                  | -0.167                   | -0.303                 | 0.146    | 0.045                 |
| B7   | -0.111 | -0.217                  | -0.080                   | -0.137                 | 0.207    | -0.014                |
| B8   | 0.111  | -0.051                  | 0.124                    | -0.048                 | 0.397    | -0.093                |
| B9   | 0.057  | -0.278                  | 0.121                    | -0.313                 | 0.384    | 0.238                 |
| B10  | -0.127 | -0.053                  | -0.124                   | -0.098                 | 0.119    | -0.128                |
| B11  | -0.167 | -0.049                  | -0.168                   | -0.092                 | 0.064    | -0.133                |
| NDVI | -0.685 | -0.654                  | -0.573                   | -0.656                 | -0.263   | 0.348                 |
| ARVI | -0.387 | -0.415                  | -0.303                   | -0.364                 | -0.387   | 0.415                 |
| SAVI | -0.303 | -0.387                  | -0.427                   | -0.415                 | -0.207   | 0.303                 |
| EVI  | -0.415 | -0.303                  | -0.364                   | -0.415                 | -0.303   | 0.397                 |
| NDBI | 0.412  | 0.450                   | 0.394                    | 0.475                  | 0.303    | 0.172                 |
| LST  | 0.687  | 0.69                    | 0.67                     | 0.562                  | 0.566    | -0.113                |

Note: Correlation Coefficient between LST and NDVI = -0.606

Correlation study has been done between radiance values of all the 11 bands of Landsat 8 OLI and TIRS data, spectral indices (NDVI, ARVI, SAVI, EVI, and NDBI), different APIs of the 50 sample points (Table 3), and LST. A negative correlation was observed of the APIs with reflectance in NIR, SWIR, TIR, and all types of vegetation indices except with API (O<sub>3</sub>). The best correlation of most of the APIs is with the radiance in NIR with a Pearson correlation coefficient of -0.692, -0.883, -0.548, and -0.740 for API, API (PM<sub>10</sub>), API (PM<sub>2.5</sub>), and API (NO<sub>2</sub>), respectively. However, the correlation between indices and APIs were analyzed and from the calculations it was perceived that comparatively there was a better correlation in case of NDVI compared to other indices. NDVI showed a high negative relation with correlation coefficient (R) equal to -0.654, -0.573, -0.656, and -0.685 with API (PM<sub>10</sub>), API (PM<sub>2.5</sub>), API (NO<sub>2</sub>), and overall API respectively, and week correlation with API (CO) and API (O<sub>3</sub>).

Strong correlation was obtained between overall API and API (PM<sub>10</sub>) with the value of R equal to 0.965, which shows that PM<sub>10</sub> has significant impact on overall air quality of the study area followed by PM<sub>2.5</sub> (R = 0.668). After analyzing the correlation matrix, most correlated band (NIR) and index (NDVI) were shortlisted and subjected to multiple linear regression (MLR) analysis. Similar results were portrayed by (Mozumder et al. 2012), where vegetation indices and NIR showed maximum correlation with air quality parameters.

For API (PM<sub>10</sub>), there is a positive correlation coefficient (R = 0.69) with LST, but a negative correlation with vegetation indices as vegetation could deposit

particulate matter. An identical interrelation between suspended particulate matter and land use was observed in representative cities of China. The strong correlation between particulate contamination and woodland and grasslands are found (Sun et al. 2016). The effect of landscape pattern on PM<sub>2.5</sub> concentrations using correlation analysis was also observed in Beijing. Vegetative cover can effectively lower PM<sub>2.5</sub> levels, whereas construction works on land escalate the level (Wu et al. 2015). LST also showed a high negative correlation ( $R = -0.606$ ) with NDVI (Kumari and Sarma 2017). In the case of trace gases, ozone showed a weak correlation with LST and negative correlations with nearly all vegetation indices. API (NO<sub>2</sub>) showed a strong positive correlation with LST, with a correlation coefficient equal to 0.562. NO<sub>2</sub> is affected profoundly by land use among other trace gases. NO<sub>2</sub> is the perfect indicator of vehicular traffic-caused air pollution. In studies, earlier done for NO<sub>2</sub> prediction employing the LUR model, NO<sub>2</sub> showed a positive correlation with urban areas and a negative correlation with agricultural fields and tree canopy (Novotny et al. 2011; Meng et al. 2015). API (CO) showed a positive correlation with ( $R = 0.566$ ) with LST. The results showed that the amount of CO is greatly affected by anthropogenic activities in urban areas (Zheng et al. 2017). Results also revealed that the geographical patterns of air contaminants were positively correlated with urban land use and satellite-driven land surface temperature (Weng and Yang 2006).

## 7.2 Regression Models

The results revealed by the regression model developed are presented in Table 4, describing how efficiently, geographical changes in air contaminants can be ascertained by implementing various regression models.

Models were developed for API of particulate matters (PM<sub>10</sub>, PM<sub>2.5</sub>), NO<sub>2</sub>, and overall API using radiance values of NIR and NDVI. The first model, which combines NIR and NDVI, provided the best fit for predicting API (PM<sub>10</sub>). It had a high R<sup>2</sup> value, that is, 0.69, implying a good linear interrelation within estimated and forecasted API (PM<sub>10</sub>) and indicated that this model could describe 69% of the variance in the API (PM<sub>10</sub>) values. Each one of these variables had quite significant *p*-values, referring to a strong correlation with API (PM<sub>10</sub>). Contrarily, third and

**Table 4** Recommended models for different APIs

| Pollutant                | Regression model  | R <sup>2</sup> |
|--------------------------|---|----------------|
| API (PM <sub>10</sub> )  | $\gamma = \beta_0 + (\beta_1 * NIR) + (\beta_2 * NDVI)$<br>Where: $\beta_0 = 210.1798785$ , $\beta_1 = (-2.15655)$ , $\beta_2 = 0.0433$ | 0.69           |
| API (PM <sub>2.5</sub> ) | $\gamma = \beta_0 + (\beta_1 * NIR) + (\beta_2 * NDVI)$<br>Where: $\beta_0 = 368.8025$ , $\beta_1 = (-1.886)$ , $\beta_2 = (-0.7688)$   | 0.34           |
| API (NO <sub>2</sub> )   | $\gamma = \beta_0 + (\beta_1 * NIR) + (\beta_2 * NDVI)$<br>Where: $\beta_0 = 126.237$ , $\beta_1 = (-1.071)$ , $\beta_2 = (-0.0739)$    | 0.55           |
| API                      | $\gamma = \beta_0 + (\beta_1 * NIR) + (\beta_2 * NDVI)$<br>Where: $\beta_0 = 189.818$ , $\beta_1 = (-1.022)$ , $\beta_2 = (-0.242)$     | 0.52           |

fourth models used for predicting API ( $\text{NO}_2$ ) and overall API with  $R^2$  values of 0.55 and 0.52 showed an average correlation between variables and APIs. While the second model used for predicting API ( $\text{PM}_{2.5}$ ) showed the least significance with the  $R^2$  value of 0.34. Hence the model is not appropriate for predicting API ( $\text{PM}_{2.5}$ ). The proposed algorithms for API ( $\text{PM}_{10}$ ), API ( $\text{NO}_2$ ), and overall API were validated using the radiance values extracted from Landsat 8 satellite images procured on February 12, 2019, along with corresponding ground truth data from SAFAR (Figs. 3, 4, and 5). Spatial distribution of all the parameters API ( $\text{PM}_{10}$ ), API ( $\text{NO}_2$ ), and overall API showed highest values over the inland waterbodies as when warm, unstable air moves out over a cool water body, a temperature inversion develops near and over the waterbody, giving a very poor dispersion condition in lower layer (Hewson and Olsson 2012).

Indeed, undoubtedly apart from the parameters used in the study, many other aspects also control suspended particulate matter and trace gases. With the exponential development in information sharing across the globe, more potential parameters can be added to the correlation analysis.

### 7.3 Model Validation

The performance of the developed regression models on the data of February 5, 2019, was quantified using the ground truth data of 50 sampling points and image of February 12, 2019. The validation results for the best regression models are shown in Figs. 6, 7 and 8. Verification results revealed that the models developed using Landsat 8 data are appropriate for APIs, whereas the data acquired from the mentioned satellite cannot be put in use for predicting  $\text{PM}_{2.5}$ , CO, and  $\text{O}_3$  (Somvanshi et al. 2019). Values of  $R^2$  equal to 0.7227 and RMSE of 0.7773 indicate that this regression model had the best fit for predicting API ( $\text{PM}_{10}$ ).

Similarly,  $R^2$  value of 0.6601 and RMSE value of 8.7290 for the regression model used for predicting API ( $\text{NO}_2$ ) indicate that the model is appropriate to predict the parameter with good accuracy using remote sensing data. Further, as per the validation results of overall API values of  $R^2$  equaling 0.798 and RMSE 1.2131, indicating that the regression model is adequate for the prediction of air quality.

## 8 Conclusion

Geospatial technology was applied for air pollution modeling of the Mumbai region. Based on the study, it was observed that the near-infrared band and remote sensing-derived NDVI showed the highest correlation with in situ air pollutant data of February 5, 2019. The IDW method was used for spatial interpolation of APIs of different air pollutants. A strong correlation was observed between overall API and API ( $\text{PM}_{10}$ ) followed by API ( $\text{PM}_{2.5}$ ) and API ( $\text{NO}_2$ ), indicating that API ( $\text{PM}_{10}$ )



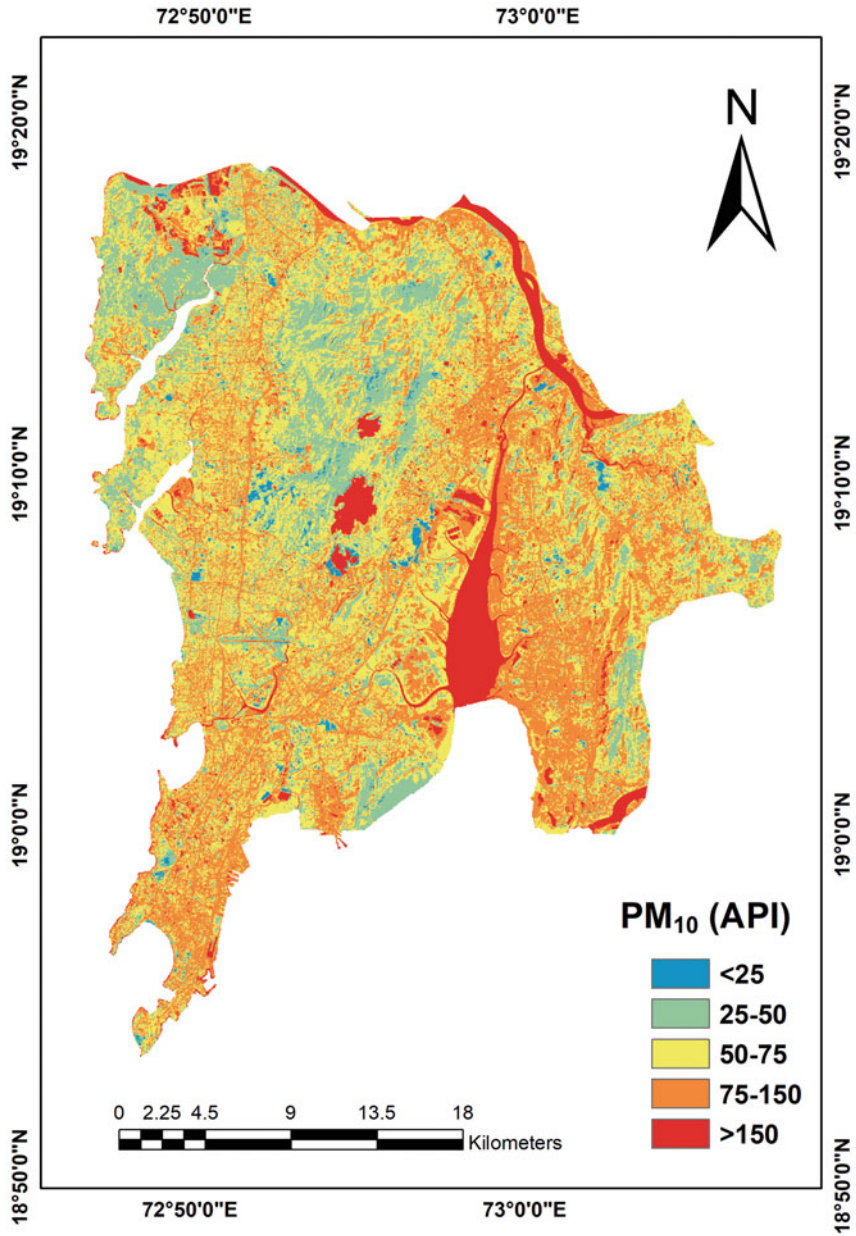


Fig. 3 Simulated map of API (PM<sub>10</sub>) using model

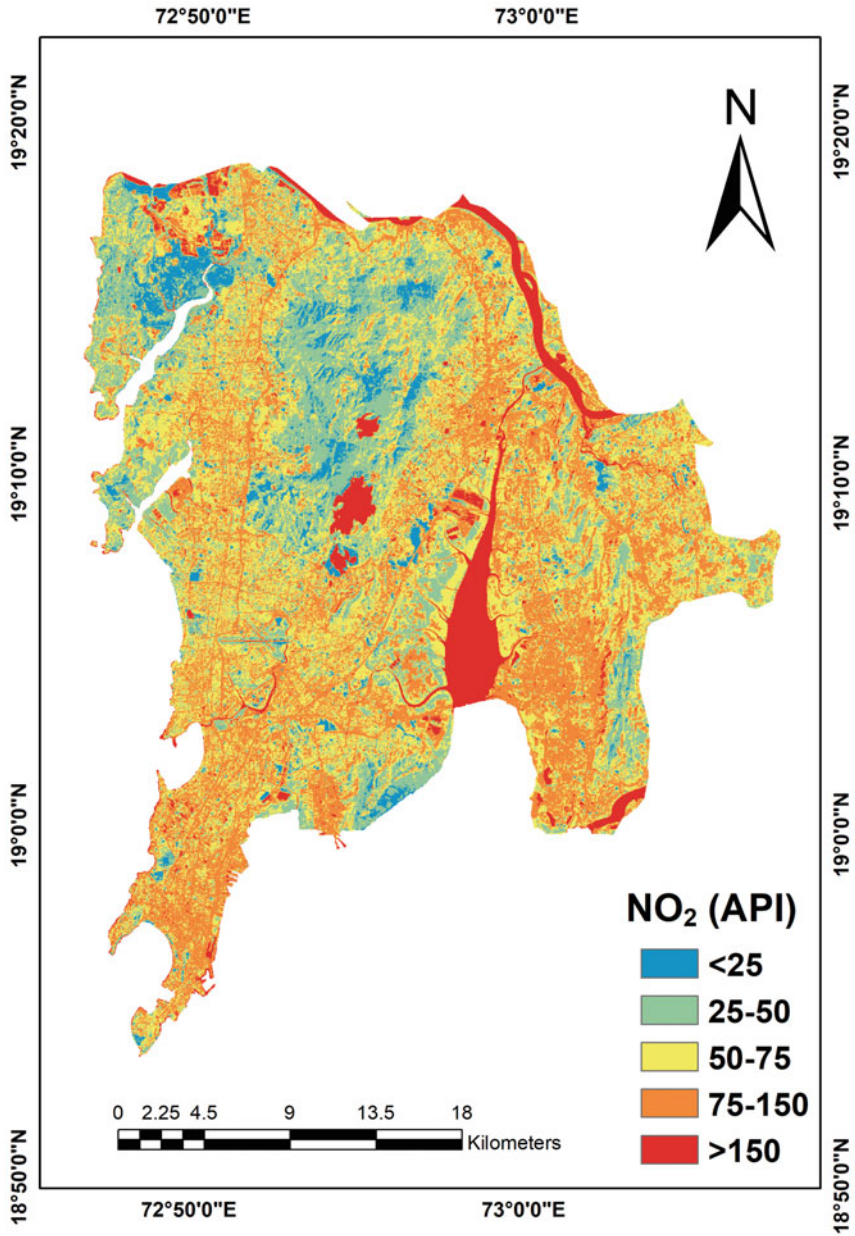


Fig. 4 Simulated map of API (NO<sub>2</sub>) using model

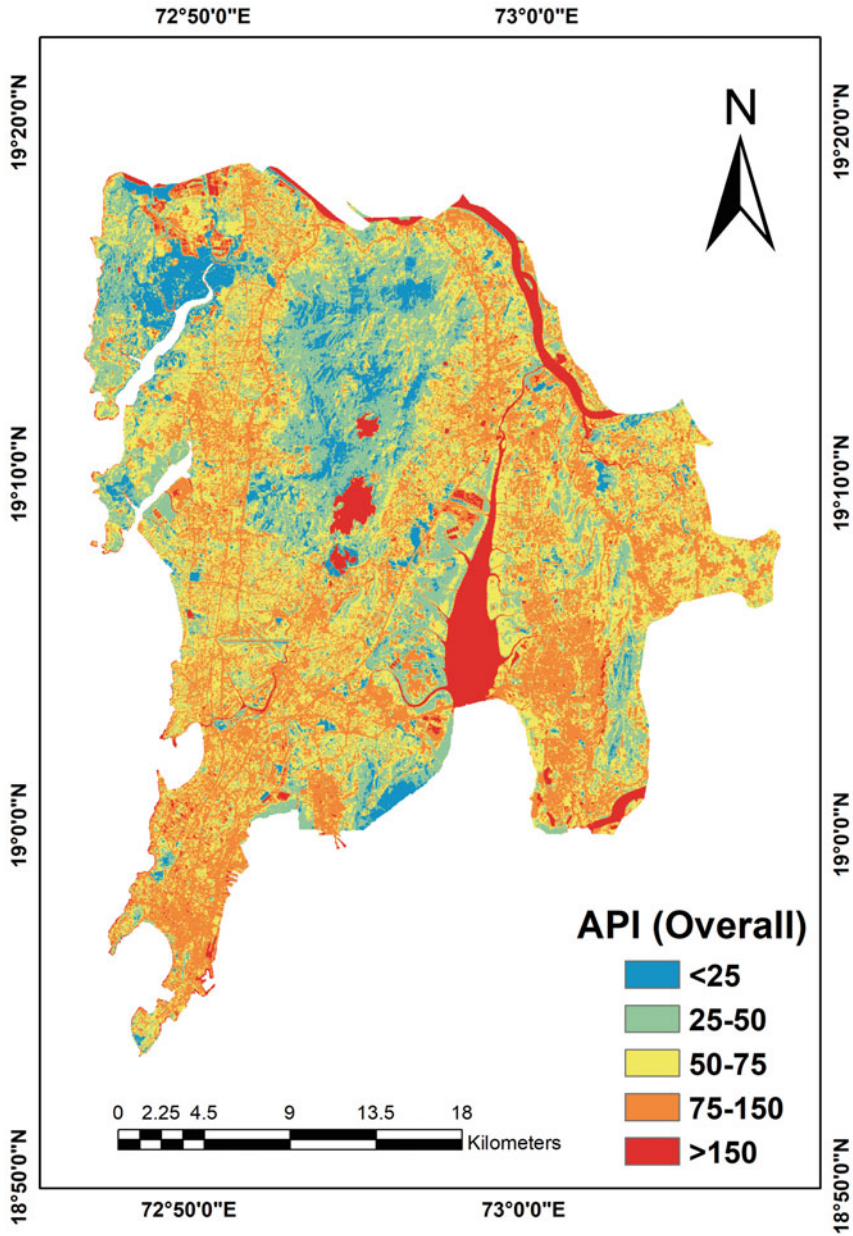


Fig. 5 Simulated map of API (overall) using model

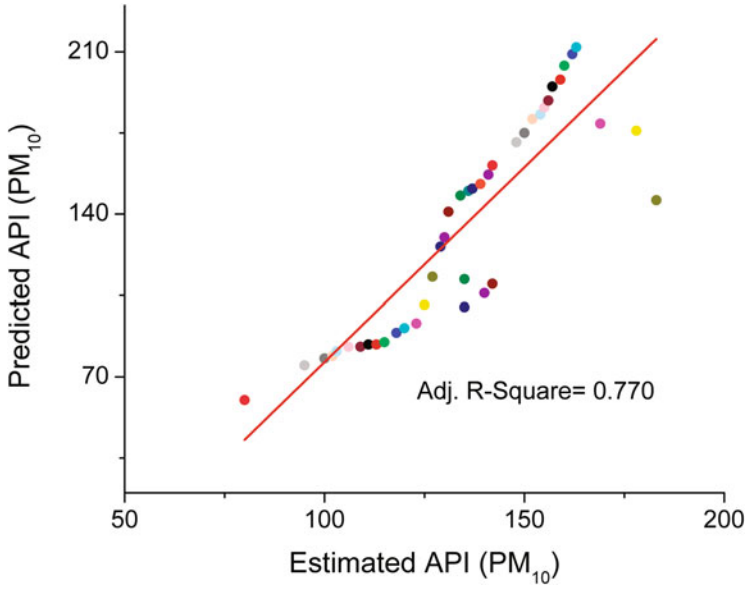


Fig. 6 Scatter plot of predicted versus measured API (PM<sub>10</sub>)

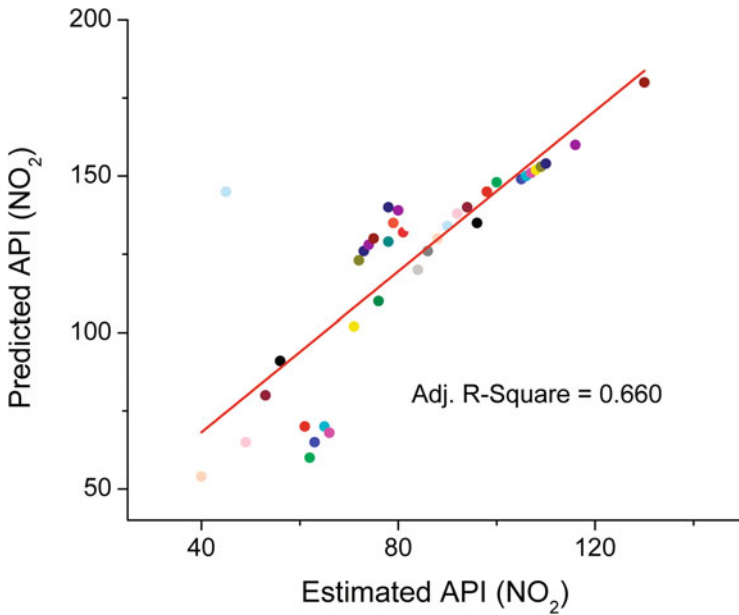
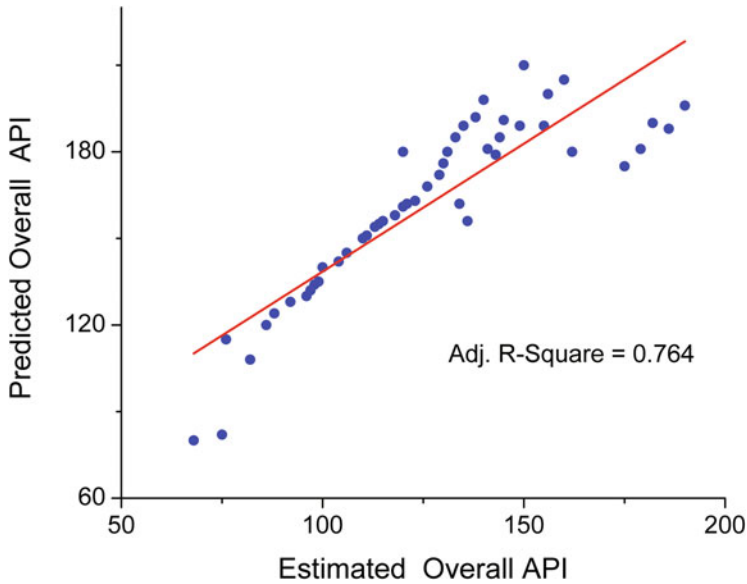


Fig. 7 Scatter plot of predicted versus measured API (NO<sub>2</sub>)



**Fig. 8** Scatter plot of predicted versus measured API (overall)

has a maximum effect on the overall air quality of the study area. The overall API was also in positive correlation with low vegetation, high built-in, and land surface temperature. New regression models were developed for most representative components for assessing air quality for the study area and the same was validated with satellite data and ground data of February 12, 2019. Therefore, remote sensing data can be efficiently used to assess pollutant levels and their potential source which can be regulated based on GIS spatial interpolated maps.

## References

- Ahmad, A., Hashim, M., Hashim, M. N., Ayof, M. N. & Budi, A. S. (2006). The use of remote sensing and GIS to estimate air quality index (AQI) over peninsular Malaysia. In *Proceedings of the map Malaysia 2006*, held in Kuala Lumpur, Malaysia.
- Artis, D. A., & Carnahan, W. H. (1982). Survey of emissivity variability in thermography of urban areas. *Remote Sensing of Environment*, 12(4), 313–329.
- Bell, M. L. (2006). The use of ambient air quality modeling to estimate individual and population exposure for human health research: A case study of ozone in the northern Georgia region of the United States. *Environmental International*, 32(5), 586–593.
- Chander, G., & Markham, B. (2003). Revised Landsat-5 TM radiometric calibration procedures and Postcalibration dynamic ranges. *IEEE Transactions on Geoscience and Remote Sensing*, 41 (11), 2674–2677.
- Girard, M. C., & Girard, C. (2003). *Processing of remote sensing data* (N. Venkat Rao, Trans.). New Delhi: Oxford and IBH Publishing Pvt. Ltd, p. 486.

- Hewson, E. W., & Olsson, L. E. (2012). Lake effects on air pollution dispersion. *Journal of the Air Pollution Control Association*, 17(11), 757–761. <https://doi.org/10.1080/00022470.1967.10469069>.
- Hogda, K. A., Tommervik, H., Solheim, I., & Lauknes, I. (1995). Mapping of air pollution effects on the vegetation cover in the Kirkenes Nickel area using remote sensing. Proceedings of the geoscience and remote sensing symposium, IGARSS 95. *Quantitative Remote Sensing for Science and Applications*, 2, 1249–1251.
- Huete, A. R. (1988). A soil-adjusted vegetation index (SAVI). *Remote Sensing of Environment*, 25(3), 259–309. [https://doi.org/10.1016/0034-4257\(88\)90106-X](https://doi.org/10.1016/0034-4257(88)90106-X).
- Huete, A., Didan, K., Miura, T., Rodriguez, E. P., Gao, X., & Ferreira, L. G. (2002). Overview of the radiometric and biophysical performance of the MODIS vegetation indices. *Remote Sensing of Environment*, 83(1), 195–213. [https://doi.org/10.1016/S0034-4257\(02\)00096-2](https://doi.org/10.1016/S0034-4257(02)00096-2).
- Kumari, M., & Sarma, K. (2017). Changing trends of land surface temperature in relation to land use/cover around thermal power plant in Singrauli district, Madhya Pradesh, India. *Spatial Information Research*, 25(6), 769–777.
- Landsat Project Science Office. (2002). *Landsat 7 science data user's handbook* (Goddard Space Flight Center). Available online at: [http://ltpwww.gsfc.nasa.gov/IAS/handbook/handbook\\_toc.html](http://ltpwww.gsfc.nasa.gov/IAS/handbook/handbook_toc.html)
- Manawadu, L., & Samarakoon, L. (2005). Identification of air pollution potential areas and its temporal and spatial patterns of the City of Colombo, Sri Lanka applying GIS and RS. *Proceedings of the 26th Asian Conference of Remote Sensing (ACRS)*, held in Hanoi, Vietnam.
- Meng, X., Chen, L., Cai, J., Zou, B., Wu, C. F., Fu, Q., Zhang, Y., Liu, Y., & Kan, H. (2015). A land use regression model for estimating the NO<sub>2</sub> concentration in Shanghai, China. *Environmental Research*, 137, 308–315.
- Moriasi, M., Bertrand-Krajewski, J. L., & Chebbo, G. (2007). Calibration and validation of multiple regression models for storm water quality prediction: Data partitioning, effect of dataset size and characteristics. *Water Science and Technology*, 52(3), 45–52.
- Mozumder, C., Reddy, K. V., & Pratap, D. (2012). Air pollution modeling from remotely sensed data using regression techniques. *Journal of Indian society of Remote Sensing*. <https://doi.org/10.1007/s12524-012-0235-2>.
- Negi, H. S., Kulkarni, A. V., & Semwal, B. S. (2009). Estimation of snow cover distribution in Beas basin, Indian Himalaya using satellite data and ground measurements. *Journal of Earth System Science*, 118(5), 525–538.
- Nichol, J. E. (1994). A GIS-based approach to microclimate monitoring in Singapore's high-rise housing estates. *Photogrammetric Engineering and Remote Sensing*, 60(10), 1225–1232.
- Novotny, E. V., Bechle, M. J., Millet, D. B., & Marshall, J. D. (2011). National satellite-based land-use regression: NO<sub>2</sub> in the United States. *Environmental Science & Technology*, 45, 4407–4414.
- Peng, W., Zhou, J., Luo, H., Yang, C., & Zhao, J. (2010). Relationship between land use change and its urban air environmental impacts. *International Soil and Water Conservation Research*, 17, 87–91.
- Rao, M. N., & Rao, H. V. N. (2001). *Air pollution* (pp. 268–271). New Delhi: Tata McGraw Hill Publishing Company Limited.
- Rao, M. P. V., Hima Bindu, V., Sagarshwar, G., Indracanti, J., & Anjaneyulu, Y. (2004). Assessment of ambient air quality in the rapidly industrially growing hyderabad urban environment. *Proceedings of the BAQ 2004*, Workshop program and presentation, Poster 3.
- Rouse, J.W., Jr., Haas, R. H., Schell, J. A., & Deering, D. W. (1973). *Monitoring the vernal advancement and retrogradation (green wave effect) of natural vegetation*. Progress Report RSC 1978-1, Remote Sensing Center, Texas A&M University, College Station, 93p. (NTIS No. E73-106393)
- Ruru, D., & Shouping, X. (2005). The coupled model of atmosphere and ground for air pollution remote sensing and its application on Guangdong Province, China. Proceedings of the geoscience and remote sensing symposium, IGARSS'05. *IEEE International*, 7, 5133–5136.

- Snyder, W. C., Wan, Z., Zhang, Y., & Feng, Y. Z. (1998). Classification-based emissivity for land surface temperature measurement from space. *International Journal of Remote Sensing*, 19(14), 2753–2774.
- Somvanshi, S. S., Kunwar, P., Tomar, S., & Singh, M. (2017). Comparative statistical analysis of the quality of image enhancement techniques. *International Journal of Image and Data Fusion*. <https://doi.org/10.1080/19479832.2017.1355336>.
- Somvanshi, S. S., Oshin, B., Kunwar, P., Singh, M., & Singh, P. (2018). Monitoring spatial LULC changes and its growth prediction based on statistical models and earth observation datasets of Gautam Buddha Nagar, Uttar Pradesh, India. *Environment Development and Sustainability (Springer)*. <https://doi.org/10.1007/s10668-018-0234-8>.
- Somvanshi, S. S., Vashisht, A., Chandra, U., & Kaushik, G. (2019). Delhi air pollution modeling using remote sensing technique. In C. Hussain (Ed.), *Handbook of environmental materials management*. Cham: Springer. [https://doi.org/10.1007/978-3-319-58538-3\\_174-1](https://doi.org/10.1007/978-3-319-58538-3_174-1).
- Sun, L., Wei, J., Duan, D., Guo, Y., Yang, D., Jia, C., & Mi, X. (2016). Impact of land-use and land-cover change on urban air quality in representative cities of China. *Journal of Atmospheric and Solar Terrestrial Physics*, 142, 43–54.
- Tanre, D., Holben, B. N., & Kaufman, Y. J. (1992). Atmospheric correction algorithm for NOAA-AVHRR products, theory and application. *IEEE Transactions on Geoscience and Remote Sensing*, 30.
- Vashisht A., Somvanshi, S., & Shrivastava, P. (2018). *Spatiotemporal modelling of air quality of Delhi using Remote Sensing and GIS, National conference on Environmental Challenges for New India*. Organized by Environment and Social Development Association (ESDA), 2nd–3rd June 2018 in Delhi.
- Weng, Q., & Yang, S. (2006). Urban air pollution patterns, land use and thermal landscape: An examination of the linkage using GIS. *Environmental Monitoring and Assessment*, 117(1–3), 463–489.
- Weng, Q., Lu, D., & Schubring, J. (2004). Estimation of land surface temperature–vegetation abundance relationship for urban heat island studies. *Remote Sensing of Environment*, 89(4), 467–483.
- Wong, D. W., Yuan, L., & Perlin, S. A. (2004). Comparison of spatial interpolation methods for the estimation of air quality data. *Journal of Exposure Analysis and Environmental Epidemiology*, 14(5), 404–415.
- Wu, J., Xie, W., Li, W., & Li, J. (2015). Effects of urban landscape pattern on PM2.5 pollution—A Beijing case study. *PLoS One*, 10.
- Zha, Y., Gao, J., & Ni, S. (2003). Use of normalized difference built-up index in automatically mapping urban areas from TM imagery. *International Journal of Remote Sensing*, 24(3), 583–594.
- Zheng, S., Zhou, X., Singh, R. P., Wu, Y., Ye, Y., & Wu, C. (2017). The spatiotemporal distribution of air pollutants and their relationship with land-use patterns in Hangzhou City, China. *Atmosphere*, 8, 110. <https://doi.org/10.3390/atmos8060110>.

# Mapping of Agriculture Productivity Variability for the SAARC Nations in Response to Climate Change Scenario for the Year 2050



Ram Kumar Singh , Vinay Shankar Prasad Sinha, Pawan Kumar Joshi, and Manoj Kumar 

**Abstract** Agriculture productivity is often guided by prevailing climate and management interventions. The climatic variations over a region on a temporal scale may have favorable or adverse feedback on productivity. Evaluation of the influences of climate change on agriculture productivity is essential to ensure food security. The South Asian Association for Regional Cooperation (SAARC) is consortium of Afghanistan, Bangladesh, Bhutan, India, Maldives, Nepal, Pakistan, and Sri Lanka, which represents a region where agriculture drives the economy and people are primarily dependent on it for their food requirements. Climate change is expected to influence the productivity of this region, which further depends on climate and other driving factors. We assessed the influences of climate change on agriculture productivity (Net Primary Productivity, NPP) using JULES (“Joint UK Land Environment Simulator”), which is a Dynamic Global Vegetation Model (DGVM). JULES was used to process NPP for the future climate change scenario of the year 2050 under low emission represented by RCP 2.6. The climate change projections-based Coordinated Regional Climate Downscaling Experiment (CORDEX) for the South-Asian region was used to simulate productivity using the JULES model. A slight decrease in productivity was witnessed which had spatial variability across the SAARC nations. However, the majority of the agriculture area (87% of the total agriculture land) is expected to witness moderate change where productivity would fall by 1 to 3 Mg-C/ha/year. We present agriculture productivity estimates of SAARC nations under climate change influence, which would assist planners in ensuring the food security of the region through proper management interventions.

---

R. K. Singh · V. S. P. Sinha (✉)

Department of Natural Resources, TERI School of Advanced Studies, New Delhi, India  
e-mail: [ram.kumarsingh@terisas.ac.in](mailto:ram.kumarsingh@terisas.ac.in); [sinhav@terisas.ac.in](mailto:sinhav@terisas.ac.in)

P. K. Joshi

Special Center for Disaster Research, Jawaharlal Nehru University, New Delhi, India

M. Kumar

GIS Centre, Forest Research Institute (FRI), Dehradun, India

© The Editor(s) (if applicable) and The Author(s), under exclusive license to Springer Nature Switzerland AG 2021

P. Kumar et al. (eds.), *Remote Sensing and GIScience*,  
[https://doi.org/10.1007/978-3-030-55092-9\\_14](https://doi.org/10.1007/978-3-030-55092-9_14)



**Keywords** Vulnerability · Climate Change · DGVM · JULES · NPP

## 1 Introduction

Global agriculture production is expected to witness various levels of threat under the influence of climate change (FAO 2009; Gregory et al. 2005; Singh et al. 2020). The impact of climate change on agriculture production is identified as one of the prime challenges that would affect food production–related consequences (Gregory et al. 2002; Roetter et al. 2007). Climate change is expected to impact agriculture productivity (Acevedo 2011; Ranuzzi and Srivastava 2012), land cover change (Singh et al. 2020a, b; Wardlow et al. 2007), changes in biodiversity (Ingram et al. 2010; Wezel and Soldat 2009), sporadic changes in temperature and precipitation (Singh et al. 2019), and sustainable food security (Herrero et al. 2017; Thomson 2003). The rapid economic development (Gerlitz et al. 2017), increasing population (Cutter and Finch 2008), agriculture–forestry land conversion (Fuss et al. 2015), and urbanization (Mishra et al. 2010) also impact agriculture directly or indirectly (West et al. 2010). The studies on agriculture food production for sustainable future production are an important and major challenge in changing climate scenarios (Kumar et al. 2018a; Tilman et al. 2011). Agriculture crop productivity is precisely estimated using agriculture crop growth models, including Dynamic Global Vegetation Models (DGVM) (Van den Hoof et al. 2011). The agriculture crop growth models simulate the growth of a crop using climatic parameters, cultivar, irrigation and soil condition, and other estimators. Crop models are useful for the estimation of regional and global agriculture crop production (Xiong et al. 2008; Yun 2003). However, for medium- and long-term predictions, models may not give a reliable estimate as to the relationship between the growth and other variables that impact the growth, as they often form nonlinear complex relationships while the models are yet evolving (Peng 2000; Singh et al. 2020a, b).

The existing DGVMs (Kalra and Kumar 2018) can simulate the productivity of vegetated region using climate drivers such as the diurnal temperature, precipitation, wind velocity, specific humidity, soil condition, geographical condition, and flux (shortwave and longwave radiations), etc. The vegetated regions are often represented in such models by Plant Functional Type (PFT), representing a conglomeration of various tree species having comparable functional traits (Kumar et al. 2018a). The various models have evolved in recent decades that could be used for the estimation of agriculture productivity (Haxeltine and Colin Prentice 1996; Van den Hoof et al. 2011), impacts on forests and agriculture crops (Kumar et al. 2019a, b), carbon estimation of forested and agriculture lands (Raich 1991; Sitch et al. 2008), monitoring of land resources (Thenkabail 2015), and the monitoring of ecosystems (Kucharik et al. 2000; Thenkabail 2015). After the evolution of mechanistic growth simulation models, the earlier approaches of indicator weight, regression, correlation, interpolation, and other statistical approaches are generally discarded where process-based growth models provide a better estimate for long-

term future projections under the stimulus of multiple drivers along with climate change (Cutter 2017; Kalra and Kumar 2018). Various DGVMs of present days that can be used for the estimation of future productivity for terrestrial landscape, including Joint UK Land Environment Simulator (JULES) (Van den Hoof et al. 2011), Lund–Potsdam–Jena (LPJ) (Sitch et al. 2003) and others. In this study, we used the JULES model to predict future agriculture productivity under a low emission scenario of RCP 2.6 for the year 2050.

### ***1.1 The Process-Based Joint UK Land Environment Simulator***

The JULES is one of the latest DGVMs developed by varied community researchers of the UK, coordinated by UK Meteorological Office (UKMO), Centre for Ecology and Hydrology (CEH) (<http://jules.jchmr.org/>). The model integrates a full suite of land-based processes, rigorously based on observations and theoretical science. The model is based on the Met Office Surface Exchange System (MOSES) land surface scheme (Cox et al. 1999) and the Top-Down Representation of Interactive Foliage and Flora Including Dynamics (TRIFFID) model (Cox 2001), but with significant improvements to allow various land processes to interact with each other.

The used JULES v. 4.8 represents five plant functional types (PFTs): shrubs, C3 and C4 grasses, broadleaf trees, and needle-leaf trees. PFTs are a driven system to classify plants based on their phylogenetic, physical, and phenological character (Diaz and Cabido 1997). PFT helps modelers to group multiple trees existing in a region to make the representation easier in the process-based models, based on the similarity of physiological process and other functional attributes to make fewer clusters. The vegetation of a region is usually fed as one of the PFT while simulating the ecosystem processes using a DGVM.

Van den Hoof et al. (2011) used JULES-SUCROS, a dynamic model to study the agricultural growth. JULES-SUCROS is specific to agroecosystem features which are based on dynamic agriculture crop growth process such as sowing to harvest phenological cycle and yield-bearing model. The study also compares fluxes against FLUXNET measured at six European sites to highlight complex connections between land surface, agriculture growth, water, and primarily energy cycles for our ecosystems was observed. The JULES-SUCROS prediction yield provides a good correlation with observed gross primary productivity (GPP), heat flux, and sensible heat flux. We used the JULES v. 4.8 model to estimate the productivity of regions dominated by agriculture for the year 2050 for the SAARC nations under the climate change scenario of RCP2.6. The PFT3 and PFT4 represent grasses in the model which was found to represent agriculture lands of the study region. We present the application of a DGVM for the following reasons:

1. To test the application of the process-based model to simulate PFT that matches with the agriculture lands.

2. To test how well a DGVM can simulate the productivity of agricultural lands in the present scenario.
3. To estimate the productivity of agricultural lands under the influence of climate change scenario for the year 2050.

## 2 Methods

### 2.1 Study Region

The study was done for the South Asian Association for Regional Cooperation (SAARC) nations represented by eight nations that include Afghanistan, Bangladesh, Bhutan, India, Maldives, Nepal, Pakistan, and Sri Lanka. It covers a total geographical area of 51,000,000 sq. km and extends between the latitudes 0.8° S and 38.5° N and longitudes 59° E and 93.6° E (Fig. 1). India contributes the largest geographical area in the SAARC, spread over 3,290,000 sq. km, while the Maldives has the smallest area of 298 sq. km. The SAARC region has a predominantly tropical climate along with arid and semiarid tropics. The region has a unique climatological distinction and is mostly under the influence of the monsoons. Most of the area of the SAARC region depends upon the monsoon for agriculture and is usually referred to as rainfed agriculture (Chatterjee and Khadka 2011; Savita et al. 2018). Agriculture and forests are the two leading land uses that provide most of the ecosystem services for the sustenance of the human population in the region which is under the impact of climate change (Kumar et al. 2018b). Thus, assessing the projected changes in the productivity of these two dominant ecosystems is often the priority of researchers. Moreover, agriculture alone contributes more than 30% of gross domestic product (GDP) of the region as per the assessment done by World Bank (2011) for the period 2000–2010, thus assessing the impressions of climate change on agriculture productivity becomes much desirable. At the same spell, the region is witnessing a swift growth of population (World Bank 2011) where most of the people would be relying on agriculture for their food security. Thus, it provides an opportunity to assess the impacts for a future time step, so that the assessment would help the planners to develop management approaches to safeguard food security in the region.

### 2.2 Data and Method

The JULES requires nine different input files for the simulation (Table 1). The desired input files needed to run the JULES were obtained from the Coordinated Regional Climate Downscaling Experiment (CORDEX), which follows World Climate Research Programme (WCRP) for the SAARC region. The projected climatic scenario and climatic data is disseminated through the Earth System Grid Federation (ESGF) and data node are available through the climate data portal of Centre for Climate Change Research, Indian Institute of Tropical Meteorology

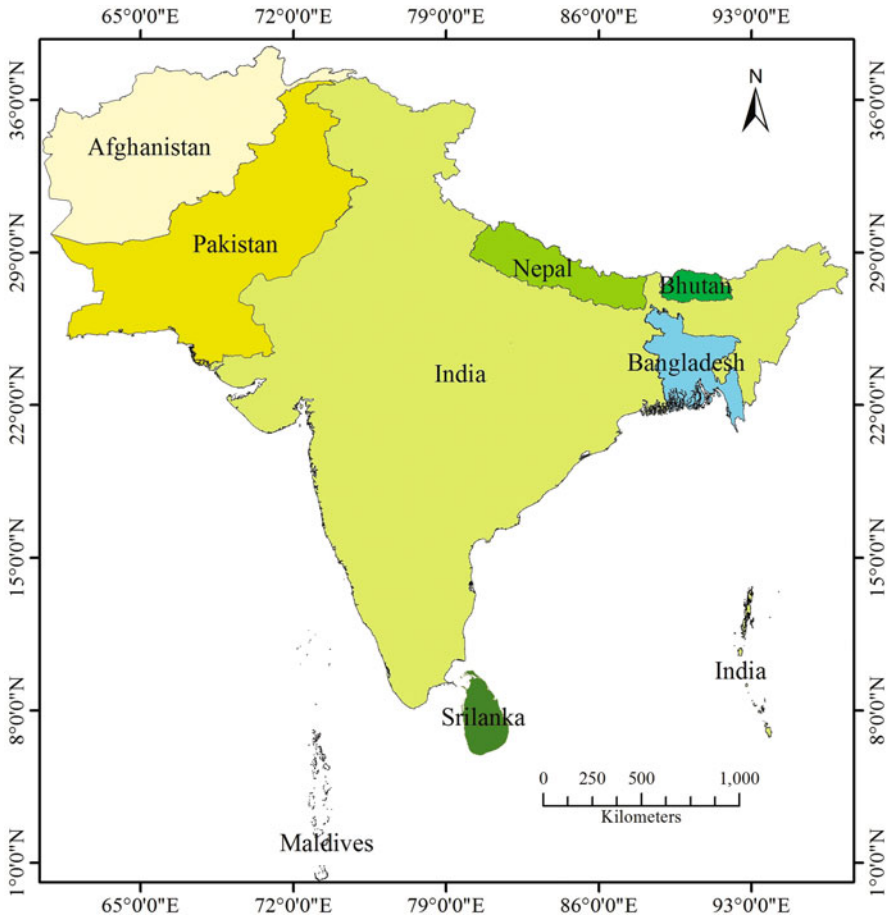


**Fig. 1** Study region showing the South Asian Association for Regional Cooperation (SAARC) nations

(CCCR-IITM), India. The climate data portal of IITM was used for retrieving necessary input files for running JULES.

The CORDEX South ASIA dataset consists of multiple models and scenarios for which daily scenarios have been produced data dynamically downscaled to project for regional analysis. Datasets spatial resolution (~56 km) for projection of regional climate that can be used to estimate change impacts on sensitive processes at large scale for climate gradients. These datasets assist the scientific community to analyze impact at the regional level.

The Fifth Assessment Report (AR5) of IPCC defines a set of scenarios denoted as Representative Concentration Pathways (RCPs) based on climate models (Moss et al. 2010). It represents the greenhouse emission scenario estimates for the future from lower, medium, and higher emissions scenarios. The CCCR-IITM data node has published datasets for multiple CORDEX South Asia Regional Climate Model

**Table 1** Input, output, and plant functional type (PFT) represented in the JULES model

| Model         | Required input  | PFTs   | Output   | Agriculture(Van den Hoof et al. 2011)  |
|---------------|---|--|--|--|
| JULES (v 4.8) | 1. Geographical location<br>2. Air temperature ( $^{\circ}\text{C}$ )<br>3. Diurnal temperature range (K)<br>4. Daily mean precipitation ( $\text{kg m}^{-2} \text{ s}^{-1}$ )<br>5. Frequency of wet days ( $\text{days month}^{-1}$ )<br>6. Incoming shortwave and longwave radiation ( $\text{W m}^{-2}$ )<br>7. Specific humidity ( $\text{kg kg}^{-1}$ )<br>8. Wind speed ( $\text{ms}^{-1}$ )<br>9. Soil type | 1. Broad-leaf trees<br>2. Needle-leaf trees<br>3. C3 grass<br>4. C4 grass<br>5. Shrubs | 1. Soil temperature (K)<br>2. Soil moisture ( $\text{kg m}^{-2} \text{ s}^{-1}$ )<br>3. Surface runoff ( $\text{kg m}^{-2} \text{ s}^{-1}$ )<br>4. Plant respiration ( $\text{kg C m}^{-2} \text{ s}^{-1}$ )<br>5. Soil evaporation ( $\text{kg m}^{-2} \text{ s}^{-1}$ )<br>6. Gross primary productivity ( $\text{kg C m}^{-2} \text{ s}^{-1}$ )<br>7. NPP ( $\text{kg C m}^{-2} \text{ s}^{-1}$ )<br>8. Soil respiration (i.e., $\text{CO}_2$ emitted) ( $\text{kg C m}^{-2} \text{ s}^{-1}$ )<br>9. Surface fluxes of heat ( $\text{W m}^{-2}$ )<br>10. Surface fluxes of carbon ( $\text{CO}_2$ and methane) ( $\text{kg C m}^{-2}$ [360 days] $^{-1}$ ). | C3 grass as crop<br>C4 grass as crop<br>Grassland biome (staple food wheat and corn) (Ellis and Ramankutty 2008) |

(RCM) experiments. For this study, low emission scenario represented by RCP 2.6 was used for assessing the productivity of the agriculture region for the year 2050.

### 2.2.1 Parameterization of the JULES Model

The simulation was done for the agriculture regions of the landscape by setting the parameters of PFT3 and PFT4 which is a representation of C3 grass and C4 grass (Essery et al. 2001). The leaf area index (LAI) along with height of canopy have been estimated for daily mean value for the geographical land cover types including crops, herds, grass in temperate and tropical ecosystems, etc. (Breuer et al. 2003; Groenendijk et al. 2011). The JULES includes parameters of rooting depth and simulates fluxes over temperate and tropical agriculture cropland. In its process, the photosynthesis of leaf equations for the agriculture to calculate the carboxylation rate and leaf nitrogen concentration are however different in agriculture crops and grasses (Schulze et al. 1994; Wullschleger 1993). Other important factors to be considered are the infiltration enhancement to identify natural and managed ecosystems and the fluxes during simulation (House et al. 2001; Ndiaye et al. 2007). The seasonal time series LAI is used for prescribing the agriculture crop phenology. The LAI, rooting depth, and canopy height in the model are used to segregate the agriculture crop species (Debaeke 2004).

The JULES v.4.8 describes vegetation in a grid box using five PFTs (PFT 1: broad-leaf trees, PFT2: needle-leaf trees, PFT3: C3 grasses, PFT4: C4 grasses, and PFT5: shrubs) (Table 1).

### 2.2.2 Assessment of Productivity of the Agriculture Landscape

The representation of a landscape in JULES is through PFTs at a grid cell size of  $0.5^\circ \times 0.5$ . The agriculture area of the study region was represented as grids of  $0.5^\circ \times 0.5$  size where a grid may have more than one PFT. In this study, we considered PFT3 and PFT4 as a proxy representation for the agriculture crops. The model was run to reach equilibrium state after a spin-up of 500 years, and the simulated PFT comprising of PFT3 and PFT4 was considered as agriculture lands. To assess the influence of climate change for the year 2050, the model was forced to simulate PFTs and their corresponding productivity using input files of future climate change projection at a spatial resolution of 0.5. To estimate the output of a grid average estimates of productivity (NPP) simulated for PFT3 and PFT4 were calculated for each of the grids and a spatial presentation was done for the study region using Hexagon-Geomedia software.

$$NPP = \frac{1}{2} \sum_{pi=1}^2 (NPPpi) \quad (1)$$

where NPP is the average NPP simulated in a grid for PFT3 and PFT4,  $NPPpi$  specifies PFT3, and PFT4 is simulated by JULES.

## 3 Results and Discussion

The agriculture land NPP for the scenarios RCP 2.6 for the year 2050 using the JULES simulation model (Fig. 1a) was a range between 0 and 3.5 Mg-C/ha/year. The recent current MODIS 17A NPP agriculture land (Fig. 1a) was in between 0.5 and 4.4 Mg-C/ha/year.

The scenarios based NPP were compared with current recent NPP was shown as decreasing change (Fig. 1b), its value ranges between 0 and 4.4 Mg-C/ha/year. The value of NPP was decreased in agricultural land with the highest value in the southern part and coastal region of Bangladesh (3%) and India (15%) (Table 2) (Fig. 1b). Least in the northern Himalayan region including Afghanistan (45%), India (2.7%), Nepal (26%), and Pakistan (6%) (Table 2). Moderate change in NPP in the region Afghanistan (55%), Bangladesh (96%), Bhutan (100%), India (82.4%), Maldives (100%), Nepal (74%), Pakistan (94%), and Sri Lanka (100%) (Table 2) (Fig. 2).



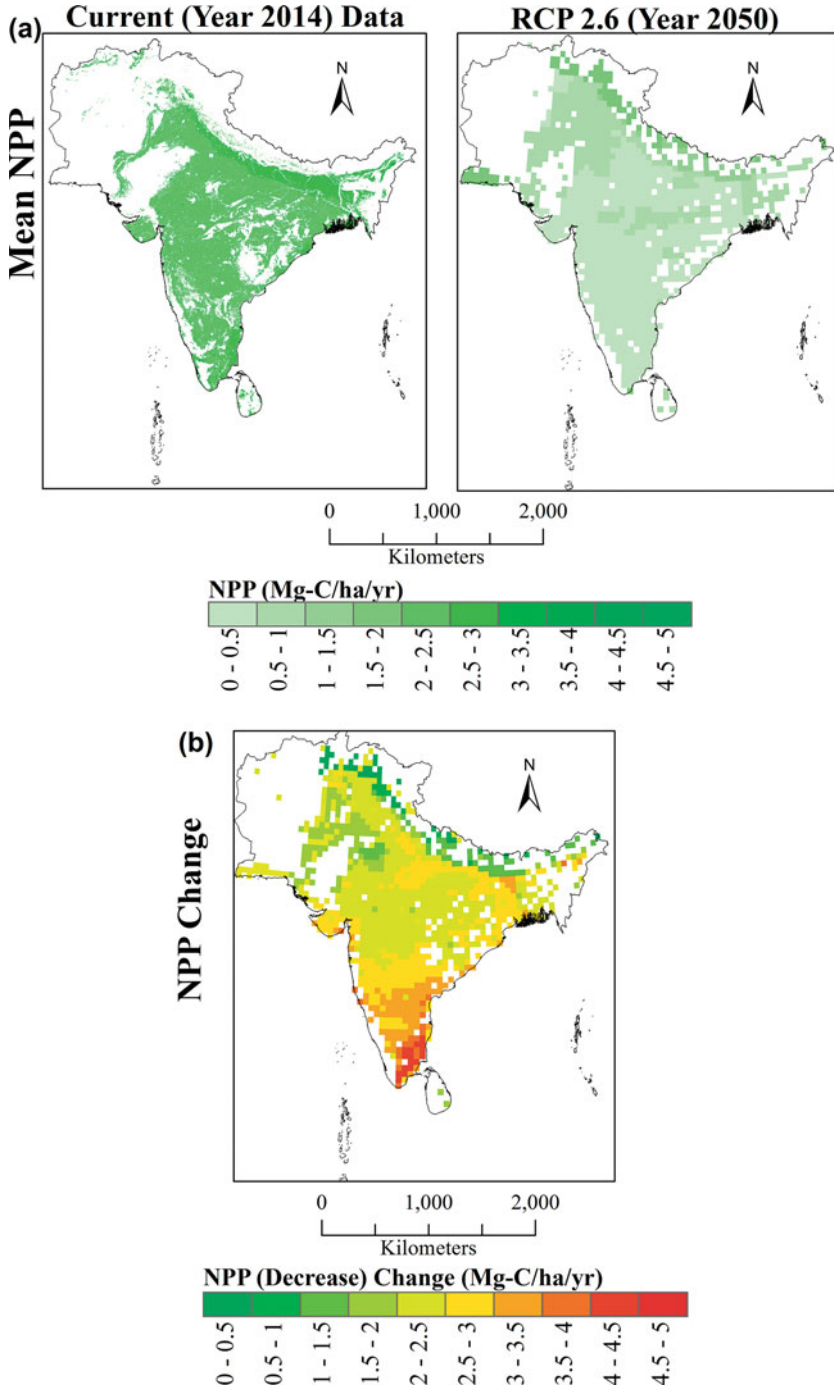


Fig. 2 (a) NPP for the current recent year 2014 and RCP 2.6, the year 2050 (b) NPP change RCP 2050 as a comparison to the current year 2014



| Input file  | Output file   | Plant functional type (PFT)  |
|---|---|--|
| 1. Geographical location<br>2. Air temperature ( $^{\circ}\text{C}$ )<br>3. Diurnal temperature range (K)<br>4. Daily mean precipitation ( $\text{kg m}^{-2} \text{ s}^{-1}$ )<br>5. Frequency of wet days ( $\text{days month}^{-1}$ )<br>6. Incoming shortwave and longwave radiation ( $\text{W m}^{-2}$ )<br>7. Specific humidity ( $\text{kg kg}^{-1}$ )<br>8. Wind speed ( $\text{ms}^{-1}$ )<br>9. Soil type | 1. Soil temperature (K)<br>2. Soil moisture ( $\text{kg m}^{-2} \text{ s}^{-1}$ )<br>3. Surface runoff ( $\text{kg m}^{-2} \text{ s}^{-1}$ )<br>4. Plant respiration ( $\text{kg C m}^{-2} \text{ s}^{-1}$ )<br>5. Soil evaporation ( $\text{kg m}^{-2} \text{ s}^{-1}$ )<br>6. Gross primary productivity ( $\text{kg C m}^{-2} \text{ s}^{-1}$ )<br>7. NPP ( $\text{kg C m}^{-2} \text{ s}^{-1}$ )<br>8. Soil respiration (i.e., $\text{CO}_2$ emitted) ( $\text{kg C m}^{-2} \text{ s}^{-1}$ )<br>9. Surface fluxes of heat ( $\text{W m}^{-2}$ )<br>10. Surface fluxes of carbon ( $\text{CO}_2$ and methane) ( $\text{kg C m}^{-2} [\text{360 days}]^{-1}$ ) | 1. PFT1: Broad-leaf trees<br>2. PFT2: Needle-leaf trees<br>3. PFT3: C3 grass<br>4. PFT4: C4 grass<br>5. PFT5: Shrubs |

The recent current MODIS 17A product time means NPP for the period in-between year 2000–2014. The MODIS 17A accessed through data its portal (<https://modis.gsfc.nasa.gov>), the sum of PFT3(C3) and PFT4(C4) time mean value is used, which is expressed in Eq. 1. The SAARC nations International Geosphere–Biosphere Programme (IGBP) land cover data used to access the agriculture land cover for the year 2014. The IGBP agriculture (2014) land cover used for masking the MODIS 17A and JULES simulated agriculture NPP data.

## 4 Conclusion

The analysis reveals that agriculture production for the scenario RCP 2.6 the year 2050 was moderately decreased and net primary productivity decrease for c.a. 87% of land cover NPP ranges between 1 and 3 Mg-C/ha/year. The highest NPP decrease for c.a. 3% of land cover ranges between 3 and 5 Mg-C/ha/year and least change for c.a. 10% of the SAARC nations' agricultural land cover. The nations fall in the moderate change in NPP were Afghanistan (55%), Bangladesh (96%), Bhutan (100%), India (82.4%), Maldives (100%), Nepal (74%), Pakistan (94%), and Sri Lanka (100%). Overall, the SAARC region NPP change moderately for the low emission scenarios RCP 2.6 in the year 2050.

The simulation model provides the NPP daily for the agriculture and forestry changes to better understand the ecosystem services (Kumar et al. 2019a, b; Wolff et al. 2018). It simulates the output based on regional data to predict the global region output for the different climate conditions, plants, and geographic areas, but other techniques fail to run together on multiple plant species. In our further studies about the agriculture and forestry, the simulation-based NPP, Leaf Area Index (LAI), and

evapotranspiration (ET) are used to access the plants sensitivity, adaptability, and vulnerability for the global perspective. It is not possible through basic methods on indicators-weight method, correlation, regression for the long term in a global perspective (Cutter 2017; Kumar et al. 2018a; Singh et al. 2020a, b). It is very useful for the global agencies for the future levels of planning and fundraising for a food security vulnerability, plant sensitivity analysis, adaptability of plant, terrestrial carbon, yield prediction, and land resources monitoring. We also emphasize on creation of local high-scale climate model data, which will be useful for mapping of the plants at high scale.

This study shapes the justification for considering Geographic Information (GI) science, which evolves new processes, integrated framework, and directions. It is progressively being used for vegetation studies to solemnise information representing location-based information. It identifies a new paradigm for remote sensing data simulation for mapping agriculture and forestry resource. The GI science DGVM simulation processes involve recent current and modelled, time-series, global multisource parameters for the geophysical process at per-pixel grid-level analysis, although it delineates vegetation productivity and other growth interpretations. The provision for the next level of improvements and customization for future advancement scope.

## References

- Acevedo, M. F. (2011). Interdisciplinary progress in food production, food security and environment research. *Environmental Conservation*. <https://doi.org/10.1017/S0376892911000257>.
- Breuer, L., Eckhardt, K., & Frede, H. G. (2003). Plant parameter values for models in temperate climates. *Ecological Modelling*. [https://doi.org/10.1016/S0304-3800\(03\)00274-6](https://doi.org/10.1016/S0304-3800(03)00274-6).
- Chatterjee, B., Khadka, M., 2011. Climate change and food security in South Asia.
- Cox, P. M. (2001). Description of the TRIFFID dynamic global vegetation model. *Hadley Centre Technical Note*, 24, 1–16.
- Cox, P. M., Betts, R. A., Bunton, C. B., Essery, R. L. H., Rowntree, P. R., & Smith, J. (1999). The impact of new land surface physics on the GCM simulation of climate and climate sensitivity. *Climate Dynamics*, 15, 183–203.
- Cutter, S. L. (2017). The perilous nature of food supplies: Natural hazards, social vulnerability, and disaster resilience. *Environment Science and Policy for Sustainable Development*. <https://doi.org/10.1080/00139157.2017.1252603>.
- Cutter, S. L., & Finch, C. (2008). Temporal and spatial changes in social vulnerability to natural hazards. *Proceedings of the National Academy of Sciences*. <https://doi.org/10.1073/pnas.0710375105>.
- Debaeke, P. (2004). Scenario analysis for cereal management in water-limited conditions by the means of a crop simulation model (STICS). *Agronomie*. <https://doi.org/10.1051/agro:2004035>.
- Diaz, S., & Cabido, M. (1997). Plant functional types and ecosystem function in relation to global change. *Journal of Vegetation Science*. <https://doi.org/10.2307/3237198>.
- Ellis, E. C., & Ramankutty, N. (2008). Putting people in the map: Anthropogenic biomes of the world. *Front. Ecological Environment*, 14, 439–447. <https://doi.org/10.1890/070062>.
- Essery, R., Best, M., & Cox, P. (2001). *MOSES 2.2 technical documentation* (Hadley Centre Technical Note, UK met office London UK Vol. 30).

- FAO. (2009). *How to feed the world in 2050: High level expert forum*. FAO. <https://doi.org/10.1111/j.1728-4457.2009.00312.x>.
- Fuss, S., Havlík, P., Szolgayová, J., Schmid, E., Reuter, W. H., Khabarov, N., Obersteiner, M., Ermoliev, Y., Ermolieva, T., & Kraxner, F. (2015). Global food security & adaptation under crop yield volatility. *Technological Forecasting and Social Change*, 98, 223–233. <https://doi.org/10.1016/j.techfore.2015.03.019>.
- Gerlitz, J.-Y., Macchi, M., Brooks, N., Pandey, R., Banerjee, S., & Jha, S. K. (2017). The multidimensional livelihood vulnerability index—an instrument to measure livelihood vulnerability to change in the Hindu Kush Himalayas. *Climate and Development*, 9, 124–140.
- Gregory, P. J., Ingram, J. S. I., Andersson, R., Betts, R. A., Brovkin, V., Chase, T. N., Grace, P. R., Gray, A. J., Hamilton, N., Hardy, T. B., Howden, S. M., Jenkins, A., Meybeck, M., Olsson, M., Ortiz-Monasterio, I., Palm, C. A., Payn, T. W., Rummukainen, M., Schulze, R. E., Thiem, M., Valentin, C., & Wilkinson, M. J. (2002). Short communication: Environmental consequences of alternative practices for intensifying crop production. *Agriculture, Ecosystems and Environment*. [https://doi.org/10.1016/S0167-8809\(01\)00263-8](https://doi.org/10.1016/S0167-8809(01)00263-8).
- Gregory, P. J., Ingram, J. S. I., & Brklacich, M. (2005). Climate change and food security. *Philosophical Transactions of the Royal Society B: Biological Sciences*. <https://doi.org/10.1098/rstb.2005.1745>.
- Groenendijk, M., Dolman, A. J., van der Molen, M. K., Leuning, R., Arneeth, A., Delpierre, N., Gash, J. H. C., Lindroth, A., Richardson, A. D., Verbeeck, H., & Wohlfahrt, G. (2011). Assessing parameter variability in a photosynthesis model within and between plant functional types using global Fluxnet eddy covariance data. *Agricultural and Forest Meteorology*. <https://doi.org/10.1016/j.agrformet.2010.08.013>.
- Haxeltine, A., & Colin Prentice, I. (1996). BIOME3: An equilibrium terrestrial biosphere model based on ecophysiological constraints, resource availability, and competition among plant functional types. *Global Biogeochemical Cycles*, 10, 693–709. <https://doi.org/10.1029/96GB02344>.
- Herrero, M., Thornton, P. K., Power, B., Bogard, J. R., Remans, R., Fritz, S., Gerber, J. S., Nelson, G., See, L., Waha, K., Watson, R. A., West, P. C., Samberg, L. H., van de Steeg, J., Stephenson, E., van Wijk, M., & Havlík, P. (2017). Farming and the geography of nutrient production for human use: A transdisciplinary analysis. *The Lancet Planetary Health*. [https://doi.org/10.1016/S2542-5196\(17\)30007-4](https://doi.org/10.1016/S2542-5196(17)30007-4).
- House, M. L., Powers, W. L., Eisenhauer, D. E., Marx, D. B., & Fekersillassie, D. (2001). Spatial analysis of machine-wheel traffic effects on soil physical properties. *Soil Science Society of America Journal*. <https://doi.org/10.2136/sssaj2001.6551376x>.
- Ingram, J., Erickson, P., & Diana, L. (2010). Food security and global environmental change. *VASA*. <https://doi.org/10.1016/j.envsci.2009.04.007>.
- Kalra, N., & Kumar, M. (2018). Simulating the impact of climate change and its variability on agriculture. In S. Sheraz Mahdi (Ed.), *Climate change and agriculture in India: Impact and adaptation* (pp. 21–28). Cham: Springer. [https://doi.org/10.1007/978-3-319-90086-5\\_3](https://doi.org/10.1007/978-3-319-90086-5_3).
- Kucharik, C. J., Foley, J. A., Delire, C., Fisher, V. A., Coe, M. T., Lenters, J. D., Young-Molling, C., & Ramankutty, N. (2000). Testing the performance of a dynamic global ecosystem model: Water balance, carbon balance, and vegetation structure. *Global Biogeochemical Cycles*, 14, 795–825. <https://doi.org/10.1029/1999GB001138>.
- Kumar, M., Rawat, S. P. S., Singh, H., Ravindranath, N. H., & Kalra, N. (2018a). Dynamic forest vegetation models for predicting impacts of climate change on forests: An Indian perspective. *Indian Journal of Forestry*, 41, 1–12.
- Kumar, M., Singh, H., Pandey, R., Singh, M. P., Ravindranath, N. H., & Kalra, N. (2018b). Assessing vulnerability of forest ecosystem in the Indian Western Himalayan region using trends of net primary productivity. *Biodiversity and Conservation*, 1–20.
- Kumar, M., Savita, & Kushwaha, S. P. S. (2019a). Managing the forest fringes of India: A national perspective for meeting the sustainable development goals. In *Sustainability perspectives: Science, policy and practice, strategies for sustainability* (p. 331). Cham: Springer Nature.

- Kumar, M., Savita, Singh, H., Pandey, R., Singh, M. P., Ravindranath, N. H., & Kalra, N. (2019b). Assessing vulnerability of forest ecosystem in the Indian Western Himalayan region using trends of net primary productivity. *Biodiversity and Conservation*, 28, 2163–2182. <https://doi.org/10.1007/s10531-018-1663-2>.
- Mishra, V., Cherkauer, K. A., Niyogi, D., Lei, M., Pijanowski, B. C., Ray, D. K., Bowling, L. C., & Yang, G. (2010). A regional scale assessment of land use/land cover and climatic changes on water and energy cycle in the upper Midwest United States. *International Journal of Climatology*. <https://doi.org/10.1002/joc.2095>.
- Moss, R. H., Edmonds, J. A., Hibbard, K. A., Manning, M. R., Rose, S. K., Van Vuuren, D. P., Carter, T. R., Emori, S., Kainuma, M., & Kram, T. (2010). The next generation of scenarios for climate change research and assessment. *Nature*, 463, 747.
- Ndiaye, B., Molénat, J., Hallaire, V., Gascuel, C., & Hamon, Y. (2007). Effects of agricultural practices on hydraulic properties and water movement in soils in Brittany (France). *Soil and Tillage Research*. <https://doi.org/10.1016/j.still.2006.04.005>.
- Peng, C. (2000). From static biogeographical model to dynamic global vegetation model: A global perspective on modelling vegetation dynamics. *Ecological Modelling*.
- Raich, J. W. (1991). Potential net primary productivity in South America: Application of a global model. *Ecological Applications*, 1, 399–429. <https://doi.org/10.2307/1941899>.
- Ranuzzi, A., & Srivastava, R. (2012). *Impact of climate change on agriculture and food security in India. ICRIER policy series, No. 16 (may)*. New Delhi: Indian Council for Research on International Economic Relations (ICRIER).
- Roetter, R. P., Van Keulen, H., Kuiper, M., & Verhagen, J. (2007). Science for agriculture and rural development in low-income countries. *Science for Agriculture and Rural Development in Low-income Countries*. <https://doi.org/10.1007/978-1-4020-6617-7>.
- Savita, Kumar, M., & Kushwaha, S. P. S. (2018). Forest resource dependence and ecological assessment of forest fringes in Rainfed districts of India. *Indian Forestry*, 144, 211–220.
- Schulze, E. D., Kelliher, F. M., Korner, C., Lloyd, J., & Leuning, R. (1994). Relationships among maximum stomatal conductance, ecosystem surface conductance, carbon assimilation rate, and plant nitrogen nutrition: A global ecology scaling exercise. *Annual Review of Ecology and Systematics*. <https://doi.org/10.1146/annurev.es.25.110194.003213>.
- Singh, R. K., Sinha, V. S. P., Joshi, P. K., & Kumar, M. (2019). Multi-temporal data anomaly removal for the agriculture. *Forest and Other Land Use. Indian J. For.*, 42, 22–25.
- Singh, R. K., Sinha, V. S. P., Joshi, P. K., & Kumar, M. (2020). A multinomial logistic model-based land use and land cover classification for the South Asian association for regional cooperation nations using moderate resolution imaging Spectroradiometer product. *Environmental Development and Sustainability*. <https://doi.org/10.1007/s10668-020-00864-1>.
- Singh, H., Yadav, M., Kumar, N., Kumar, A., & Kumar, M. (2020a). Assessing adaptation and mitigation potential of roadside trees under the influence of vehicular emissions: A case study of *Grevillea robusta* and *Mangifera indica* planted in an urban city of India. *PLoS One*. <https://doi.org/10.1371/journal.pone.0227380>.
- Singh, R. K., Sinha, V. S. P., Joshi, P. K., & Kumar, M. (2020b). Modelling agriculture, forestry and other land use (AFOLU) in response to climate change scenarios for the SAARC nations. *Environmental Monitoring and Assessment*, 192, 236. <https://doi.org/10.1007/s10661-020-8144-2>.
- Sitch, S., Smith, B., Prentice, I. C., Arneth, A., Bondeau, A., Cramer, W., Kaplan, J. O., Levis, S., Lucht, W., & Sykes, M. T. (2003). Evaluation of ecosystem dynamics, plant geography and terrestrial carbon cycling in the LPJ dynamic global vegetation model. *Global Change Biology*, 9, 161–185.
- Sitch, S., Huntingford, C., Gedney, N., Levy, P. E., Lomas, M., Piao, S. L., Betts, R., Ciais, P., Cox, P., Friedlingstein, P., Jones, C. D., Prentice, I. C., & Woodward, F. I. (2008). Evaluation of the terrestrial carbon cycle, future plant geography and climate-carbon cycle feedbacks using five Dynamic Global Vegetation Models (DGVMs). *Global Change Biology*. <https://doi.org/10.1111/j.1365-2486.2008.01626.x>.

- Thenkabail, P. S. (2015). Remote sensing of land resources: Monitoring, modeling, and mapping advances over the last 50 years and a vision for the future. *Land Resources Monitoring Modeling, and Mapping with Remote Sensing*. <https://doi.org/10.1201/b19322>.
- Thomson, K. (2003). World agriculture: Towards 2015/2030: An FAO perspective. *Land Use Policy*, 20, 375. [https://doi.org/10.1016/s0264-8377\(03\)00047-4](https://doi.org/10.1016/s0264-8377(03)00047-4).
- Tilman, D., Balzer, C., Hill, J., & Befort, B. L. (2011). Global food demand and the sustainable intensification of agriculture. *Proceedings of the National Academy of Sciences of the United States of America*. <https://doi.org/10.1073/pnas.1116437108>.
- Van den Hoof, C., Hanert, E., & Vidale, P. L. (2011). Simulating dynamic crop growth with an adapted land surface model – JULES-SUCROS: Model development and validation. *Agricultural and Forest Meteorology*, 151, 137–153. <https://doi.org/10.1016/j.agrformet.2010.09.011>.
- Wardlow, B. D., Egbert, S. L., & Kastens, J. H. (2007). Analysis of time-series MODIS 250 m vegetation index data for crop classification in the U.S. Central Great Plains. *Remote Sensing of Environment*, 108, 290–310. <https://doi.org/10.1016/j.rse.2006.11.021>.
- West, P. C., Gibbs, H. K., Monfreda, C., Wagner, J., Barford, C. C., Carpenter, S. R., & Foley, J. A. (2010). Trading carbon for food: Global comparison of carbon stocks vs. crop yields on agricultural land. *Proceedings of the National Academy of Sciences of the United States of America*. <https://doi.org/10.1073/pnas.1011078107>.
- Wezel, A., & Soldat, V. (2009). A quantitative and qualitative historical analysis of the scientific discipline of agroecology. *International Journal of Agricultural Sustainability*. <https://doi.org/10.3763/ijas.2009.0400>.
- Wolff, N. H., Masuda, Y. J., Meijaard, E., Wells, J. A., & Game, E. T. (2018). Impacts of tropical deforestation on local temperature and human Well-being perceptions. *Global Environmental Change*. <https://doi.org/10.1016/j.gloenvcha.2018.07.004>.
- World Bank, (2011). World Bank Data Base [WWW document]. URL. <http://databank.worldbank.org/data/reports.aspx?source=population-estimates-and-projections>. Accessed 1 Jan 16.
- Wullschleger, S. D. (1993). Biochemical limitations to carbon assimilation in C3 plants – A retrospective analysis of the A/Ci curves from 109 species. *Journal of Experimental Botany*. <https://doi.org/10.1093/jxb/44.5.907>.
- Xiong, W., Conway, D., Holman, I., & Lin, E. (2008). Evaluation of CERES-wheat simulation of wheat production in China. *Agronomy Journal*. <https://doi.org/10.2134/agronj2008.0081>.
- Yun, J. I. (2003). Predicting regional rice production in South Korea using spatial data and crop-growth modeling. *Agricultural Systems*. [https://doi.org/10.1016/S0308-521X\(02\)00084-7](https://doi.org/10.1016/S0308-521X(02)00084-7).

**Part V**  
**GIScience for Revolution in Science and**  
**Society**

# Future Direction of GIScience for Revolution in Science and Society Over the Past 20 Years



Bharat Lal, Susheel Kumar Singh, Meenu Rani, Abhishek Kumar Shukla, and Pavan Kumar 

**Abstract** Geographic Information Science (GIScience) plays a vital role in today's era. Prior to the development of GIScience, all these tasks were done on a human level in which not only a lot of time and capital was used but actual knowledge of the subject matter was also not possible, because it was not always possible to reach a particular place. GIScience is based on Sudur sensor calculators, so that no aspect of the Earth can be hidden. It is partly covered with the various traditional disciplines like environmental science, applied mathematics, geophysics, geography, oceanography, spatial statistics, etc. GIScience came into the market between 1990 and 1992 as a game changer which contributed to the formation of geographical information science (GIS). The work potential of contributing to the work was discovered through this science, including database designing and modeling can be done in any area. This technology is used in scientific research, resource management, asset management, archaeological work, urbanization, and criminology. There are a variety of applied fields of GIScience which are used in current scenarios for the better understanding, interpretation, and visualization of the data.

**Keywords** GIScience · GIS · Digital technology

Geographic Information Science (GIScience) is a recent, universal, up-and-coming, hi-tech, interdisciplinary scientific discipline. The concept of GIScience was first advocate by Professor Michael F. Goodchild, University of California. Goodchild is

---

B. Lal · S. K. Singh · A. K. Shukla  
College of Agriculture, Rani Lakshmi Bai Central Agricultural University, Jhansi, Uttar Pradesh, India

M. Rani  
Department of Geography, Kumaun University, Nainital, Uttarakhand, India

P. Kumar (✉)  
College of Horticulture and Forestry, Rani Lakshmi Bai Central Agricultural University, Jhansi, Uttar Pradesh, India

globally known as the Father of GIScience in the present age of g-Governance (Goodchild 1992). As presented by Goodchild, the evolution of GIScience is traced back to two keynote addresses entitled “Spatial Information Science and Progress on the GIS Research Agenda” at the Fourth International Symposium on Spatial Data Handling held in Zurich, Switzerland, July 1990; and Second European Geographic Information System (GIS) Conference held in Brussels, Belgium, April 1991, respectively (Peucker et al. 1978; Tobler 1970; Tomlin 1990; Tomlinson 1968). GIScience includes the accessible technologies and cartographic research areas (map-making), geographic information systems (GIS), surveying (accurate measurement of features on the Earth surface), digital image processing (processing and analyzing of satellite data), geodesy (understanding the Earth’s orientation in space, gravity field, and geometric shape), photogrammetry (photography in surveying and mapping), global positioning system or GPS (position information on Earth’s surface assisted by use of satellites), spatial analysis, modeling, and remote sensing (surveillance of Earth observatory distance) (Goodchild 2010; Guttman 1984).

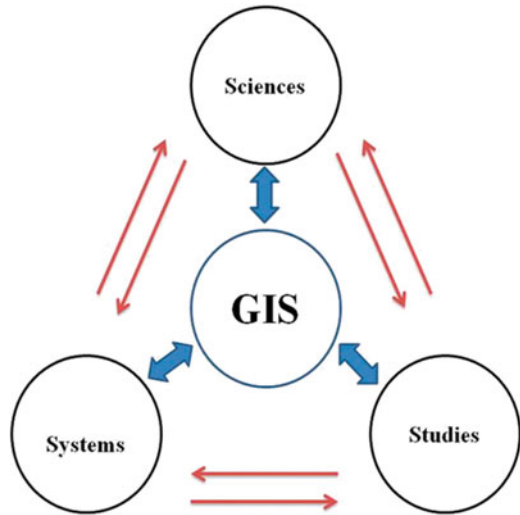
GIScience includes inquiry of visualization, accuracy, cognition, spatial data structures, analysis, meaning, etc. It overlaps with the research area of several traditional disciplines which have mainly focused their research on Earth’s physical processes (e.g., environmental science, geophysics, geography, applied mathematics, oceanography, geology, ecology, physics, spatial statistics, etc.). GIScience also concerned about human–machine interaction (e.g., artificial intelligence, information science, computer science, cognitive psychology, cognitive science, etc.). Despite the fact, GIScience represent a new kind of scientific collaborative among all these disciplines. In view of application of GIScience in governance, civil society, academia industry, research and development, curriculum of GIScience was designed first time under the coordinatorship of Professor Michael Frank Goodchild in USA (Goodchild 2003). GIScience was introduced at postgraduate level first time in the University of California under Department of Geography. Presently, the GIScience is a Master’s degree program in more than two dozen universities of Malaysia, Canada, USA, UK, Australia, and many more. GIScience provide tools that facilitate end users to execute spatial analysis and queries, help to improve spatial data, and create printed maps (Fig. 1).

## 1 History of GIScience

The GIScience history can be dated back when Michael F. Goodchild challenged the academic community of GI science to budge beyond the principal focus of the practical prospective to more substantial intellectual confronts and logical enquiry arise by GIS use, or the hindrance to its use, as he addressed at the Fourth International Symposium entitled “Spatial Information Science.” GIScience has played a crucial and significant role in the assessment of the physical characteristics of the Earth surface over a decade. With the advancement of GIScience technologies specifically in GIS, geomorphologic mapping has provided us with core data of



**Fig. 1** Conceptual relation among the sciences, systems, and studies of GIS technologies



landform development (Fisher 2001; Goodchild 2006). Geophysical or climatic events includes earthquakes, volcanic eruptions, landslides, cyclones, etc. Awareness of GIScience has increased significantly, for example, Web GIS, Volunteer GIS, Geo-Portal, g-Governance, Cloud Server, Neighborhood Mapping, Mobile Mapping, Ontology, LBS, GeoDesign, etc., and the discipline has developed with a much broader set of applications for the dissemination of output results. GIScience has become functional and almost obligatory in a wide range of anthropogenic activities, from Earth science to human health, and from transportation to management of resources. GIScience is the potent technology that has facilitated convenience companies to budge to a higher level of efficiency in their management of network distribution, and package delivery companies to save millions in delivery costs (Goodchild and Hill 2008; Goodchild 2009). Advances in GIScience are indispensable to the further GIS progress and the strategy to the success of the future generations of technology. GIScience history may start between 1990 and 1992, when the game changer contributed to the foundation of geographical information science (Table 1).

National Center for Geographic Information and Analysis (NCGIA) was established in 1988 by the efforts of U.S. National Science Foundation, and these consortiums have three institutions: the University of Maine, the State University of New York at Buffalo, and the University of California situated at Santa Barbara. The primary objectives of NCGIA is to carry out basic research and also providing needful services for the foreign members of geographic information science society (Abler 1987; Bush 1945). A series of meetings at professional conferences were organized by the NCGIA, from which in August 1995 the University Consortium for Geographic Information Science (UCGIS) emerged and it was officially accepted as nonprofit organization in Washington (Caron et al. 2008). The NCGIA initiated Project Varenus in 1997 which focused on different crucial areas of GIScience

**Table 1** Chronological contribution for GIScience before Goodchild

| Scientists          | Contributions on GIScience   |
|---------------------|--|
| Bush 1945           | As we may think  |
| Tomlinson 1968      | GIS development for local and regional planning  |
| Hagerstraand, 1970  | What people think in regional and local science  |
| Tobler 1970         | A computer-based simulation modeling through urban growth                                      |
| Dutton 1978         | Topological statistical infrastructure for GIS in first international advanced study symposium |
| Peucker et al. 1978 | Triangulated irregular network (TIN)   |
| Hayes, 1979         | The naive physics policy   |
| Guttman 1984        | A dynamic index infrastructure for spatial modeling (R-trees)                                  |
| Abler 1987          | Center for GIS and analysis (NCGIA)  |
| Tomlin 1990         | GIS and cartographic modeling  |

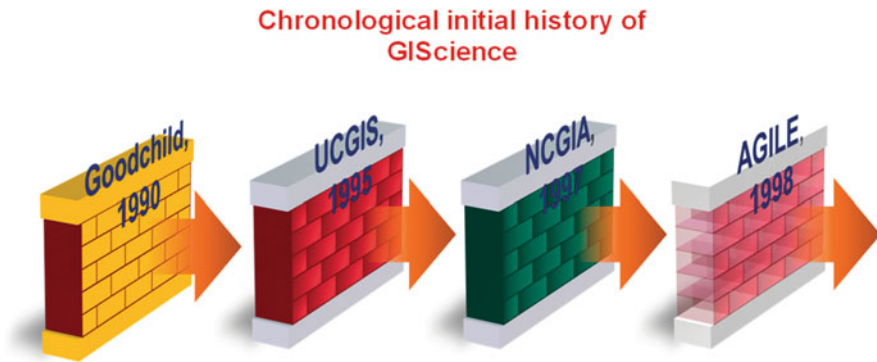


**Fig. 2** Chronological initial history of GISciences

important for twenty-first century; these areas were cognitive representation of geographical area, computational implementation of geographic concept, etc. UCGIS is non-profitable organization which forms and endorses the scientific community of GIScience research and education. Major research priorities of UCGIS is cartography, geodetic science, geography, computer science, statistics, cognitive science, environmental science, landscape architecture, remote sensing and photogrammetry, public policy, engineering, and land surveying law, etc.

Established in 1998, the Association of Geographic Information Laboratories for Europe (AGILE) has a similar goal as UCGIS and works toward continuing the European GIS conferences. AGILE promotes and helps to develop GIScience initiatives. The aim of the AGILE is to speed up the research and teaching on GIS up to the European level. It gives a permanent scientific forum for exchanging knowledge throughout the geographic information researchers (Dutton 1978; Egenhofer et al. 2003) (Fig. 2).

## 2 Propagation of the Term GIScience in the World in Last Two Decades

### 2.1 GIScience in Human Society

GIScience is an emerging science which is becoming most popular in the developing scientific world because it creates interest in current generation of scientific world for understand the things involved in the system and that help to the resolve the upcoming problems. We tried to quantify the popularity of this science on the basis of searching key terms of GIScience in the *ScienceDirect*, a peer-reviewed journal of Elsevier library (Elwood 2010; Hagerstraandh 1970). The publication of various researches on GIScience started from 1999 in the Elsevier library, and the publication data of GIScience paper were taken up to the March 2020. The publication details on GIScience are presented in Fig. 3 and Table 2. While Table 2 shows the publication of GIScience in a 5-year interval, there are only two publications reported up to the year 2000, which increased to 35 after the 5-year interval, and reached 229 publications up to March 2020. This shows that the publication on GIScience enlarged after the emergence of GIScience, increasing day by day. The increasing data represents how the popularity of GIScience has enhanced from the period of its emergence till March 2020 (Hayesh 1979).

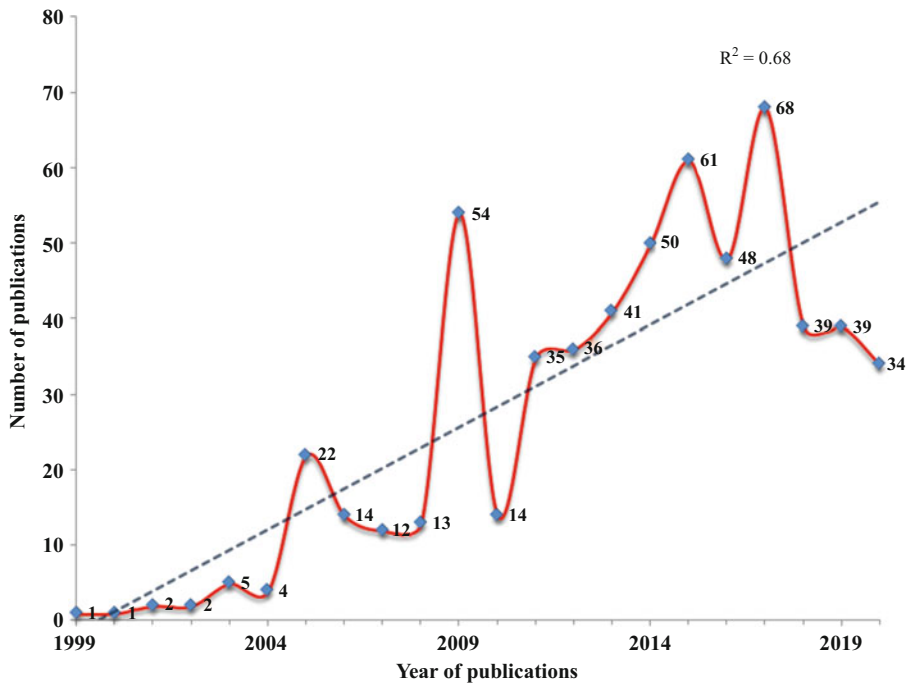


**Fig. 3** Total number of publications, given chronologically, of GIScience literature in Elsevier library during the last 20 years

**Table 2** List of GIScience publications in *ScienceDirect*

| Year of publications | No of publications |
|----------------------|--------------------|
| Up to 2000           | 2                  |
| 2001–2005            | 35                 |
| 2006–2010            | 107                |
| 2011–2015            | 223                |
| 2016–March 2020      | 229                |

The chronological development of research agenda of GIScience under the Elsevier peer-review library searched by using keywords of GIScience in last 20 years are depicted in Fig. 3. The graph showed that very few publications were reported in the early stage of development, that is, only one publication on the title integrating GIS with hydrological modeling: practice, problems, and prospects which published in the journal *Computers, Environment and Urban Systems*; the publication rate increased with the increasing intervals after the emergence of GIScience (Kuhn 2003; Longley et al. 2005). During 2009, the total number of publications enhanced above 50 (i.e., 54) and the maximum number of publications on GIScience in Elsevier library was recorded (68) in the year 2017; while 34 papers have been published in first three months of 2020, they will increase before the end of the year.

## 2.2 Research Priority of GIScience

There are various applied fields of GIScience which are used in current scenario for the better understanding, interpretation, and visualization of the data which helps future decision-making (Mark 2000, 2003). The NCGIA have been categorized the GIScience research areas into different categories that are follows.

### 2.2.1 Geographic Information Technologies

There areas under this discipline include remote sensing, photogrammetry, image processing, geodesy, surveying, and cartography.

- Cartography is the art and science of map-making.
- Remote sensing is the science of obtaining information about Earth from space or observation without any physical contact.
- Geodesy is the science of precisely measurement about the Earth.
- Surveying is nothing but the technique or art and science of accurate measurement of all physical and cultural features on the surface of Earth.
- Photogrammetry is the science and technology of extracting reliable information from photographs and images.
- Digital image processing is the science of image data processing, analyzing, and handling of the digital image data.

### 2.2.2 Digital Technology

Under this discipline, databases, computer science, image processing, computational geometry, pattern reorganization, etc. are used for better understanding the data and information. The disciplines of geology, geography, geophysics, oceanography, environmental science, agriculture, ecology, biogeography, biology, political science, sociology, and anthropology help to understand the surface and near-surface phenomena and objects of Earth science (McMaster and Userly 2004; Montello 2009). Nature of human interactions with artificial intelligence, cognitive science, cognitive psychology, and environmental psychology are the major areas which help us to know more about the GIScience and thier allied sectors.

## References

- Abler, R. F. (1987). The national science foundation national center for geographic information and analysis. *International Journal of Geographical Information System*, 1(4), 303–326.
- Bush, V. (1945). As we may think. *The Atlantic Monthly.*, 176(1), 101–108.
- Caron, C., Roche, S., Goyer, D., & Jatou, A. (2008). GIScience journals ranking and evaluation: An international Delphi study. *Transactions in GIS*, 12(3), 293–321.
- Dutton, G. (1978). *First international advanced study symposium on topological data structures for geographic information systems* (pp. 1–8). Cambridge: Harvard University.
- Egenhofer, M. J., Clarke, K. C., Gao, S., Quesnot, T., Franklin, W. R., Yuan, M., & Coleman, D. (2003). *Contribution of GIScience over the past twenty years, advancing geographic information science*. GSDI Association Press.
- Elwood, S. (2010). Geographic information science: Emerging research on the societal implications of the geospatial web. *Progress in Human Geography*, 34(3), 349–357.
- Fisher, P. F. (2001). Citations to the international journal of geographical information systems and science: The first 10 years. *International Journal of Geographical Information Science*, 15, 1–6.
- Goodchild, M. F. (1992). Geographical information science. *International Journal of Geographical Information System*, 6(1), 31–45.
- Goodchild, M. F. (2003). Geographic information science and system for environmental management. *Annual Review of Environment and Resources*, 28, 493–519.
- Goodchild, M. F. (2006). GIScience ten years after ground truth. *Transactions in GIS*, 10(5), 687–692.
- Goodchild, M. F. (2009). Geographical information system and science: Today and tomorrow. *Procedia Earth and Planetary Science*, 1, 1037–1043.
- Goodchild, M. F. (2010). Twenty years of progress: GIScience in 2010. *Journal of Spatial Information Science*, 1, 3–20.
- Goodchild, M. F., & Hill, L. (2008). Introduction to digital gazetteer research. *International Journal of Geographical Information Science*, 22(10), 1039–1044.
- Guttman. (1984). R-trees: A dynamic index structure for spatial searching in SIGMOD'84, international conference on management of data (New York, USA), ACM Press, pp. 47–57.
- Hagerstraandh, T. (1970). What about people in regional science. *Regional Science*, 24(1), 7–24.
- Hayesh, P. J. (1979). The naive physics manifesto. In D. Michie (Ed.), *Expert systems in the micro-electronic age* (pp. 242–270). Edinburgh: Edinburgh University Press.
- Kuhn, W. (2003). Semantic reference systems. *International Journal of Geographical Information Science*, 17(5), 405–409.

- Longley, P. A., Goodchild, M. F., Maguire, D. J., & Rhind, D. W. (2005). *Geographic information system and science*. Hoboken: Wiley.
- Mark, D. M. (2000). Geographic information science: critical issues in an emerging cross-disciplinary research domain. *Journal of the Urban & Regional Information System Association*, 12(1), 45–54.
- Mark, D. M. (2003). Geographic information science: Defining the field. In *Foundations of geographic information science* (pp. 1–18). New York: Taylor and Francis.
- McMaster, R. B., & Usery, E. L. (2004). *Eds; a research agenda for geographic information science*. CRC Press.
- Montello, D. R. (2009). Cognitive research in GIScience: Recent achievements and future prospects. *Geography Compass*, 3(5), 1824–1840.
- Peucker, T. K., Fowler, R. J., Little, J. J., & Mark, D. M. (1978). The triangulated irregular network. In *American Society of Photogrammetry, digital terrain models symposium, USA*, pp. 516–540.
- Tobler, W. R. (1970). A computer movie simulating urban growth in the Detroit region. *Economic Geography*, 46, 234–240.
- Tomlin, C. D. (1990). *Geographic information systems and cartographic modeling*. Englewood: Prentice-Hall.
- Tomlinson, R. F. (1968). A geographic information system for regional planning. In: G.A. Stewart (Ed.), *Symposium on land evaluation, commonwealth scientific and industrial research organization*, Melbourne, Australia.